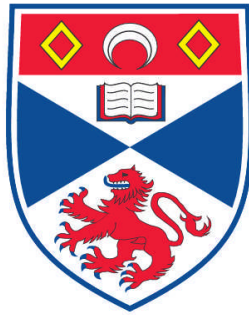


**MHD EVOLUTION OF MAGNETIC NULL POINTS
TO STATIC EQUILIBRIA**

Jorge Fuentes-Fernández

**A Thesis Submitted for the Degree of PhD
at the
University of St. Andrews**



2011

**Full metadata for this item is available in
Research@StAndrews:FullText
at:**

<http://research-repository.st-andrews.ac.uk/>

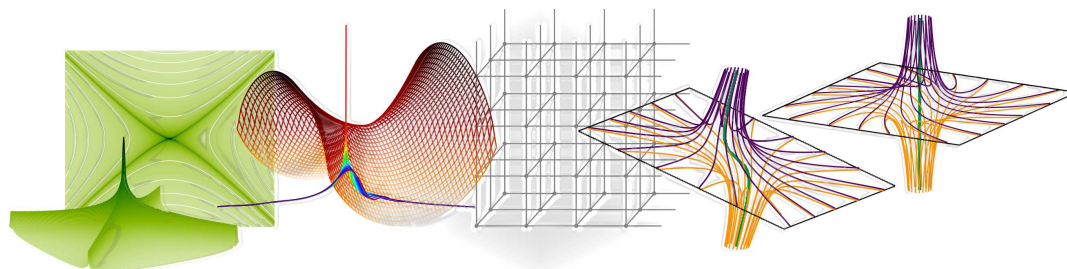
Please use this identifier to cite or link to this item:

<http://hdl.handle.net/10023/1897>

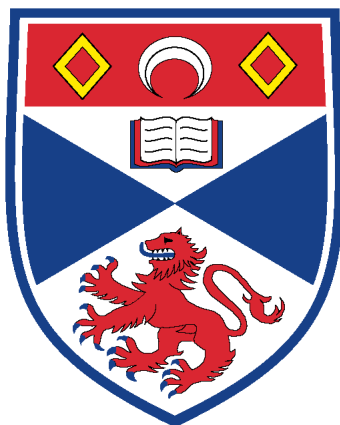
This item is protected by original copyright

**This item is licensed under a
Creative Commons License**

MHD Evolution of Magnetic Null Points to Static Equilibria



Jorge Fuentes-Fernández



Thesis submitted for the degree of Doctor of Philosophy
of the University of St Andrews

November 29, 2010

Declarations

1. Candidate's declarations:

I, Jorge Fuentes Fernández, hereby certify that this thesis, which is approximately 45 000 words in length, has been written by me, that it is the record of work carried out by me and that it has not been submitted in any previous application for a higher degree.

I was admitted as a research student in October 2007 and as a candidate for the degree of Doctor of Philosophy in October 2008; the higher study for which this is a record was carried out in the University of St Andrews between 2008 and 2010.

Date: _____ Signature of Candidate: _____

2. Supervisor's declaration:

I hereby certify that the candidate has fulfilled the conditions of the Resolution and Regulations appropriate for the degree of Doctor of Philosophy in the University of St Andrews and that the candidate is qualified to submit this thesis in application for that degree.

Date: _____ Signature of Supervisor: _____

3. Permission for electronic publication:

In submitting this thesis to the University of St Andrews we understand that we are giving permission for it to be made available for use in accordance with the regulations of the University Library for the time being in force, subject to any copyright vested in the work not being affected thereby. We also understand that the title and the abstract will be published, and that a copy of the work may be made and supplied to any bona fide library or research worker, that my thesis will be electronically accessible for personal or research use unless exempt by award of an embargo as requested below, and that the library has the right to migrate my thesis into new electronic forms as required to ensure continued access to the thesis. We have obtained any third-party copyright permissions that may be required in order to allow such access and migration, or have requested the appropriate embargo below.

The following is an agreed request by candidate and supervisor regarding the electronic publication of this thesis:

Access to Printed copy and electronic publication of thesis through the University of St Andrews.

Date: _____

Signature of Candidate: _____ Signature of Supervisor: _____

Abstract

In magnetised plasmas, magnetic reconnection is the process of magnetic field merging and recombination through which considerable amounts of magnetic energy may be converted into other forms of energy. Reconnection is a key mechanism for solar flares and coronal mass ejections in the solar atmosphere, it is believed to be an important source of heating of the solar corona, and it plays a major role in the acceleration of particles in the Earth's magnetotail. For reconnection to occur, the magnetic field must, in localised regions, be able to diffuse through the plasma. Ideal locations for diffusion to occur are electric current layers formed from rapidly changing magnetic fields in short space scales. In this thesis we consider the formation and nature of these current layers in magnetised plasmas.

The study of current sheets and current layers in two, and more recently, three dimensions, has been a key field of research in the last decades. However, many of these studies do not take plasma pressure effects into consideration, and rather they consider models of current sheets where the magnetic forces sum to zero. More recently, others have started to consider models in which the plasma beta is non-zero, but they simply focus on the actual equilibrium state involving a current layer and do not consider how such an equilibrium may be achieved physically. In particular, they do not allow energy conversion between magnetic and internal energy of the plasma on their way to approaching the final equilibrium.

In this thesis, we aim to describe the formation of equilibrium states involving current layers at both two and three dimensional magnetic null points, which are specific locations where the magnetic field vanishes. The different equilibria are obtained through the non-resistive dynamical evolution of perturbed hydromagnetic systems. The dynamic evolution relaxes via viscous damping, resulting in viscous heating.

We have run a series of numerical experiments using LARE, a Lagrangian-remap code, that solves the full magnetohydrodynamic (MHD) equations with user controlled viscosity and resistivity. To allow strong current accumulations to be created in a static equilibrium, we set the resistivity to be zero and hence simply reach our equilibria by solving the ideal MHD equations.

We first consider the relaxation of simple homogeneous straight magnetic fields embedded in a plasma, and determine the role of the coupling between magnetic and plasma forces, both analytically and numerically. Then, we study the formation of current accumulations at 2D magnetic X-points and at 3D magnetic nulls with spine-aligned and fan-aligned current. At both 2D X-points and 3D nulls with fan-aligned current, the current density becomes singular at the location of the null. It is impossible to precisely achieve an exact singularity, and instead, we find a gradual continuous increase of the peak current over time, and small, highly localised forces acting to form the singularity. In the 2D case, we give a qualitative description of the field around the magnetic null using a singular function, which is found to vary within the different topological regions of the field. Also, the final equilibrium depends exponentially on the initial plasma pressure. In the 3D spine-aligned experiments, in contrast, the current density is mainly accumulated along and about the spine, but not at the null. In this case, we find that the plasma pressure does not play an important role in the final equilibrium.

Our results show that current sheet formation (and presumably reconnection) around magnetic nulls is held back by non-zero plasma betas, although the value of the plasma pressure appears to be much less important for torsional reconnection. In future studies, we may consider a broader family of 3D nulls, comparing the results with the analytical calculations in 2D, and the relaxation of more complex scenarios such as 3D magnetic separators.

Acknowledgements



This work has been done under the umbrella of the SOLAIRE European training network, and was originally designed as a collaboration between the Eötvös Lorand University of Budapest and the University of St Andrews. Although, circumstances have meant that it has become a project undertaken solely at the University of St Andrews, within the Solar and Magnetospheric Theory Group. The work that has been carried for this thesis would not have been possible without all the help and encouragement from,

My parents and sister, because it is thanks to them that I am who I am now, for encouraging me to choose my own paths, and for giving me all their support in all the good and bad moments throughout my academic studies and my PhD.

My friends from Tenerife, and all the lecturers from the University of La Laguna, that led me to develop a keen interest in Astrophysics, and in solar and plasma physics, in particular.

All my friends in Budapest, for keeping me alive during one year of confusion and desperation, and all my friends in St Andrews for making it possible for me to build a life here in Scotland.

Nuri, for lots of things, because from the day I met her she has always been there for all my worries, and all my joys. And because by now, even though she is neither a physicist nor a mathematician, she knows more about the structure of magnetic null points than many.

All the people from the Solar Theory Group in St Andrews, for understanding my situation when I first arrived at the University, giving me all their help and support, and allowing me to finish my work with them, which was not originally stipulated.

Clare Parnell, for taking care of the full supervision of this work, for her neverending trust in me, and for giving me the opportunity to continue my academic career, here, in the University of St Andrews.

Alan Hood, for being a deep well of brilliant ideas, for his dedication, and for his ability to see the light when no one else could, and Dana Longcope, for a couple of interesting chats, and his ideas about X-points equilibria.

The SOLAIRE research network, for giving me this great opportunity, and for setting up an enormous number of international meetings and schools in which I have learnt much, met many interesting people and friends, and for providing an alternative point of view to scientific research, based on the collaboration and interaction between different institutions, people and cultures.

Fernando Moreno-Insertis, coordinator of SOLAIRE, for his tremendous dedication and care for every single member of the network, and especially, for his empathy and extraordinary help, which made it possible for me to finish my PhD in the University of St Andrews.

Marie Curie Actions for their financial support through the SOLAIRE European research network.

Contents

1	Introduction	1
1.1	A stairway to solar magnetohydrodynamics	1
1.1.1	Nanautzin and the Sun	1
1.1.2	About magnetism	6
1.1.3	Ionised gases	7
1.1.4	Describing the dynamics of conducting fluids	9
1.2	The Equations of magnetohydrodynamics	10
1.2.1	Maxwell's equations and Ohm's law	11
1.2.2	Field lines and flux tubes	12
1.2.3	Induction equation	12
1.2.4	Fluids equations	13
1.2.5	Restrictions and special terms	15
1.2.6	Summary of MHD equations	16
1.2.7	Energy considerations	17
1.2.8	Magnetic forces	18
1.3	MHD equilibria: Magnetohydrostatics	19
1.3.1	MHS equilibria in 2D	20
1.3.2	Classification of the MHS equilibria	21
1.3.3	Models of MHS equilibria	23
1.4	Magnetic null points	25
1.4.1	Two-dimensional null points	25
1.4.2	Three-dimensional null points	27
1.5	Current sheets and reconnection	33
1.5.1	Tangential discontinuities	33
1.5.2	Current sheet formation	33
1.5.3	Magnetic relaxation theory	36
1.5.4	Magnetic reconnection	37
1.6	Non-dimensional equations: Normalization	39
1.7	Summary and main goals	40

2	The LARE Code	45
2.1	Introduction	45
2.2	Equations	45
2.2.1	Viscous terms	47
2.2.2	Shock viscosity	47
2.3	The grid	48
2.4	The Lagrangian step	50
2.4.1	Predictor step	51
2.4.2	Corrector step	52
2.5	The remap step	53
2.6	Resistive terms	56
2.7	Stability condition	56
2.8	Summary	57
3	Relaxation of Parallel Magnetic Fields	59
3.1	Introduction	59
3.2	Linear equations in 2D	59
3.2.1	1D Perturbation across field lines	62
3.2.2	1D perturbation along field lines	65
3.2.3	2D perturbation	66
3.2.4	Overview	69
3.3	Numerical experiments: Setup	69
3.3.1	Numerical specifications	69
3.3.2	Initial conditions	70
3.3.3	Perturbed total pressure	72
3.4	Numerical experiments: Results	72
3.4.1	Energetics	73
3.4.2	Equilibrium	75
3.4.3	Overview	75
3.5	Importance of non-linear effects	79
3.6	Parallel magnetic fields in 3D	81
3.6.1	Linear equations	81
3.6.2	Numerical experiments	83
3.6.3	Overview	84
4	Relaxation of 2D Magnetic Null Points	89
4.1	Introduction	89
4.2	General properties	90
4.2.1	Magnetohydrostatic equilibrium around an X-point	90
4.2.2	Conservation of total current density	90

4.3	Previous work on current singularities in planar magnetic X-points	91
4.3.1	Analytical studies in force-free fields	91
4.3.2	Numerical studies in non-force-free fields	93
4.3.3	Our approach to the problem	93
4.4	Numerical experiments	94
4.4.1	Numerical setup	94
4.4.2	Energetics	95
4.4.3	Final equilibrium	96
4.4.4	Current density layer	101
4.4.5	Singular current	105
4.4.6	Overview	105
4.5	Analytical description of the field	107
4.5.1	Sample experiment	107
4.5.2	Dependence with initial quantities	110
4.5.3	Overview	112
5	Relaxation of 3D Magnetic Null Points	113
5.1	Introduction	113
5.2	Magnetic field configurations and numerical setup	115
5.3	3D nulls with spine-aligned current	116
5.3.1	Initial state	116
5.3.2	Final equilibrium state	118
5.3.3	Changes in current density and plasma pressure	121
5.3.4	Overview	121
5.4	3D nulls with fan-aligned current	124
5.4.1	Initial state	124
5.4.2	Final equilibrium state	124
5.4.3	Current singularity	128
5.4.4	Changes in current density and plasma pressure	130
5.4.5	Overview	132
6	Conclusions and Future Work	133
6.1	Discussion	133
6.1.1	Results overview	133
6.1.2	Implications for current sheet formation and magnetic reconnection	135
6.1.3	General conclusions	136
6.2	Future work	136
	Bibliography	138

Chapter 1

Introduction

1.1 A stairway to solar magnetohydrodynamics

1.1.1 Nanautzin and the Sun

“Five worlds and five suns were created, one after the other. The first world was destroyed because its people acted wrongfully. They were eaten by ocelots and the sun destroyed. The second sun saw its people turned into monkeys due to lack of wisdom. The third sun had its world destroyed by fire, earthquakes, and volcanoes because the people didn’t make sacrifices to the gods. The fourth world perished in a flood which also drowned its sun. Before creating the fifth world, our world, the gods met in the darkness to see who would have the honor of igniting the fifth sun. Tecciztecatl volunteered. The gods built a big fire on top of a pyramid and the volunteer prepared to throw himself into the flames. He was dressed in beautiful hummingbird feathers, with gold and turquoise. Four times he tried to force himself into the suicidal fire but each time his fear drove him back. Then the lowliest of all the gods, Nanautzin, dressed in humble reeds, threw himself into the fire. Tecciztecatl was so ashamed that he too jumped into the fire. The new sun rose into the sky giving light to the fifth world.”

Credit: “Fifth World”, Toltec myth. WWU Planetarium.

Toltecs dominated the central part of Mexico from centuries X to XII. They are believed to be the predecessors of the Aztec culture, who thought of them as their wise ancestors. Most of the information that we now have about the Toltecs comes embedded in their myths, in which, as many other civilizations from the past, they recognised the Sun as a powerful divinity, able to provide the Earth with heat and light.



Figure 1.1: *Nanautzin in the flames.* Nanautzin was known as the Scabby One, and was the ugliest and smallest of all gods, but with a modest courage, nonetheless. Credit: nativeweb.org.

What the Central American natives didn't know is the true nature of what Nanautzin started by jumping into the sacred fire and therefore creating our Sun. He would have been, without doubt, a great alchemist, although his humility would not have let him think about lead and gold, or at least, not before having had control over the most basic of the nuclear fusions: from single protons.

So, our humble Sun, being a relatively small young star, is powered continuously by nuclear fusion happening in its *core*, mainly combining two pairs of ionised hydrogen (protons) plus two electrons to create one alpha particle. This alpha particle is no more than a nucleus of Helium-4, containing two protons and two neutrons. Plus some extra energy is released in the form of 6 photons of high energy in the range of gamma rays. Nowadays these reactions are responsible for about 85% of the total nuclear energy produced in the Sun. The other 15% is due to slightly heavier elements, with which Nanautzin would have gone a little step further on his alchemy project, such as Helium, Beryllium and Lithium. For all these reactions to happen, the Sun's core needs to have a temperature of about 15 million degrees. Gravitational attraction is responsible for this, pulling the matter inwards, and thus building the required pressures and temperatures.

The gamma ray photons that are created in the core of the Sun travel out through the *radiative zone*. Here, they are absorbed and re-emitted, "bouncing around" for several million years. This *radiative transfer* of the energy causes the gamma rays to lose energy such that by the time they reach the top of the radiative zone the photons are now in the visible range. Above, in the *convective zone*, large parcels of hot plasma move outwards carrying the energy efficiently to the surface, where they cool before coming back down again. The radius of the core is around 0.25 times the total radius of the Sun, R_{\odot} (R_{\odot} covering the core, radiative and convective zones), the radiative zone is about $0.45R_{\odot}$, and the thickness of the convective zone is $0.3R_{\odot}$ (see Figure 1.2). The layer that separates the radiative and the convective zones is the *tachocline*.

Why there exists a region within the Sun's interior in which convection dominates, making the transfer of energy much more efficient, is due to the high gradients of the thermal quantities, temperature in particular. At a certain height, the rapid changes of these gradients, caused by the heating from below, drive instabilities in the density of the matter which ends up rising by buoyancy. That is, the *Schwarzschild criterion* of stability for convective flows.

Finally, after having reached the surface of the Sun, most of the light is allowed to escape in the planetary system, arriving at the Earth in the perfect conditions that Nanautzin would have liked for life and reason to exist.



Around the same time that the Toltecs were imagining their ugly deity jumping into the fires at the beginning of times, other civilizations were observing the Sun at the other side of the World. During a solar eclipse on 22 December 968, in Constantinople, the Byzantine historian Leo Diaconus wrote in the *Annales Sangallenses*:
 "... at the fourth hour of the day ... darkness covered the earth and all the brightest stars shone forth. And it was possible to see the disk of the Sun, dull and unlit, and a dim and feeble glow like a narrow band shining in a circle around the edge of the disk."

After the energy coming from the Sun's core reaches its surface, this energy has to pass through the solar atmosphere. Most of the radiation emitted from the Sun comes from the *photosphere*, a thin layer below which it is completely opaque, so it is usually understood as the solar surface. Although most of the photons cross the solar atmosphere without any effect, some of them do not.

During a solar eclipse in 1868, a deep red emission from the outer atmosphere was registered due to the emission of the Hydrogen alpha spectral line. This emission came from the layer above the photosphere, named,

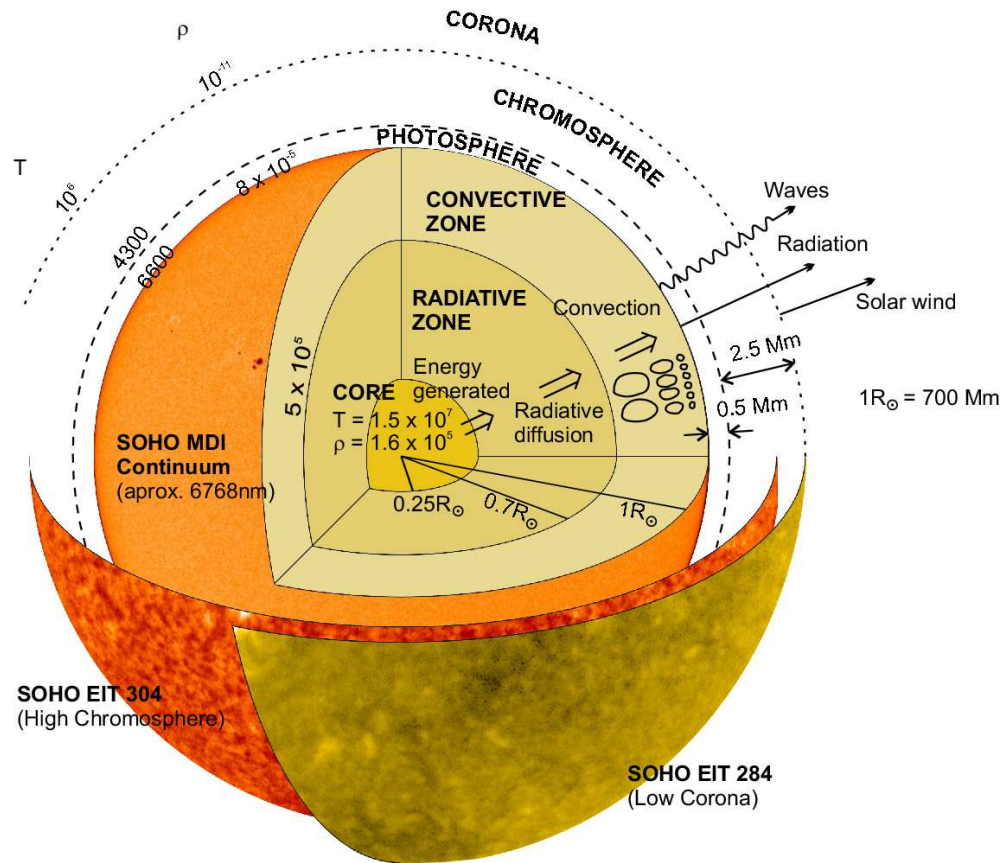


Figure 1.2: The overall structure of the Sun, with the sizes of the various regions and their temperatures (in degrees K) and densities (in kgm^{-3}). The thicknesses of the photosphere and chromosphere are not to scale. The image of the photosphere is from the indicated MDI instrument (Michelson Doppler Imager), taken in the continuum near the Ni I 6768 nm line. The high chromospheric and coronal images are from EIT (Extreme ultraviolet Imager Telescope), taken at 304 and 284 Angstroms respectively. Images are courtesy of SOHO (Solar and Heliospheric Observatory). Figure based on: Priest (1982), Fig. 1.1.

by the English astronomer Sir Joseph Norman Lockyer (1836-1920), as the *chromosphere*, which, unless the disk of the Sun is covered, for example in an eclipse, is not possible to see with a naked eye, because of the strong emission coming from the photosphere.

This glow described by Diaconus is probably the oldest reference to the *solar corona*, which extends to the Earth and far beyond. Like the chromosphere, it can only be observed when the strong emission from the photosphere is blocked by natural or artificial manners (Figure 1.3). Last, but certainly not least, in between the chromosphere and the corona, there exists a very narrow layer called the *transition region*.

Common sense suggests that the temperature of the Sun decreases as one moves away from the core, and that it keeps decreasing throughout the solar atmosphere. The first statement is initially right, with the temperature decreasing from $1.5 \times 10^7 K$ in the core, to about $6600K$ at the bottom of the photosphere, and about $4300K$ at the top of the photosphere. But in 1940, when the Swedish scientist Bengt Edlén (1906-1993) analyzed the

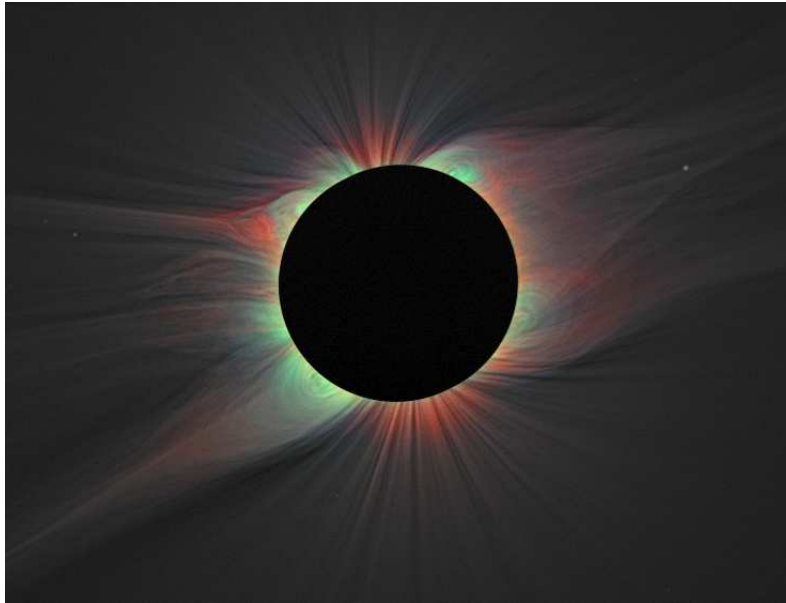


Figure 1.3: This image of the solar corona contains a color overlay of the emission from highly ionised iron lines and white light taken of an eclipse in 2008. Red indicates iron line Fe XI 789.2 nm, blue represents iron line Fe XIII 1074.7 nm, and green shows iron line Fe XIV 530.3 nm. This is the first such map of the 2D distribution of coronal electron temperature and ion charge state. Credit: Habbal et al. (2010)

spectral lines from the solar corona, it was found that these lines were produced by highly ionised elements at temperatures of $10^6 K$. After reaching its minimum value at the photosphere, the temperature rises slowly through the chromosphere, and then extremely quickly within the transition region, reaching temperatures of more than a million degrees in the low corona. Further out from the low corona, the temperature starts decreasing again slowly as the corona expands throughout the planetary system, as the *solar wind*.

The mechanisms to explain the heating of the chromosphere and corona are yet not well understood. Magnetoacoustic waves are believed to come out from the convection zone, damping their energy and rising the temperature to chromospheric levels (e.g. Osterbrock, 1961; Narain and Ulmschneider, 1996). The sudden increase of temperature observed in the transition region is mainly believed to be a consequence of the release of energy stored by highly dynamic magnetic fields (e.g. Walsh and Ireland, 2003; Hood, 2010). But despite the extremely high temperatures of the corona, its density is so low that its heat content is fairly negligible, i.e. a human body having a bath in the solar corona would freeze anyway.

Throughout the years, astronomers of many civilizations have observed temporary dark spots on the surface of the Sun. Early explanations suggested that these were transits of other planets. The first record of the observation of *sunspots* comes from the Chinese astronomer Gan De, in 364 BC, but it was at the beginning of the 17th century when three astronomers independently pointed a telescope at the Sun and discovered that those spots were structures on the surface of the Sun. The astronomers were Galileo Galilei (1564-1642), Johann Fabricius (1587-1616) and Christopher Scheiner (1573-1650). Their tracking permitted the astronomers to calculate the rotation period of the Sun, and their appearance and disappearance over longer periods showed how the Sun changed its activity in a defined cycle of 11 years. Galileo guessed that sunspots should be clouds floating over the Sun's

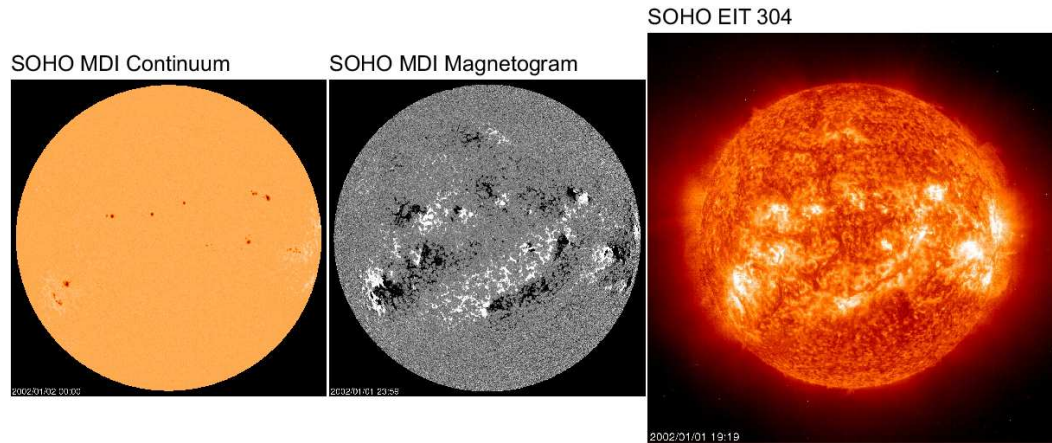


Figure 1.4: SOHO images from (left) MDI continuum, (middle) MDI magnetogram and (right) EIT 304, from 2002, around the solar maximum of cycle 23. The magnetogram shows line-of-sight magnetic field at the photospheric level. White is north polarity (magnetic field lines pointing outwards), and black is south polarity (magnetic field lines pointing inwards). Images are courtesy of SOHO MDI/EIT.

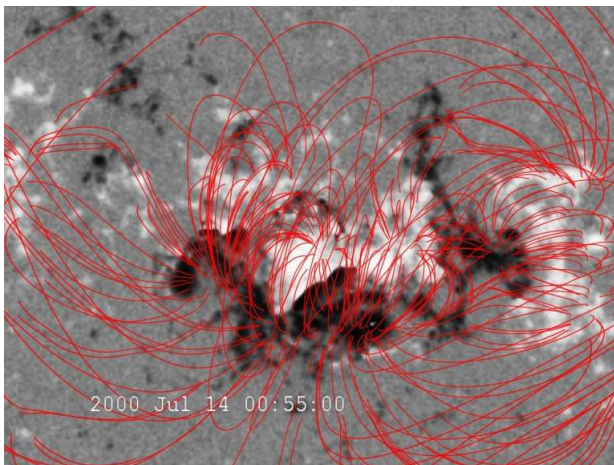


Figure 1.5: SOHO MDI magnetogram combined with a magnetic field extrapolation in the low solar corona, using the Potential-Field Source-Surface (PFSS). Credit: NASA/Goddard Space Flight Center Scientific Visualization Studio.

surface, which would cover the light coming from the Sun.

In 1908, the American solar astronomer George Ellery Hale (1868-1938) discovered their true nature as magnetic structures on the Sun (Figure 1.4). He did the first measurements of magnetic fields out of the Earth, in sunspots. He also attempted to detect a general solar magnetic field, about which he had speculated a dipole-type field such as the one of a magnetised sphere. His first attempts gave a very weak magnetic field with which he could conclude nothing, but in 1912, Hale was able to observe the Sun's magnetic field with better instrumentation, and found the dipole structure that he had speculated.

Soon, magnetic fields became a key unavoidable issue for solar physics. The Sun appeared to have an extremely complex and highly changing magnetic field, both in small and large scales (Figures 1.4 and 1.5). These magnetic fields are created by the internal rotation of the ionised gas in the interior of the Sun which acts as a giant magnetic dynamo. The solar 11-year cycle is a magnetic phenomenon. Down in the convection zone, the Sun shows a *differential rotation*. That is, the solar gas rotates with a speed that is maximum at the equator, and decreases as

one moves up or down to the poles. The movements of the equatorial zones drag the originally poloidal north-south orientated magnetic fields and wrap them around the Sun (*omega effect*) producing toroidal magnetic fields. After this process, the toroidal magnetic fields exhibit highly twisted *flux tubes* which may emerge to the surface by buoyancy (*alpha effect*), in the form of giant arcades. Some of these strong magnetic flux tubes are able to inhibit the bulk motions of the plasma in the convection zone (which carry the energy out from the radiation zone). Thus they produce regions with lower temperatures than their surroundings, and hence, lower emission, i.e. they appear as dark spots in the photosphere. Magnetic sunspots tend to come in pairs with positive and negative polarities, where positive means magnetic field pointing out of the Sun, and negative, pointing into the Sun, also referred as to “north” and “south” polarities, respectively.

Once in the solar atmosphere, the strong magnetic fields coming from the interior undergo all kinds of strong chaotic interactions, giving rise to enormous explosive events, called solar flares, which release huge amounts of energy, and can cause “solar tsunamis”, vast plasma and magnetic waves that expand over the whole solar disk, discovered in 1997 by SOHO (Narukage et al., 2002), or accelerate massive numbers of particles out into the interplanetary medium. After most of the magnetic field that causes these big magnetic structures in the atmosphere is diffused away, the Sun recovers its original poloidal configuration, but with a reversed polarity of the magnetic field. This whole big scale process is called the Sun’s magnetic cycle. However, even when the large scale magnetic field in the Sun has a poloidal configuration (this is known as the *quiet Sun*), there is a permanent turbulent magnetic field of local character which is responsible for many “micro-events” of energy release, and is regenerated by a *small scale dynamo* driven by the convection movements of the plasma below the solar surface (Petrovay and Szakaly, 1993).

The cycle of magnetic activity and of sunspots on the Sun is approximately 11 years. Hence, the complete magnetic cycle, including the polarity reversal, is approximately 22 years.

1.1.2 About magnetism

“*A lodestone attracts a needle*”. This has long been a well know fact, even when there was no explanation for it. A lodestone is a naturally magnetised piece of the mineral magnetite. It was during the Qin dynasty (221-206 B.C.), in China, when it was first noticed that a lodestone needle, suspended so that it could turn, would always point in the same fixed direction, to the magnetic north (or south) pole. These directions were noted to very closely relate to the cardinal points given by astronomy. Some centuries later, again in China, the compass was first used in navigation by Zheng He (1371-1435), and it soon became a world wide used artifact. At the time, the reason why it worked was unknown. Some thought it was the actual polaris star that was attracting the needle, others thought it was some kind of magnetic island at the Earth’s poles.

The English physicist William Gilbert (1544-1603) published a large work on magnetism, magnetic bodies and the great magnet of the Earth, being the first to argue that the center of the Earth contained iron, making the Earth a magnet itself, explaining the reason why compasses pointed north.

In 1820, the Danish physicist Hans Christian Oersted (1777-1851) was giving a science demonstration to some friends and students about electric currents, and also wanted to show some experiments on magnetism for which he needed a compass. While performing his electric demonstration, he noticed how every time the electric current was switched on, the needle of the compass moved. He said nothing at the time and finished his demonstration, but in the following months he tried hard to explain the behaviour: The needle of the compass would orientate itself perpendicular to the electric current flowing along a wire. Unluckily for him, he could not find an explanation, and

had to content himself publishing just the results he found. In the coming years of the same century, other scientists, in particular, André-Marie Ampère (1775-1836) and Michael Faraday (1791-1867), kept doing experiments relating electricity and magnetism.

Shortly after the experiments of Oersted, that same year, Ampère discovered that moving electric charges create a magnetic field, which is perpendicular to the movement of the charges. The magnetic field wraps around the electric current in circles, and it is related to the electric field by Ampère's law, which states that the line integral of the magnetic field around a closed path equals the electric current times a constant known as the magnetic permeability, μ .

Around 1834, Faraday discovered electromagnetic induction, stating that a changing magnetic field induces an electric field perpendicular to it. Faraday introduced the concept of magnetic field lines, which he called "lines of force". Similar to the velocity streamlines that are followed by the particle of a fluid in motion, a magnetised needle will always point along the field lines.

In the same way that electric fields, discovered by Johann Carl Friedrich Gauss (1777-1855), can be generated by isolated charges, a magnetic field must be generated by a dipole configuration, which appears like a positive and negative charge "inseparably bound together". There are no magnetic monopoles, which, in mathematical language is transcribed as the divergence of the magnetic field equals zero. Gauss's law of electricity shows how the divergence of the electric field is proportional to the electric charge. By comparison, there does not exist such thing as a magnetic charge.

Ampère was the first to notice that two electric currents are attracted if running in parallel, and repelled if they are antiparallel. This force is perpendicular to both the magnetic field, \mathbf{B} , and the velocity of the electric current carriers \mathbf{v} , and has the form $q\mathbf{v} \times \mathbf{B}$ (in mks units), where q is the electric charge. If we also have an electric field, \mathbf{E} , the total force is the *Lorentz force*, $\mathbf{F} = q(\mathbf{E} + \mathbf{v} \times \mathbf{B})$.

Finally, despite the rejection of the ideas of Faraday's lines of force by many scientists of the time, mainly because of lack of mathematical formulation, the Scottish physicist and mathematician James Clerk Maxwell (1831-1879) took Faraday's ideas and Ampère discoveries, and put all the theory of electric and magnetic fields together into a quantitative electromagnetic theory, formulating what we nowadays know as *Maxwell equations for electromagnetism*. These are described in Section 1.2.1.

Some years later, the theory of special relativity of Albert Einstein (1879-1955) provided more of an explanation to that "field generated by moving charges", found observationally, but somehow hard to assimilate, known as a magnetic field. The defining postulate of special relativity is that physics must be consistent in every "frame of reference", defined by an observer moving at a certain velocity respect to others. If we consider the experiment of a long wire carrying an electric current, and a negative charge moving parallel to it at the same velocity, then in the "lab frame", the moving charge is attracted to the wire by the magnetic field generated by the current. Now, for an observer that moves together with the electric charge, then there is no magnetic force! Instead, in the charge's frame of reference, there is an attractive electric field. Sometimes, what looks like a pure magnetic field in one frame of reference, looks like a pure electric field in a different one.

1.1.3 Ionised gases

In 1927, the American scientist Irving Langmuir (1881-1957) studied electronical devices based on highly ionised gases for General Electric Co. Perhaps, the way in which that electrified fluid carried the electrons and the ions reminded him of the way the blood fluid carries its red and white corpuscles. Whatever the reason, Langmuir took

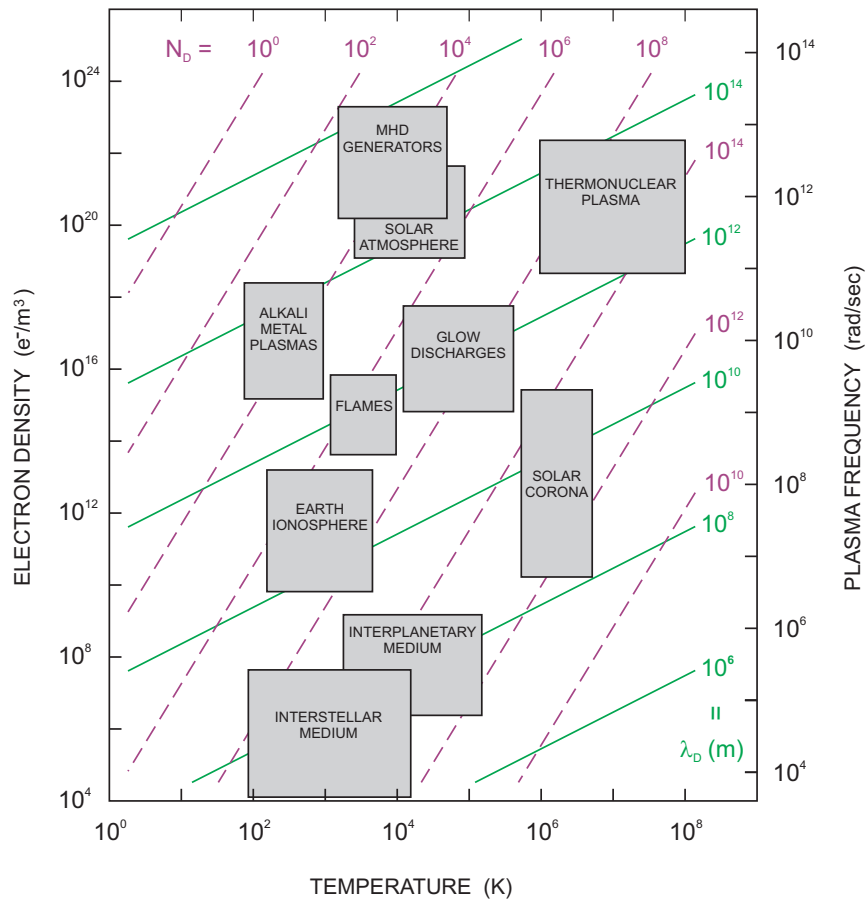


Figure 1.6: Ranges of temperature and electron density for several laboratory and cosmic plasmas and their characteristic physical parameters: Debye length λ_D , plasma frequency ω_{pe} and number of electrons N_D in a Debye sphere. Based on: Bittencourt (2004), Fig. 2.

the word given around one hundred years earlier by the Czech medical scientist Johannes Purkinje (1787-1869) to that clear blood liquid, *plasma*, and called an electrified fluid by the same name.

Unlike most people tend to think, a plasma cannot be quite understood as *the fourth* state of matter. Liquid, solid and gas states are based on intermolecular relationships, and their change of phase is well defined at a constant temperature for a given pressure, for each of the elements in nature. The change to a plasma, on the other side, is necessarily an ionization process, which can be either radiative or collisional, and will not happen at a fixed temperature, although the number of ionizations will directly depend on the temperature.

Plasmas conduct electric currents, and are strongly affected by magnetic fields. There are four main criteria for defining a plasma, described in Bittencourt (2004), “*Fundamentals of plasma physics*”. 1) A plasma must be macroscopically neutral, containing the same overall number of negative and positive charges. 2) A plasma must follow collective phenomena, and its length-scales need to be much larger than the minimum radius of neutrality, known as the *Debye length*, named after the Dutch scientist Peter Debye (1884-1966), who experimentally discovered that this length of neutrality must be proportional to $T^{1/2}$ and $n_e^{-1/2}$, where T and n_e are the temperature and electron density. 3) A plasma must have a large amount of free electrons inside the Debye sphere in order to

follow a statistic behaviour. 4) A plasma must have a low rhythm of collisions with neutral particles. The eventual localised overdensities of electrons in the plasma cause it to oscillate with a given frequency, namely, the *Langmuir frequency*, which only depends on the electron density. This should be considerably larger than the frequency of collisions with neutral particles for the plasma not to behave as a normal, i.e. non ionised, fluid.

After the studies of relatively cool and dense plasmas on Earth, this field of research expanded in several directions. Around the same year that Langmuir came up with the term “plasma”, the English physicist Edward Victor Appleton (1892-1965) confirmed the existence of a “plasma roof” above the Earth’s atmosphere, which is ionised by the high energy radiation coming from the Sun, but with low enough density so that collisions are not frequent enough to recombine the ions. This layer is called the *ionosphere*. Since it has a strong influence on the propagation of radio waves, it has been used to study a variety of properties of plasma waves. Furthermore, the possibility of a new source of energy from nuclear reactions became quite popular after the creation of the atomic bomb. These reactions require quite high temperatures, so scientists have had to deal with the problem of trapping and controlling a plasma using magnetic fields. Finally, in 1958, observations from satellites revealed the radiation belts in the Earth’s magnetosphere, and heralded the birth of space plasma physics. This branch of plasma physics has utilised the knowledge of magnetic trapping of plasmas from fusion research, of plasma waves from ionospheric physics, and must include magnetic processes for energy release and particle acceleration.

Here, on Earth we struggle to confine a plasma and keep it under control, due to the cool temperatures and high densities that we have, but as one moves out into space, plasmas exist in almost all astrophysical objects. In particular, the temperatures in the solar corona are such that all its atoms appear ionised, and those atoms with many electrons have lost several or all of them. For instance, characteristic light has been detected in the corona from iron which has lost 15 electrons (from a spectral line at $33.5nm$ observed over active regions at the corona, at a temperature of $5 \times 10^6 K$). As one moves away from the low corona, high velocities are found related to the high temperatures of the corona, making the gravitational effects of the Sun negligible in many cases, thus allowing the particles of the corona to expand throughout the interplanetary medium and creating the solar wind.

1.1.4 Describing the dynamics of conducting fluids

“If a conducting liquid is placed in a constant magnetic field, every motion of the liquid gives rise to an EMF [electromotive force] which produces electric currents. Owing to the magnetic field, these currents give mechanical forces which change the state of motion of the liquid. Thus a kind of combined electromagnetic-hydrodynamic wave is produced which, so far as I know, has as yet attracted no attention.” (Alfvén, 1942)

Apart from a few isolated experiments, the influence of magnetic fields in conducting fluids did not start being fully studied until the first half of the twentieth century, when astrophysicists realised how common magnetic fields and plasmas are outwith our cool and dense planet. The study of hydromagnetic flows became important after a letter from Hannes Alfvén (1908-1995) was published in *Nature*, in 1942, in which he wrote about a certain type of wave that could be of importance in solar physics, since solar matter is a very good conductor with a general magnetic field permeating it.

The study of the mutual interaction between a magnetic field and a conducting fluid flow is called magnetohydrodynamics (MHD). Conducting fluids are restricted to liquid metals, ionised gases (plasmas) or strong electrolytes (solutes that are completely, or almost fully, ionised in a solution).

The nature of the coupling between a magnetic field, \mathbf{B} , and a velocity field \mathbf{v} , is described in Davidson (2001) “*An introduction to magnetohydrodynamics*”, as a split into three processes.

The first arises from electromagnetic induction, discovered by Faraday in 1831. When the magnetic flux through a closed circuit changes, it induces an electromotive force (EMF) of order $\mathbf{v} \times \mathbf{B}$, which causes an electrical current of order $\sigma(\mathbf{v} \times \mathbf{B})$, with σ being the electrical conductivity. This applies whether the magnetic field itself changes in strength, or the conducting fluid is moved through it. Hence, the relative movement of a conducting fluid and a magnetic field, causes an EMF, with a subsequent electric current density.

Secondly, according to Ampère's law, these induced currents give rise to a second induced magnetic field around a closed loop, perpendicular to the current density vector, \mathbf{j} . This provokes a change in the original magnetic field, so that the overall consequence is that the fluid appears to drag the magnetic field lines along with it.

The third process is the interaction between the combined magnetic field and the induced current density. When an electric charge moves through a magnetic field, there is a force on the charge perpendicular to both the movement of the charge and the direction of the magnetic field. This is the (magnetic) Lorentz force (per unit volume), $\mathbf{j} \times \mathbf{B}$. This force acts on the conducting fluid, and is generally directed so as to inhibit the relative movement of the fluid and the magnetic field.

The last two processes have in common the effect of reducing the relative movement of the magnetic field and the conducting fluid. It is important to consider the parameters that define how weak or strong the influence of the velocity field is over the magnetic field (or vice versa). If the velocity field is negligible, the induced magnetic field will not be significant. Similarly, if the conductivity of the fluid is very small, so too is the magnetic field. Also, a current density spread over a large area can produce a higher magnetic field than the same current density spread over a smaller area. Hence, the ratio of the induced field to the applied magnetic field depends on the product of these three quantities, i.e. the velocity field \mathbf{v} , the conductivity of the fluid σ , and the characteristic size, or length scale, l . To this we may add the magnetic permeability μ , which defines the ability of a material to acquire high magnetization in response to an applied magnetic field. Hence, If $\mathbf{v}l\sigma\mu \rightarrow \infty$, both the induced and imposed magnetic field are of the same order, and the combined magnetic field behaves as if it were frozen into the fluid. On the other hand, if $\mathbf{v}l\sigma\mu \rightarrow 0$, the imposed magnetic field remains relatively unperturbed, and any possible perturbation is immediately diffused away.

Mainly because of the enormous characteristic length scales of most of the astrophysical plasmas, due to their small mass densities, it is the first case that dominates, so they are said to behave under the *frozen-in* condition, where the magnetic field lines have to move together with the plasma. Motions along the field lines do not change them, but motions across the field lines carry the field with them.

1.2 The Equations of magnetohydrodynamics

The equations of magnetohydrodynamics (MHD) include the fluid conservation equations, such as the continuity equation (conservation of mass), equation of motion (conservation of linear momentum) and energy equation (conservation of energy), together with Maxwell's equations of electromagnetism plus Ohm's law. The macroscopic conservation equations are derived from the Boltzmann transport equation of the distribution function. Those derivations are not shown here for simplicity. The resulting equations are given in mks units. They may be found, with further considerations, in Priest (1982) "*Solar magnetohydrodynamics*".

1.2.1 Maxwell's equations and Ohm's law

Maxwell's equations, as discussed earlier, are the set of electromagnetic equations that relate the electric and magnetic fields to their sources, charge density and electric current density, respectively.

Ampère's law describes how magnetic fields can be generated by electric currents and by changing electric fields (the latter extension was made by Maxwell, and it is not in the original equation of Ampère), and are perpendicular to both the electric currents and electric fields,

$$\nabla \times \mathbf{B} = \mu \mathbf{j} + \frac{1}{c^2} \frac{\partial \mathbf{E}}{\partial t}, \quad (1.2.1)$$

where \mathbf{B} is the magnetic induction (usually referred as to magnetic field in astrophysical contexts), \mathbf{j} is the current density, \mathbf{E} is the electric field, and c and μ are the speed of light and the magnetic permeability, respectively, in a vacuum.

Solenoidal constraint, states that there are no magnetic charges, or magnetic monopoles,

$$\nabla \cdot \mathbf{B} = 0. \quad (1.2.2)$$

Faraday's law shows that a changing magnetic field induces an perpendicular electric field,

$$\nabla \times \mathbf{E} = -\frac{\partial \mathbf{B}}{\partial t}. \quad (1.2.3)$$

Gauss' law states that an electric field is generated by electric charges,

$$\nabla \cdot \mathbf{E} = \frac{1}{\epsilon} \rho^*, \quad (1.2.4)$$

where ϵ is the permittivity of free space, and ρ^* is the charge density.

Under the *MHD approximation*, it is assumed that the plasma is non-relativistic, i.e. the typical plasma velocities are much smaller than the speed of light. Thus the second term on the right hand side in equation (1.2.1) is neglected, so that Ampère's law becomes

$$\nabla \times \mathbf{B} = \mu \mathbf{j}. \quad (1.2.5)$$

Finally, *Ohm's law* states that the current in a non-relativistic moving plasma, in the presence of a magnetic field, is proportional to the *total* electric field, in a frame of reference moving with the plasma. This *total* electric field is the sum of the electric field that would act on the material at rest, \mathbf{E} , plus the electric field due to the moving magnetic field, $(\mathbf{v} \times \mathbf{B})$, hence,

$$\mathbf{j} = \sigma(\mathbf{E} + \mathbf{v} \times \mathbf{B}), \quad (1.2.6)$$

where \mathbf{v} is the plasma velocity, and σ is the electrical conductivity. This equation can be generalised in models that consider electrons, ions and neutral atoms as three different fluids, mixed together, but with different behaviours. These considerations are, however, outwith the scope of this thesis.

It is worth noting that the current density is defined as $\mathbf{j} = \rho^* \mathbf{v}_d$, where $\rho^* (= \sum q n_q)$ is the charge density (q is electric charge, and n_q is number of particles with charge q) and \mathbf{v}_d is the drift velocity of the current carriers,

which is different from the mean bulk velocity of the plasma, and, therefore, it can coexist with a static equilibrium. The MHD model uses macroscopical quantities and ignores the microscopical effects. Then, the current density is simply understood as a changing magnetic field of the form $\nabla \times \mathbf{B}$, as given by Ampère's law (1.2.5).

1.2.2 Field lines and flux tubes

For a known three dimensional magnetic field, $\mathbf{B} = (B_x, B_y, B_z)$, the magnetic lines of force, or magnetic field lines are defined as

$$\frac{dx}{B_x} = \frac{dy}{B_y} = \frac{dz}{B_z} = \frac{ds}{B},$$

where $B = \sqrt{B_x^2 + B_y^2 + B_z^2}$ is the magnitude of the magnetic field, and s is the distance along the field line. The spacing between field lines corresponds to the magnitude of the field: the closer the field lines the stronger the magnetic field. Also, field lines have a direction, defined by the direction of the magnetic field vector.

We define a magnetic flux tube as the volume enclosed by a set of field lines that intersect a simple closed curve, so that both the cross section of area S , and the magnetic field, \mathbf{B} , may vary along the length of the tube, but the magnetic flux, defined as

$$\phi_m = \iint_S \mathbf{B} \cdot d\mathbf{S},$$

is always constant along the length of the flux tube. The volume of a flux tube is $\int_L S(l) dl$, where $S(l)$ is the cross section of the flux tube at l and L represents the total length. The volume of a single field line, understood as the differential volume of an infinitesimally thin flux tube, is defined as

$$V = \int_L \frac{dl}{B}. \quad (1.2.7)$$

1.2.3 Induction equation

From Ohm's law (1.2.6) and Ampère's law (1.2.5), the electric field may be written as

$$\mathbf{E} = \frac{\nabla \times \mathbf{B}}{\sigma\mu} - \mathbf{v} \times \mathbf{B}.$$

Taking the curl of this equation, defining the magnetic diffusivity as $\eta = 1/(\sigma\mu)$, and making use of Faraday's law (1.2.3), we get

$$\frac{\partial \mathbf{B}}{\partial t} = \nabla \times (\mathbf{v} \times \mathbf{B}) - \nabla \times (\eta \nabla \times \mathbf{B}). \quad (1.2.8)$$

The magnetic diffusivity is often assumed to be *spatially uniform*. Thus we can make use of the vector identity

$$\nabla \times (\nabla \times \mathbf{B}) = \nabla(\nabla \cdot \mathbf{B}) - \nabla^2 \mathbf{B},$$

where the first term in the right hand side is zero because of the solenoidal constraint (1.2.2), to get

$$\frac{\partial \mathbf{B}}{\partial t} = \nabla \times (\mathbf{v} \times \mathbf{B}) + \eta \nabla^2 \mathbf{B}. \quad (1.2.9)$$

This is the *induction equation*. The first term in this equation is the *advection term*, which covers the transport or dragging of the magnetic field by the motion of the plasma. The second term is the *diffusion term*, which indicates that irregularities in an initial magnetic field will diffuse away. We define the *magnetic Reynolds number* as the ratio of the advection and the diffusion terms in the induction equation,

$$R_m = \frac{|\nabla \times (\mathbf{v} \times \mathbf{B})|}{|\eta \nabla^2 \mathbf{B}|}. \quad (1.2.10)$$

If l_0 is a scale of spatial variation of the magnetic field (characteristic length scale), and v_0 the characteristic velocity of the plasma, we can approximate the magnetic Reynolds number, in order of magnitude, as

$$R_m \approx \frac{v_0 B / l_0}{\eta B / l_0^2} = \frac{\tau_D}{\tau},$$

where $\tau = l_0 / v_0$ is the characteristic advection time (time to travel a length l_0 at the characteristic velocity of the plasma), and $\tau_D = l_0^2 / \eta$ is the characteristic time of diffusion of magnetic irregularities. Thus, the magnetic Reynolds number can be expressed as a ratio of two time scales.

Typically, laboratory plasmas have very short length scales, which, in many cases, makes the diffusion time much shorter than the advection time, so that $R_m \ll 1$. On the other hand, astrophysical plasmas have, in general, very large length scales, so $R_m \gg 1$, and it is the advection term that dominates in the induction equation. This is the case for most of the solar atmosphere, so it is common to work within the advection limit, in which the diffusivity is neglected (not so much because of the value of the diffusivity itself, but for the huge length scales we deal with), and the induction equation reduces to

$$\frac{\partial \mathbf{B}}{\partial t} = \nabla \times (\mathbf{v} \times \mathbf{B}). \quad (1.2.11)$$

In 1943, that plasma physicist that discovered the magnetohydrodynamic waves in plasmas, Hannes Alfvén, enunciated the *frozen-in-flux theorem*: “In a perfectly conducting fluid ($R_m \rightarrow \infty$), magnetic field lines move with the fluid, i.e. the field lines are *frozen* into the plasma”. In other words, when the electrical conductivity tends to infinity, $\sigma \rightarrow \infty$, the magnetic diffusivity tends to zero, $\eta \rightarrow 0$, and a plasma moving across the magnetic field lines has to carry the magnetic field with it.

In scenarios where rapid changes in the magnetic field occur over short spatial scales, the magnetic diffusivity becomes important, and the frozen-in condition breaks down.

1.2.4 Fluids equations

The changes in time of any macroscopic quantity Q in a moving plasma, can be split into two different terms. The first one is due to inner changes in Q with time, and it may be expressed as $\partial Q / \partial t$, and the second is due to gradients of Q . Consider a tall building which has a spatial gradient of, say, temperature, in the vertical direction. Assume the temperature does not vary in time. Someone who takes the elevator up this building and measures

temperature on the way, would register a change in temperature with time, due to the combined velocity of the elevator and the spatial gradient of temperature. This time variation may be expressed as $\mathbf{v} \cdot \nabla Q$, and may be due to the observer in the elevator or, in a plasma, to a velocity of the plasma itself. The combined effect results in the *total derivative* of the quantity Q , also called the *material derivative*, *convective derivative* or *Lagrangian derivative*, namely,

$$\frac{D}{Dt} = \frac{\partial}{\partial t} + \mathbf{v} \cdot \nabla . \quad (1.2.12)$$

The equations describing the dynamics of fluids are presented as a set of three conservation equations, together with an equation of state that relates the gas pressure to the density and temperature.

Mass continuity or mass conservation, states that matter can not be created nor destroyed, i.e. changes in density can only be produced by the plasma moving.

$$\frac{D\rho}{Dt} + \rho \nabla \cdot \mathbf{v} = 0 , \quad (1.2.13)$$

or, using equation (1.2.12),

$$\frac{\partial \rho}{\partial t} + \nabla \cdot (\rho \mathbf{v}) = 0 , \quad (1.2.14)$$

where ρ is the plasma density and \mathbf{v} is the plasma velocity. For incompressible flows, $\nabla \cdot \mathbf{v} = 0$, so $D\rho/Dt = 0$, meaning that the density is constant following the movement of the material element.

Equation of motion or momentum conservation. This is Newton's second law: *mass* \times *acceleration* = *applied force*. The forces are a sum of the gradient pressure force (high pressure regions push the plasma towards low pressure regions), plus the magnetic Lorentz force, and other external forces, \mathbf{F} , such as gravitational or viscous forces.

$$\rho \left(\frac{\partial \mathbf{v}}{\partial t} + (\mathbf{v} \cdot \nabla) \mathbf{v} \right) = -\nabla p + \mathbf{j} \times \mathbf{B} + \mathbf{F} , \quad (1.2.15)$$

where p is the plasma pressure.

Equation of state, which for simplicity, is taken as the perfect gas law,

$$p = \frac{k_B}{m} \rho T , \quad (1.2.16)$$

where k_B is the Boltzmann constant, m is the mean particle mass, and T is the temperature. For an ideal polytropic gas, the internal energy per unit mass is $\epsilon = c_v T$, where c_v is the *specific heat at a constant volume*, which relates to c_p , the *specific heat at a constant pressure*, as

$$c_v = c_p - \frac{k_B}{m} = \frac{1}{\gamma - 1} \frac{k_B}{m} , \quad (1.2.17)$$

where $\gamma = c_p/c_v$ is the *ratio of specific heats*. Hence, temperature and internal energy are related by

$$T = \epsilon(\gamma - 1) \frac{m}{k_B} , \quad (1.2.18)$$

and using (1.2.17), we can rewrite equation (1.2.16) as

$$p = \rho \epsilon (\gamma - 1) . \quad (1.2.19)$$

The ratio of specific heats may also be written as

$$\gamma = \frac{n + 2}{n} ,$$

where n is the number of degrees of freedom of the molecules in the plasma. For fully ionised hydrogen, $n = 3$, and so $\gamma = 5/3$.

Energy equation or energy conservation. Energy is not created nor destroyed. This equation can be expressed in many ways, involving internal energy, enthalpy, entropy, pressure or temperature. The most fundamental form of the energy equation is

$$\rho T \frac{Ds}{Dt} = -\mathcal{L} ,$$

where s represents the entropy, and may be written as $s = c_v \log(p/\rho^\gamma) + \text{constant}$, and \mathcal{L} is the energy loss function, which is the net effect of all sinks and sources of energy. For our convenience, we write this equation using the plasma pressure, as

$$\frac{\rho^\gamma}{\gamma - 1} \frac{D}{Dt} \left(\frac{p}{\rho^\gamma} \right) = -\mathcal{L} ,$$

where the quantity p/ρ^γ is directly related to the entropy of the system. Using mass continuity (1.2.14), the energy equation can be expressed as

$$\frac{\partial p}{\partial t} + \mathbf{v} \cdot \nabla p = -\gamma p \nabla \cdot \mathbf{v} - (\gamma - 1) \mathcal{L} . \quad (1.2.20)$$

A perfectly isolated process with no exchange of heat is called *adiabatic*. For such processes, the energy loss function must be identically zero, $\mathcal{L} = 0$, and the entropy is conserved. This may be written as $p/\rho^\gamma = \text{constant}$, or $pV^\gamma = \text{constant}$, with V denoting volume.

1.2.5 Restrictions and special terms

The complete set of MHD equations is extremely complex. There are many terms which take account of many different effects. Four of the fundamental equations may be extended to account for extra effects. The first one is Ohm's law (1.2.6), which can be generalised for multi-fluid models in which electrons, protons and ions are treated as separate fluids. Some examples are Hall MHD (decoupling of electrons from ions) and Cowling conductivity (three-fluids models for partially ionised plasmas). These have a knock on effect for the induction equation (1.2.9), as the electrical conductivity is directly related to the magnetic diffusivity, which may not be uniform. The third equation is the equation of motion (1.2.15), in which the effects of any kind of external force may be added, such as gravitational and viscous forces. Finally, there is the energy equation (1.2.20), which has an energy loss function, that is only zero if the process is adiabatic. Otherwise, terms for thermal conduction, radiation or heating (e.g. ohmic dissipation or viscous dissipation) may be included.

The equations that are to be solved here are a very simplified version of the whole set. We do not take into consideration any of the extra terms in Ohm's law, nor in the induction equation. These extra terms account for collisionless effects and appear in models which are based on either a two-fluid or a kinetic description of the field. They are important, for instance, in small-scale reconnection processes for which the classic resistive MHD models have some deficiencies, such as the long energy release time, the absence of a well-defined mechanism for breaking the frozen-in condition, the onset problem, and the particle heating problem (Birn and Priest, 2007, "*Reconnection of Magnetic Fields*"). These effects do not affect the results of this thesis, as, for reasons that will soon arise, we will be working with the frozen-in condition, for which the induction equation is reduced to the advection limit (1.2.11), and the conductivity is assumed infinite. Under the frozen-in condition, the diffusivity tends to zero, so we talk of *non-resistive* MHD.

For simplicity, we assume that gravitational effects are negligible in the context of our experiments. However, we are interested in viscous forces, which can be understood as a fluid's internal resistance to flow, and will have the main effect of damping out plasma motions. Together with this viscous force, there will be an associated viscous heating term in the energy equation. This is our only *non-adiabatic* term, although in general it will be small. These two terms are controlled by the *kinematic viscosity*, ν .

1.2.6 Summary of MHD equations

The magnetohydrodynamic equations we are going to be working with are the compressible, viscous, non-resistive equations, with no gravitational force.

$$\text{Mass continuity : } \frac{\partial \rho}{\partial t} + \nabla \cdot (\rho \mathbf{v}) = 0 , \quad (1.2.21)$$

$$\text{Equation of motion : } \rho \left(\frac{\partial \mathbf{v}}{\partial t} + (\mathbf{v} \cdot \nabla) \mathbf{v} \right) = -\nabla p + \mathbf{j} \times \mathbf{B} + \mathbf{F}_\nu , \quad (1.2.22)$$

$$\text{Energy equation : } \frac{\partial p}{\partial t} + \mathbf{v} \cdot \nabla p = -\gamma p \nabla \cdot \mathbf{v} + (\gamma - 1) H_\nu , \quad (1.2.23)$$

$$\text{Ideal gas law : } p = \rho \epsilon (\gamma - 1) , \quad (1.2.24)$$

$$\text{Ampère's law : } \mathbf{j} = \frac{\nabla \times \mathbf{B}}{\mu} , \quad (1.2.25)$$

$$\text{Solenoidal constraint : } \nabla \cdot \mathbf{B} = 0 , \quad (1.2.26)$$

$$\text{Faraday's law : } \frac{\partial \mathbf{B}}{\partial t} = -\nabla \times \mathbf{E} , \quad (1.2.27)$$

$$\text{Ohm's law : } \mathbf{E} + \mathbf{v} \times \mathbf{B} = 0 , \quad (1.2.28)$$

where \mathbf{F}_ν and H_ν are the viscous force and the viscous heating, respectively, given by

$$\mathbf{F}_\nu = \rho \nu \left(\nabla^2 \mathbf{v} + \frac{1}{3} \nabla (\nabla \cdot \mathbf{v}) \right) , \quad (1.2.29)$$

$$H_\nu = \rho \nu \left(\frac{1}{2} e_{ij} e_{ij} - \frac{2}{3} (\nabla \cdot \mathbf{v})^2 \right) , \quad \text{with } e_{ij} = (\partial v_i / \partial x_j) + (\partial v_j / \partial x_i) . \quad (1.2.30)$$

The electric field may be eliminated from equations (1.2.27) and (1.2.28), to give the ideal induction equation,

$$\frac{\partial \mathbf{B}}{\partial t} = \nabla \times (\mathbf{v} \times \mathbf{B}) . \quad (1.2.31)$$

1.2.7 Energy considerations

In any physically consistent system, total energy is conserved. The only way this may change is due to the presence of inflows and outflows within the domain in consideration. However, energy does not necessarily have to maintain the same form. It is therefore worth considering the three different types of energy that will occur in our magnetohydrodynamic system.

Kinetic energy is due to the macroscopic motions of the fluid, and its magnitude, per unit volume, is $\rho v^2/2$. The *internal energy* of a system is due to the translational, rotational and vibrational motion of the particles and the potential energy associated to electric forces. It is directly related to the temperature of the system, as seen in equation (1.2.18). The internal energy per unit mass is $\epsilon = p/\rho(\gamma - 1)$, with $\rho\epsilon$ being the internal energy per unit volume. Finally, the energy stored in a magnetic field is the *magnetic energy*, and its expression per unit volume is $B^2/2\mu$. The density of the flow of electromagnetic energy is given by the *Poynting flux*, $\mathbf{E} \times \mathbf{B}/\mu$.

The temporal evolutions of these three energies are expressed as follows,

$$\frac{\partial}{\partial t} \left(\frac{p}{\gamma - 1} \right) + \nabla \cdot \left(\frac{p}{\gamma - 1} \mathbf{v} \right) = Q_e , \quad (1.2.32)$$

$$\frac{\partial}{\partial t} \left(\frac{B^2}{2\mu} \right) + \nabla \cdot (\mathbf{E} \times \mathbf{B}/\mu) = Q_m , \quad (1.2.33)$$

$$\frac{\partial}{\partial t} \left(\frac{1}{2} \rho v^2 \right) + \nabla \cdot \left(\frac{1}{2} \rho v^2 \mathbf{v} \right) = Q_k , \quad (1.2.34)$$

where the second terms on the left hand side on each equation account for the inflows and outflows of energy, and the right hand side terms, Q_e , Q_m and Q_k , are given by

$$\begin{aligned} Q_e &= -\mathcal{L} , \\ Q_m &= -\frac{j^2}{\sigma} - \mathbf{v} \cdot \mathbf{j} \times \mathbf{B} , \\ Q_k &= -\nabla \cdot (p\mathbf{v}) + \mathbf{v} \cdot \mathbf{j} \times \mathbf{B} + \mathbf{v}\mathbf{F} . \end{aligned}$$

For the total energy to be conserved, the sum of the three expressions, (1.2.32) to (1.2.34), must equal zero. For our particular case, we are assuming infinite conductivity, and so the only external forces and heating are given by the viscous terms, $\mathcal{L} = -H_\nu$ and $\mathbf{F} = \mathbf{F}_\nu$, of equations (1.2.29) and (1.2.30). So our equation of energy conservation is

$$H_\nu - \nabla \cdot (p\mathbf{v}) + \mathbf{v}\mathbf{F}_\nu = 0 .$$

Thus, in a closed scenario, the gains (or losses) from one of these energies must be completely balance by losses (or gains) from the others. This will need to be looked at closely in the study of dynamical processes in magnetised plasmas, as their evolution will directly depend on the exchanges between the different types of energy.

1.2.8 Magnetic forces

Magnetic fields produce magnetic forces, which act directly on the plasma motions, changing their velocity. This is the magnetic Lorentz force, $\mathbf{j} \times \mathbf{B}$, which, according to Ampère's law (1.2.5), can be written as

$$\mathbf{j} \times \mathbf{B} = \frac{1}{\mu} (\nabla \times \mathbf{B}) \times \mathbf{B} .$$

Using the vector identity

$$\nabla(\mathbf{B} \cdot \mathbf{B}) = 2\mathbf{B} \times (\nabla \times \mathbf{B}) + 2(\mathbf{B} \cdot \nabla)\mathbf{B} ,$$

the magnetic Lorentz force reduces to

$$\mathbf{j} \times \mathbf{B} = \frac{1}{\mu} (\mathbf{B} \cdot \nabla)\mathbf{B} - \nabla \left(\frac{B^2}{2\mu} \right) . \quad (1.2.35)$$

The first term is the *magnetic tension force*, and it appears when the magnetic field lines are curved. It acts to try to make the field lines straight, like the tension along a string. The second term is the magnetic pressure force, and it appears when there exists a gradient in the field strength (or the magnitude of the magnetic field). Like the plasma pressure, it pushes from regions with high field strength towards regions with low field strength. On its own, it would homogenise the magnetic field. By similarity with the plasma pressure force, we define the magnetic pressure as $B^2/2\mu$.

Note, that the Lorentz force is always perpendicular to the magnetic field, since

$$\mathbf{B} \cdot (\mathbf{j} \times \mathbf{B}) = 0 ,$$

although magnetic tension and magnetic pressure force can separately have parallel components to the magnetic field, but these must cancel each other.

Ignoring plasma effects, for a magnetic field to be in equilibrium, the Lorentz force must equal zero. In the absence of a magnetic tension force, the magnetic field must be *straight and homogeneous*. However, magnetic tension and pressure forces can balance each other, for instance in *hyperbolic X-points*. These two simple cases are sketched in Figure 1.7, and will be the basis for our two-dimensional relaxation experiments.

If the magnetic field is embedded in a plasma, the pressure force can hold a non-zero Lorentz force in a *magnetohydrostatic* equilibrium. In this case, we can define the (non-dimensional) *plasma beta*, β , as the ratio of the gas pressure to the magnetic pressure,

$$\beta = \frac{\text{gas pressure}}{\text{plasma pressure}} = \frac{p}{B^2/2\mu} ,$$

hence

$$\beta = \frac{2\mu p}{B^2} . \quad (1.2.36)$$

If $\beta \ll 1$ then the plasma pressure force is negligible with respect to the magnetic forces, and if $\beta \gg 1$, the plasma pressure force dominates. The plasma beta tells us how important plasma effects are compared to magnetic

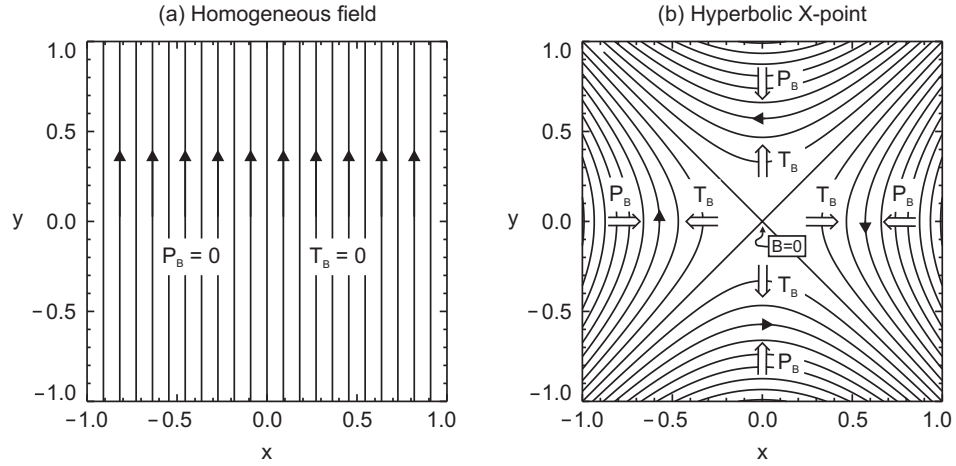


Figure 1.7: Two different configurations for magnetostatic equilibria. (a) Straight magnetic field, $\mathbf{B} = B_0(0, 1, 0)$, with zero magnetic pressure force P_B and magnetic tension T_B , and (b) hyperbolic X-point, $\mathbf{B} = -B_0(y, x, 0)$, with $P_B = -T_B$ at every point. In (b), the magnetic field contains a *magnetic null point*, where $B = 0$, at the origin.

effects, and whether they can be neglected or not. In general terms, most of the studies of coronal magnetic fields assume $\beta = 0$, as the densities of the solar corona are extremely low. However, lower in the chromosphere and near locations where the magnetic field is very weak, or zero, this assumption is no longer valid.

1.3 MHD equilibria: Magnetohydrostatics

Magnetic fields in the solar atmosphere change continuously, and together with the solar plasma, they form a highly dynamic environment. However, understanding MHD equilibrium conditions is extremely important for studying these complex hydromagnetic scenarios, for various reasons. Firstly, the set of MHD equations described above has an immense degree of complexity, and so, studying the associated stationary states provides a much simpler solution to start with. Secondly, for every analytical and numerical study, it is essential to understand the initial equilibrium state, depending on the demands of the study. Also, in relaxation-type experiments, one needs to know and understand the properties of the final states, whose mathematical descriptions must be provided by the MHD equilibrium theory. Lastly, from the point of view of modelling, many of the physical processes studied in solar plasma physics occur *slowly*, i.e. on time-scales much longer than the typical time-scale of the system, so the evolution of these systems can be modelled with a sequence of static equilibria. As an example, Schindler and Birn (1986) used this *quasi-static theory* to model the dynamics of the Earth's magnetotail.

The theory of the static solutions of the equations of MHD is called magnetohydrostatics (MHS). For such a state, there are no macroscopic velocities and the dependence with time disappears. The equations and derivations shown in this section, including more general cases, are explained in detail in Edenstrasser (1980*b,a*). They are also discussed by Priest (1982) and Biskamp (1993) "*Nonlinear magnetohydrodynamics*".

Under the static assumptions, $\mathbf{v} = 0$ and $\partial/\partial t = 0$, the above equation of motion (1.2.22), gives rise to the

fundamental equation of MHS,

$$\mathbf{j} \times \mathbf{B} - \nabla p = 0 , \quad (1.3.1)$$

which can be rewritten using Ampère's law (1.2.25), as

$$\nabla p = \frac{1}{\mu} (\nabla \times \mathbf{B}) \times \mathbf{B} . \quad (1.3.2)$$

The very first result of magnetohydrostatics comes directly from equation (1.3.1), and is that the dot product of \mathbf{B} and ∇p is zero,

$$\mathbf{B} \cdot \nabla p = 0 , \quad (1.3.3)$$

so the only spatial changes in the pressure p must be perpendicular to the magnetic field. In other words, in any static equilibrium, *the plasma pressure is constant along field lines*.

Combining the vector identity $\nabla \cdot (\nabla \times \mathbf{A}) = 0$ and the solenoidal constraint (1.2.26), the magnetic field \mathbf{B} can be written as the curl of the *vector potential* \mathbf{A} , perpendicular to the magnetic field, where

$$\mathbf{B} = \nabla \times \mathbf{A} . \quad (1.3.4)$$

1.3.1 MHS equilibria in 2D

In a system with a translational invariance such as $\partial/\partial z = 0$ (this is usually referred as to two and a half dimensions), we can rewrite \mathbf{B} as

$$\mathbf{B} = \nabla A_z(x, y) \times \mathbf{e}_z + B_z(x, y) \mathbf{e}_z , \quad (1.3.5)$$

where A_z is the z -component of the vector potential \mathbf{A} . The scalar product of \mathbf{B} and ∇A_z equals zero,

$$\mathbf{B} \cdot \nabla A_z = (\nabla A_z \times \mathbf{e}_z) \cdot \nabla A_z + B_z \mathbf{e}_z \cdot \nabla A_z = 0 , \quad (1.3.6)$$

since the first term on the right hand side of (1.3.6) is the scalar product of two orthogonal vectors, and the second term is zero since $\partial A_z / \partial z = 0$. Hence, in two (and two and a half) dimensions, A_z is constant along magnetic field lines. This is a big advantage, as, in fact, the contours of A_z are the projections of the magnetic field lines onto the xy -plane. The function $A_z(x, y)$ is known as the *flux function*.

Using equations (1.3.3) and (1.3.5), we get

$$\mathbf{B} \cdot \nabla p = (\nabla A_z \times \mathbf{e}_z) \cdot \nabla p + B_z \mathbf{e}_z \cdot \nabla p = 0 . \quad (1.3.7)$$

Again, $p = p(x, y)$, so the second term on the right of equation (1.3.7) is zero. Hence, the first term on the right hand side must be zero, and expanding it in terms of partial derivatives, we obtain

$$\frac{\partial A_z}{\partial y} \frac{\partial p}{\partial x} - \frac{\partial A_z}{\partial x} \frac{\partial p}{\partial y} = 0 ,$$

which implies that the pressure p is a function of the flux function A_z ,

$$p = \mathcal{F}(A_z) , \quad (1.3.8)$$

where \mathcal{F} is an unknown function that is dependent on the initial conditions and evolution.

Now, in a strictly two-dimensional system, the magnetic field components are given by

$$B_x = \frac{\partial A_z}{\partial y} , \quad B_y = -\frac{\partial A_z}{\partial x} , \quad B_z = 0 , \quad (1.3.9)$$

and both the vector potential \mathbf{A} and the current density \mathbf{j} have an only non-zero z -component, i.e. $\mathbf{A} = A_z \mathbf{e}_z$ and $\mathbf{j} = j_z \mathbf{e}_z$. The curl of the magnetic field is then given by

$$\nabla \times \mathbf{B} = (0, 0, -\frac{\partial^2 A_z}{\partial y^2} - \frac{\partial^2 A_z}{\partial x^2}) = -\nabla^2 A_z \mathbf{e}_z ,$$

so that, from Ampère's law (1.2.25), we get

$$j_z = -\frac{1}{\mu} \nabla^2 A_z . \quad (1.3.10)$$

Now, substituting (1.3.9) into equation (1.3.2), we obtain

$$\nabla p = -\frac{1}{\mu_0} \nabla^2 A_z \nabla A_z ,$$

and since $\nabla p = \nabla A_z dp/dA_z$, we get

$$\frac{dp}{dA_z} = -\frac{1}{\mu_0} \nabla^2 A_z = j_z . \quad (1.3.11)$$

This is the *Grad-Shafranov equation*, for two-dimensional magnetic fields. Finally, combining equation (1.3.11) with (1.3.8), we get

$$j_z = \mathcal{F}'(A_z) = \frac{d\mathcal{F}}{dA_z} . \quad (1.3.12)$$

Equations (1.3.8) and (1.3.12) tell us that, *for two dimensional fields* in equilibrium, the *plasma pressure and current density are constant along field lines*. This Grad-Shafranov equation gives the relation between these two quantities, and *uniquely* characterises a 2D MHS equilibrium.

1.3.2 Classification of the MHS equilibria

Looking at the fundamental equation of MHS (1.3.1), the equilibria can be classified into three different types, depending on if the two terms involved are identically zero, or they balance each other. Furthermore, the first case also depends on whether the current density, \mathbf{j} , is zero itself, or is parallel to the magnetic field everywhere. We shall present the three different cases in order of complexity, starting from the case where $\mathbf{j} = 0$, $\nabla p = 0$, then with $\mathbf{j} \parallel \mathbf{B}$, $\nabla p = 0$, and finally, the case where $\mathbf{j} \times \mathbf{B} = \nabla p$.

Potential fields

A magnetohydrostatic equilibrium is said to be potential if there exists no current density, i.e. $\mathbf{j} = 0$. Thus the Lorentz force, $\mathbf{j} \times \mathbf{B}$, is zero, and in order to satisfy equation (1.3.1), the plasma pressure force must also equal zero. Ampère's law (1.2.25) gives

$$\nabla \times \mathbf{B} = 0 ,$$

and from the vector identity $\nabla \times (\nabla \phi) = 0$, the solution for potential fields is given by $\mathbf{B} = \nabla \phi$, where $\phi(x, y, z)$ is the *scalar magnetic potential*. Using the solenoidal constraint (1.2.26), we get

$$\nabla^2 \phi = 0 . \tag{1.3.13}$$

Equation (1.3.13) is Laplace's equation. Solutions can be obtained by various methods including separation of variables, and are uniquely determined by the boundaries of the system. Hence, given an initial magnetohydrodynamic system where the normal components to all boundaries are prescribed and fixed, subject to "external" disturbances, there exists one and only one potential equilibrium.

Force-free fields

If both the gradient of pressure and the Lorentz force are zero, the equilibrium is known as force-free,

$$\mathbf{j} \times \mathbf{B} = 0 . \tag{1.3.14}$$

Notice, that the potential fields are one particular solution of this. Equation (1.3.14) implies that in the force-free case, the current density vector is parallel to the magnetic field, and from Ampère's law (1.2.25),

$$\nabla \times \mathbf{B} = \alpha \mathbf{B} , \tag{1.3.15}$$

where α may be a function of position, \mathbf{r} . If $\alpha = 0$, the equilibrium is potential.

From the vector identity $\nabla \cdot (\nabla \times \mathbf{B}) = 0$, we have

$$\nabla \cdot (\alpha \mathbf{B}) = \alpha \nabla \cdot \mathbf{B} + \mathbf{B} \cdot \nabla \alpha = 0 ,$$

and using the solenoidal constraint (1.2.26), we can get a restriction for the scalar function $\alpha(\mathbf{r})$,

$$\mathbf{B} \cdot \nabla \alpha = 0 . \tag{1.3.16}$$

Hence, α is constant along field lines, although it may vary from field line to field line.

Taking the curl of equation (1.3.15), we get

$$\begin{aligned} \nabla \times (\nabla \times \mathbf{B}) &= \nabla \times (\alpha \mathbf{B}) \\ &= \alpha (\nabla \times \mathbf{B}) + \nabla \alpha \times \mathbf{B} \\ &= \alpha^2 \mathbf{B} + \nabla \alpha \times \mathbf{B} , \end{aligned}$$

and using the vector identity $\nabla \times (\nabla \times \mathbf{B}) = \nabla(\nabla \cdot \mathbf{B}) - \nabla^2 \mathbf{B}$, where the first term on the right hand side is

zero, we obtain

$$\nabla^2 \mathbf{B} = -\alpha^2 \mathbf{B} - \nabla \alpha \times \mathbf{B} . \quad (1.3.17)$$

If α is constant everywhere, the equilibrium is known as a *linear force-free field*, and equation (1.3.17) reduces to

$$\nabla^2 \mathbf{B} = -\alpha^2 \mathbf{B} . \quad (1.3.18)$$

Otherwise, the field is known as a *non linear force-free field*, and the equations (1.3.17) and (1.3.16) need to be solved together.

Non-force-free fields

The above force-free conditions involve zero Lorentz and plasma pressure forces. These approximations are valid for many of the studies of coronal magnetic fields, where the plasma density is very low, and the effects of plasma pressure in the highly magnetised atmosphere are negligible. However, there are regions in which the magnetic field weakens to a point at which plasma effects are no longer insignificant, and hence, the above considerations do not hold. In these cases, one must address the complete equation of MHS (1.3.1), which, for two dimensional fields, reduces to equation (1.3.11).

Furthermore, the inclusion of pressure effects adds in an extra complication, since the energetics of the system must then be considered. The *cold plasma approximation* neglects the effects of plasma pressure, and so, treats the dynamical process as purely magnetic. In this case, the plasma behaves, ignoring thermal effects, *as if* the temperature were zero, and so too for the internal energy. Note, this does not mean that there is no plasma density. Hence, if the internal energy is zero, from the above equations (1.2.32), (1.2.33) and (1.2.34), only the last two have to be considered, and so, the conversion of magnetic energy to internal energy (or vice versa) is not allowed, and so, a rapid release of magnetic energy can only be used to accelerate particles or to cause a bulk plasma flow, but not to heat the plasma. On the other hand, when pressure effects are included, the exchange of magnetic and internal energy is possible, and it is precisely that detail which permits a wider family of different equilibria. Hence, non-force-free effects will become important in regions of weak magnetic field in the solar atmosphere, such as the surroundings of possible localised points where the magnetic field vanishes.

1.3.3 Models of MHS equilibria

The magnetic field of the solar corona is believed to evolve through a series of force-free states (Heyvaerts and Priest, 1984). Since the solar corona involves a low-beta plasma in which magnetic forces dominate over plasma forces, this is not an unreasonable assumption, and so, most of the recent studies on the relaxation of coronal magnetic fields (e.g. Mackay and van Ballegooijen, 2006; Ji et al., 2007; Inoue et al., 2008; Janse and Low, 2009; Miller et al., 2009; Pontin et al., 2009) have been done by considering the approximation of an extremely tenuous plasma, for which the plasma pressure does not play an important role, and the persistent hydromagnetic structures of the solar corona are assumed to be in magnetic balance, with zero pressure gradients.

However, getting information about the magnetic field distribution in the solar corona is not a trivial problem. Unfortunately, the weak plasma emission due to the low density of the corona makes direct measurements of coronal magnetic fields extremely difficult. Even if some coronal lines show a sufficiently large Zeeman split and measurements could be made, knowing exactly the height where those lines are formed is not easy, and even if

known, the number of points would be small for this information to be conveniently used. Thus it becomes necessary to resort to magnetic field extrapolations from the relatively easily measured photospheric or chromospheric line-of-sight, or vector magnetograms. A large variety of studies have been made with current-free potential extrapolations (e.g. Altschuler and Newkirk, 1969; Hoeksema, 1991; Gary, 1996; Rudenko, 2001), which, after showing their inaccuracy in active regions (Schrijver et al., 2005), have been improved with force-free extrapolations (e.g. Wiegmann et al., 2006; Schrijver et al., 2006; Mackay and van Ballegoijen, 2006; Régnier, 2008).

In addition, there are many codes available to calculate those force-free fields from the observed magnetic field in the photosphere (Amari et al., 1998; Wiegmann et al., 2006, 2008; Schrijver et al., 2006; Metcalf et al., 2008). These codes have been used with varying degrees of success to determine the magnetic field of solar flares and active regions (e.g. Schrijver et al., 2008; Régnier, 2008; De Rosa et al., 2009; Wheatland and Régnier, 2009). However, problems remain with these approaches. In particular, a non-linear force-free field determined from a line-of-sight photospheric magnetic field, fixed at the rigid boundaries of the domain, is not unique, but is one of an infinite number of possible solutions. This fact is well known and has been discussed by several authors (see Low, 2006). The main problem is that the observed boundary data are inconsistent with the nonlinear force-free model. Recently, Wheatland and Régnier (2009) have studied a self-consistent solution for a particular Solar Active Region.

Placing aside extra contributions such as radiative losses, if a substantial fraction of the magnetic energy released goes into the internal energy, then the plasma beta cannot be small. Hence, considering the behaviour of the plasma is important even if it has little effect on the final magnetic equilibrium. Gary (2001) suggested the possibility that there is high beta plasma in the solar corona above active regions.

There are many studies on the MHS equilibrium with force balance in the Earth's magnetotail, both numerical (e.g. Hesse and Birn, 1993; Lemon et al., 2003) and analytical (e.g. Birn, 2005; Zaharia et al., 2005), but only within the past few years, the reconstruction of the global coronal magnetic field including a finite Lorentz force balanced by magnetic and gravity forces have started to be considered, independently, by Ruan et al. (2008) and Gary (2009).

Some years before, Low (1982*a*, 1984, 1985, 1991, 1992, 1993*a,b*) and Bogdan and Low (1986) carried out a wide analytical investigation of the full set of MHS equations, under different special assumptions. They prescribed a special type of current flow which allowed the reduction of the mathematical problem to one single partial differential equation. This procedure requires an external force dependent on the plasma density, such as a gravitational force. Later, Neukirch (1995) used these derivations to develop a self-consistent three-dimensional analytic solution of the MHS equations, reducing them to a Schrödinger type equation. Also, there exist various other approaches which give analytical solutions to the three-dimensional MHS Equations, as studied by Neukirch and Rastätter (1999) and Petrie and Neukirch (2000). The model of Neukirch (1995) has been used by Ruan et al. (2008) to extrapolate the magnetic field in the corona from photospheric magnetic field measurements, finding noticeable differences in comparison to both potential and force-free field models. Also, this model has been recently used for rotating magnetized coronae by Al-Salti et al. (2010).

In parallel to the above studies, Dasgupta et al. (1998) used the principle of a minimum dissipative rate (MDR), based on the idea that a dissipative system naturally tends towards a state in which its dissipation rate is minimum, to study the relaxed states of a turbulent magnetised plasma, obtaining a MHD equilibrium which could support a pressure gradient in a non-force-free state. Then, Bhattacharyya et al. (2007) used this same principle for modelling solar arcades using a two-fluid description, obtaining a relaxed state which was non-force-free in nature. Last, Gary (2009) evaluated the MRD method for deriving a coronal non-force-free magnetic field solution.

1.4 Magnetic null points

In most magnetic environments with a certain degree of complexity, there exist certain points in which the magnetic field vanishes, $B = 0$. We call these magnetic null points, or magnetic neutral points. They are key locations for magnetic dissipation and energy conversion, as they are regions about which high current density layers may be built in the form of a tangential discontinuity (see Section 1.5). Hence, studying in detail the local magnetic configuration around magnetic nulls is necessary for the understanding of such processes. We follow the mathematical description of two and three dimensional null points described in Parnell et al. (1996), using a linear analysis about the null in Cartesian geometry.

Taking the null point to be situated at the origin, without loss of generality, and assuming that the magnetic field approaches zero linearly, the magnetic field \mathbf{B} near a null point may be expressed as

$$\mathbf{B} = \mathbf{M} \cdot \mathbf{r} , \quad (1.4.1)$$

where \mathbf{M} is a matrix with elements $M_{ij} = \partial B_i / \partial x_j$ and \mathbf{r} is the position vector $(x, y, z)^T$.

1.4.1 Two-dimensional null points

In two dimensions, the matrix \mathbf{M} is given by

$$\mathbf{M} = \begin{pmatrix} a_{11} & a_{12} \\ a_{21} & a_{22} \end{pmatrix} = \begin{pmatrix} \frac{\partial B_x}{\partial x} & \frac{\partial B_x}{\partial y} \\ \frac{\partial B_y}{\partial x} & \frac{\partial B_y}{\partial y} \end{pmatrix} .$$

The solenoidal constraint (1.2.26) gives $a_{11} = -a_{22} \equiv p$, and Ampère's law (1.2.25) gives the current density associated with the null point as $j_z = (a_{21} - a_{12})/\mu$. Let us define a parameter q such that

$$a_{12} = \frac{1}{2}(q - j_z) \quad \text{and} \quad a_{21} = \frac{1}{2}(q + j_z) .$$

For a potential (i.e. current-free) null point, $a_{12} = a_{21} = q/2$. Finally, the matrix \mathbf{M} can be written as

$$\mathbf{M} = \begin{pmatrix} p & \frac{1}{2}(q - j_z) \\ \frac{1}{2}(q + j_z) & -p \end{pmatrix} . \quad (1.4.2)$$

The flux function A_z is obtained using (1.3.9) and (1.4.2), as

$$A_z = \frac{1}{4}[(q - j_z)y^2 - (q + j_z)x^2] + pxy .$$

Now, the xy -axis can be rotated conveniently so that the last term on the right hand side disappears. Choosing the angle of rotation, θ , so that $\tan 2\theta = -2p/q$, the flux function becomes

$$A_z = \frac{1}{4}[(j_{thresh} - j_z)y^2 - (j_{thresh} + j_z)x^2] , \quad (1.4.3)$$

where the x' and y' coordinates have been renamed back as x and y , for simplicity, and j_{thresh} is a threshold

current defined by

$$j_{threshold} = \sqrt{4p^2 + q^2}. \quad (1.4.4)$$

In this new coordinate system,

$$B_x = \frac{1}{2}(j_{threshold} - j_z)y \quad \text{and} \quad B_y = \frac{1}{2}(j_{threshold} + j_z)x,$$

so the matrix \mathbf{M} is given by

$$\mathbf{M} = \begin{pmatrix} 0 & \frac{1}{2}(j_{threshold} - j_z) \\ \frac{1}{2}(j_{threshold} + j_z) & 0 \end{pmatrix}. \quad (1.4.5)$$

The eigenvalues λ of this matrix are obtained by solving $\det(\mathbf{M} - \lambda\mathbf{I}) = 0$, giving

$$\lambda = \pm \frac{1}{2} \sqrt{j_{threshold}^2 - j_z^2}. \quad (1.4.6)$$

So the eigenvalues will be real if $|j_z| < j_{threshold}$ and imaginary if $|j_z| > j_{threshold}$, defining the geometry of the two-dimensional null point.

Potential two-dimensional null points

For a potential null point in two dimensions, the current density is zero, $j_z = 0$, \mathbf{M} is symmetric, and its eigenvalues are $\lambda = \pm j_{threshold}/2$. The flux function is given by

$$A_z = \frac{j_{threshold}}{4}(y^2 - x^2),$$

and the field lines are rectangular hyperbolae, and trace out a *potential X-point*, as in Figure 1.8a, with exactly 90° between the separatrices (the field lines through the null point). It was shown in Figure 1.7b how, in absence of a plasma pressure gradient, this configuration is in complete force balance. This is the only possible current-free configuration for a two-dimensional null point.

Non-potential two-dimensional null points

If $j_z \neq 0$, we can distinguish three different types of two-dimensional magnetic null points. 1) If $|j_z| < j_{threshold}$, the eigenvalues of \mathbf{M} are real, and the field lines form a *hyperbolic X-point* with less (or greater) than 90° between the separatrices, as in Figure 1.8b, which tends to the potential case when $j_z \rightarrow 0$. 2) If $|j_z| = j_{threshold}$, the eigenvalues are zero, the flux function depends only on one coordinate, and the field lines are anti-parallel, with a null line along the x or y axis, as in Figure 1.8c. 3) If $|j_z| > j_{threshold}$, the eigenvalues are imaginary, and the field lines form an *elliptic O-point*, as in Figure 1.8d, which becomes circular when $j_{threshold} = 0$.

In two dimensions, we define a *separatrix* as the line that separates two magnetic domains with different connectivities. In Figure 1.8, the separatrices, which all go through the null point, are shown with dashed lines.

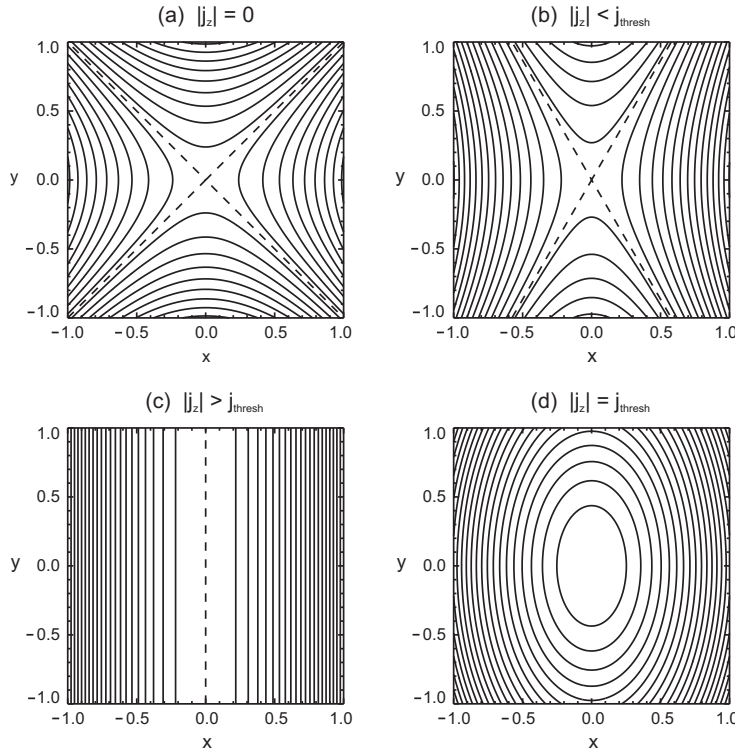


Figure 1.8: Two-dimensional null points, showing (a) a potential X-point, (b) a non-potential hyperbolic X-point, (c) antiparallel field lines and (d) an elliptic O-point. Dashed lines show the *separatrices* of the different magnetic regions. Based on Parnell et al. (1996), Fig. 2.

1.4.2 Three-dimensional null points

In three dimensions, the matrix \mathbf{M} becomes

$$\mathbf{M} = \begin{pmatrix} a_{11} & a_{12} & a_{13} \\ a_{21} & a_{22} & a_{23} \\ a_{31} & a_{32} & a_{33} \end{pmatrix} = \begin{pmatrix} \frac{\partial B_x}{\partial x} & \frac{\partial B_x}{\partial y} & \frac{\partial B_x}{\partial z} \\ \frac{\partial B_y}{\partial x} & \frac{\partial B_y}{\partial y} & \frac{\partial B_y}{\partial z} \\ \frac{\partial B_z}{\partial x} & \frac{\partial B_z}{\partial y} & \frac{\partial B_z}{\partial z} \end{pmatrix}.$$

The solenoidal constraint (1.2.26) gives $a_{11} + a_{22} + a_{33} = 0$, and this condition implies that the sum of the three eigenvalues λ_1 , λ_2 and λ_3 is also zero. Let us represent the position along a single magnetic field line near the null in terms of a position vector $\mathbf{r} = (x, y, z)^T$, which depends on an arbitrary parameter k which varies along the length of the field line. The magnetic field along the field line may be written as

$$\mathbf{B} = \frac{d\mathbf{r}(k)}{dk} = \mathbf{M} \cdot \mathbf{r}(k), \quad (1.4.7)$$

and, using the substitution $\mathbf{r}(k) = \mathbf{P}\mathbf{u}(k)$, where $\mathbf{P} = (\mathbf{x}_1, \mathbf{x}_2, \mathbf{x}_3)$ is the matrix of the eigenvectors of \mathbf{M} which satisfy

$$\mathbf{M}\mathbf{x}_1 = \lambda_1\mathbf{x}_1,$$

$$\mathbf{M}\mathbf{x}_2 = \lambda_2\mathbf{x}_2,$$

$$\mathbf{M}\mathbf{x}_3 = \lambda_3\mathbf{x}_3,$$

we rewrite equation (1.4.7) as

$$\frac{d\mathbf{u}(k)}{dk} = \mathbf{P}^{-1}\mathbf{M}\mathbf{P} \cdot \mathbf{u}(k) . \quad (1.4.8)$$

There are two cases that have to be considered separately, depending on if the matrix \mathbf{M} is diagonalizable or not.

First, we assume that \mathbf{M} can be diagonalised to a matrix \mathbf{A} whose elements can be either real or complex, according to the nature of the eigenvalues. Then, three different eigenvectors exist, and the solution of equation (1.4.8) for a given field line can be written as

$$\mathbf{u}(k) = \mathbf{A}e^{\mathbf{A}k} \quad (1.4.9)$$

where \mathbf{A} is also a diagonal matrix with its non-zero elements given by A , B and C , which are constant along a field line. Hence, the solution of equation (1.4.7) is given by

$$\mathbf{r}(k) = Ae^{\lambda_1 k} \mathbf{x}_1 + Be^{\lambda_2 k} \mathbf{x}_2 + Ce^{\lambda_3 k} \mathbf{x}_3 . \quad (1.4.10)$$

We shall now consider the different cases, depending on if the eigenvalues are real or complex. The fact that $\lambda_1 + \lambda_2 + \lambda_3 = 0$ gives us only two possibilities: either the three eigenvalues are real, or two of them are complex and one is real.

1) If all the eigenvalues are real, since the sum of the three eigenvalues is zero, there is always one eigenvalue of opposite sign to the other two, say $\lambda_1, \lambda_2 > 0$ and $\lambda_3 < 0$. Then, for field lines going towards and away from the null, we have

$$\mathbf{r}(k \rightarrow -\infty) \rightarrow Ce^{\lambda_3 k} \mathbf{x}_3 ,$$

$$\mathbf{r}(k \rightarrow \infty) \rightarrow Ae^{\lambda_1 k} \mathbf{x}_1 + Be^{\lambda_2 k} \mathbf{x}_2 .$$

Hence, field lines that head towards the null are parallel to one single eigenvector, and field lines that are directed away from the null lie parallel to a plane defined by the remaining two eigenvectors. The line defined by the path of the first eigenvector is the *spine*, and the plane defined by the other two is the *fan*. If the spine field line heads towards the null, and the fan field lines go away from it, as the examples above, the null is called a *positive null point*. If, on the contrary, we exchange the signs of the eigenvalues (i.e. $\lambda_1, \lambda_2 < 0$ and $\lambda_3 > 0$), then the fan field lines head towards the null, and the spine field line go away from it. In this case, the null is called a *negative null point*. Figure 1.9 shows the geometry of a generic three-dimensional (positive) null point.

2) If we have two complex and one real eigenvalues, say $\eta \pm i\nu$ and -2η , with corresponding eigenvectors $\mathbf{x}_1 = (\mathbf{x}'_1 + i\mathbf{x}'_2)/2$, $\mathbf{x}_2 = (\mathbf{x}'_1 - i\mathbf{x}'_2)/2$ and \mathbf{x}_3 , we can rewrite equation (1.4.10) in terms of two new constants R and Θ to get, for $\eta > 0$,

$$\mathbf{r}(k \rightarrow -\infty) \rightarrow Ce^{-2\eta k} \mathbf{x}_3 ,$$

$$\mathbf{r}(k \rightarrow \infty) \rightarrow Re^{\eta k} \cos(\Theta k + \nu k) \mathbf{x}'_1 - Re^{\eta k} \sin(\Theta k + \nu k) \mathbf{x}'_2 .$$

Again, if $\eta > 0$ and the null is positive, field lines that head towards the null are parallel to one single eigenvector, defining the spine, and field lines that go away from the null lie parallel to the fan plane defined by \mathbf{x}'_1 and \mathbf{x}'_2 . The fan field lines produce a pattern of a spiral.

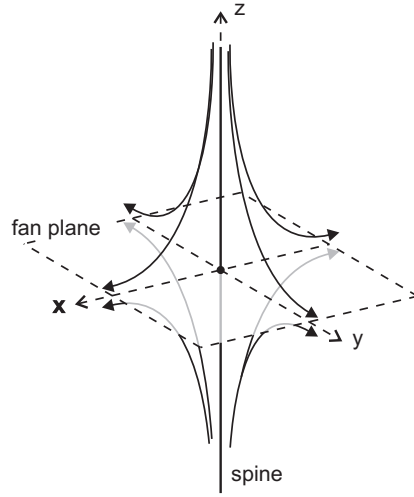


Figure 1.9: Structure of a 3D null point, showing the spine and the fan plane.

Secondly, if the matrix \mathbf{M} is not diagonalizable, two of the eigenvalues are repeated and the matrix \mathbf{M} can only reduce to a *Jordan normal form* that looks like,

$$\mathbf{J}_n = \begin{pmatrix} \lambda & 1 & 0 \\ 0 & \lambda & 0 \\ 0 & 0 & -2\lambda \end{pmatrix}.$$

We now write the equation for the field lines using the substitution $\mathbf{r}(k) = \mathbf{P}\mathbf{u}(k)$, where this time $\mathbf{P} = (\mathbf{x}_1, \mathbf{x}_2^*, \mathbf{x}_3)$, with

$$\begin{aligned} \mathbf{M}\mathbf{x}_1 &= \lambda\mathbf{x}_1, \\ \mathbf{M}\mathbf{x}_2^* &= \mathbf{x}_1 + \lambda\mathbf{x}_2^*, \\ \mathbf{M}\mathbf{x}_3 &= -2\lambda\mathbf{x}_3, \end{aligned} \tag{1.4.11}$$

such that

$$\frac{d\mathbf{u}}{dk} = \mathbf{J}_n\mathbf{u}.$$

The solution of equation (1.4.7) for a given field line can be now written as

$$\mathbf{r}(k) = (A + Bk)e^{\lambda k}\mathbf{x}_1 + Be^{\lambda k}\mathbf{x}_2^* + Ce^{-2\lambda k}\mathbf{x}_3. \tag{1.4.12}$$

Assuming $\lambda > 0$, the solutions away from the null are

$$\mathbf{r}(k \rightarrow -\infty) \rightarrow Ce^{-2\lambda k}\mathbf{x}_3,$$

$$\mathbf{r}(k \rightarrow \infty) \rightarrow (A + Bk)e^{\lambda k}\mathbf{x}_1 + Be^{\lambda k}\mathbf{x}_2^*,$$

so that field lines heading towards the null are parallel to the eigenvector related to the single eigenvalue, \mathbf{x}_3 , and field lines going away from the null lie parallel to the plane defined by the eigenvector \mathbf{x}_1 and the Jordan basis vector \mathbf{x}_2^* .

Following the method in Parnell et al. (1996), we can define a way of reducing \mathbf{M} to its simplest form, in order to examine all possible configurations around a 3D null point. We do this by choosing the local orthogonal coordinate system such that the spine is always aligned with the z -axis, and by rotating the system so that the x -axis lies in the direction of the current density in the xy -plane, so that the current is defined as

$$\mathbf{j} = \frac{1}{\mu}(j_{\perp}, 0, j_{\parallel}). \quad (1.4.13)$$

where j_{\parallel} and j_{\perp} are the components parallel and perpendicular to the spine, respectively, and \mathbf{M} results in

$$\mathbf{M} = \begin{pmatrix} 1 & \frac{1}{2}(q - j_{\parallel}) & 0 \\ \frac{1}{2}(q + j_{\parallel}) & p & 0 \\ 0 & j_{\perp} & -(p + 1) \end{pmatrix}, \quad (1.4.14)$$

where $p \geq -1$, and $q^2 \leq j_{\parallel}^2 + 4p$. Similar to the 2D case, a threshold current, j_{thresh} , can be defined as

$$j_{thresh} = \sqrt{(p - 1)^2 + q^2}. \quad (1.4.15)$$

The eigenvalues associated with \mathbf{M} can be written as

$$\begin{aligned} \lambda_1 &= \frac{p + 1 + \sqrt{j_{thresh}^2 - j_{\parallel}^2}}{2}, \\ \lambda_2 &= \frac{p + 1 - \sqrt{j_{thresh}^2 - j_{\parallel}^2}}{2}, \\ \lambda_3 &= -(p + 1). \end{aligned} \quad (1.4.16)$$

In situations where $j_{\perp} = 0$, the matrix \mathbf{M} can be reduced, after the appropriate rotation about the spine, to

$$\mathbf{M} = \begin{pmatrix} 1 & -\frac{1}{2}j_{\parallel} & 0 \\ \frac{1}{2}j_{\parallel} & p & 0 \\ 0 & 0 & -(p + 1) \end{pmatrix}. \quad (1.4.17)$$

Potential three-dimensional null points

For a potential field, both j_{\perp} and j_{\parallel} are zero, and the matrix \mathbf{M} is symmetric, and can be written as

$$\mathbf{M} = \begin{pmatrix} 1 & 0 & 0 \\ 0 & p & 0 \\ 0 & 0 & -(p + 1) \end{pmatrix}.$$

Thus the related eigenvalues are $\lambda_1 = 1$, $\lambda_2 = p$ and $\lambda_3 = -(p + 1)$, and the associated eigenvectors are

$$\mathbf{x}_1 = \begin{pmatrix} 1 \\ 0 \\ 0 \end{pmatrix}, \quad \mathbf{x}_2 = \begin{pmatrix} 0 \\ 1 \\ 0 \end{pmatrix}, \quad \mathbf{x}_3 = \begin{pmatrix} 0 \\ 0 \\ 1 \end{pmatrix},$$

so for a potential null, the fan plane is perpendicular to the spine. With this choice for the matrix \mathbf{M} , where the

spine lies along the z -axis, we must have $p \geq 0$. The eigenvectors \mathbf{x}_1 and \mathbf{x}_2 define the fan plane. The threshold current is $j_{thresh} = |p - 1|$, and depending on the value of p and j_{thresh} , we get the different types of potential three-dimensional null points. 1) If $j_{thresh} = 0$, then $p = 1$ and the field is a positive proper radial null, symmetric in the eight 3D quadrants, as shown in Figure 1.10a. 2) If $j_{thresh} > 0$ and $p > 0$, the field is an improper radial null: Field lines gather to run parallel (as $k \rightarrow \infty$) to the x -axis if $0 < p < 1$, or parallel to the y -axis if $p > 1$, as in Figure 1.10b. 3) If $p = 0$, there are only two non-zero eigenvalues, and the field becomes a sequence of two-dimensional potential X-points lying in planes parallel to the xz -plane and forming a null line along the y -axis.

Non-potential three-dimensional null points

Here, the matrix \mathbf{M} is asymmetric, and we can study three different cases: $|j_{\parallel}| < j_{thresh}$, $|j_{\parallel}| = j_{thresh}$ and $|j_{\parallel}| > j_{thresh}$.

▷ When $|j_{\parallel}| < j_{thresh}$, the three eigenvalues are real and distinct, and all three eigenvectors exist. 1) If $j_{\perp} = 0$ and $j_{\parallel} \neq 0$, the fan and spine are perpendicular, but the eigenvectors \mathbf{x}_1 and \mathbf{x}_2 are not. At $k \rightarrow \infty$, the field lines in the fan plane run parallel to a line $y(x)$ in the fan plane, defining a skewed improper null. 2) If $j_{\perp} \neq 0$ and $j_{\parallel} = 0$, the fan is not perpendicular to the spine, and the angle between them reduces as j_{\parallel} increases. The fan does not necessarily tilt about the x -axis (the direction of the current) and so, the current (which is perpendicular to the spine) does not generally lie in the plane of the fan. 3) If $j_{\perp} \neq 0$ and $j_{\parallel} \neq 0$, the fan is tilted towards the spine, so j_{\perp} does not lie in the plane of the fan, and the field lines again define a skewed improper null.

▷ When $|j_{\parallel}| = j_{thresh}$, two of the eigenvalues are repeated. 1) If $j_{\perp} \neq 0$ and $j_{\parallel} = 0$, the fan does not lie in the xy -plane, but field lines extend radially and symmetrically in the plane of the fan (Figure 1.11a). 2) If $j_{\perp} = 0$ and $j_{\parallel} \neq 0$, there exist only two different eigenvectors, so an extra vector must be calculated using equation (1.4.11), the Jordan basis vector. The fan plane is perpendicular to the spine, and the field lines in the fan form a spiral, called a *critical spiral*, in which the field lines orientate towards the line of one single eigenvector (Figure 1.11b). 3) If $j_{\perp} \neq 0$ and $j_{\parallel} \neq 0$, we again have to look for a Jordan basis vector, and we find another critical spiral, with the fan not perpendicular to the spine.

▷ When $|j_{\parallel}| > j_{thresh}$, the two eigenvalues associated with the plane of the fan are complex conjugates. 1) If $j_{\perp} = 0$ and $j_{\parallel} \neq 0$, the spine is perpendicular to the fan, and the field lines spiral around the spine until they spread spiraling outwards parallel to the fan plane (Figure 1.11c). 2) It is not possible to create a spiral null without a parallel component of the current. 3) If $j_{\perp} \neq 0$ and $j_{\parallel} \neq 0$, we have a spiral null with the fan not perpendicular to the spine.

In general, the geometry of three-dimensional nulls will depend on the four parameters $(p, q, j_{\parallel}, j_{\perp})$. In the case of a potential null, they reduce to one single parameter p , and for the non-potential case, the field lines about the null are radial, critical spiral or spiral, depending on the relative size of the current parallel to the spine with respect to the threshold current. The current perpendicular to the spine determines the inclination of the fan plane to the spine.

A complete understanding of the geometry around magnetic null points is of extreme importance for studies of coronal magnetic fields. Longcope and Parnell (2009) have found that magnetic nulls have a reasonable population density in the solar corona. Null points are found directly from extrapolations of the photospheric magnetic field, but also their density is estimated from the Fourier spectrum of the magnetogram coming from the solar photosphere.

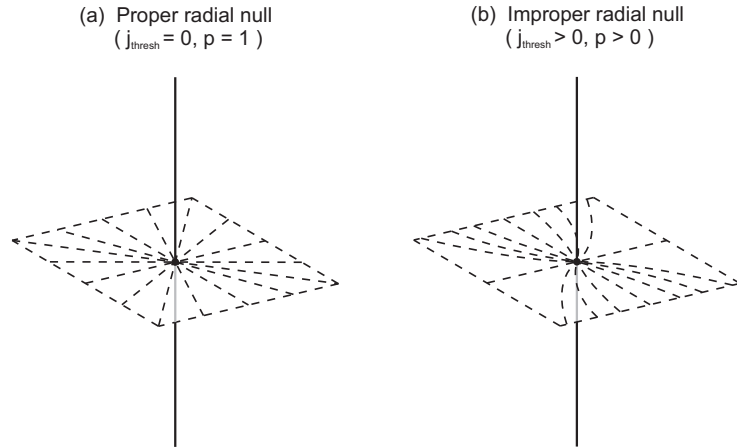


Figure 1.10: Sketch of the magnetic configuration of two 3D potential nulls. For simplicity we show only the spine and the fan, with field lines lying in the fan plane itself (dashed), for (a) a proper radial null, and (b) an improper radial null with the field lines aligned along the y -axis.

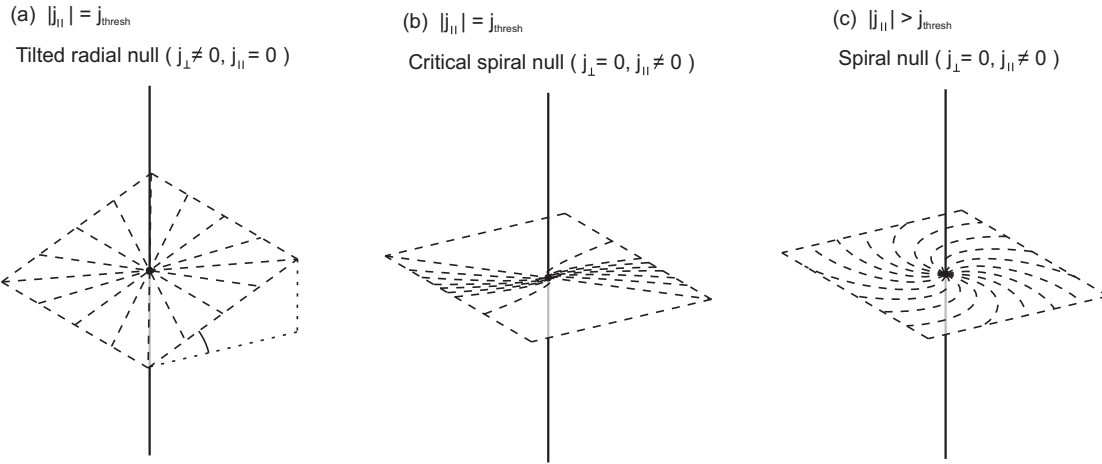


Figure 1.11: Sketch of the magnetic configuration of 3D non-potential nulls, for the cases with (a) current perpendicular to spine, showing a tilted fan plane, and (b) and (c) current parallel to the spine, showing the fan orthogonal to the spine, and field lines in (b) a critical spiral and (c) a coiled spiral.

Parnell et al. (1997) showed that a linear three-dimensional null point in equilibrium must be potential ($\mathbf{j} = 0$), so cannot hold in a MHS equilibrium (in which the Lorentz force $\mathbf{j} \times \mathbf{B}$ is balanced with a pressure gradient, ∇p). To show this, let's take the curl of the fundamental equation of MHS, equation (1.3.1), making use of the vector identity $\nabla \times (\nabla f) = 0$,

$$\nabla \times (\mathbf{j} \times \mathbf{B}) = \nabla \times \nabla p = 0.$$

Now, we use the vector identity

$$\nabla \times (\mathbf{j} \times \mathbf{B}) = (\mathbf{B} \cdot \nabla)\mathbf{j} - (\mathbf{j} \cdot \nabla)\mathbf{B} + (\nabla \cdot \mathbf{B})\mathbf{j} - (\nabla \cdot \mathbf{j})\mathbf{B}.$$

As shown in Parnell et al. (1997), if we stay in the linear regime, the current density remains constant, hence, the first and last terms in the right hand side are zero, and the third term is also zero because of the solenoidal constraint

(1.2.26). Since $\mathbf{B} = \mathbf{M} \cdot \mathbf{r}$, we get

$$\nabla \times (\mathbf{j} \times \mathbf{B}) = -(\mathbf{j} \cdot \nabla)(\mathbf{M} \cdot \mathbf{r}) = -\mathbf{M} \cdot \mathbf{j} = \mathbf{0}, \quad (1.4.18)$$

and as \mathbf{M} is a non-singular matrix, the only solution to equation (1.4.18) is $\mathbf{j} = \mathbf{0}$ and the null must be in a potential equilibrium.

1.5 Current sheets and reconnection

1.5.1 Tangential discontinuities

A tangential discontinuity is a structure where the magnetic field on both sides of the discontinuity has no component normal to the surface, and involves a change in the direction of the magnetic field, or in its magnitude, or in both. In equilibrium, it is an example of a pressure balance structure (Burlaga, 1995, “*Interplanetary magnetohydrodynamics*”), a surface across which the total pressure (plasma plus magnetic) is constant. A tangential discontinuity separates two different magnetic domains, and can also have different plasma motions, creating a velocity shear across the discontinuity, but the plasma flow through the surface must be zero.

From Ampère’s law (1.2.25), the change in magnetic field creates an accumulation of electric current which is confined in the surface of the discontinuity. These are called *current sheets*, and in MHD studies they are infinitesimally thin. A detailed compendium of the possible sheet configurations and the development of the theory can be found in Priest and Forbes (2000), “*Magnetic Reconnection*”.

A simple form for a current sheet is a *Harris sheet*, given by the one-dimensional model of Harris (1962), where the magnetic field is parallel to the x -axis and varies only with y , and is defined as $\mathbf{B}(y) = (B_x(y), 0, 0)$ with $B_x = B_0 \tanh(y/L)$. The current density has a non-zero z -component given by

$$j_z = -\frac{1}{\mu} \frac{\partial B_x}{\partial y}.$$

A Harris sheet is an example of a neutral sheet, where the magnetic field vanishes in the center. A study of the collisionless Vlasov-Maxwell equilibria in force free Harris sheets has been recently made by Harrison and Neukirch (2009) and Neukirch et al. (2009).

1.5.2 Current sheet formation

The analytical form of current sheets in two-dimensional fields, created following the collapse of a hyperbolic X-point, were firstly studied by Green (1965), who suggested an expression for a one-dimensional current sheet of the form

$$B_y + iB_x = \sqrt{Z^2 + a^2}, \quad (1.5.1)$$

where $Z = x + iy$ represents the complex plane, and $2a$ is the length of the sheet. The four separatrices open from both ends of the current sheet in two so called *Y-points*, inclined to one another with an angle of $2\pi/3$ (see Figure 1.12 for a schematic categorization of the possible magnetic 2D singular points described in this section).

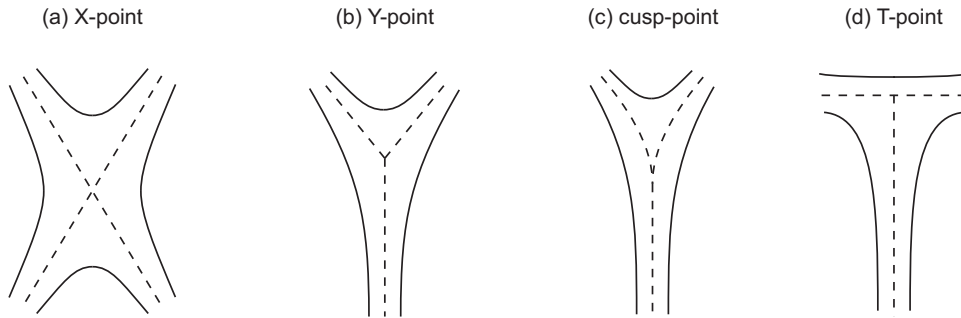


Figure 1.12: Special magnetic points in two-dimensions.

Somov and Syrovatskii (1976) described the collapse of a two-dimensional X-point with a more general solution given by

$$B_y + iB_x = \frac{Z^2 + l^2}{\sqrt{Z^2 + a^2}}, \quad (1.5.2)$$

where $l^2 < a^2$. The two null points at the ends of the sheets are singular. This case reduces to Green's solution when $l^2 = a^2$.

Later on, Bungey and Priest (1995) extended the solution of Somov & Syrovatsky, providing an analytical expression for all the possible potential and force-free configurations around a linear current sheet,

$$B_y + iB_x = -B_0 \left[\frac{bd^2 + 2dcZ - Z^2 + \frac{1}{2}d^2}{\sqrt{Z^2 + a^2}} \right], \quad (1.5.3)$$

where b , c , d and B_0 are constants.

In all these cases, the current sheet is assumed to be infinitesimally thin, and the current density has a δ -like singularity across the sheet.

The above theory has been applied to more general planar current sheets in the potential and force-free solar corona, involving the magnetic field associated with two bipolar regions, by Priest and Raadu (1975) and Tur and Priest (1976), as in Figure 1.13. In these models, a curved current sheet replaces the linear sheet found in previous studies of X-point collapse, and the extremes of the sheet show a pair of *cusp points* (see Figure 1.12c), where the separatrices are curved in space. This configuration has been used in a variety of models of equilibria for solar coronal magnetic arcades and loops by Low (1981, 1982b, 1986). Also, Vainshtein (1990) and Vekstein and Priest (1993) tried to give analytical expressions for magnetic fields near special points, such as cusp points, assuming a potential, and force-free solution outside and inside the cusp, respectively, in the first case, and a MHS combined with a potential solution in the second case.

Before that, Parker (1972) considered the evolution of three dimensional braided magnetic flux tubes, finding rapid dissipation and reconnection, which enabled the topology of the magnetic field to reduce to a simple equilibrium form. Parker suggested that *to first order*, changes in pressure along a flux tube would only modify the vertical z -component of the field, and in general, “the pattern of the field does not vary along the general direction of the field”, in other words, an equilibrium exists only if the variations in the field consist of simple twisting of the

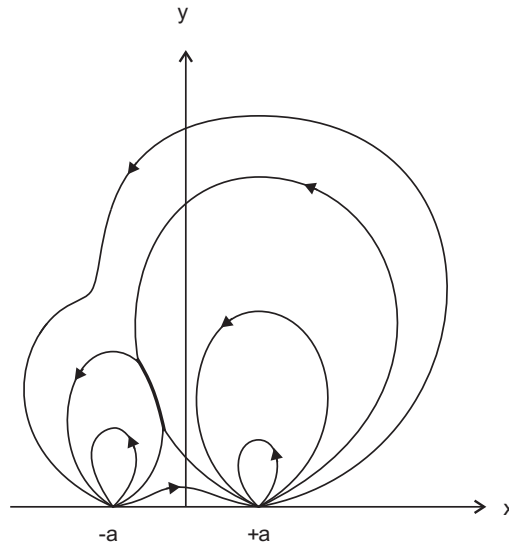


Figure 1.13: Schematic representation of the magnetic field configuration in the plane perpendicular to two line dipoles at $x = \pm a$, based on Tur and Priest (1976), Fig. 1, after an increase in the moment of the smaller dipole, creating a current sheet, here shown as a thick curve.

lines. In a more complex topology case, such as braided flux tubes wrapped around each other, he suggested that no equilibrium field was possible, and current would form at the boundaries of the tubes, leading to topological dissipation and merging of field lines in the process known as magnetic reconnection. Syrovatskii (1978) also suggested that the problem of continuous deformation of such fields had no solution in general. However, these results were disputed by van Ballegoijen (1985), who argued against Parker's scheme. Instead he suggested that an equilibrium should always exist, without the need for any form of symmetry of the field, implying that the coronal field adjusts itself to the motions of the photosphere, and that current sheets are a result of photospheric motions and would appear only when the boundaries have discontinuities. More recently, the properties of three-dimensional current sheets have been developed by Longcope (1996, 1998).

All the above studies involve potential and force-free solutions and, in fact, the thin current sheet configurations from Bungey and Priest (1995) are *not* in equilibrium, even if the regions around them are. This is because the current varies along the sheet, but there is no plasma pressure to hold the Lorentz force within the current sheet. More recently, Rastätter et al. (1994), Craig and Litvinenko (2005) and Pontin and Craig (2005) have studied the magnetohydrostatic relaxation of X-type null points, considering plasma pressure forces, reaching a cusp-like equilibrium sheet with the Lorentz force being balanced by the plasma pressure gradient. Common features of these studies are the appearance of current accumulations along the field separatrices. Also, they find evidence to suggest that a singularity in current is formed at the location of the null, as in the potential and force-free cases, whose nature is unknown. Craig and Litvinenko (2005) find the plasma pressure to be enhanced in the regions inside the cusps, and decreased in the regions outside the cusps, as sketched in Priest and Forbes (2000). Figure 1.14 shows some schematic views of the different two-dimensional sheet configurations coming from the collapse of a magnetic X-point.

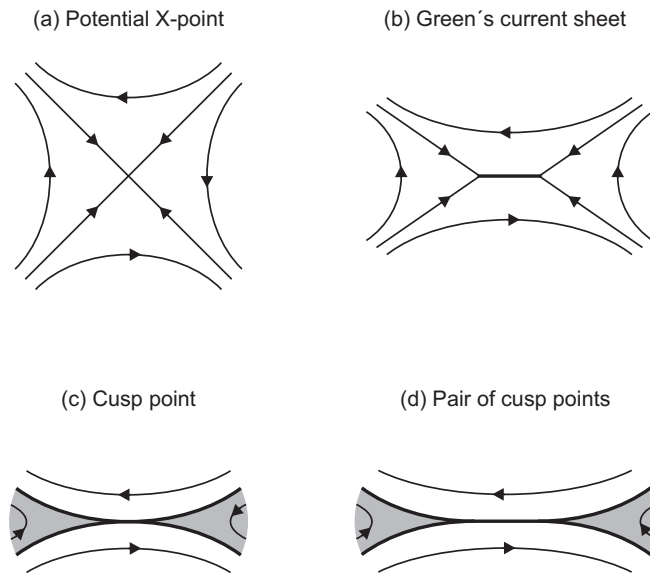


Figure 1.14: Sketch of two-dimensional equilibria, based on Priest and Forbes (2000), Fig. 2.10. Thick curves represent current sheets, and shaded regions are regions of enhanced plasma pressure. In the absence of plasma, if a hyperbolic X-point (a) is squashed in the vertical direction, a current sheet is formed, with Y-points at both ends, as in (b). In the presence of a non-zero beta plasma, if the X-point in (a) is squashed, the pressure is enhanced in the shaded regions, producing the equilibrium in (c), where a pair of cusp-points have formed, preserving the X-point geometry at the center, while, in a non-zero beta plasma, (b) produces the equilibrium in (d), where the current sheet has developed two cusp points at its ends, in which the pressure is enhanced.

1.5.3 Magnetic relaxation theory

A common method for the study of dynamical processes in magnetised fluids, such as current sheet formation in the solar atmosphere, is magnetic relaxation. An initially stressed system of magnetic field is allowed to evolve to an equilibrium, driven by a velocity damping mechanism which may or may not be physical. The evolution of the field is constrained, as required by the demands of the study, obtaining different possible solutions. The plasma effects are ignored in many of these models.

Taylor (1974) considered the relaxation of toroidal laboratory plasmas, which he found to be reaching a relaxed “quiescent” state which was largely stable. The plasma was confined in a rigid perfectly conducting vessel with both magnetic and current density tangential to its surface. For simplicity, he assumed the plasma internal energy negligible compared to the magnetic energy, so that any analytical form of the equilibrium would be force-free. The final equilibrium would be the one with minimum magnetic energy (Note, that in this ideal and purely magnetic process, the difference in energy from initial and final state is lost).

In the case of a perfectly conducting fluid, under the frozen-in condition, with no change in the magnetic connectivity, he found that the quantity

$$K = \int_V \mathbf{A} \cdot \mathbf{B} \, dV, \quad (1.5.4)$$

is an invariant of motion, with V being the volume of an infinitesimal flux tube. This quantity is the *magnetic helicity*, and it is a measure of twisting and kinking of a flux tube (*self-helicity*) or of different linked flux tubes (*mutual helicity*). Hence, the magnetic helicity was conserved for every field line. Under this constraint, the state of minimum energy was found to be given by the non-linear force-free solution, $\nabla \times \mathbf{B} = \alpha \mathbf{B}$, with α being a function constant along field lines, but varying from one field line to another.

When considering small departures from idealness, Taylor found changes in the connectivity of the field lines, which implied that the magnetic helicity was not conserved for each field line. However, he found the sum of K over all field lines almost unchanged, due to the fact that changes in topology entailed very small changes of the field itself. Hence, the effect of the reconnection of the field lines was to redistribute the magnetic helicity among the field lines involved. In this case, the state of minimum energy was given by the linear force-free field, with α constant everywhere.

Then, Heyvaerts and Priest (1984), examined the consequences of Taylor's relaxation on the evolution of the coronal magnetic fields, where the magnetic helicity is not constant in time, even in ideal MHD, as it varies as a result of the field lines foot-points motions. Nonetheless, they generalised Taylor's hypothesis by saying that the change of magnetic helicity must be a well known function not equal to zero, given by

$$\frac{DK}{Dt} = \int_S (\mathbf{A} \cdot \mathbf{v})(\mathbf{B} \cdot d\mathbf{S}),$$

where S is the boundary of the volume V in which the helicity is defined. They show how this evolution of coronal magnetic fields can be understood as a series of force-free states, preserving the change of magnetic helicity. They start from a quasi-static change of the initial linear force-free field which changes the state to a slightly non-linear force-free field with new helicity, which then relaxes, following Taylor's hypothesis, by reconnection processes, to the linear force-free field with the same helicity, and back to the beginning.

Heyvaerts and Priest (1984) made an essential point, which is that the "convertible energy" is not the difference between the initial energy and the energy of the potential state, as this last one is not readily accessible, but rather the difference in energy between the initial configuration, and the linear force-free state with the same helicity.

Taylor's relaxation theory has been extended to solar coronal magnetic fields by many authors (e.g. Nandy et al., 2003; Miller et al., 2009). In particular, Browning et al. (2008) and Hood et al. (2009) investigated Taylor relaxation through a series of non-linear 3D simulations of a cylindrical coronal loop model, initiated by MHD instabilities, finding rapid magnetic reconnection which allowed the system to relax towards a constant- α force-free solution.

1.5.4 Magnetic reconnection

Under ideal conditions, plasmas have infinite conductivity and the field must be frozen to the fluid, such that its connections are preserved. This is, in general, the case in the solar corona, where the characteristic lengths of the plasma are so high that the diffusion term is negligible in the induction equation, (1.2.9). However, it is possible

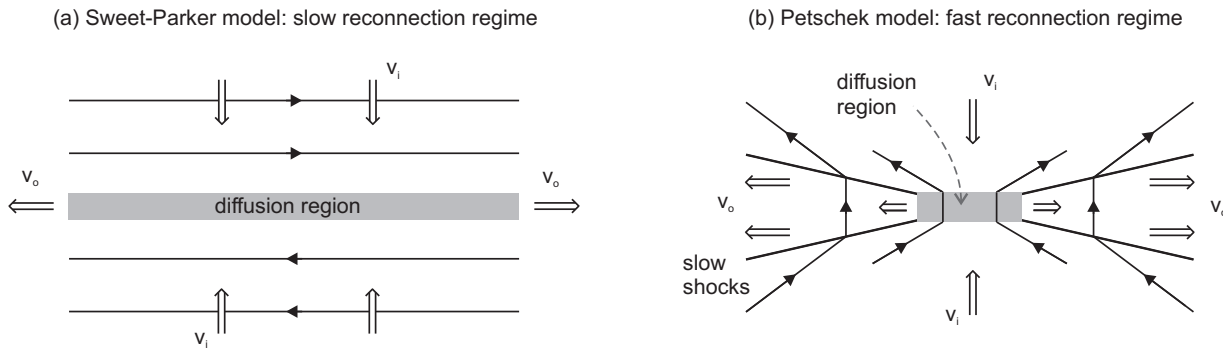


Figure 1.15: Comparison between (a) the Sweet-Parker model of slow reconnection, where energy conversion happens in a large diffusion region, and (b) the Petschek model, of fast reconnection, where most of the energy conversion takes place in four slow-mode shocks that come out of a small diffusion region.

that, in certain regions, the magnetic diffusivity becomes important locally, allowing non-ideal effects to occur. Two and three dimensional null points are potential locations for that non-ideality to happen.

Magnetic reconnection is the process in which field lines break and then merge with other field lines, allowing them to change their connectivity. The process is directly linked to the diffusion of the field and associated with the release of magnetic energy, which is partly converted into internal energy of the plasma. The characteristics of these processes in two-dimensions are well gathered and exposed in Priest and Forbes (2000). Reconnection may occur in presence of high electric fields and electric currents. Some effects of magnetic reconnection can be: 1) the partial conversion of magnetic energy into heat, a process known as *ohmic dissipation*, 2) acceleration of plasma by converting magnetic energy into bulk kinetic energy, 3) Generation of shock waves and current filamentation and 4) changes of global connections of the field lines, that allow the field to relax to a lower energy state, affecting the paths of fast particles and heat, which are generally directed along magnetic field lines.

Magnetic reconnection may be studied by either resistive (non-ideal) MHD models, with the classical ohmic dissipation, which can be mainly applied for highly collisional plasmas, or using particle models, involving multi-fluid theory, applicable in the higher corona, where collisionless effects dominate. Nevertheless, even in the latter case, an MHD approach can give a valid characterization and provides a macroscopical view of the general process.

A very brief history of the study of magnetic reconnection starts with Dungey (1953), who showed that the collapse of a magnetic X-point would create a current sheet capable of accelerating particles and generating heat in solar flares (pointed out earlier by Cowling, 1953), and first stated that "lines of force can be broken and rejoined". The first model came with Parker (1957) and Sweet (1958), who studied the process of two bipolar magnetic fields coming together. Parker was the first to use the term reconnection of field lines. They showed that the reconnection rate was equivalent to the inflow plasma speed, which turned out to be way too small for solar flares. This mechanism is now referred as to *slow reconnection*. Furth et al. (1963) showed that resistive instabilities occur in a one-dimensional current sheet. This is known as the *tearing mode instability*. Then, Petschek (1964) showed how conversion of magnetic energy into heat and kinetic energy was also possible in slow-mode shock waves, generated by a diffusion region much smaller than the one formed in the Sweet-Parker model. This was the first of many regimes of *fast reconnection*. Biskamp (1986) found a different solution to Petschek, which, finally

Priest and Forbes (1986) included into a whole family of solutions for both fast and slow reconnection, with the cases of Petschek and Biskamp as particular solutions. Figure 1.15 shows a comparison between the Sweet-Parker and the Petschek models.

In three dimensions, magnetic reconnection is very different from reconnection in 2D (Priest et al., 2003). Schindler et al. (1988) showed how, in contrast to the two-dimensional case, in three dimensions, reconnection can happen either at the location of magnetic null points or in absence of them. Instead, the condition for reconnection to occur is that, within a region of non-idealness, the integral along a field line of the electric field parallel to it is different from zero,

$$\int E_{\parallel} ds \neq 0 . \quad (1.5.5)$$

In fact, if the region of non-idealness is a single isolated region with a singly peaked form for this integral, then its maximum value gives the rate of three-dimensional reconnection. The different regimes of three-dimensional reconnection may be classified as follows. 1) *torsional fan and torsional spine reconnection*, where torsional motions concentrate the current along the spine or in the plane of the fan (Pontin et al., 2004; Priest and Pontin, 2009; Wyper and Jain, 2010), 2) *spine-fan reconnection*, where shearing motions concentrate the current along both (Pontin et al., 2005; Priest and Pontin, 2009), 3) *separator reconnection*, where current concentrates along the separator line that joins two nulls and represents the intersection of two separatrix surfaces (Parnell et al., 2010), and 4) *QSL reconnection*, where reconnection occurs at quasi-separatrix layers, where the mapping of magnetic field lines changes continuously but extremely rapidly (Priest and Démoulin, 1995).

1.6 Non-dimensional equations: Normalization

Before moving on, we shall go back to our fundamental equations. For simplicity, it is convenient to non-dimensionalise all the fundamental equations and quantities. The purpose of this is twofold. First, the process consists of measuring quantities relatively to some appropriate values (normalization), which allows us to work with easy numbers, i.e. numbers that are not overly large or overly small, and “eliminates” certain constants from the equations. Second, it provides a full removal of units by a suitable substitution of variables, making all quantities easier to work with, and scalably to many different situations.

The normalization can be made in various ways. We do it by normalising the magnetic field, plasma density and length, following the same approach as the numerical code that we are going to be using (described in Chapter 2). We denote dimensionless quantities with a hat, so that

$$\begin{aligned} x &= L_0 \hat{x} , \\ \mathbf{B} &= B_0 \hat{\mathbf{B}} , \\ \rho &= \rho_0 \hat{\rho} . \end{aligned}$$

The nabla operator is normalised as $\nabla = \hat{\nabla}/L_0$. From Ampère’s Law (1.2.25), we get

$$\mathbf{j} = j_0 \hat{\mathbf{j}} = \frac{B_0}{L_0} \frac{\hat{\nabla} \times \hat{\mathbf{B}}}{\mu} ,$$

and we can define the normalised current as $\hat{\mathbf{j}} = \hat{\nabla} \times \hat{\mathbf{B}}$. Repeating the process with the equations (1.2.25)[Ampère’s

law], (1.2.31)[ideal induction equation], (1.2.22)[equation of motion], (1.2.23)[energy equation], (1.2.24)[perfect gas law] and (1.2.18)[temperature], we get

$$j_0 = B_0/(\mu L_0) ,$$

$$v_0 = \frac{B_0}{\sqrt{\mu\rho_0}} ,$$

$$t_0 = \frac{L_0}{v_0} ,$$

$$p_0 = \frac{B_0^2}{\mu} ,$$

$$\epsilon_0 = \frac{p_0}{\rho_0} ,$$

$$T_0 = \epsilon_0 \frac{m}{k_B} .$$

Note, that the normalization is such that temperature and internal energy are related by $\hat{T} = \hat{\epsilon}(\gamma - 1)$, so we have $\hat{p} = \hat{\rho}\hat{T}$. Also, in resistive MHD, the normalised diffusivity is commonly known as the *resistivity*, $\eta = 1/\sigma$. From the expression for the plasma beta, $\beta = 2\mu p/B^2$, we get an expression for the plasma beta in terms of the normalised quantities (note that β is a non-dimensional quantity by definition) as

$$\beta = \frac{2\hat{p}}{\hat{B}^2} .$$

From this point, all the expressions and quantities we are going to refer to are the normalised ones, and for simplicity, the hats are dropped from the normalised quantities. Hence, after the normalization, the equations governing our MHD dynamical processes are summarised, finally, as

$$\frac{\partial \rho}{\partial t} + \nabla \cdot (\rho \mathbf{v}) = 0 , \tag{1.6.1}$$

$$\frac{\partial \mathbf{v}}{\partial t} + (\mathbf{v} \cdot \nabla) \mathbf{v} = -\frac{1}{\rho} \nabla p + \frac{1}{\rho} (\nabla \times \mathbf{B}) \times \mathbf{B} + \frac{1}{\rho} \mathbf{F}_\nu , \tag{1.6.2}$$

$$\frac{\partial p}{\partial t} + \mathbf{v} \cdot \nabla p = -\gamma p \nabla \cdot \mathbf{v} + H_\nu , \tag{1.6.3}$$

$$\frac{\partial \mathbf{B}}{\partial t} = \nabla \times (\mathbf{v} \times \mathbf{B}) , \tag{1.6.4}$$

where \mathbf{F}_ν and H_ν are given by equations (1.2.29) and (1.2.30), the current density is $\mathbf{j} = \nabla \times \mathbf{B}$, and internal energy is given by the ideal gas law, $p = \rho\epsilon(\gamma - 1)$, with $\gamma = 5/3$.

The above set of differential equations can be solved analytically for the first order terms, using linear perturbation theory. Otherwise, they require a powerful numerical tool. For our experiments, we have used LARE, a full MHD code, to solve equations (1.6.1) to (1.6.4) in two and three dimensions. The code is described in detail in Chapter 2.

1.7 Summary and main goals

The Sun, our star, is an amazing object that controls the life on our planet. The majority of the processes occurring in the outer layers of the star are driven by highly dynamic magnetic fields, at temperatures far above what we

are used to on Earth. Understanding the behaviour of these magnetic fields, and their interactions with the high temperature conducting plasma in which they are embedded, is crucial for our own comprehension of how our star works. The rapid release of magnetic energy is a burning issue, but it requires a detailed study of the characteristics of the hydromagnetic structures which lie behind. The aim of this thesis is to study in detail the current density accumulations in two and three dimensional magnetohydrostatic equilibria around magnetic null points, which are locations where reconnection can occur.

Many of the studies of current sheet formation in the past assume the cold plasma approximation (e.g. Vainshtein, 1990; Vekstein and Priest, 1993; Bungey and Priest, 1995), i.e. they do not take into account the effects of plasma pressure, so magnetic effects dominate. Scientists have studied these sorts of models for twenty years, from the 70's up to the 90's. But if we think it over again, we will soon see a clear inconsistency in this approach. Reconnection may happen around locations in which the magnetic field vanishes, and the previous models assume that the magnetic effects dominate over the plasma effects. How can that be true, even for a low density plasma, in regions about which the magnetic field is zero? Certainly, in those regions, the plasma effects will have to become important. An extra consideration is the energetics, since if the thermal energy of a system is neglected, what happens with the energy released by the magnetic field?

Hence, in the last decades, scientists have started to take plasma pressure into consideration in studies of relaxation around magnetic null points (Rastätter et al., 1994; Craig and Litvinenko, 2005; Pontin and Craig, 2005). Now, a non-force-free equilibrium is allowed to be reached, as magnetic and pressure forces can be balanced without vanishing individually. They have found substantial differences with the cold plasma approximation, as the nature of the equilibrium is now completely different.

But there is a last point that has to do with the mechanism which drives the relaxation, in charge of damping out the plasma velocities. In a numerical experiment, this can be done as physically as desired, and therefore, the choice of the latter studies has been to include a fictitious term to the equations, referred as to *frictional damping term*, such that the final equilibrium state can be achieved directly with no further complications. This, however, forbids another physical effect, which is energy exchange. By adding only that fictitious term, they cannot investigate exchanges of magnetic energy and thermal energy of the plasma, which will affect the role of plasma and magnetic field in the final equilibrium. Even if the dynamical process in between is not important in these studies, the plasma may gain or lose some energy during the process, which may alter its final state.

The approach in this thesis has been different. We have run experiments of magnetic relaxation about magnetic null points in two and three dimensions, considering the effects of the plasma pressure during the relaxation, which is driven by a viscous damping term. This, leads to a certain amount of viscous heating which drives, at the same time as the relaxation occurs, exchanges between magnetic and internal energy. We attempt to give a valid equilibrium, which is reached by allowing no reconnection, and we look at the redistributions of the plasma and magnetic quantities. A key difference with force-free studies is that infinitesimally thin current sheets are not formed in the presence of a plasma pressure. We obtain current accumulations with finite widths and lengths, hence, the term "current sheet" is not appropriate. Instead, we shall refer to our large current accumulations as current layers.

We shall now describe the common characteristics of all the experiments. The method that we follow is essentially the same in all. We start from an initial non-equilibrium field, which has no initial flows in it (i.e. initial kinetic energy is zero), with a constant background plasma density and current density, and we allow the field to relax via ideal (i.e. non-resistive) MHD processes to an equilibrium. We list the common characteristics for our dynamical evolutions.

- ▷ The relaxation is driven by **physical viscous forces**, implying that viscous heating will always be associated with the final state.
- ▷ In general, the evolution of the fluid is **non adiabatic**, due to the viscous heating term. This implies that there are exchanges of internal energy of the plasma and magnetic energy of the field. Only to first order, the heating term disappears and the process may be treated as adiabatic.
- ▷ The domain is **in every sense closed**, and magnetic field lines are tied at all the boundaries.
- ▷ **Mass is conserved** within the whole domain: inflows and outflows of plasma are not allowed.
- ▷ **Total energy is conserved**, which means that when comparing the initial and final states (which are supposed to be in equilibrium), the gain or losses of magnetic energy *must* be entirely balanced by losses or gains in internal energy. Throughout the whole process, the sum of magnetic, internal and kinetic energy *must* remain constant.
- ▷ All the processes are **non resistive**, which implies a number of consequences. 1) The connectivity of field lines cannot change, i.e. there is no magnetic reconnection. 2) This restriction forbids ohmic dissipation from occurring. Magnetic energy dissipation can take place, however, via viscous heating. 3) The field is frozen to the plasma, hence, motions of plasma across the field lines must carry the field with them, so that mass is not only conserved within the whole domain, but also within single flux tubes, and for each field line. And 4) magnetic flux is conserved for the entire domain.

In order to do this, we have run a number of numerical experiments, making use of a full MHD code which solves the set of MHD equations described before, with user controlled viscosity. However, as with all numerical codes, the domain is discretised on a grid of points (resolution elements), which, in practice, means that all the considerations above are not true. That is, there are going to be some small losses through the boundaries, and some reconnection might take place. Nonetheless, in most cases, these *numerical effects* are **very small**, and we always find a way to deal with them, allowing us to continue our analysis without major problems. The characteristics and special features of the code are described in detail in Chapter 2.

We start by looking at a simple scenario with a straight and homogeneous magnetic field embedded in a plasma, with no special magnetic points or locations. We are able to observe, for the simpler cases, the effects of the plasma pressure and plasma energy in the relaxation, and we are able to predict the equilibrium from the initial perturbations, using linear wave theory. The main result is that the inclusion of plasma effects matter in the relaxation, and even if simple, the final state cannot be described using an evolution where pressure forces and thermal energies are neglected. These experiments are addressed in Chapter 3.

Then, in Chapter 4, we look at the relaxation around two-dimensional magnetic X-type points, which are a relatively simple scenario in which magnetic reconnection can occur. We follow the study of Craig and Litvinenko (2005), which takes plasma pressure into consideration, but does not consider the possibility of energy exchange, and we attempt to give a qualitative description of the field about the null, by following the work of Vekstein and Priest (1993). In Chapter 5, we present two sets of experiments for two specific types of three-dimensional magnetic nulls, by following the study of Pontin and Craig (2005), which again, does not allow energy exchange in the relaxation scheme.

Finally, we summarise our results, going over the main characteristics of the MHS equilibrium states that we find, evaluate their implications for current sheet formation and magnetic reconnection, and present possible future work in Chapter 6.

It is worthwhile mentioning that relaxation via Ohmic dissipation, due to the effect of resistivity, or magnetic diffusivity, represents a substantially different problem to relaxation via viscous dissipation. While viscosity dissipates the plasma velocity, diffusivity tends to eliminate the electric current density, and such a relaxed state can only involve potential fields, which are mathematically well defined and are uniquely determined by the components of the magnetic field normal to the boundaries. Furthermore, the time-scales for an Ohmic relaxation in very high magnetic Reynolds number environments, such as the solar corona, are in general probably larger than the age of the Sun itself, outwith regions with very small length scales (see Priest, 1982).

Given these, the main goal of our experiments and analysis is to provide a series of controlled MHS equilibria through a realistic dynamical evolution, studying the locations in which current accumulations occur, and derive their nature, as far as possible, without allowing the field to dissipate currents away and hence, forcing them to achieve a purely **non-force-free state in equilibrium**. When a valid equilibrium is found, it may provide the start point for magnetic reconnection studies.

By considering the effects of the plasma pressure in the relaxation, we are facing a totally different problem from that of the force-free relaxation studied by many others. In our non-resistive MHD relaxations, the plasma displacements will carry the magnetic field with them, generating an electric current and a magnetic pressure. Hence, the resulting equilibria has to involve a balance between the Lorentz force and the plasma-pressure gradient. The effects of including a finite plasma beta are relevant not only in the high plasma beta regions of the solar atmosphere such as the photosphere and chromosphere, but will also be relevant in the solar corona. Obvious regions where the plasma beta is likely to have a significant effect are in the vicinities of magnetic null points, where the magnetic field vanishes.

Chapter 2

The LARE Code

2.1 Introduction

LARE is a Lagrangian remap code that solves the full equations of MHD in two and three dimensions. The code is second order accurate in space and time and is parallelised via MPI and known to scale linearly up to 1000 cores of a cluster. A full description of the code, put in context and compared with other commonly used numerical methods, together with some advantages and disadvantages, and some standard numerical tests, can be found in Arber et al. (2001). This approach for solving multidimensional MHD problems is based on control volume averaging, with a staggered grid where scalars and vectors are defined at different points in the computational cell.

In an Eulerian code's mesh, the grid is stationary and mass flows between the cells. On the other hand, a Lagrangian code's mesh moves with the material and is deformed on each timestep, so no mass flows between cells. The code can be separated into two main parts: The Lagrangian step, that solves the MHD equations in a frame that moves with the fluid, and a remap step, which puts the variables back onto the original grid. All the physics is contained in the Lagrangian step, and the remap step is purely geometrical. At the remap step, gradient limiters are applied so that the monotonicity in the density and internal energy remaps is preserved. The code includes artificial viscosity, as an added scalar term to the plasma pressure, which avoids some known numerical problems at shocks. This kind of scheme has been used widely for hydrodynamic problems (see Woodward and Collela, 1984; Benson, 1992), but the LARE code is the first of its kind to introduce magnetic field calculations.

The LARE code was motivated to be easily adaptable to a variety of problems in solar coronal physics: It conserves energy to machine accuracy, correctly handles shocks, finds accurate values for the temperature even for low-beta plasmas such as the solar corona, and makes the addition of extra physics easy through the Lagrangian step.

2.2 Equations

LARE solves the normalised resistive MHD equations. Resistivity is not assumed to be constant in the code, so the non-ideal induction equation is taken to be equation (1.2.8), instead of (1.2.9). The normalization of the resistivity

is given by

$$\hat{\eta} = \frac{\eta}{\mu L_0 v_0} .$$

The equations with which the code works are the analogous to equations (1.6.1) to (1.6.4), with the inclusion of a resistive term, and are written in Lagrangian form, using (1.2.12). The energy equation is written in terms of the internal energy density (energy per unit mass), with the plasma pressure given by $p = \rho\epsilon(\gamma - 1)$. For the induction equation, we make use of the vector identity

$$\nabla \times (\mathbf{v} \times \mathbf{B}) = (\mathbf{B} \cdot \nabla)\mathbf{v} - (\mathbf{v} \cdot \nabla)\mathbf{B} + (\nabla \cdot \mathbf{B})\mathbf{v} - (\nabla \cdot \mathbf{v})\mathbf{B} .$$

and the solenoidal constraint, $\nabla \cdot \mathbf{B} = 0$. Thus the equations solved in the code are

$$\frac{D\rho}{Dt} = -\rho \nabla \cdot \mathbf{v} , \quad (2.2.1)$$

$$\frac{D\mathbf{v}}{Dt} = -\frac{1}{\rho} \nabla p + \frac{1}{\rho} (\nabla \times \mathbf{B}) \times \mathbf{B} + \frac{1}{\rho} \mathbf{F}_\nu , \quad (2.2.2)$$

$$\frac{D\epsilon}{Dt} = -\frac{p}{\rho} \nabla \cdot \mathbf{v} + \frac{\eta}{\rho} j^2 + \frac{1}{\rho} H_\nu , \quad (2.2.3)$$

$$\frac{D\mathbf{B}}{Dt} = (\mathbf{B} \cdot \nabla)\mathbf{v} - (\nabla \cdot \mathbf{v})\mathbf{B} - \nabla \times (\eta \nabla \times \mathbf{B}) . \quad (2.2.4)$$

The density change is calculated directly from volume changes and using mass conservation, so equation (2.2.1) is not actually used. If a plasma element is initially at a point $\mathbf{X} = (X_1, X_2, X_3)$ and moves to a point $\mathbf{x} = (x_1, x_2, x_3)$, then the change in element length is given by

$$dx_i = \sum_{\alpha} \frac{\partial x_i}{\partial X_{\alpha}} dX_{\alpha} ,$$

so that the density can be found from

$$\rho = \frac{\rho_0}{\Delta} ,$$

where ρ_0 is the original density and Δ is the determinant of the Jacobian transformation matrix,

$$\Delta = \begin{vmatrix} \frac{\partial x_1}{\partial X_1} & \frac{\partial x_2}{\partial X_1} & \frac{\partial x_3}{\partial X_1} \\ \frac{\partial x_1}{\partial X_2} & \frac{\partial x_2}{\partial X_2} & \frac{\partial x_3}{\partial X_2} \\ \frac{\partial x_1}{\partial X_3} & \frac{\partial x_2}{\partial X_3} & \frac{\partial x_3}{\partial X_3} \end{vmatrix} .$$

When dealing with control volumes, this is the ratio of the final volume to the initial volume, and it is evaluated as

$$\Delta = 1 + (\nabla \cdot \mathbf{v})dt . \quad (2.2.5)$$

Equation (2.2.5) is second order accurate.

2.2.1 Viscous terms

The viscous terms are implemented through the stress tensor σ_{ij} and strain rate ε_{ij} , which add an additional viscous force to the momentum equation, as

$$\mathbf{F}_\nu = \frac{\partial \sigma_{ij}}{\partial x_j}, \quad (2.2.6)$$

and a heating term to the energy equation,

$$H_\nu = \varepsilon_{ij} \sigma_{ij}, \quad (2.2.7)$$

with σ_{ij} and ε_{ij} given by

$$\begin{aligned} \sigma_{ij} &= \nu_r \left(\varepsilon_{ij} - \frac{1}{3} \delta_{ij} \nabla \cdot \mathbf{v} \right), \\ \varepsilon_{ij} &= \frac{1}{2} \left(\frac{\partial v_i}{\partial x_j} + \frac{\partial v_j}{\partial x_i} \right), \end{aligned}$$

where the viscosity is defined as $\nu_r = \nu \rho$, being ν the kinematic viscosity. Note, that the viscous heating is an added contribution to the internal energy density. These equations are completely equivalent to (1.2.29) and (1.2.30). The normalization for the viscosity is the same as the one for the resistivity above, hence,

$$\hat{\nu}_r = \frac{\nu_r}{\mu L_0 v_0}.$$

2.2.2 Shock viscosity

At shocks, the gradients become singular and the differential equations are not defined. Hence, LARE uses the integrated form of the equations to get jump conditions across shocks. Let's first describe the problem for the one-dimensional equations with $B = 0$ (i.e. non magnetic). The jump condition for the pressure across the shock can be derived, using the *Rankine-Hugoniot relations* (see, for example, Wesseling, 2001), as

$$p_1 - p_0 = \frac{\gamma + 1}{4} \rho_0 (\Delta v)^2 + \rho_0 |\Delta v| \sqrt{\left(\frac{\gamma + 1}{4} \right)^2 (\Delta v)^2 + c_s^2},$$

where p_1 is the pressure behind the shock, p_0 is the pressure in front of the shock, $c_s = \sqrt{\gamma p / \rho}$ is the sound speed, and $|\Delta v|$ is the jump in velocity across the shock. The difference approximation for the derivative of an arbitrary function f , to second order, may be written as

$$\frac{df}{dx}(x_i) = \frac{f(x_{i+1}) - f(x_i)}{\Delta x} - \frac{f(x_{i+1}) - 2f(x_i) + f(x_{i-1}))}{2\Delta x}.$$

The first order scheme has excessive diffusion away from shocks, but the second order scheme introduces false oscillations behind the shock. To avoid these problems, one could introduce some dissipation, only at steep gradients, consistent with the jump conditions, by adding a scalar q to the pressure p when the computational cells are

compressed. In one dimension, $\Delta v = \Delta x \nabla \cdot \mathbf{v}$, where Δx is the cell size, and

$$q = \nu_1 \rho c_s \Delta x |\nabla \cdot \mathbf{v}| + \nu_2 \rho \Delta x^2 (\nabla \cdot \mathbf{v})^2. \quad (2.2.8)$$

Note, that q is always positive, and should only be applied when the cell is being compressed, i.e. when $\nabla \cdot \mathbf{v} < 0$. The parameters ν_1 and ν_2 are fixed by experimentation, and this additional term is only used when required, depending on the nature of the experiment. The default values that the code works with are $\nu_1 = 0.1$ and $\nu_2 = 0.5$. They are both dimensionless by construction. Associated with this *artificial viscosity*, there is an additional heating term in the energy equation, given by $-q \nabla \cdot \mathbf{v} / p$.

In three dimensions, equation (2.2.8) can be generalised to

$$q = \nu_1 \rho c_s L_\perp |s_\perp| + \nu_2 \rho L_\perp^2 s_\perp^2, \quad (2.2.9)$$

where s_\perp is the rate of the strain tensor in the direction normal to the shock front, and L_\perp is the distance across the cell in the direction normal to the shock front.

Remember that the expression above is for non-magnetic problems. In general, LARE uses a tensor shock viscosity, similar to equation (2.2.9), where the sound speed has been replaced by the fast magnetoacoustic speed c_f , as

$$\sigma_{i,j}^{shock} = (\nu_1 \rho c_f L_\perp + \nu_2 \rho L_\perp^2 |s_\perp|) \left(\varepsilon_{ij} - \frac{1}{3} \delta_{ij} \nabla \cdot \mathbf{v} \right), \quad (2.2.10)$$

This is applied to all cells, as significant shear forces may exist across expanding cells, but the associated heating term is always positive.

2.3 The grid

LARE uses a staggered grid, where scalars and vectors are defined in different points of the computational cell. This avoids some numerical instabilities known as checkerboard instabilities, and helps with central derivative calculations. However, it implies an extra degree of complexity when combining different quantities, as we must make use of (linear) interpolations to define all the required quantities at the exact same location. By not doing this, results may not be what one is expecting.

All the scalar quantities are defined at the cell volume center, magnetic field components are staggered and lie on the cell faces, which helps with maintaining $\nabla \cdot \mathbf{B} = 0$, and the components of the velocity are staggered with respect to the magnetic field and the pressure, to avoid checkerboard instabilities, and are defined at the vertices of the cell. This layout is shown in Figure 2.1. As an additional feature of LARE, the mesh can be stretched in any of the three spatial directions, so that the volume of the cells might not be the same within the whole computational domain.

In what follows, we define the notation within a computational cell, following the terminology of Arber et al. (2001), to be used in the finite difference scheme. In three dimensions, each cell is defined by the indices (i, j, k) . We begin by defining the *control volume* as the volume of each cell, $vol_{i,j,k}$ (Figure 2.2).

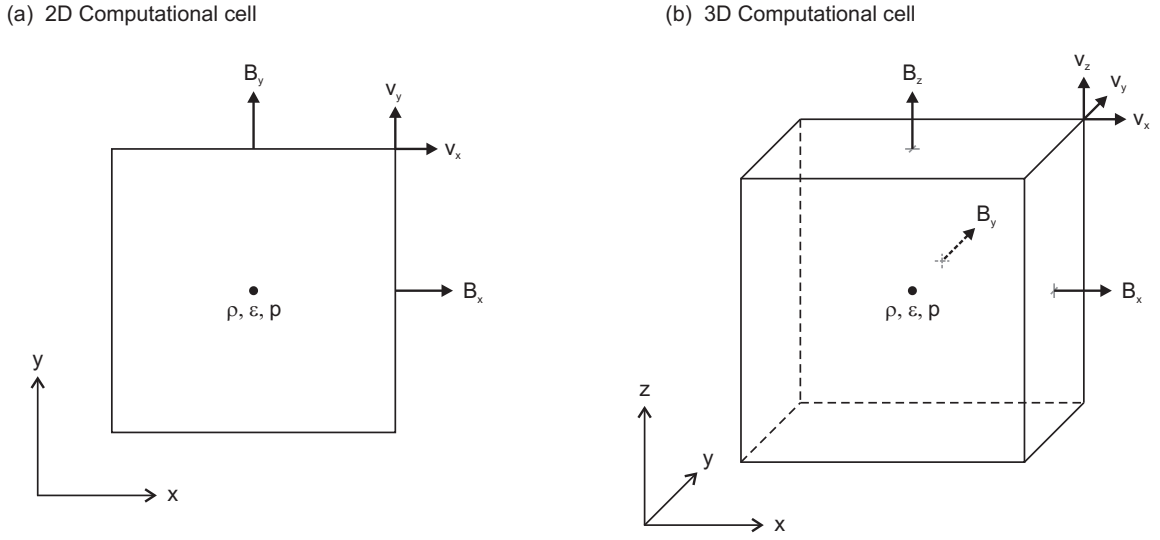


Figure 2.1: The staggered grid for LARE2D and LARE3D.

- ▷ The distances between cell faces in the x , y and z directions are $dx_{i,j,k}$, $dy_{i,j,k}$ and $dz_{i,j,k}$, respectively, while the distances between the cell centers are $dx_{i,j,k}$, $dy_{i,j,k}$ and $dz_{i,j,k}$ (i.e. $dx_{i,j,k}$ is the distance between the centers of the control volume $cvol_{i,j,k}$ and $cvol_{i+1,j,k}$).
- ▷ The density, internal energy density and plasma pressure, averaged over $cvol_{i,j,k}$ are $\rho_{i,j,k}$, $\epsilon_{i,j,k}$ and $p_{i,j,k}$, respectively, and are defined at the cell volume center, at $(xc, yc, zc)_{i,j,k}$.
- ▷ The x -component of the magnetic field is $Bx_{i,j,k}$, and is defined in the center of the right face at $(xb, yc, zc)_{i,j,k}$, where $xb_{i,j,k} = xc_{i,j,k} + dx_{i,j,k}/2$. The y and z components of the magnetic field are similarly defined as $By_{i,j,k}$ and $Bz_{i,j,k}$, at the center of the back and top faces, respectively, at $(xc, yb, zc)_{i,j,k}$ and $(xc, yc, zb)_{i,j,k}$, where yb and zb are defined in the same way as xb .
- ▷ All the components of the velocity field are defined at the right-top-back vertex, at $(xb, yb, zb)_{i,j,k}$. These are $vx_{i,j,k}$, $vy_{i,j,k}$ and $vz_{i,j,k}$.

Given these, the density at the cell vertex, namely $\rho_{i,j,k}^v$, can be obtained by *control volume averaging*, as

$$\rho_{i,j,k}^v = \frac{1}{8cvol_{i,j,k}^v} \sum_{l=i}^{i+1} \sum_{m=j}^{j+1} \sum_{n=k}^{k+1} \rho_{l,m,n} cvol_{l,m,n}, \quad (2.3.1)$$

where $cvol_{i,j,k}^v$ is the *velocity cell control volume*, given by

$$cvol_{i,j,k}^v = \frac{1}{8} \sum_{l=i}^{i+1} \sum_{m=j}^{j+1} \sum_{n=k}^{k+1} cvol_{l,m,n}.$$

The magnetic field components at the cell center are simply the averages of the values on opposing faces, and the velocity components defined on cell faces, e.g. $vx_{i,j,k}$, are the averages of the four vertex values.

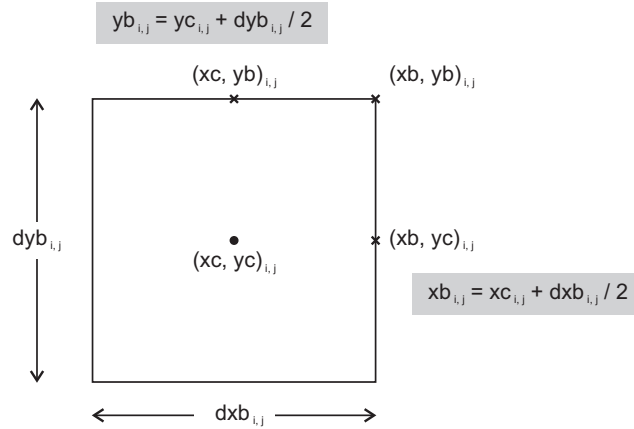


Figure 2.2: Notation for the finite difference scheme, in 2D.

From the induction equation, (2.2.4), we can derive the Lagrangian evolutions of the averaged magnetic field in the control volume,

$$\frac{D}{Dt} \int B_i d\tau = \int v_i \mathbf{B} \cdot d\mathbf{S} - \int [\nabla \times (\eta \nabla \times \mathbf{B})]_i d\tau, \quad (2.3.2)$$

and of the control volume flux,

$$\frac{D}{Dt} \int \mathbf{B} \cdot d\mathbf{S} = - \int \eta \mathbf{j} \cdot d\mathbf{l}, \quad (2.3.3)$$

where integrals over $d\tau$ and $d\mathbf{S}$ in equation (2.3.2) refer to integrals over the volume of a control volume, and its surface, respectively, and the integral over $d\mathbf{l}$ in equation (2.3.3) refers to the line integral around the open surface integrated over in the $d\mathbf{S}$ integral, which is not the same as the closed volume in equation (2.3.2). The remap step deals only with magnetic fluxes.

In Figure 2.3 we show how the components of the magnetic field are defined at the four boundaries of a two-dimensional box, including the *ghost cells*, in grey, whose values must be specified by the user as boundary conditions.

2.4 The Lagrangian step

The Lagrangian step is where all the physics takes place. The movement of the plasma carries the grid with it, deforming it in the three spatial coordinates. It is a simple predictor-corrector scheme, where predicted values are calculated with timestep $\delta t/2$, and the corrected at the full timestep δt . All the derivatives are evaluated on the original Eulerian grid, resulting in a fully three-dimensional second order scheme, both in time and space. To distinguish between different time levels, variables with no superscript, e.g. \mathbf{v} , refer to variables on the Eulerian grid at the start of the step; variables with a star superscript, e.g. \mathbf{v}^* , are the values after the predictor step, at half timestep; and variables with the superscript 1, e.g. \mathbf{v}^1 , represent the values at the end of the Lagrangian step, at the full timestep. The core solver is made for ideal MHD, so we show the equations for the scheme without resistive terms. Those are introduced separately at the end.

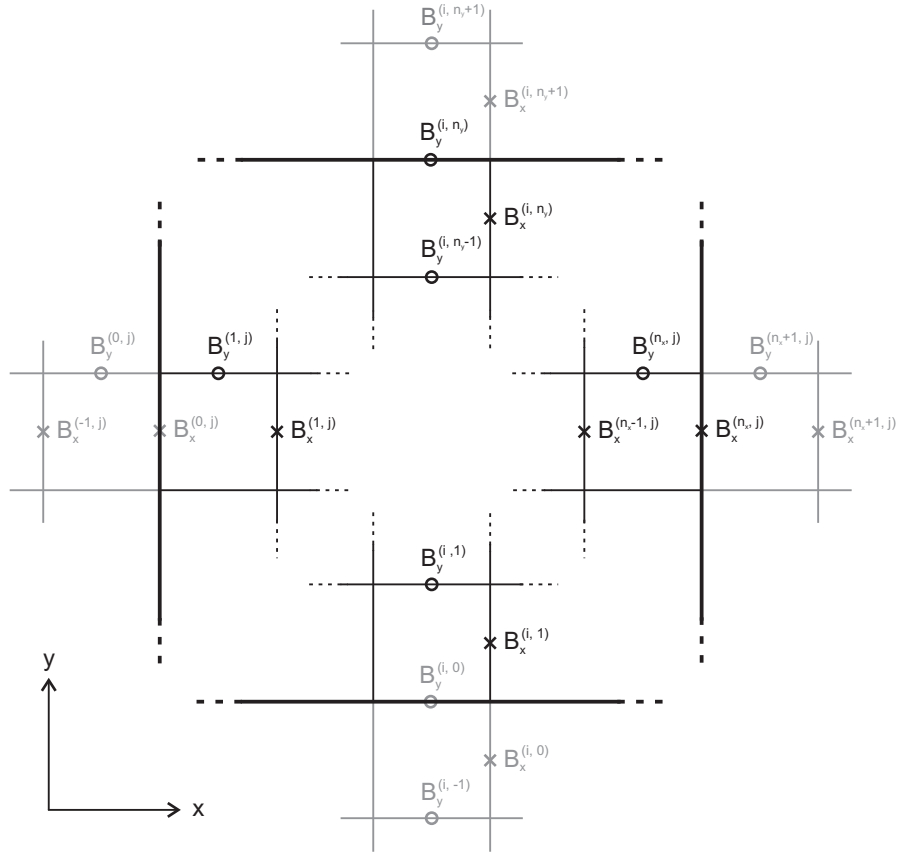


Figure 2.3: Magnetic field at the LARE2D boundaries and ghost cells, in grey.

2.4.1 Predictor step

First, we can define a total plasma pressure by adding the term of equation (2.2.9) to the common plasma pressure, so that $P_{total} = p + q$, where $p = \rho\epsilon(\gamma - 1)$. Hence, the predictor value for the internal energy density is

$$\epsilon^* = \epsilon - \frac{\delta t}{2} \frac{P_{total} \nabla \cdot \mathbf{v}}{\rho}, \quad (2.4.1)$$

where $\nabla \cdot \mathbf{v}$ is found from the interpolated values of the velocities in the cell faces, as

$$\nabla \cdot \mathbf{v} = \frac{v_x b_{i,j,k} - v_x b_{i-1,j,k}}{dx b_{i,j,k}} + \frac{v_y b_{i,j,k} - v_y b_{i,j-1,k}}{dy b_{i,j,k}} + \frac{v_z b_{i,j,k} - v_z b_{i,j,k-1}}{dz b_{i,j,k}}.$$

The Jacobian of the predictor step is found from equation (2.2.5), as

$$\Delta^* = 1 + \frac{\delta t}{2} \nabla \cdot \mathbf{v},$$

so that the density in the predictor step is

$$\rho^* = \frac{\rho}{\Delta^*}, \quad (2.4.2)$$

and the total plasma pressure is given by

$$P_{total}^* = \rho^* \epsilon^* (\gamma - 1) + q. \quad (2.4.3)$$

Note, that the artificial viscous pressure q is not advanced to the predictor level. From equation (2.3.2), ignoring the resistive terms in the right hand side, we get the predictor magnetic field components, as

$$Bx^* = \frac{1}{\Delta^*} \left\{ Bx + \frac{\delta t}{dx} [(vx Bx)^{x^+} - (vx Bx)^{x^-}] + \frac{\delta t}{dy} [(vx By)^{y^+} - (vx By)^{y^-}] + \frac{\delta t}{dz} [(vx Bz)^{z^+} - (vx Bz)^{z^-}] \right\}, \quad (2.4.4)$$

where $(vx Bx)^{x^+}$ is the product of vx and Bx averaged to the center of the right x face at $xb_{i,j,k}$, and $(vx Bx)^{x^-}$ is averaged to the center of the left x face at $xb_{i-1,j,k}$. Similarly, we can derive the expressions for B_y^* and B_z^* . All of the magnetic components are calculated in the cell volume center.

Finally, in order to get the predictor velocity at the cell vertex, we use equation (2.2.2), for which we need to derive the vector force at the cell vertex, which is found from $\mathbf{F}^* = (\nabla \times \mathbf{B}^*) \times \mathbf{B}^* - \nabla p^*$, with components (Fx^*, Fy^*, Fz^*) , assuming there are no viscous forces, after applying control volume averaging to p^* and \mathbf{B}^* , as in equation (2.3.1), as they are both defined in the cell volume center. The components of the predictor velocity are given by

$$vx^* = vx + \frac{\delta t}{2} \frac{Fx^{*v}}{\rho^v}, \quad (2.4.5)$$

and so on, where the superscript v denotes the control volume averaging at the cell vertex.

In order to include the viscous forces, the term in equation (2.2.6) can be directly added to the calculations of the predictor velocity. The viscous heating is added to the internal energy calculations using equation (2.2.7).

2.4.2 Corrector step

For the corrector step, flux conservation is used, since the Lagrangian step is written for ideal MHD. The components of the magnetic field are first converted into fluxes using

$$\begin{aligned} \phi_x &= Bx \, dyb \, dzb, \\ \phi_y &= By \, dzb \, dxb, \\ \phi_z &= Bz \, dxb \, dyb. \end{aligned}$$

The update of the density control volume for each cell is $\Delta^1 = 1 + \delta t \nabla \cdot \mathbf{v}^*$, and for the internal energy density, density and velocity at the end of the Lagrangian step, we have

$$\epsilon^1 = \epsilon - \delta t P_{total}^* \frac{F x^*}{\rho}, \quad (2.4.6)$$

$$\rho^1 = \frac{\rho}{\Delta}, \quad (2.4.7)$$

$$v x^1 = v x + \delta t \frac{F x^{*v}}{\rho^v}, \quad (2.4.8)$$

with similar equations for $v y^1$ and $v z^1$. Also, the terms corresponding to the viscous force and heating may be added if required. The magnetic field does not need to be updated, as the remap step deals only with magnetic flux. Note, that the update of the internal energy density, density and velocities uses the density of the original Eulerian grid, ensuring control volume mass conservation during the Lagrangian step. To finalise, the positions of the grid cells at the end of the Lagrangian step are calculated using

$$\begin{aligned} dx b_{i,j,k}^1 &= dx b_{i,j,k} + (v x b_{i,j,k}^* - v x b_{i-1,j,k}^*) \delta t, \\ dy b_{i,j,k}^1 &= dy b_{i,j,k} + (v y b_{i,j,k}^* - v y b_{i,j-1,k}^*) \delta t, \\ dz b_{i,j,k}^1 &= dz b_{i,j,k} + (v z b_{i,j,k}^* - v z b_{i,j,k-1}^*) \delta t. \end{aligned}$$

2.5 The remap step

The remap step is a purely geometrical mapping of the Lagrangian grid back to the original Eulerian grid. Gradient limiters are used to maintain monotonicity, and the magnetic field remap is done so that $\nabla \cdot \mathbf{B} = 0$ is preserved. The scheme for remapping uses mass coordinates, for conserving mass, internal energy density and momentum, to machine precision. However, kinetic and magnetic energy are not conserved in the remap step: This is only significant at shocks where the limiters flatten gradients in the remap step. However, further calculations can be added, by user specification, to conserve kinetic energy in each remap step, by considering the change in kinetic energy summed over the cells and finding the energy which is lost in the remap, which is then added into the internal energy as a heating term, thus conserving the energy. This same procedure could be applied to the magnetic energy losses in the remap step, but that is not implemented in the code. Hence, possible errors in total energy conservation can be identified as errors in the magnetic field energy.

The remap is done in one-dimensional sweeps. To go over the process we shall then drop the indices (j, k) and work purely in one dimension. In what follows, the prime superscript, e.g. $v x^1$, refers to the values before the remap, and the superscript $n + 1$, e.g. $v x^{n+1}$, refers to the values after the remap.

The condition for the remapping is mass conservation in each cell, so that the mass in the cell after the remap, $\rho^{n+1} dx b$, equals the mass before the remap, $\rho^1 dx b^1$ minus the mass from this Lagrangian cell which overlaps the Eulerian cell at $i + 1$, dM_i , plus the mass from the Lagrangian cell $i - 1$ which overlaps the Eulerian cell i , dM_{i-1} , as shown in Figure 2.4. Since the mass before the remap is the same as the initial mass in the original Eulerian cell, i.e. $\rho^1 dx b^1 = \rho dx b$, we have

$$\rho_i^{n+1} = \rho + \frac{1}{dx b_i} (dM_{i-1} - dM_i), \quad (2.5.1)$$

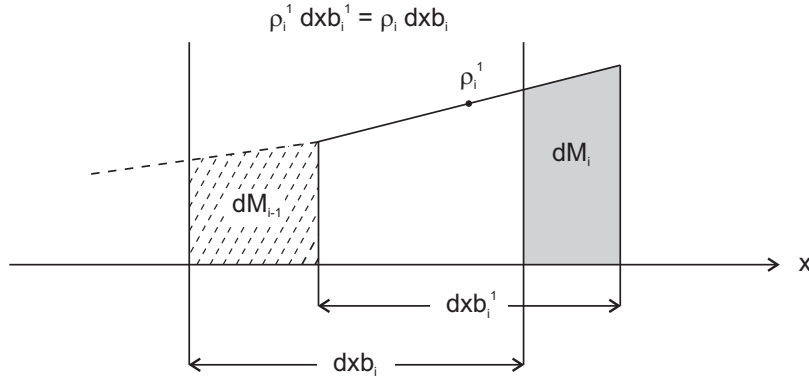


Figure 2.4: Lagrangian displacement of a cell after a timestep.

where

$$dM_i = \left(\rho_i^1 + \frac{dx_b_i}{2} D_i (1 - \psi_i) \right) vx_i^* \delta t, \quad (2.5.2)$$

and

$$\psi_i = \frac{|vx_i^*| \delta t}{dx_b_i^1}.$$

Note, that in these two equations, vx_i^* is the velocity of the boundary, and in 3D this needs to be replaced by the face-centered velocity $vx_b_i^*$. The variable D_i is the *van Leer gradient limiter* (van Leer, 1979), which is found as follows. Initially, given a general variable f , the third-order upwind gradient is given by

$$\begin{aligned} |\bar{D}_i| &= \frac{2 - \psi_i}{3} \frac{|f_{i+1} - f_i|}{dxc_i} + \frac{1 + \psi_i}{3} \frac{|f_i - f_{i-1}|}{dxc_{i-1}} \quad \text{for } vx_i^1 > 0, \\ |\bar{D}_i| &= \frac{2 - \psi_i}{3} \frac{|f_{i+1} - f_i|}{dxc_i} + \frac{1 + \psi_i}{3} \frac{|f_{i+2} - f_{i+1}|}{dxc_{i+1}} \quad \text{for } vx_i^1 \leq 0. \end{aligned}$$

The reason of these being third-order here is simply because it costs nothing computationally, but in some cases it might reduce slightly the numerical dissipation. Now, the magnitude of the gradient obtained is limited using

$$D_i = \text{sgn} \max(|\bar{D}_i| dx_b_i, 2|f_{i+1} - f_i|, 2|f_i - f_{i-1}|), \quad (2.5.3)$$

where

$$\text{sgn} = \begin{cases} \text{sign}(f_{i+1} - f_i) & \text{if } \text{sign}(f_{i+1} - f_i) = \text{sign}(f_i - f_{i-1}), \\ 0 & \text{otherwise.} \end{cases}$$

The internal energy density remap follows the same procedure as the density remap, such that

$$\epsilon_i^{n+1} = \frac{1}{\rho_i^{n+1} dx_b_i} (\epsilon_i^1 \rho_i^1 dx_b_i^1 + d\epsilon_{i-1} - d\epsilon_i), \quad (2.5.4)$$

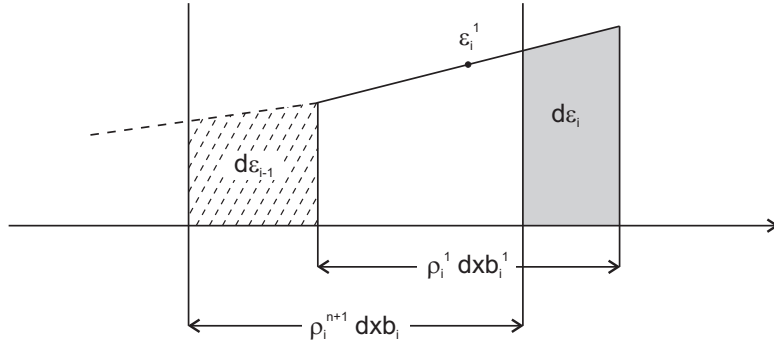


Figure 2.5: Lagrangian energy change in mass coordinates.

where

$$d\epsilon_i = \left(\epsilon_i^1 + \frac{dx b_i}{2} D_i \left(1 - \frac{dM_i}{\rho_i^1 dx b_i^1} \right) \right) dM_i, \quad (2.5.5)$$

as in Figure 2.5. Now, D_i is the van Leer limited gradient of the internal energy density, and $d\epsilon_i$ denotes energy, while ϵ_i is energy density (energy per unit mass).

The velocity remap is also done by using mass coordinates, thus ensuring conservation of momentum. The remap is the same as the one for the internal energy density, only taking into account that velocities must first be averaged to the appropriate faces of the velocity control volume.

The calculations for the magnetic flux remap follow the same approach as that of the density. The total flux through the y face at $y b_{i,j,k}$ is unchanged during the Lagrangian step and is given by $\phi_y = B y dx b dz b$. This is remapped using $v x^*$ to find the area of Lagrangian cells overlapping neighboring Eulerian cells in the x pass of the remap. Now, since the flux is defined as a face surface averaged quantity, the velocity must be averaged at the edge center, being replaced with $(v x_{i,j,k}^* + v x_{i,j,k-1})/2$.

The calculations of $d\phi_{y_{i,j,k}}$, the y flux remapped from cell (i, j, k) to cell $(i+1, j, k)$, follows the calculations of dM_i . To preserve the solenoidal condition, $\nabla \cdot \mathbf{B} = 0$, the code uses Evans and Hawley's constrained transport method (Evans and Hawley, 1988). This requires that

$$\begin{aligned} \phi_{y_{i,j,k}}^{n+1} &= \phi_{y_{i,j,k}} - d\phi_{y_{i,j,k}}, \\ \phi_{y_{i+1,j,k}}^{n+1} &= \phi_{y_{i+1,j,k}} + d\phi_{y_{i,j,k}}, \\ \phi_{x_{i,j,k}}^{n+1} &= \phi_{x_{i,j,k}} + d\phi_{y_{i,j,k}}, \\ \phi_{x_{i+1,j,k}}^{n+1} &= \phi_{x_{i+1,j,k}} - d\phi_{y_{i,j,k}}, \end{aligned}$$

and similarly for the rest of the components. Finally, converting the fluxes back into field components then completes the remap step.

2.6 Resistive terms

We are now going to discuss briefly the introduction of non-ideal terms in the LARE code. These come added in a separate module which calculates the resistivity, diffusion and ohmic heating terms.

Resistivity is not homogeneous in the code. In fact, it is computed as a function of the current density, so that it activates when the value of the current is above a given critical value j_{crit} , as follows,

$$\eta = \eta_0 \max\left(0, \frac{|j|}{j_{crit}} - 1\right).$$

This approach allows reconnection only in certain isolated regions. A background value for the current may also be given as an input to the code.

The diffusion of the magnetic field is carried out in the Lagrangian step. If it is allowed to happen, conservation of magnetic flux can no longer be applied, and the magnetic field must be calculated explicitly. This is done by adding the missing resistive term in the predictor step to the calculations in (2.3.2), taken from equation (2.4.4), given by

$$\int [\nabla \times (\eta \nabla \times \mathbf{B})]_i d\tau.$$

This term is, by construction, defined at the centers of the cell faces, as it is the magnetic field, so it does not require any further averaging. In the corrector step, equation (2.3.3) is used to calculate the change in magnetic flux, from which the magnetic field components can be directly obtained. Then, the remap step is carried out as in the ideal case.

The magnetic diffusion creates an extra heating term, the *ohmic heating*, given by ηj^2 , which is calculated at the cell edges and averaged to the cell center to be used in the energy update.

The inclusion of artificial viscosity handles shocks correctly, but also makes the solutions more diffusive. To avoid this, the code includes a term of artificial resistivity through equations (2.3.2) and (2.3.3). This resistivity has the form $v_A^2 \Delta t$, where v_A is the local Alfvén speed, and is added in the same manner as the artificial viscosity.

2.7 Stability condition

There exists a constraint in the timestep, related to the spatial stepsize, which defines a stability criterion in numerical computations. It has to do, as usual, with the fact that the domain of the numerical experiments is discretised in points. And it appears from the finite differentiation scheme, which is never exact.

Let's define the *domain of dependence* of a partial differential equation (PDE) for a given point as the portion of the problem domain that influences the value of the solution at that given point. Similarly, the domain of dependence of an explicit finite difference scheme for a given mesh point is the set of mesh points that affect the value of the approximate solution at that given mesh point. The *Courant-Friederichs-Lewy (CFL) condition* (Courant et al., 1928, English translation: Courant et al. (1967)) requires that the domain of dependence of the PDE must lie within the domain of dependence of the finite difference scheme, for each mesh point. Any explicit finite difference scheme that violates the CFL condition is necessarily unstable, although satisfying the CFL condition does not necessarily guarantee stability.

This condition may be derived using *von Neumann* stability analysis for the differentiation scheme (see, for example, Isaacson and Keller, 1966). In a diffusion type equation, i.e.

$$\frac{dQ}{dt} = \kappa \frac{d^2Q}{dx^2},$$

stability can not be guaranteed, unless the numerical timestep, δt , satisfies $\delta t \leq \frac{1}{2} \delta x^2 / \kappa$. This condition can be interpreted as requiring that the typical length $(\kappa \delta t)^{1/2}$ for the diffusion of Q does not exceed one spatial step δx , or equivalently that the physical diffusion κ is not bigger than the numerical diffusion $(\delta x)^2 / \delta t$.

Hence, in the LARE code, the time-step can be restricted by taking the smaller value from the restriction for the resistive diffusive term and the viscous diffusive term, so that

$$\delta t \leq \min \left[\frac{1}{2} \frac{(\delta s)^2}{\eta}, \frac{1}{2} \frac{(\delta s)^2}{\nu} \right], \quad (2.7.1)$$

for the code to have a chance of being stable.

2.8 Summary

We have presented in this chapter the code we are going to be using for the numerical experiments of this thesis. The code solves the full set of MHD equations and can include both viscous and resistive terms. Each timestep is split into a Lagrangian step followed by a remap onto the original grid. This allows all of the physics to be included into the Lagrangian step, which is built through a simple predictor-corrector scheme. The remap step includes gradient limiters to help control shocks. The code uses a staggered grid to prevent the checkerboard instability and to build conservation laws into the finite difference scheme.

For our purposes, viscosity is switched on, but we work with the non-resistive version of the code. Nonetheless, we must expect a small amount of numerical diffusion of the magnetic field when situations are pushed to the limit, i.e. when very small length scales occur and hence large electric current densities are present. This will, however, decrease considerably when using high spatial resolution, although such runs require more computational power.

The code has been tested widely for solar coronal phenomena, and it has been proved to handle shocks correctly, allowing the inclusion of non-hyperbolic physics such as resistivity and viscosity, and to accurately find local temperatures. A set of tests which are well established in the literature are presented in Arber et al. (2001), in order to prove the validity of the code.

In practise, what is needed for the numerical experiments is a set of initial conditions for the magnetic field, density, internal energy and velocity, plus the specification of how those quantities should behave at each of the boundaries of the domain. Boundary conditions have to be set by specifying the values at ghost cells (see Figure 2.3) right outside each boundary of the domain. Those are then taken on each timestep to calculate derivatives at boundaries.

There is a number of control parameters to be specified by the user, such as grid-size, timestep, viscosity, and shock viscosity parameters, among others. The last ones are set to zero when possible. Also, we specify the kinetic energy remap to be applied on each timestep, to ensure energy conservation at shocks.

Chapter 3

Relaxation of Parallel Magnetic Fields

3.1 Introduction

In our first set of experiments, we consider the case of a hydromagnetic perturbation over a homogeneous two-dimensional magnetic field with parallel field lines in a given spatial direction. This configuration is absolutely general and might be compared with different solar environments such as a region in a coronal prominence or part of a coronal loop. The results shown in this chapter can be found in Fuentes-Fernández et al. (2010).

Looking at this simple structure allows us to study in detail the direct consequences of introducing a non-zero plasma beta in relaxation experiments. Also, it provides an easy context to look closely at the energy evolution during the dynamical process. Furthermore, making use of perturbation theory, we are able to *predict* mathematically the final equilibrium states as functions of the initial disturbances, which could be purely magnetic, thermal, or both.

To test the analytical calculations, we show a series of experiments in which the system is perturbed by a local small enhancement in the plasma pressure. We analyse one specific experiment in detail, and then we evaluate the validity of the linear predictions for the whole series of experiments. According to equation (1.3.8), for final state to be in equilibrium it is required that the plasma pressure is constant along field lines. In principle, the system would be allowed to relax to the minimum magnetic energy state, redistributing the plasma pressure evenly over the whole domain, but that is not possible, as there are no resistive terms in the equations, and hence, no magnetic diffusion by ohmic dissipation in the relaxation. The field is frozen to the plasma. Thus the plasma, trying to expand because of the pressure enhancement, has to carry the magnetic field with it and destroy its homogeneity.

3.2 Linear equations in 2D

Let x and y be the coordinates of the two-dimensional problem. The initial setup involves a uniform magnetic field pointing in the vertical y -direction, $\mathbf{B}_0 = B_0 \hat{e}_y$, and a background plasma with constant pressure p_0 , density ρ_0 and internal energy ϵ_0 , with no initial flow (i.e. $\mathbf{v}_0 = 0$). The initial disturbances are supposed to be small, in order to stay in the linear regime. Expressing each quantity $q(x, y, t)$ as the sum of a background constant value plus a perturbation, $q(x, y, t) = q_0 + q_1(x, y, t)$, where the subscript 0 indicates the background constant value, and the subscript 1 indicates the first order perturbation, we get the expressions for the relevant quantities as functions of

space and time, as

$$\begin{aligned}\rho(x, y, t) &= \rho_0 + \rho_1(x, y, t) && \text{(with } \rho_1 \ll \rho_0 = \text{const) ,} \\ \epsilon(x, y, t) &= \epsilon_0 + \epsilon_1(x, y, t) && \text{(with } \epsilon_1 \ll \epsilon_0 = \text{const) ,} \\ p(x, y, t) &= p_0 + p_1(x, y, t) && \text{(with } p_1 \ll p_0 = \text{const) ,} \\ \mathbf{B}(x, y, t) &= \mathbf{B}_0 + \mathbf{B}_1(x, y, t) && \text{(with } |\mathbf{B}_1| \ll |\mathbf{B}_0| = \text{const) ,} \\ \mathbf{v}(x, y, t) &= \mathbf{v}_1(x, y, t) && \text{(with } |\mathbf{v}_1| \text{ very small) .}\end{aligned}$$

To derive the set of first order equations that describe the linear evolution of the field and the plasma, we have to take into account that the derivatives of the background quantities are always zero, and we neglect the second order terms that involve quadratic or higher order terms (i.e. products of the perturbations).

We first consider the linearised equation of state. The background and first order perturbation of the plasma pressure are related to the plasma density and internal energy through equation (1.2.24), such that

$$p_0 = \rho_0 \epsilon_0 (\gamma - 1) , \quad (3.2.1)$$

$$p_1 = (\rho_0 \epsilon_1 + \rho_1 \epsilon_0) (\gamma - 1) . \quad (3.2.2)$$

Also, the total pressure, defined as the sum of the plasma pressure, p , and the magnetic pressure, $B^2/2$, may be written as $p_T = p_{T0} + p_{T1}$, using

$$p_{T0} = p_0 + B_0^2/2 , \quad (3.2.3)$$

$$p_{T1} = p_1 + (\mathbf{B}_0 \cdot \mathbf{B}_1) . \quad (3.2.4)$$

Now, from the normalised ideal MHD equations, (1.6.1) to (1.6.4), we get

$$\frac{\partial \rho_1}{\partial t} = -\rho_0 \nabla \cdot \mathbf{v}_1 , \quad (3.2.5)$$

$$\rho_0 \frac{\partial \mathbf{v}_1}{\partial t} = -\nabla p_1 + (\nabla \times \mathbf{B}_1) \times \mathbf{B}_0 + \mathbf{F}_{\nu 1} , \quad (3.2.6)$$

$$\frac{\partial p_1}{\partial t} = -\gamma p_0 \nabla \cdot \mathbf{v}_1 , \quad (3.2.7)$$

$$\frac{\partial \mathbf{B}_1}{\partial t} = \nabla \times (\mathbf{v}_1 \times \mathbf{B}_0) , \quad (3.2.8)$$

with $\mathbf{F}_{\nu 1}$ being the linearized viscous force, from equation (1.2.29),

$$\mathbf{F}_{\nu 1} = \rho_0 \nu \left(\nabla^2 \mathbf{v}_1 + \frac{1}{3} \nabla (\nabla \cdot \mathbf{v}_1) \right) .$$

where ν is the kinematic viscosity. Note, that the heating term does not appear in equation (3.2.7), since it is purely second order. Thus the process is adiabatic within the linear regime, and there is no heating of any kind taking place: The entropy per unit mass, $s \sim p/\rho^\gamma$, is conserved, for each single fluid element, and for the entire box. For the two-dimensional problem, we can rewrite the equations above in scalar form, decomposing all the vectorial

quantities in components, as

$$\frac{\partial \rho_1}{\partial t} = -\rho_0 \nabla \cdot \mathbf{v}_1, \quad (3.2.9)$$

$$\rho_0 \frac{\partial v_{1x}}{\partial t} = -\frac{\partial p_1}{\partial x} - B_0 \frac{\partial B_{1y}}{\partial x} + B_0 \frac{\partial B_{1x}}{\partial y} + \rho_0 \nu \left(\nabla^2 v_{1x} + \frac{1}{3} \frac{\partial}{\partial x} (\nabla \cdot \mathbf{v}_1) \right), \quad (3.2.10)$$

$$\rho_0 \frac{\partial v_{1y}}{\partial t} = -\frac{\partial p_1}{\partial y} + \rho_0 \nu \left(\nabla^2 v_{1y} + \frac{1}{3} \frac{\partial}{\partial y} (\nabla \cdot \mathbf{v}_1) \right), \quad (3.2.11)$$

$$\frac{\partial p_1}{\partial t} = -\gamma p_0 \nabla \cdot \mathbf{v}_1, \quad (3.2.12)$$

$$\frac{\partial B_{1x}}{\partial t} = B_0 \frac{\partial v_{1x}}{\partial y}, \quad (3.2.13)$$

$$\frac{\partial B_{1y}}{\partial t} = -B_0 \frac{\partial v_{1x}}{\partial x}, \quad (3.2.14)$$

where v_{1x} , v_{1y} , B_{1x} and B_{1y} are the x and y components of the perturbed velocity and perturbed magnetic field, respectively. Plasma pressure, density and internal energy are related by the perfect gas law, equations (3.2.1) and (3.2.2), with $\gamma = 5/3$.

From the conservation of entropy, a relation between the plasma pressure and density perturbations may be obtained, within first order (i.e. neglecting the terms involving products of perturbations), using

$$\begin{aligned} \frac{p_0 + p_1}{(\rho_0 + \rho_1)^\gamma} &= \frac{p_0 + p_1}{\rho_0^\gamma + \gamma \rho_1 \rho_0^{\gamma-1}} \\ &= \frac{p_0}{\rho_0^\gamma} \left(1 + \frac{p_1}{p_0} \right) \left(1 + \frac{\gamma \rho_1}{\rho_0} \right)^{-1} \\ &= \frac{p_0}{\rho_0^\gamma} \left(1 + \frac{p_1}{p_0} \right) \left(1 - \frac{\gamma \rho_1}{\rho_0} \right) \\ &= \frac{p_0}{\rho_0^\gamma} \left(1 + \frac{p_1}{p_0} - \frac{\gamma \rho_1}{\rho_0} \right) = \text{constant}. \end{aligned}$$

Hence,

$$\frac{\Delta p_1}{p_0} - \frac{\gamma \Delta \rho_1}{\rho_0} = 0,$$

where Δ indicates the difference between final and initial state of the perturbation, such that

$$\Delta p_1 = c_s^2 \Delta \rho_1, \quad (3.2.15)$$

where $c_s = \sqrt{\gamma p_0 / \rho_0}$ is the *sound speed*.

In order to get a solution of the above equations, by properly understanding what is happening and being able to make some analytical progress, we first consider perturbations that are purely perpendicular and purely parallel to the magnetic field, and solve the set of equations (3.2.9) to (3.2.14) for the two one-dimensional cases separately, for then combining them to find the solution for a general two-dimensional hydromagnetic perturbation.

3.2.1 1D Perturbation across field lines

Let's consider first a perturbation varying only in the direction perpendicular to the magnetic field lines, x . The magnetic field vector has a non-zero y -component, $\mathbf{B}_1(x, t) = B_{1y}(x, t)\hat{e}_y$, while the velocity has a non-zero x -component, $\mathbf{v}_1(x, t) = v_{1x}(x, t)\hat{e}_x$. Equations (3.2.9) to (3.2.14) reduce to

$$\frac{\partial \rho_1}{\partial t} = -\rho_0 \frac{\partial v_{1x}}{\partial x}, \quad (3.2.16)$$

$$\rho_0 \frac{\partial v_{1x}}{\partial t} = -\frac{\partial p_{T1}}{\partial x} + \rho_0 \nu' \frac{\partial^2 v_{1x}}{\partial x^2}, \quad (3.2.17)$$

$$\frac{\partial p_1}{\partial t} = -\gamma p_0 \frac{\partial v_{1x}}{\partial x}, \quad (3.2.18)$$

$$\frac{\partial B_{1y}}{\partial t} = -B_0 \frac{\partial v_{1x}}{\partial x}, \quad (3.2.19)$$

where $\nu' = 4\nu/3$, and p_{T1} is the perturbed total pressure, from equation (3.2.4), given by

$$p_{T1} = p_1 + B_0 B_{1y}. \quad (3.2.20)$$

The equation governing the final equilibrium state can be obtained using equation (3.2.17). In a static equilibrium, the time dependence disappears, and the velocity is zero, thus, the equilibrium requires constant total pressure everywhere,

$$\frac{\partial p_{T1}}{\partial x} = 0. \quad (3.2.21)$$

That is, total pressure is constant everywhere in the final equilibrium state. Combining equations (3.2.18) and (3.2.19), we get the evolution of the total pressure as

$$\frac{1}{\rho_0} \frac{\partial p_{T1}}{\partial t} = -(c_s^2 + c_A^2) \frac{\partial v_{1x}}{\partial x}, \quad (3.2.22)$$

where $c_A = B_0/\sqrt{\rho_0}$ is the (normalised) *Alfvén speed* (normally defined as $c_A = B_0/\sqrt{\mu\rho_0}$).

With a bit of manipulation, we can derive a differential equation for the total pressure. Differentiating (3.2.22) with respect to x , substituting the value of $\partial^2 v_{1x}/\partial x^2$ given by (3.2.10), and differentiating all with respect to x again, we get

$$\frac{1}{\rho_0} \frac{\partial}{\partial t} \left(\frac{\partial^2 p_{T1}}{\partial x^2} \right) = -\frac{c_s^2 + c_A^2}{\nu'} \left(\frac{1}{\rho_0} \frac{\partial^2 p_{T1}}{\partial x^2} + \frac{\partial^2 v_{1x}}{\partial t \partial x} \right).$$

The differentiating of (3.2.22) with respect to t gives us the last term in this equation, obtaining, finally,

$$\frac{\partial^2 p_{T1}}{\partial t^2} = (c_s^2 + c_A^2) \frac{\partial^2 p_{T1}}{\partial x^2} + \nu' \frac{\partial}{\partial t} \left(\frac{\partial^2 p_{T1}}{\partial x^2} \right). \quad (3.2.23)$$

Equation (3.2.23) is the *wave equation for fast magnetoacoustic waves*. These are longitudinal waves that propagate in the direction perpendicular to the magnetic field, compressing and expanding both the magnetic field and the plasma. Their speed of propagation is given by the *fast magnetoacoustic speed*,

$$c_f = \sqrt{c_s^2 + c_A^2}, \quad (3.2.24)$$

and the second term in the right hand side of (3.2.23) is the damping mechanism, which is controlled by the kinematic viscosity.

Assuming that the total pressure can be considered as a continuous, periodic function, the solution of last equation is given by Fourier analysis, and can be expressed as a superposition of plane waves, such as

$$p_{T1}(x, t) = \mathcal{R}e \left(\sum_k \varphi_k e^{i(kx - \omega t)} \right), \quad (3.2.25)$$

Each value of the *wave number* k (where k is real) corresponds to a different oscillation mode. In general, ω will be a complex quantity dependent on k , with a real part, representing the frequency, and an imaginary part, representing the damping rate for each mode. In the same way, the constant φ_k is a complex quantity as well, and may be decomposed into real and imaginary constants. Each single mode, characterized by the different values of k , is not coupled to the other modes, and is a solution of the wave equation itself. Hence, we can consider each wave with a generic wave number separately.

Forgetting for one moment the fact that only the real part of this expression makes physical sense, we may substitute (3.2.25) into (3.2.23), replacing the spatial derivatives by ik , and the time derivatives by $-i\omega$, to obtain a second grade equation for $\omega(k)$, referred as to the *dispersion relation*:

$$\omega^2 + ik^2\nu'\omega - c_f^2k^2 = 0. \quad (3.2.26)$$

Equation (3.2.26) has the solution $\omega = a \pm bi$, where a , the real frequency of the wave, and b , the damping term, are given by

$$a = \frac{k}{2} \sqrt{4c_f^2 - k^2\nu'^2}, \quad (3.2.27)$$

$$b = \frac{1}{2}k^2\nu'. \quad (3.2.28)$$

Notice, from the square root in (3.2.27), that in order to have a harmonic mode, the wave number k must satisfy $k^2\nu'^2 < 4c_f^2$, and higher modes will be damped without any type of oscillation.

On the other hand, from equations (3.2.27) and (3.2.28), we find that the mode with $k = 0$ has $\omega = 0$. From equation (3.2.25), the expression for $p_{T1}(x, t)$ can be written as a constant coefficient, say φ_0 , plus a sum of terms which will be proportional to a mix of cosines and sines of kx and at and to the exponential e^{-bt} . It is this last term which matters, as it vanishes at the final equilibrium, for $t \rightarrow \infty$, thus leaving the total pressure as a constant given by φ_0 everywhere, in agreement with equation (3.2.21). As this constant does not vary in time, it can be calculated for $t = 0$ as the first coefficient of the Fourier expansion of $p_{T1}(x, 0)$, namely

$$p_{T1}(x, 0) = \frac{a_0}{2} + \sum_n [a_n \cos(2\pi nx/L_x) + b_n \sin(2\pi nx/L_x)],$$

where L_x is the length of the x -domain, and the coefficients are given by

$$\begin{aligned} a_0 &= \frac{2}{L_x} \int p_{T1}(x, 0) dx , \\ a_n &= \frac{2}{L_x} \int p_{T1}(x, 0) \cos(2\pi nx/L_x) dx , \\ b_n &= \frac{2}{L_x} \int p_{T1}(x, 0) \sin(2\pi nx/L_x) dx . \end{aligned}$$

The key point is that $\varphi_0 = a_0$, i.e. the constant coefficient from the Fourier analysis of (3.2.25) for $p_{T1}(x, t)$ is the same as the constant coefficient from the Fourier expansion for $p_{T1}(x, 0)$, so the perturbed total pressure in the final equilibrium is given by that constant, which is the *homogeneous redistribution of the initial total pressure*, given by

$$p_{T1}(\infty) = \frac{1}{L_x} \int p_{T1}(x, 0) dx = \frac{1}{L_x} \int (p_1(x, 0) + B_0 B_{1y}(x, 0)) dx , \quad (3.2.29)$$

where the dx integrals are integrals over the length of the x -domain, L_x .

From equation (3.2.22) we get an expression for the velocity gradient, as

$$\frac{\partial v_{1x}}{\partial x} = -\frac{1}{\rho_0 c_f^2} \frac{\partial p_{T1}}{\partial t} ,$$

which we can substitute into equations (3.2.16), (3.2.18) and (3.2.19), giving

$$\frac{\partial \rho_1}{\partial t} = \frac{1}{c_f^2} \frac{\partial p_{T1}}{\partial t} , \quad (3.2.30)$$

$$\frac{\partial p_1}{\partial t} = \frac{c_s^2}{c_f^2} \frac{\partial p_{T1}}{\partial t} , \quad (3.2.31)$$

$$\frac{\partial B_{1y}}{\partial t} = \frac{B_0}{\rho_0 c_f^2} \frac{\partial p_{T1}}{\partial t} . \quad (3.2.32)$$

Equations (3.2.30) to (3.2.32) show the time evolution of plasma density, pressure and magnetic field during the whole dynamical process. We emphasize the fact that all the time dependencies appear *only* on the total pressure of the system. Integrating now from $t = 0$ to $t = \infty$, we obtain the perturbed quantities for the final equilibrium state, as functions of the perturbed total pressure, to be added to the background values:

$$\rho_1^{\text{eq}}(x) = \rho_1(x, 0) + \frac{1}{c_f^2} [p_{T1}(\infty) - p_{T1}(x, 0)] , \quad (3.2.33)$$

$$p_1^{\text{eq}}(x) = p_1(x, 0) + \frac{c_s^2}{c_f^2} [p_{T1}(\infty) - p_{T1}(x, 0)] , \quad (3.2.34)$$

$$B_{1y}^{\text{eq}}(x) = B_{1y}(x, 0) + \frac{B_0}{\rho_0 c_f^2} [p_{T1}(\infty) - p_{T1}(x, 0)] . \quad (3.2.35)$$

Equations (3.2.33), (3.2.34) and (3.2.35) state that no matter how we set our initial disturbance, the final equilibrium distributions are completely determined by the initial and the final total pressures of the system, which are given by the solution of the wave equation. Also, they are completely independent of the viscosity, but the dependence with the spatial coordinate remains. That is, the pressure gradient is not zero, and so, the equilibrium

described by these equations is not force-free in nature, but the pressure gradient must be balanced by a non-zero Lorentz force. Note, that also the adiabatic equation for the linear regime given in equation (3.2.15) is satisfied.

The distribution of the flux function, A_z , for the final equilibrium can be derived from $B_y = -\partial A_z / \partial x$, as

$$A_z^{\text{eq}}(x) = -B_0 x - \int_{x_{\min}}^x \left\{ B_1(x, 0) + \frac{B_0}{\rho_0 c_f^2} [p_{T1}(\infty) - p_{T1}(x, 0)] \right\} dx, \quad (3.2.36)$$

where the first term is given by the integration of the constant background B_0 . Last, the current density is given by

$$j_z^{\text{eq}}(x) = -\frac{\partial^2 A_z(x, t)}{\partial x^2} = \frac{\partial B_y}{\partial x}. \quad (3.2.37)$$

Finally, we may want to express the final pressure as a function of A_z , since in the equilibrium, the plasma pressure is constant along field lines, as seen in equation (1.3.8). This may be achieved by combining equations (3.2.34) and (3.2.36). For a small perturbation, things can be a lot easier if we neglect the second term on the right hand side of equation (3.2.36), assuming that

$$\left| \int_{x_{\min}}^x \left\{ B_1(x, 0) + \frac{B_0}{\rho_0 c_f^2} [p_{T1}(\infty) - p_{T1}(x, 0)] \right\} dx \right| \ll |B_0 x|.$$

Then, our equilibrium state is defined by

$$p^{\text{eq}}(A_z) = p_0 + p_1(-A_z/B_0, 0) + \frac{c_s^2}{c_f^2} [p_{T1}(\infty) - p_{T1}(-A_z/B_0, 0)]. \quad (3.2.38)$$

3.2.2 1D perturbation along field lines

Let's consider now a perturbation varying only in the direction of the main magnetic field, y . The magnetic field vector remains unperturbed, as it points along the direction of the perturbation and the velocity has a non-zero y -component, $\mathbf{v}_1(y, t) = v_{1y}(y, t)\hat{\mathbf{e}}_y$. Hence, the evolution is purely non-magnetic, and will lead to a homogeneous redistribution of the plasma pressure all along the field lines. Equations (3.2.9) to (3.2.14) reduce to

$$\frac{\partial \rho_1}{\partial t} = -\rho_0 \frac{\partial v_{1y}}{\partial y}, \quad (3.2.39)$$

$$\rho_0 \frac{\partial v_{1y}}{\partial t} = -\frac{\partial p_1}{\partial y} + \rho_0 \nu' \frac{\partial^2 v_{1y}}{\partial y^2}, \quad (3.2.40)$$

$$\frac{\partial p_1}{\partial t} = -\gamma p_0 \frac{\partial v_{1y}}{\partial y}, \quad (3.2.41)$$

and the equilibrium is now given by a constant plasma pressure everywhere,

$$\frac{\partial p_1}{\partial y} = 0.$$

From equation (3.2.41), we get

$$\frac{1}{\rho_0} \frac{\partial p_1}{\partial t} = -c_s^2 \frac{\partial v_{1y}}{\partial y}. \quad (3.2.42)$$

By the appropriate combination of equations (3.2.40) and (3.2.42), we get now a wave equation for the plasma pressure,

$$\frac{\partial^2 p_1}{\partial t^2} = c_s^2 \frac{\partial^2 p_1}{\partial y^2} + \nu' \frac{\partial}{\partial t} \left(\frac{\partial^2 p_1}{\partial y^2} \right). \quad (3.2.43)$$

Equation (3.2.43) define acoustic waves, which are also longitudinal, but propagate in the direction along the magnetic field, with the speed of propagation being the sound speed of the medium, defined before as $c_s = \sqrt{\gamma p_0 / \rho_0}$. Note, that this speed is by definition slower than the fast magnetoacoustic speed defined in equation (3.2.24) for the horizontal propagation.

As before, the plasma pressure can be expressed as a superposition of plane waves, as in equation (3.2.25), with the dispersion relation

$$\omega^2 + ik^2 \nu' \omega - c_s^2 k^2 = 0,$$

where $\omega = a \pm bi$, and

$$a = \frac{k}{2} \sqrt{4c_s^2 - k^2 \nu'^2},$$

$$b = \frac{1}{2} k^2 \nu'.$$

The solution is given by a redistribution of the plasma pressure along the field lines, and may be written as

$$p_1(\infty) = \frac{1}{L_y} \int p_1(y, 0) dy, \quad (3.2.44)$$

$$\rho_1^{\text{eq}}(y) = \rho_1(y, 0) + \frac{1}{c_s^2} [p_1(\infty) - p_1(y, 0)], \quad (3.2.45)$$

where the dy is the integral over the y -domain, L_y . This time, there is no magnetic Lorentz force to counteract a plasma pressure gradient, hence, the plasma pressure just redistributes evenly all along the field lines.

3.2.3 2D perturbation

We combine now the results of the two previous sections to obtain a general solution for equations (3.2.9) to (3.2.14). Once again, setting the velocities to zero, we get the equations governing the 2D equilibrium, from equations (3.2.10) and (3.2.11), as

$$\frac{\partial}{\partial x} (p_1 + B_0 B_{1y}) - B_0 \frac{\partial B_{1x}}{\partial y} = 0, \quad (3.2.46)$$

$$\frac{\partial p_1}{\partial y} = 0. \quad (3.2.47)$$

Equation (3.2.47) tells us that the final plasma pressure cannot depend on y , so the solution for the pressure must remain one-dimensional, i.e. only dependent on x . On the other hand, equation (3.2.46) does not have a direct interpretation, as both spatial derivatives are involved. The term $p_1 + B_0 B_{1y}$ represents the perturbed total pressure from Section 3.2.1, and the new term $B_0 B_{1x}$ represents the magnetic tension due to the curvature of the field lines, which was zero in the one-dimensional cases. As usual, when looking for a periodic solution, Fourier

analyzing makes life simpler. Only if our functions are periodic in both x and y , we can express the first order terms as functions of $e^{i(kx+ly-\omega t)}$, where each pair (k, l) represents one single mode of oscillation in the global time evolution. Then, equations (3.2.46) and (3.2.47) can be rewritten as

$$\begin{aligned} k(p_1 + B_0 B_{1y}) - l B_0 B_{1x} &= 0, \\ l p_1 &= 0. \end{aligned}$$

- 1) The mode $k = 0, l = 0$ represents the unperturbed background values.
- 2) For $k \neq 0, l = 0$, the equation of the equilibrium is

$$\frac{\partial}{\partial x}(p_1 + B_0 B_{1y}) = 0. \quad (3.2.48)$$

These modes only depend on x , and represent the homogeneous redistribution of the total pressure studied in Section 3.2.1.

- 3) For $k = 0, l \neq 0$ we get

$$\frac{\partial p_1}{\partial y} = 0, \quad (3.2.49)$$

$$\frac{\partial B_{1x}}{\partial y} = 0. \quad (3.2.50)$$

These modes do not modify B_{1y} , instead they simply remove both the vertical gradients of magnetic tension and plasma pressure as in Section 3.2.2. Each of them is treated individually, as they are not coupled in the equations.

- 4) Finally, for those modes with $k \neq 0, l \neq 0$, we get

$$k B_{1y} - l B_{1x} = 0,$$

which can be combined with the solenoidal condition for the magnetic field, $\nabla \cdot \mathbf{B} = 0$, or, within our Fourier notation,

$$k B_{1y} + l B_{1x} = 0.$$

From these equations, we can conclude that, in the final equilibrium, the existence of a variation of B_{1y} in the x -direction is totally incompatible with a variation of B_{1x} in the y -direction. Hence, the modes with both wave numbers k and l non-zero may appear in the dynamical evolution, but *not* in the final equilibrium distributions.

Therefore, with our uniform background magnetic field pointing straight in the vertical y -direction, the final equilibrium state is a combination of the background values ($k = 0, l = 0$), plus the vertical non-magnetic evolution to a state with plasma pressure that is constant along y , and/or the smoothing of the horizontal component of the magnetic field ($k = 0, l \neq 0$), plus the one-dimensional hydromagnetic evolution across the field lines ($k \neq 0, l = 0$). Note, that a perturbed magnetic field in the horizontal direction, B_{1x} (i.e. a curved magnetic field), is not coupled with either p_1 or B_{1y} , so the final magnetic field lines remain straight, and B_{1x} is not involved in the final equilibrium.

Hence, we may calculate the analytical two-dimensional final equilibrium in two steps. Let's denote the quantities after the vertical non-magnetic evolution with a star superscript, e.g. p_1^* . First, the non-magnetic evolution in

the vertical direction, along the field lines,

$$p_1^*(x) = \frac{1}{L_y} \int p_1(x, y, 0) dy, \quad (3.2.51)$$

$$\rho_1^*(x, y) = \rho_1(x, y, 0) + \frac{1}{c_s^2} [p_1^*(x) - p_1(x, y, 0)], \quad (3.2.52)$$

with the total pressure given by

$$p_{T1}^*(x) = p_1^*(x) + B_0 B_{1y}(x, 0). \quad (3.2.53)$$

And second, the hydromagnetic evolution in the horizontal direction, across the field,

$$\rho_1^{\text{eq}}(x, y) = \rho_1^*(x, y) + \frac{1}{c_f^2} [p_{T1}(\infty) - p_{T1}^*(x)], \quad (3.2.54)$$

$$p_1^{\text{eq}}(x, y) = p_1^*(x) + \frac{c_s^2}{c_f^2} [p_{T1}(\infty) - p_{T1}^*(x)], \quad (3.2.55)$$

$$B_{1y}^{\text{eq}}(x, y) = B_{1y}(x, 0) + \frac{B_0}{\rho_0 c_f^2} [p_{T1}(\infty) - p_{T1}^*(x)], \quad (3.2.56)$$

not forgetting to add the respective constant background values.

When analyzing the validity of the results above for a non-ideal experiment, it is important to remember that equations (3.2.52) to (3.2.56) are restricted by the linear approximation, while equation (3.2.51) is not. Hence, we expect our analytical calculations for the pressure to hold for much larger initial perturbations than the ones for the density. If the initial pressure disturbance is not small, but the linear expression for the plasma pressure is still valid, the adiabatic condition (i.e. $p/\rho^\gamma = \text{constant}$) gives us a better approximation for the final equilibrium plasma density, calculated as

$$\rho^{\text{eq}}(x, y) = \left(\frac{p^{\text{eq}}(x, y) \rho^\gamma(x, y, 0)}{p(x, y, 0)} \right)^{1/\gamma}. \quad (3.2.57)$$

We shall make a note about the two speeds involved in the solutions (3.2.54) to (3.2.56). The sound speed, c_s , is calculated from the background plasma pressure and density, but note how our choice of an ideal polytropic gas, i.e. equation (1.2.24), removes the dependence on the density in the sound speed. And the fast magnetoacoustic speed is defined in equation (3.2.24). Hence, we can derive the general expressions of our two characteristic speeds as

$$c_s = \sqrt{\epsilon_0 \gamma (\gamma - 1)}, \quad (3.2.58)$$

$$c_f = \sqrt{\frac{B_0^2}{\rho_0} + \epsilon_0 \gamma (\gamma - 1)}. \quad (3.2.59)$$

Equation (3.2.58) defines the characteristic speed of the vertical non-magnetic evolution, and (3.2.59) defines the characteristic speed of the horizontal evolution. Of course, the dynamical process is more complicated than that. These two evolutions do not occur independently, as the process is two-dimensional. The system does not evolve in the vertical direction first, and then in the horizontal direction, nor the opposite. In fact, there might be a whole family of magnetoacoustic waves relaxing the system down to the final equilibrium. However, the equations are

such that we can find the final equilibrium state *as if* the two one-dimensional evolutions occurred separately, and thus allowing us to make predictions.

3.2.4 Overview

So far, we have derived explicit analytical expressions for the solution of a generic hydromagnetic perturbation imposed over a straight and uniform magnetic field, embedded in a thermal plasma. To do this, we restricted the calculations to the linear regime, in which the perturbations are assumed to be small. In general terms, “small” means that the products of these perturbed quantities have to be negligible when compared with the linear terms. But the character of being “negligible” can only be examined by direct comparison with the exact results to the equations. Although, in general, physical processes that evoke natural events are not linear, in some cases, one can find a regime where terms of higher order than linear do not add significant effects, and hence, the first-order approximation does a good job.

Next, we consider a series of numerical experiments to evaluate for what range of parameters our linear results are valid. If the results from above are only valid for a regime of really small perturbations, then those results are meaningless. If they work for perturbations in some way comparable with the background quantities, then they may have some potential.

3.3 Numerical experiments: Setup

The numerical results are obtained through a series of experiments, using the LARE code, where the magnitude of the same type of perturbation is increased systematically. Since these are the first series of experiments discussed in this thesis, we present the numerical setup in careful detail, specifying the way we imposed the boundary conditions of the code, using values at ghost cells outside the numerical domain, together with the specification of the initial conditions, which include the background unperturbed quantities and the initial perturbations which break the equilibria, and the calculations of the perturbed total pressure, which determines the characteristics of the final equilibrium states.

3.3.1 Numerical specifications

The numerical domain is a square box with a uniform grid of 256×256 points. The length of the domain is $L_x \times L_y = 1 \times 1$, and both x and y vary from 0 to 1. The background magnetic field is pointing in the vertical y -direction and all the perturbations depend on both x and y . The top and bottom boundaries of the box are periodic, so that the field lines are not line-tied, allowing them to move entirely together with the movement of the plasma fluid. The boundaries on the left and right sides are closed. The precise conditions that has been set at the boundaries of LARE are specified below.

The periodic boundaries on the top and bottom mean that outflows at the top are coded as inflows at the bottom, and vice versa. The code has this option to be set up automatically by just choosing the boundaries to be periodic. For the LARE discretization terminology, this is transcribed into two rows of ghost cells for each boundary (see

Figure 2.3), as

Top boundaries :

$$B_x(i, n_y + 1) = B_x(i, 1)$$

$$B_x(i, n_y + 2) = B_x(i, 2)$$

$$B_y(i, n_y + 1) = B_y(i, 1)$$

$$B_y(i, n_y + 2) = B_y(i, 2)$$

$$\epsilon(i, n_y + 1) = \epsilon(i, 1)$$

$$\epsilon(i, n_y + 2) = \epsilon(i, 2)$$

$$\rho(i, n_y + 1) = \rho(i, 1)$$

$$\rho(i, n_y + 2) = \rho(i, 2)$$

Bottom boundaries :

$$B_x(i, 0) = B_x(i, n_y)$$

$$B_x(i, -1) = B_x(i, n_y - 1)$$

$$B_y(i, -1) = B_y(i, n_y - 1)$$

$$B_y(i, -2) = B_y(i, n_y - 2)$$

$$\epsilon(i, 0) = \epsilon(i, n_y)$$

$$\epsilon(i, -1) = \epsilon(i, n_y - 1)$$

$$\rho(i, 0) = \rho(i, n_y)$$

$$\rho(i, -1) = \rho(i, n_y - 1)$$

On the other hand, closed boundaries on the left and right mean that flows approaching the boundary must bounce back into the numerical domain. In general, specifying closed boundaries is not a trivial problem, and doing it incorrectly can cause losses through the boundaries, involving the breaking of conservation laws. Our specification of closed boundaries is made by setting the quantities to be constant (or maxima or minima) across them, or, in other words, setting their derivatives with respect to the coordinate normal to the boundary as zero. This is translated into LARE as

Right boundaries :

$$B_x(n_x + 1, j) = B_x(n_x - 1, j)$$

$$B_x(n_x + 2, j) = B_x(n_x - 2, j)$$

$$B_y(n_x + 1, j) = B_y(n_x, j)$$

$$B_y(n_x + 2, j) = B_y(n_x - 1, j)$$

$$\epsilon(n_x + 1, j) = \epsilon(n_x, j)$$

$$\epsilon(n_x + 2, j) = \epsilon(n_x - 1, j)$$

$$\rho(n_x + 1, j) = \rho(n_x, j)$$

$$\rho(n_x + 2, j) = \rho(n_x - 1, j)$$

Left boundaries :

$$B_x(-1, j) = B_x(1, j)$$

$$B_x(-2, j) = B_x(2, j)$$

$$B_y(0, j) = B_y(1, j)$$

$$B_y(-1, j) = B_y(2, j)$$

$$\epsilon(0, j) = \epsilon(1, j)$$

$$\epsilon(-1, j) = \epsilon(2, j)$$

$$\rho(0, j) = \rho(1, j)$$

$$\rho(-1, j) = \rho(2, j)$$

Note, how the value $B_y(i, 0)$ is not specified as a boundary in LARE, but as an initial condition. For the experiments of this section, this choice of closed boundaries behaves perfectly, and in fact, it has been confirmed that the choice of periodic or closed boundaries makes no difference. We have shown here the specification for closed boundaries to illustrate the two different options. In the case of closed boundaries, all the velocities at the ghost cells are set to zero.

3.3.2 Initial conditions

The initial equilibrium is a uniform magnetic field, pointing along the vertical y -direction, which is embedded in a plasma with uniform pressure, density and internal energy, and with no velocities. The strength of the background uniform magnetic field and the background internal energy are fixed, and have the values of $B_y = 1.0$ and $\epsilon_0 = 1.5$, respectively. The background density, ρ_0 , is constant everywhere, and its value is varied from experiment to

	Background	Perturbation
q	q_0	$q_1(t=0)$
ρ	ρ_0	0.0
ϵ	1.5	$\epsilon_1(x, y, 0)$
p	$2\rho_0$	$\frac{2}{3}\rho_0\epsilon_1$
$ \mathbf{B} $	1.0	0.0
$ \mathbf{v} $	0.0	0.0

Table 3.1: Constant background values and initial perturbations for the numerical experiments.

experiment, as it controls the background plasma beta, i.e. the ratio of the plasma pressure to the magnetic pressure, which is defined as

$$\beta_0 = \frac{2p_0}{B_0^2} = \frac{2\rho_0\epsilon_0(\gamma-1)}{B_0^2} = 2\rho_0, \quad (3.3.1)$$

The initial perturbation is chosen to be a Gaussian enhancement of the internal energy. The initial perturbation of the density is set to zero, so that the enhancement in the plasma pressure is proportional to that of the internal energy. The magnetic field is left unperturbed initially, so the initial perturbed total pressure is just the perturbed plasma pressure. The expression for the internal energy perturbation is

$$\epsilon_1(x, y, 0) = a \exp\left[-\frac{(x-b)^2}{2c^2}\right] \exp\left[-\frac{(y-b)^2}{2c^2}\right], \quad (3.3.2)$$

hence, the perturbation in the plasma pressure, according to equation (3.2.2), is given by

$$p_1(x, y, 0) = \rho_0(\gamma-1) a \exp\left[-\frac{(x-b)^2}{2c^2}\right] \exp\left[-\frac{(y-b)^2}{2c^2}\right], \quad (3.3.3)$$

where the Gaussian is taken to be centered in the domain, i.e. $b = 0.5$, its width is held fixed for all the experiments, $c = 0.05$, and a defines the amplitude of the perturbation, which, as the background plasma density, varies from experiment to experiment.

The value of a defines the ratio of the maximum value of the perturbed plasma pressure to the background plasma pressure, what we have called \mathcal{P} , as follows

$$\mathcal{P} = \frac{\max(p_1)}{p_0} = \frac{\rho_0(\gamma-1)a}{\rho_0\epsilon_0(\gamma-1)} = \frac{a}{\epsilon_0} = \frac{2}{3}a. \quad (3.3.4)$$

In Table 3.1 we summarise the values for the background quantities and the initial perturbations for our experiments. The values which are not specified with a number are subject to changes in the plasma beta and the amplitude of the perturbation. Lastly, we can also give a number to the sound speed, which, as we discussed earlier, depends only on the background internal energy. This is $c_s = \sqrt{5/3} \approx 1.29$. This speed will be compared later with the fast magnetoacoustic speed of the experiments.

The viscosity parameters are the same for all the experiments, for consistency. There are three parameters to be set, namely the linear and quadratic shock viscosities from equation (2.2.10), ν_1 and ν_2 , respectively, and the real viscosity, ν_r , which is the kinematic viscosity times the plasma density, $\nu_r = \nu\rho$. The real viscosity is set to $\nu_r = 0.001$, and both shock viscosities are set to *zero*. The choice of no shock viscosity does not cause problems in

the relaxation, and may avoid extra complications when analyzing the dynamical evolution of the system. Hence, we maintain this choice, if possible, throughout the whole thesis.

3.3.3 Perturbed total pressure

Before the results are discussed, let's get the expression for the one and only quantity that needs to be calculated for comparing the equilibrium solutions with the analytical equilibrium results. That is, the total pressure. Combining equations (3.2.51) and (3.2.53) with the initial conditions of our numerical experiments, we can get the perturbed total pressure after the non-magnetic vertical evolution, as

$$\begin{aligned} p_{T1}^*(x) &= p_1^*(x) \\ &= \int_0^1 p_1(x, y, 0) dy \\ &= \psi \rho_0 (\gamma - 1) a \exp \left[-\frac{(x-b)^2}{2c^2} \right], \end{aligned} \quad (3.3.5)$$

where ψ is a constant given by the error function, $\text{erf}(x) = \frac{2}{\sqrt{\pi}} \int_0^x e^{-x^2} dx$, as

$$\psi = \int_0^1 \exp \left[-\frac{(y-b)^2}{2c^2} \right] dy = c \sqrt{\frac{\pi}{2}} \text{erf}(1).$$

The final analytical perturbed total pressure is constant, and is given by

$$p_{T1}(\infty) = \int_0^1 p_{T1}^*(x) dx = \int_0^1 \int_0^1 p_1(x, y, 0) dy dx. \quad (3.3.6)$$

Equations (3.3.5) and (3.3.6), together with the background quantities, from which we can calculate the sound and fast magnetoacoustic speeds given in (3.2.58) and (3.2.59), give all the necessary ingredients for obtaining all the equilibrium distributions, within the linear regime.

3.4 Numerical experiments: Results

In this section, we analyse closely the results from one single experiment, for which we have specified the background density and the amplitude of the perturbation as $\rho_0 = 0.1$ and $a = 1.5$, respectively. Hence, the background plasma beta and the ratio \mathcal{P} , for the sample experiment, are

$$\begin{aligned} \beta_0 &= 0.2, \\ \mathcal{P} &= 1. \end{aligned}$$

The fast magnetoacoustic speed for this experiment is given by equation (3.2.59), as $c_f \approx 3.42$, which is about two and a half times larger than the sound speed. For completeness, the value of the Alfvén speed is $c_A \approx 3.16$, which is slightly smaller than the fast speed.

Below, we first have a look to the evolution at the integrated energies of the system: internal energy, kinetic energy and magnetic energy. Then we look at the distributions of plasma pressure, density and current density

for the initial perturbed state and final equilibrium state, and finally we compare the results of the numerical experiments with the results from the linear analysis.

3.4.1 Energetics

We shall first look at the evolution of the energies in the system, to check that the experiment has been carried out successfully. Figures 3.1 and 3.2 show the time evolution of the four energies of the system: kinetic, magnetic, internal and total, integrated over the whole box, using sound wave time units, as the time for a sound wave to get from the perturbation at the center of the box, to the top or bottom boundary, $\tau_s = 0.5/c_s$. We can appreciate the complex pattern of oscillations as a result of an infinite sum of individual modes.

First, as we expect the system to be relaxed at the end of the experiments, the kinetic energy must have dropped to zero. Remember that this energy starts at zero as well, since the initial prescribed velocity is zero everywhere. Thus the kinetic energy grows quickly from zero and then relaxes slowly until it vanishes, showing a series of oscillations which account for the different families of waves that propagate and are damped during the relaxation process.

The system also starts with a certain amount of internal and magnetic energy. These two show the same types of complex oscillations as the kinetic energy, which have to be damped out in the final equilibrium. The contractions and dilatations of the plasma carrying the magnetic field imply that the magnetic field gets stressed at the first timesteps of the dynamical process, before it relaxes back to a different equilibrium state. Hence, the overall magnetic energy is increased during the dynamical relaxation process.

Now, if there are no losses across the boundaries, then the total energy, as a sum of the three energies above, must be conserved in the whole process. Hence, if the value of both the kinetic and magnetic energy rises during the relaxation, then the internal energy must drop. In other words, the energy to drive the relaxation process comes from the enhanced internal energy of the plasma.

Note, that the initial magnetic field is unperturbed, and so, the initial magnetic configuration is the state with minimum magnetic energy. Therefore, the final magnetic energy has to be equal or higher than the initial. Any difference of energy must be taken from the internal energy. At the final equilibrium, the internal energy is reduced by the same amount as the magnetic energy has increased. The higher the amplitude of the initial perturbation, the higher the amount of the transferred energy. Since the perturbations are small, these exchanges of energy have to be so too.

We check that energy conservation is achieved, within numerical error. The exchange of energy (second order effect) from internal to magnetic is of 4×10^{-6} , and the overall losses of total energy are approximately 8×10^{-8} , which is about 0.02 times the non linear effects (amount of exchanged energy). We can then conclude firmly that energy conservation is well behaved for these experiments with LARE, with no significant losses in the magnetic energy during the remap steps, as discussed in Chapter 2.

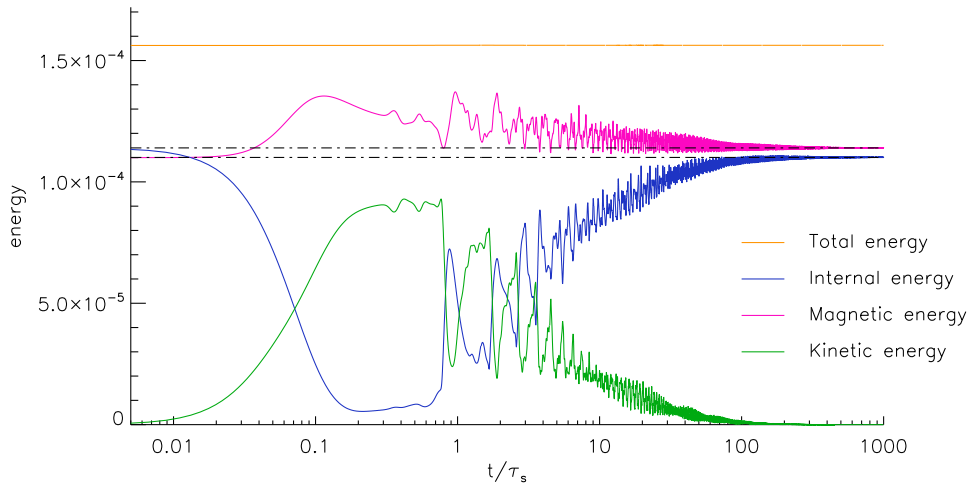


Figure 3.1: Time evolution of the energies of the system, for the experiment with $\rho_0 = 0.1$ and $a = 1.5$, integrated over the whole two-dimensional box. The final losses of internal energy are entirely balanced with a net increase of magnetic energy. The plot is logarithmic in time and covers the whole relaxation. The magnetic, internal and total energy have been shifted on the y -axis by subtracting a given value, but their amplitudes are not scaled. These constants are 0.499890, 0.152242 and 0.652200, respectively.

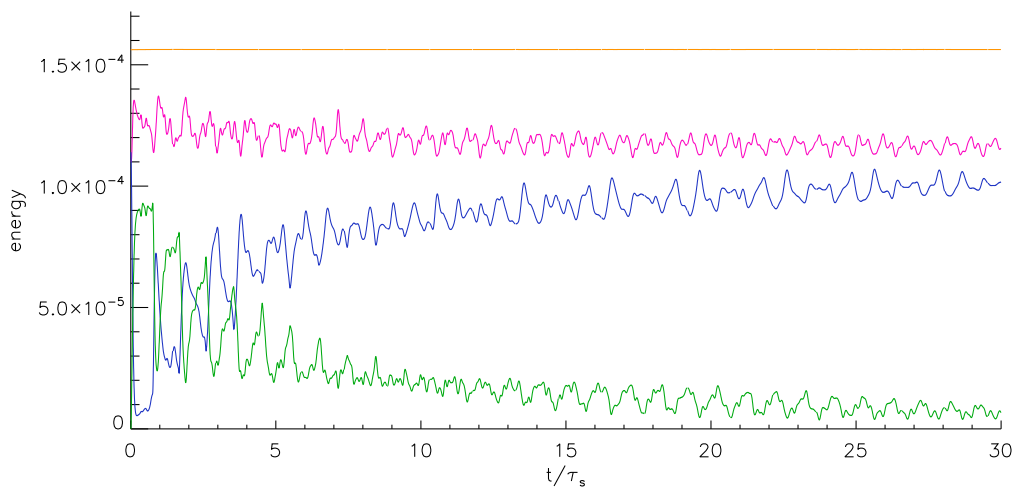


Figure 3.2: Reproduction of Figure 3.1 with a linear axis. It only covers the first part of the relaxation. The complex oscillation periods are a result of the sum of the different plane waves that drive the relaxation.

3.4.2 Equilibrium

At the end of the numerical experiment, the kinetic energy drops to zero and the system has reached an equilibrium. In two dimensions, a double check can be done by evaluating the plasma pressure, p , as a function of the flux function, A_z . At equilibrium, the plasma pressure is constant along field lines, and in 2D, that translates to plasma pressure being a unique function of the flux function, as stated in equation (1.3.8). This is equivalent to $\mathbf{B} \cdot \nabla p = 0$. For this set of experiments, this is satisfied straight forwardly, and no further considerations have to be made.

We now look at the distributions of plasma pressure, density, current density and magnetic field, in the final equilibrium. Figures 3.3, 3.4 and 3.5 show two-dimensional maps of plasma pressure, density and perpendicular current density, respectively, with magnetic field lines overplotted in both the initial and final states. At first sight, we can get the main characteristics of the final equilibrium. There are horizontal gradients on the plasma pressure, and at the same locations, we find current density accumulations. That is, there is an equilibrium and it is non-force-free. Plasma density is not constant along field lines. A deficit in density occurs at the location of the initial pressure perturbation, which is mainly balanced by an increase in the direction of the magnetic field (Figure 3.4b). This is in agreement with the adiabatic condition, $p/\rho^\gamma = \text{constant}$.

Hence, from a qualitative point of view, the numerical results seem to agree with the predictions of the linear analysis made at the beginning of the chapter. Now, the question is how accurate are these predictions, and how far are the numerical results from the linear solutions.

Figures 3.6 and 3.7 show vertical cuts of plasma pressure and density, and horizontal cuts of plasma density, plasma pressure, magnetic field and total pressure, respectively, in the final equilibrium. These are compared with the linear analysis predictions given by equations (3.2.54), (3.2.55), (3.2.56) and (3.3.6), and, in case of the plasma density, we also compare with the solution given by the approximation of adiabaticity, equation (3.2.57), which we have already discussed is probably a better approximation.

We show that the match is almost perfect for the plasma pressure, total pressure and magnetic field, but does not work well for the plasma density. This is not surprising, as *the vertical evolution of the plasma pressure is accurate*, i.e. it is not constrained by the linear analysis, as shown in equation (3.2.51). Hence, the magnitude of the initial perturbation for the plasma pressure that must be taken into account when checking the accuracy of the linear analysis, is the one after the vertical non-magnetic redistribution, which is, of course, much smaller than the original one.

The calculation of the plasma density are determined by the linear approximation all way through, as seen in equation (3.2.52), and hence, the prediction for the density in the final equilibrium cannot be expected to be good. However, if the process is adiabatic, the density can be obtained directly from the final plasma pressure distribution, using equation (3.2.57). In contrast with the linear analysis, this adiabatic approximation does a very good job, as shown in Figures 3.6b and 3.7b. In Figure 3.8 we plot the quantity p/ρ^γ in the final state compared to the initial state, for both the vertical and horizontal cuts. Since the numerical experiments have been performed using a full MHD code that solves the non-linear equations, the process is not entirely adiabatic, but has a finite amount of viscous heating that will become important as the initial perturbation is increased.

3.4.3 Overview

We have been able to predict the distributions of the final equilibrium quantities after a two-dimensional hydromagnetic perturbation over a background homogeneous magnetic field embedded in a plasmas. The linear calculations

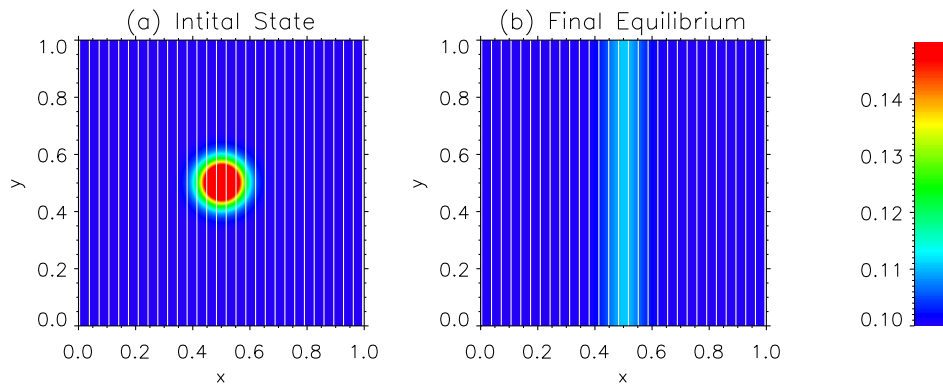


Figure 3.3: Two-dimensional contour plots of plasma pressure in (a) the initial state and (b) the final equilibrium, for the same experiment as in Figure 3.1. White lines are magnetic field lines.

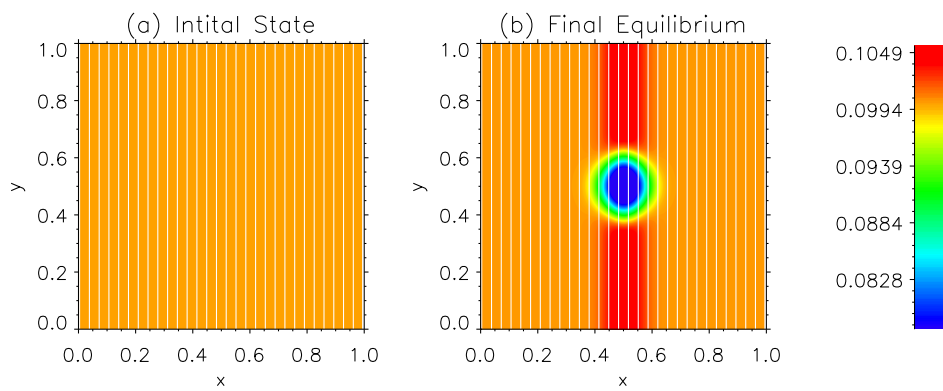


Figure 3.4: As Figure 3.3, with plasma density in (a) the initial state and (b) the final equilibrium.

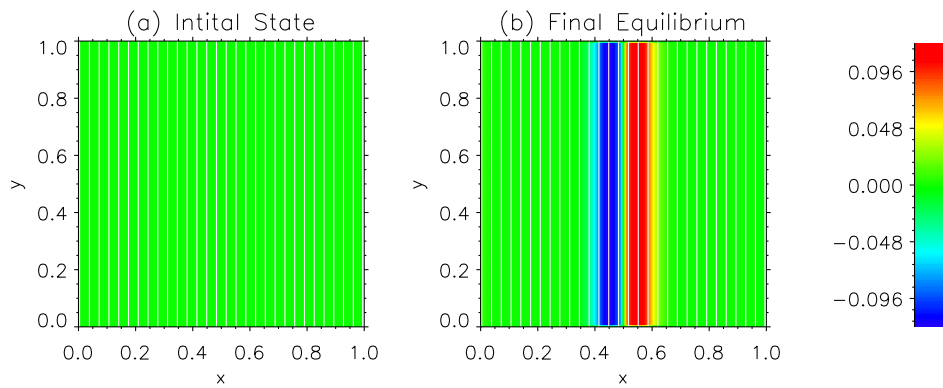


Figure 3.5: As Figure 3.3, with current density in (a) the initial state and (b) the final equilibrium.

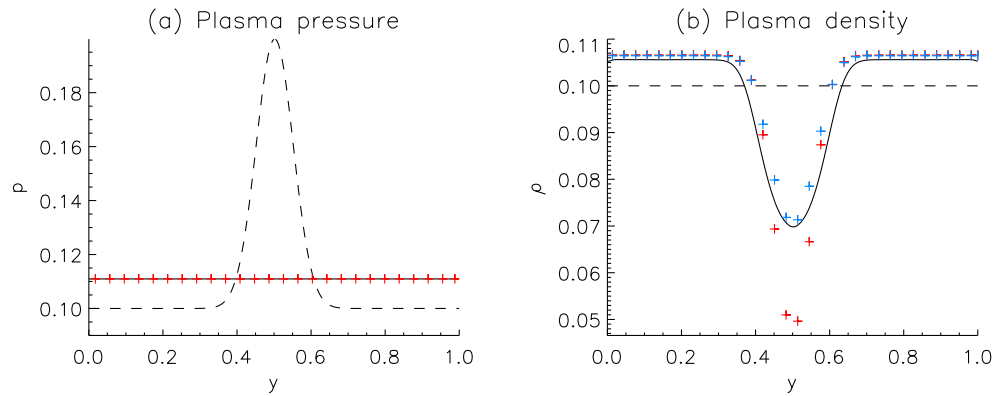


Figure 3.6: Vertical cuts of (a) plasma pressure and (b) plasma density, for the same experiment as in Figure 3.1. Initial perturbed state (dashed) is compared with the final equilibrium, as found by the full MHD numerical simulations (solid) and predicted by the linear analysis (red crosses). For the density predictions, the blue crosses represent the prediction from the adiabatic condition given by equation (3.2.57).

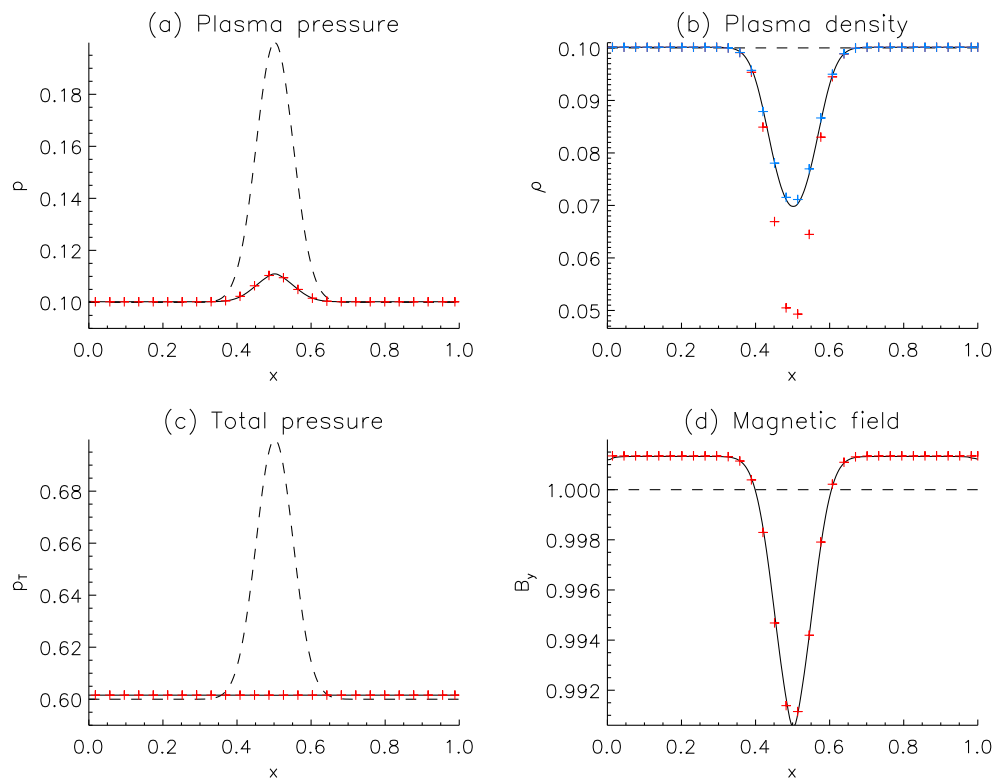


Figure 3.7: Horizontal cuts for (a) plasma pressure, (b) plasma density, (c) total pressure and (d) magnetic field strength, for the same experiment as in Figure 3.1.

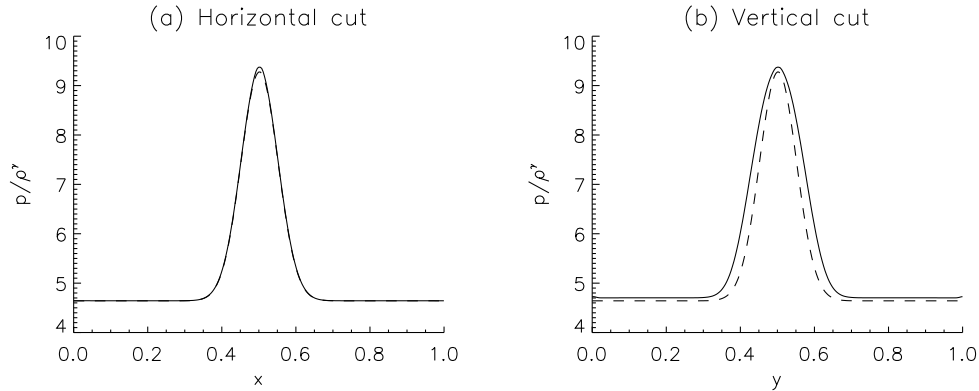


Figure 3.8: Adiabaticity condition for the same numerical experiment as in Figure 3.1. Plots of p/ρ^γ in the initial (dashed) and final (solid) state, for (a) horizontal cut, across the field lines, and (b) vertical cut, along the field lines.

are well behaved for the experiment presented in this section, and are based in the one-dimensional propagations by fast magnetoacoustic waves in the direction across the field, and slow sound waves in the direction along the field lines. Although in reality, the initial disturbance evolves into the final relaxed state through different families of magnetoacoustic waves. There exist an extra contribution of slow magnetoacoustic waves propagates along the magnetic field lines, which introduce a magnetic tension term during the relaxation (i.e. curve the magnetic field as they propagate up and downwards). Nevertheless, these dissipate the magnetic tension in such a way that it is totally unimportant when determining the final equilibrium distributions. The vertical redistribution of the plasma pressure to a homogeneous value demands the magnetic tension to disappear completely, so both the plasma pressure and total pressure are one-dimensional at the end of the relaxation.

Within the linear regime, the final distributions are completely independent of the viscosity, even though it is required to permit the relaxation to occur, as it is the only damping mechanism of the waves. An increase in the viscosity enhances the diffusive term in the wave equation, and so, accelerates the process, but the final distribution is not modified. Second order terms, however, might be dependent on the kinematic viscosity, since the heating term is proportional to it. Within the linear regime, in the final equilibrium, all the quantities are simply determined by the behavior of the final equilibrium total pressure, involving plasma and magnetic effects. Hence, the final equilibrium states for plasma pressure and magnetic field do not differ if the initial perturbation is of the density or internal energy.

Now, we compare the results with experiments in which the initial perturbations are increased systematically, evaluating the validity of the analytical calculations for the total pressure and plasma density in the final equilibrium state, and their departure from the linear and adiabatic regime.

3.5 Importance of non-linear effects

To study how non-linearity affects the results as the magnitude of the initial perturbation increases, we focus again on the total pressure. The total pressure of the final numerical equilibrium must be constant, whether the relaxation remains in the linear regime or not. On the other hand, the analytical definition of total pressure given by (3.2.20) is an approximation from the linear analysis, and will become less valid as the non-linear terms become more important. We perform a series of experiments for various plasma beta values in which the relative amplitude of the initial perturbation is changed from a very small value, well within the linear regime, to a large value way outside it. Using these experiments, we investigate how the final total pressure departs from the linear predictions for different background plasma beta values.

But first, we recall that the equilibrium results after the 2D relaxation may be separated into a vertical non-magnetic evolution (vertical redistribution of plasma pressure) and a horizontal evolution (horizontal redistribution of total pressure), in which the total pressure in the vertical case is *not* constrained by the linear analysis. This suggests that, effectively, in order to find a significant deviation in the final total pressure for the 2D experiment, we will need very large values of the initial two-dimensional perturbation. Hence, the following experiments have been made for just a one-dimensional perturbation *across the field lines*. The ratio of the maximum value of the perturbed plasma pressure to the background plasma pressure, as defined in equation (3.3.4), is

$$\mathcal{P} = \frac{\max(p_1)}{p_0},$$

and may be mapped from the perturbation of the 1D experiments, onto those for our initial 2D perturbation, using

$$\mathcal{P}_{2D} = \left\{ \int \exp \left[-\frac{(y-b)^2}{2c^2} \right] dy \right\}^{-1} \mathcal{P}_{1D}.$$

This is obtained taking into account that the maximum value of the perturbed plasma pressure, for our initial 2D perturbation, is that of the 1D perturbation across the field lines, after the homogeneous non-magnetic redistribution of the plasma pressure along the field lines, given by the integral inside the curly brackets.

Figure 3.9 shows the relative deviation of the linear approximation in both 1D and 2D for the total pressure, as a function of the amplitude of the initial perturbation, for five different values of the plasma beta ($\beta = 0.05$, $\beta = 0.1$, $\beta = 0.2$, $\beta = 1.3$ and $\beta = 2$). The bottom x -axis shows the magnitude of the one-dimensional perturbation, and the top x -axis shows the magnitude of the initial two-dimensional perturbation before its vertical expansion. The deviation on the y -axis is calculated as the maximum difference between the linear prediction and the numerical results for the total pressure,

$$E_{pT} = \frac{\max(|p_T^{lin} - p_T^{num}|)}{p_T^{num}},$$

where p_T^{num} is the final constant total pressure obtained from the numerical simulations, and p_T^{lin} is the linear total pressure calculated from the numerical solutions from the final equilibrium, given by

$$p_T^{lin}(x) = p_0 + p_1(x, \infty) + \frac{B_0^2}{2\mu_0} + \frac{B_0 B_{1y}(x, \infty)}{\mu_0},$$

with $p_1(x, \infty)$ and $B_{1y}(x, \infty)$ being the final plasma pressure and magnetic field from the numerical simulations.

As $\beta \rightarrow \infty$, we expect the relative deviation of the linear analysis to tend to zero, independently of the perturbation, as in this case, the magnetic effects disappear, and the initial pressure perturbation completely redistributes

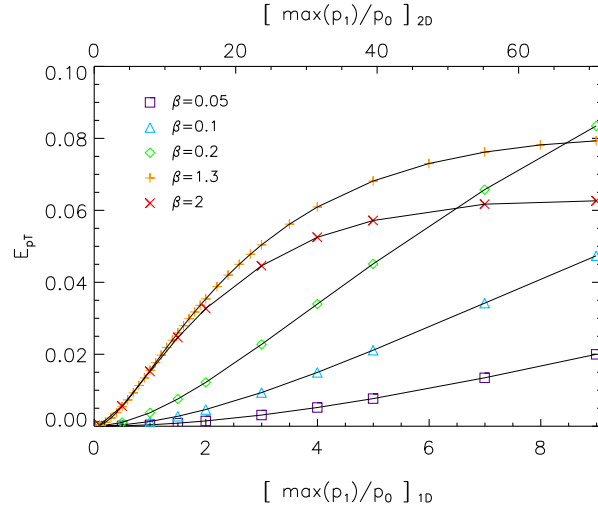


Figure 3.9: Relative deviation in the linear prediction of the total pressure against the magnitude of the initial pressure perturbation (bottom axis is \mathcal{P}_{1D} and top axis is \mathcal{P}_{2D}), for five different values of the plasma beta. The slow growth rate of the deviation (non-linear effects) indicates the validity of the linear analysis.

to a well defined constant value in the whole box. On the other hand, if $\beta \ll 1$, then the magnetic field will dominate over the plasma contributions, and large values for \mathcal{P} will be needed to depart from the linear regime. These two behaviors can be seen in Figure 3.9, where the plots for large plasma-betas tend to a smaller deviation, while the plots for small plasma-betas take longer to reach significant deviations, i.e. to escape from the linear regime. Furthermore, we must not forget that here we are only talking about the initial background plasma beta, so a large background beta combined with a large initial perturbation will make the final plasma beta even higher. Thus, $\mathcal{P} \rightarrow \infty$ will imply $\beta \rightarrow \infty$ for the final equilibrium, so we expect the curves of the relative deviation of the linear analysis to turn back to zero as the initial perturbation is greatly increased. In terms of energy conservation, as the velocity is zero at the initial and final states, the integral over the whole domain of internal energy plus magnetic energy must be conserved: If $\beta \rightarrow \infty$, then the internal energy is much larger than the magnetic energy, and will just redistribute the plasma pressure, without transferring any energy into the magnetic field.

On the contrary, the final plasma density is entirely determined by the linear analysis, in both the vertical and the horizontal directions along and across the field lines, or in a better approximation, by the adiabatic condition. Hence, the non-linear effects for the plasma density will grow much quicker, as shown in Figure 3.10. These last numerical experiments have been made for the original two-dimensional Gaussian perturbation, for three different values of the plasma beta ($\beta = 0.05$, $\beta = 0.2$ and $\beta = 2$). The x -axis shows the magnitude of the initial two-dimensional perturbation, to be compared with the top x -axis in Figure 3.9. The deviation on the y -axis is given by

$$E_\rho = \frac{\max(\rho^{ad} - \rho^{num})}{\rho^{num}},$$

where ρ^{ad} is the plasma density given by equation (3.2.57), and ρ^{num} is the final density obtained with the numerical experiments.

The relative deviation in the plasma density is considerably larger than the relative deviation in pressure, and

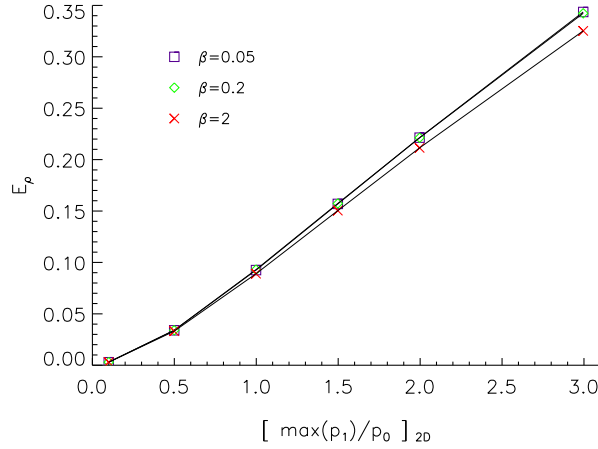


Figure 3.10: Relative deviation of the density predicted assuming an adiabatic evolution, with equation 3.2.57, against the magnitude of the 2D initial pressure perturbation, for three values of the plasma beta. Note, that the x -axis in this plot is to be compared with the top x -axis in Figure 3.9.

so, for only a small change in p_1/p_0 in the 2D case, we find a large deviation in ρ . As this deviation quickly reaches significant values, the plasma beta plays much less of a role for the non-linear effects in the plasma density than in the above total pressure.

The linear predictions remain remarkably valid even outside the linear regime, as the growth rate of the non-ideal effects is very small, compared to the initial perturbations. We next consider the same kind of perturbation in a more realistic three dimensional flux tube, following the same analysis as we have done for the two-dimensional case. The system has cylindrical symmetry, so the qualitative results must be the same as in the 2D case.

3.6 Parallel magnetic fields in 3D

The results above can be easily generalised for a three dimensional system. To do this we follow the same steps as before, with one added coordinate which will be analogous to the previous x . Now the magnetic field is pointing along the z -axis, i.e. $\mathbf{B}_0 = B_0 \hat{e}_z$, and has cylindrical symmetry with respect to the axis at $(x, y) = (0.5, 0.5)$. The results, however, are presented in cartesian coordinates, but that is not restrictive for the derivation of the equations, and for the presentation of the results.

3.6.1 Linear equations

At the beginning of the chapter, we derived the MHD equations for a generic two-dimensional linear hydromagnetic perturbation, which we wrote in coordinates, as in equations (3.2.9) to (3.2.14). This set of equation can be expanded to their equivalent set for a three-dimensional system, where this time, z is the direction of the back-

ground magnetic field,

$$\frac{\partial \rho_1}{\partial t} = -\rho_0 \nabla \cdot \mathbf{v}_1, \quad (3.6.1)$$

$$\rho_0 \frac{\partial v_{1x}}{\partial t} = -\frac{\partial p_1}{\partial x} - B_0 \frac{\partial B_{1z}}{\partial x} + B_0 \frac{\partial B_{1x}}{\partial z} + \rho_0 \nu \left(\nabla^2 v_{1x} + \frac{1}{3} \frac{\partial}{\partial x} (\nabla \cdot \mathbf{v}_1) \right), \quad (3.6.2)$$

$$\rho_0 \frac{\partial v_{1y}}{\partial t} = -\frac{\partial p_1}{\partial y} - B_0 \frac{\partial B_{1z}}{\partial y} + B_0 \frac{\partial B_{1y}}{\partial z} + \rho_0 \nu \left(\nabla^2 v_{1y} + \frac{1}{3} \frac{\partial}{\partial y} (\nabla \cdot \mathbf{v}_1) \right), \quad (3.6.3)$$

$$\rho_0 \frac{\partial v_{1z}}{\partial t} = -\frac{\partial p_1}{\partial z} + \rho_0 \nu \left(\nabla^2 v_{1z} + \frac{1}{3} \frac{\partial}{\partial z} (\nabla \cdot \mathbf{v}_1) \right), \quad (3.6.4)$$

$$\frac{\partial p_1}{\partial t} = -\gamma p_0 \nabla \cdot \mathbf{v}_1, \quad (3.6.5)$$

$$\frac{\partial B_{1x}}{\partial t} = B_0 \frac{\partial v_{1x}}{\partial z}, \quad (3.6.6)$$

$$\frac{\partial B_{1y}}{\partial t} = B_0 \frac{\partial v_{1y}}{\partial z}, \quad (3.6.7)$$

$$\frac{\partial B_{1z}}{\partial t} = -B_0 (\nabla \cdot \mathbf{v}_1)^*, \quad (3.6.8)$$

where $(\nabla \cdot \mathbf{v}_1)^*$ is the two-dimensional divergence of \mathbf{v}_1 , defined as

$$(\nabla \cdot \mathbf{v}_1)^* = \frac{\partial v_{1x}}{\partial x} + \frac{\partial v_{1y}}{\partial y}. \quad (3.6.9)$$

As before, we may divide the process in a vertical one-dimensional evolution, along the field lines, which is non magnetic, and completely equivalent to the evolution described in Section 3.2.2, and a two-dimensional evolution across field lines, which is analogous to the one-dimensional evolution across the field derived in Section 3.2.2, as we show below.

If we consider a perturbation varying with the two coordinates across the field, x and y , the perturbed magnetic field has a non-zero z component, i.e. $\mathbf{B}_1(x, y, t) = B_z(x, y, t)\hat{\mathbf{e}}_z$, and the perturbed velocity may be written as $\mathbf{v}_1(x, y, t) = v_{1x}(x, y, t)\hat{\mathbf{e}}_x + v_{1y}(x, y, t)\hat{\mathbf{e}}_y$. Then we write

$$\frac{\partial \rho_1}{\partial t} = -\rho_0 (\nabla \cdot \mathbf{v}_1)^*, \quad (3.6.10)$$

$$\rho_0 \frac{\partial v_{1x}}{\partial t} = -\frac{\partial p_{T1}}{\partial x} + \rho_0 \nu \left(\nabla^2 v_{1x} + \frac{1}{3} \frac{\partial}{\partial x} (\nabla \cdot \mathbf{v}_1)^* \right), \quad (3.6.11)$$

$$\rho_0 \frac{\partial v_{1y}}{\partial t} = -\frac{\partial p_{T1}}{\partial y} + \rho_0 \nu \left(\nabla^2 v_{1y} + \frac{1}{3} \frac{\partial}{\partial y} (\nabla \cdot \mathbf{v}_1)^* \right), \quad (3.6.12)$$

$$\frac{\partial p_1}{\partial t} = -\gamma p_0 (\nabla \cdot \mathbf{v}_1)^*, \quad (3.6.13)$$

$$\frac{\partial B_{1y}}{\partial t} = -B_0 (\nabla \cdot \mathbf{v}_1)^*. \quad (3.6.14)$$

where $p_{T1} = p_1 + B_0 B_{1z}$ is the perturbed total pressure, whose temporal evolution is given by the combination of equations (3.6.13) and (3.6.14), as

$$\frac{1}{\rho_0} \frac{\partial p_{T1}}{\partial t} = -c_f^2 (\nabla \cdot \mathbf{v}_1)^*, \quad (3.6.15)$$

in analogy with equation (3.2.22). Note, how in this case, the horizontal evolution cannot be treated separately in two one-dimensional evolutions for x and y , precisely because the problem has cylindrical symmetry. One way to approach the problem would be to apply the same one-dimensional evolution as in Section (3.2.1), to a radial coordinate r , and then apply cylindrical symmetry. However, this is not necessary. As seen in previous sections, the final equilibrium is independent of the dynamical evolution, hence, equations (3.6.11) and (3.6.11) are irrelevant for calculating the distribution of the equilibrium, and one just has to substitute the value of $(\nabla \cdot \mathbf{v}_1)^*$ given by equation (3.6.15) into equations (3.6.10), (3.6.13) and (3.6.14), obtaining the exact same set of equations as in (3.2.33), (3.2.34) and (3.2.35), namely,

$$\begin{aligned}\rho_1^{\text{eq}}(x, y) &= \rho_1(x, y, 0) + \frac{1}{c_f^2} [p_{T1}(\infty) - p_{T1}(x, y, 0)] , \\ p_1^{\text{eq}}(x, y) &= p_1(x, y, 0) + \frac{c_s^2}{c_f^2} [p_{T1}(\infty) - p_{T1}(x, y, 0)] , \\ B_{1z}^{\text{eq}}(x, y) &= B_{1z}(x, y, 0) + \frac{B_0}{\rho_0 c_f^2} [p_{T1}(\infty) - p_{T1}(x, y, 0)] .\end{aligned}$$

Now, we can combine these with the vertical non-magnetic evolution of the thermal quantities, adding the constant background quantities, and thus getting the final equilibrium solution, which is in every sense analogous to the previous two-dimensional case.

3.6.2 Numerical experiments

We can check the results for a three-dimensional flux tube with an enhancement in pressure in the center of the tube, which is completely analogous to the previous two-dimensional perturbation, and is defined through a centered Gaussian enhancement in the internal energy, given by

$$\epsilon_1(x, y, z, 0) = a \exp \left[-\frac{(x-b)^2}{2c^2} \right] \exp \left[-\frac{(y-b)^2}{2c^2} \right] \exp \left[-\frac{(z-b)^2}{2c^2} \right] . \quad (3.6.16)$$

The resolution of the three dimensional numerical box is $128 \times 128 \times 64$, the length of the domain is $L_x \times L_y \times L_z = 1 \times 1 \times 1$, and x , y and z all vary from 0 to 1. Boundary conditions are the same as those in the 2D experiments, e.g. the side boundaries are closed and the top and bottom boundaries are periodic. There is no initial perturbation in the magnetic field, nor the plasma density. As before, the initial perturbed total pressure is the initial perturbed plasma pressure, the perturbed total pressure after the vertical evolution, $p_{T1}^*(x, y)$ is the integral of the initial perturbation along z , and so the final constant total pressure is given by

$$p_{T1}(\infty) = \int_0^1 \int_0^1 p_{T1}^*(x, y) dx dy = \int_0^1 \int_0^1 \int_0^1 p_1(x, y, z, 0) dz dx dy . \quad (3.6.17)$$

The initial quantities and parameters of the initial perturbations are defined in the same way as for the experiment discussed in Section 3.4, i.e. $\rho_0 = 0.1$, $\epsilon_0 = 1.5$, $B_0 = 1$, and $a = 1.5$, leaving the values for the background plasma beta and the ratio of the maximum value of the perturbed plasma pressure to the background plasma pressure as $\beta_0 = 0.2$ and $\mathcal{P} = 1$.

In Figure 3.11 we show the evolution of the three energies of the system, plus the total energy. The exchange of energy from internal to magnetic (non linear effects) is about 4×10^{-7} , and the losses of total energy are

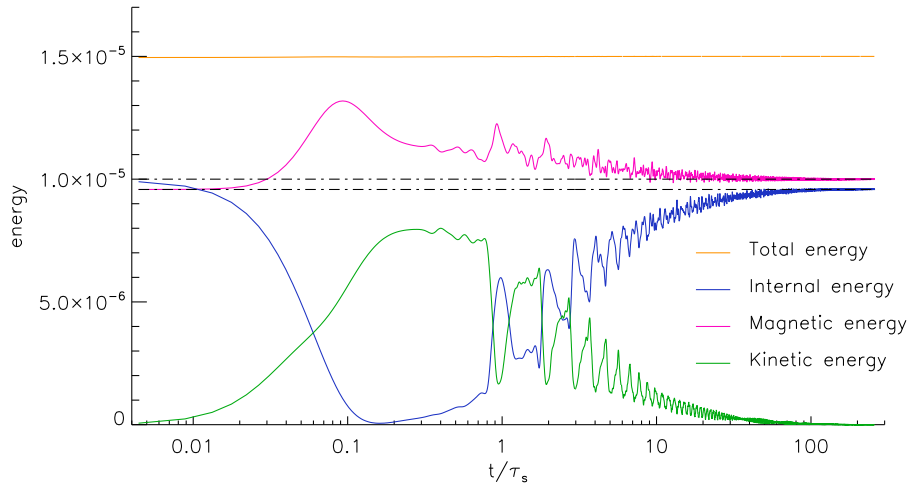


Figure 3.11: Time evolution of the energies of the three-dimensional system, integrated over the whole two-dimensional box, for an experiment with $\rho_0 = 0.1$, $\epsilon_0 = 1.5$, $B_0 = 1$ and $a = 1.5$. The magnetic, internal and total energy have been shifted on the y -axis by subtracting 0.499990, 0.150285 and 0.650280, respectively.

approximately of 4×10^{-8} . As in the two-dimensional experiments, there is no significant change in the total energy of the system.

Figures 3.12 and 3.13 show three-dimensional contour plots of the final equilibrium plasma pressure and density, with a few field lines drawn in grey. The behaviour is very similar to the two-dimensional experiments. As expected, plasma pressure is constant along field lines, and we observe a deficit of the plasma density at the location of the initial pressure perturbation, and an increase along the z direction, in the center of the box. In Figures 3.14 we compare the vertical cuts at $(x = 0.5, y = 0.5)$ through the contour plots in Figures 3.12 and 3.13, for density and plasma pressure with the final equilibrium predicted by the linear analysis. As for the 2D system, the plasma pressure fits well, however, the plasma density does not match the straight forward linear prediction well, but it does match the prediction for density from the adiabatic condition given in equation (3.2.57). Figure 3.15 shows horizontal cuts across the field lines at $(y = 0.5, z = 0.5)$, for density, plasma pressure, total pressure and magnetic field. These are completely analogous to any family of cuts perpendicular to the field lines, through the middle of the box, as the system has cylindrical symmetry. The numerical results are compared with the prediction of the linear analysis, and for the plasma density, with the adiabatic condition, as in Figures 3.6 and 3.7. Again, the match between the numerical experiments and the analytical calculations is fairly accurate.

3.6.3 Overview

In the first few sections of this chapter, we have presented analytical and numerical calculations for the 2D magnetohydrodynamic relaxation of an untwisted perturbed magnetic system embedded in non-zero beta plasmas, which resulted in a final equilibrium state that differs substantially from the initial background configuration. The equilibrium reached is non-force-free in nature. Plasma pressure gradients are balanced by the magnetic forces. For a set of specified boundaries, all the hydromagnetic quantities are fully determined by the initial perturbed state.

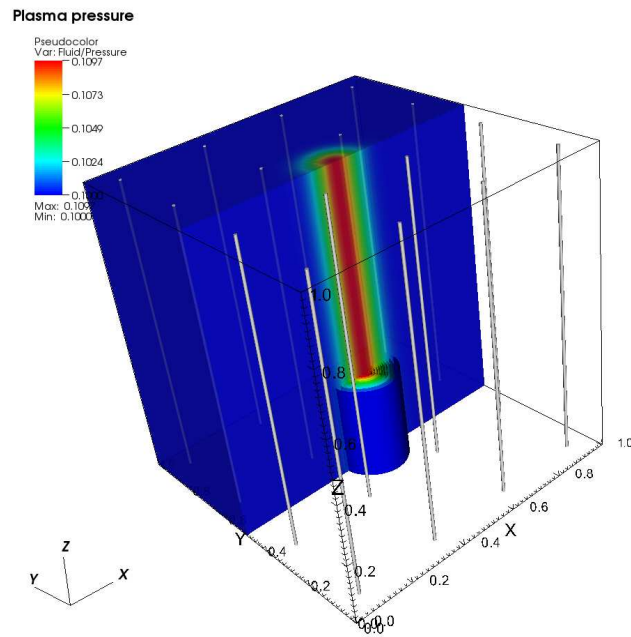


Figure 3.12: Final equilibrium plasma pressure and field lines inside a 3D squared flux tube, for the same experiment as in Figure 3.11.

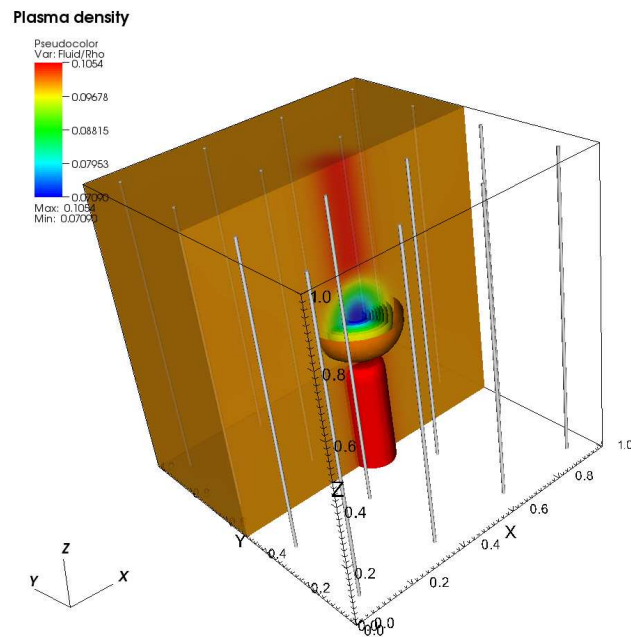


Figure 3.13: Final equilibrium plasma density and field lines inside a 3D squared flux tube, for the same experiment as in Figure 3.11.

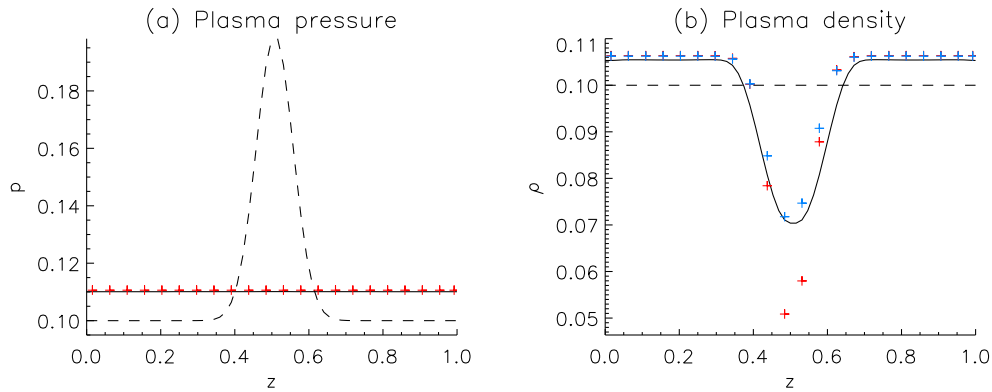


Figure 3.14: Cuts along field lines, through the middle of the box, at $x = 0.5$ and $y = 0.5$, for (a) plasma pressure and (b) plasma density, for the same experiment as in Figure 3.11. Initial perturbed state (dashed) is compared with the final equilibrium, as found by the full MHD numerical simulations (solid) and predicted by the linear analysis (red crosses). For the density predictions, the blue crosses represent predictions from the adiabatic condition given by equation (3.2.57).

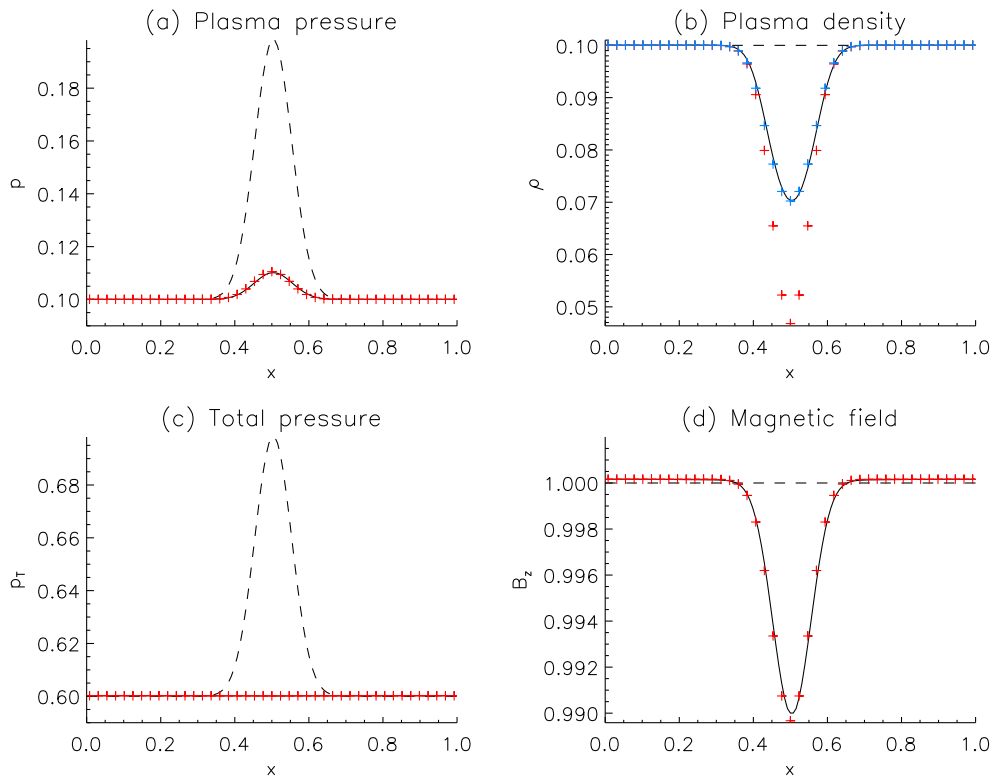


Figure 3.15: Cuts across field lines, parallel to the x -axis, through the middle of the box, at $y = 0.5$ and $z = 0.5$, for (a) plasma pressure, (b) plasma density, (c) total pressure and (d) magnetic field strength, for the same experiment as in Figure 3.11. Note, the experiment is cylindrically symmetric, so any horizontal line through $(0.5, 0.5, 0.5)$ gives the same answer.

The generalization of the problem into three dimensions has been direct, and all the equations have been easily derived from the two-dimensional case. The analytical calculations are analogous, and no further implications need to be taken into account.

The problem raised in this chapter is extremely simple, but also quite instructive in many ways. First, we have approached the problem of non-zero, but finite, beta plasmas, with the most basic experiments, showing their direct implications for equilibrium force balance and energy conversion. Second, we have shown here how a linear approximation to the equations that describe the system may be relevant for a wide range of scenarios, with localised non negligible perturbations of the field and/or the plasma quantities. And third, a comparison between one, two and three dimensional cases has been made directly by approaching the problem in natural steps from the simpler to the more complex scenario.

By comparison of Figures 3.12 and 3.13 to Figures 3.3 and 3.4, we see how the solutions for the two-dimensional case are analogous to cuts of the solutions for the three-dimensional problem in planes parallel to the magnetic field, through the center of the box. The comparison here is trivial, because we are working with the same physical environment.

However, in the coming chapters we analyse equilibria of magnetic null points in two and three dimensions, and the complexity rises enormously. The physics around a two-dimensional null point is different to that around a three-dimensional null. In most cases, one cannot just take a two-dimensional cut of the 3D problem and find the results from the 2D experiments. Nonetheless, having first studied in detail the properties of two-dimensional fields, we might find some interesting similarities.

Chapter 4

Relaxation of 2D Magnetic Null Points

4.1 Introduction

In two-dimensions, magnetic X-points are the locations at which magnetic reconnection can occur, being potential sites for energy conversion. Current sheet formation at these geometries has been widely studied in many astrophysical contexts, both analytically and numerically, but only very recently have a few of these studies taken finite plasma beta effects into consideration, and at the moment, there exists no description of the formation of a non-force-free equilibrium around a two-dimensional X-point.

Two-dimensional reconnection at X-point geometries have been studied for decades, starting with Dungey (1953) and followed up by many (e.g. Parker, 1957; Sweet, 1958; Petschek, 1964; Biskamp, 1986; Priest and Forbes, 1986; Craig, 1994), with direct applications to solar environments such as in the CME's breakout model (Antiochos et al., 1999), which have been applied extensively in the last decade (e.g. Forbes et al., 2006; Zuccarello et al., 2009), and in other interplanetary scenarios such as the reconnection site in the Earth's magnetotail (e.g. Hesse and Schindler, 2001). Also, they have been used in wave propagation experiments involving a zero beta plasma (McLaughlin and Hood, 2004), and a finite beta plasma (McLaughlin and Hood, 2006), finding in both cases that the waves wrap around the null point, causing an exponential build up of current density at the location of the null.

The aim of the present chapter is to provide a valid magnetohydrostatic equilibrium from the collapse of a two-dimensional X-point. Under ideal, non-resistive conditions, the energy bound up in the global magnetic field has to manifest itself as localized accumulations of current density.

It is well known that under the cold plasma approximation (e.g. zero plasma beta), an initially perturbed X-point field relaxes to a potential equilibrium with a Y-type infinitesimally thin current sheet where the current is zero everywhere except within the magnetic tangential discontinuity, where it develops a singularity of the form $j_z = \delta(A_z - A_{z0})$. These potential configurations are described by Green (1965) and Somov and Syrovatskii (1976), as in equations (1.5.1) and (1.5.2). Later, Bungey and Priest (1995) expanded these solutions for potential and force-free fields giving a general expression, equation (1.5.3), for these force-free current sheets. Latter studies have found the formation of localised infinite current layers in the Earth's magnetotail (Birn et al., 2003), relevant for the initiation of the subsequent energy release phase.

First evidence of current sheets extending along the separatrices in sheared magnetic field structures were studied by Zwingmann et al. (1985) for force-free equilibria, where they found mathematical singularities in the current sheet which they interpreted as terms that “would become large in a real physical situation”. Later, Vekstein and Priest (1993) made a mathematical analysis of the magnetic field around cusp-points, after the shearing of a magnetic field with an X-type null point, and suggested an analytical form for the resulting singular current density.

Here, we show how a type of singularity is also formed in the non-force-free case, in agreement with the numerical studies of Rastätter et al. (1994) and Craig and Litvinenko (2005), described in Section 4.3.2. Our numerical results show how the initial X-point collapses to a cusp-like geometry in which the current density accumulates around the neutral point and along the four separatrices. Again, the results agree, in this aspect, with the previous numerical works of non-force-free X-point collapse. However, we attempt to go a step further in the description of the field, by running a series of very high resolution experiments, which allow us to look closer at the current accumulations, in order to resolve them in both length and width, and also to investigate the nature of the singularity as a function of the initial disturbance.

4.2 General properties

4.2.1 Magneto-hydrostatic equilibrium around an X-point

In this section, we revisit the fundamental equations of two-dimensional magneto-hydrostatics around an X-type neutral point. In force balance, the fundamental MHS equation, (1.3.1), must be satisfied, i.e.

$$\mathbf{j} \times \mathbf{B} - \nabla p = 0 ,$$

which, for a two-dimensional field, reduces to the Grad-Shafranov equation, (1.3.11),

$$\frac{dp}{dA_z} = -\frac{1}{\mu_0} \nabla^2 A_z = j_z ,$$

where the flux function A_z , defined by (1.3.9), is constant along field lines. In principle, the Grad-Shafranov condition states that both the plasma pressure and the current density have to be constant along every field line for a two-dimensional equilibrium. Magnetic separatrices are defined as the field lines that separate domains of different magnetic connectivities. For an X-point configuration, there exist four separatrices, coming out from the neutral point, that divide the domain into four regions. Because of the definition of the flux function, A_z , this can be shifted by an arbitrary integration constant, without loss of generality. Hence, it is commonly defined so that $A_z = 0$ at the separatrices, and thus also at the location of the null.

4.2.2 Conservation of total current density

We are now going to show how the symmetry of the system must ensure total current density conservation throughout the dynamical relaxation of our two-dimensional X-point. Using normalised quantities, the time derivative of the integrated current can be expressed as

$$\frac{d}{dt} \int_S \mathbf{j} \cdot d\mathbf{s} = \frac{d}{dt} \int_S \nabla \times \mathbf{B} \cdot d\mathbf{s} ,$$

where S is the whole surface of our experiment and $d\mathbf{s}$ is a vector normal to that surface. We can now apply the *Stokes theorem* for differential geometry to get

$$\frac{d}{dt} \int_S \mathbf{j} \cdot d\mathbf{s} = \frac{d}{dt} \oint_C \mathbf{B} \cdot d\mathbf{l} ,$$

where, now, C is the contour of the boundary of S , and $d\mathbf{l}$ is a vector tangent to C at each point, so that, if we denote B_T as the component of the vector magnetic field tangential to the boundary at each point, we then have

$$\frac{d}{dt} \int_S \mathbf{j} \cdot d\mathbf{s} = \frac{d}{dt} \oint_C B_T dl = 0 . \quad (4.2.1)$$

The properties of symmetry of the system ensure that the expression (4.2.1) equals zero, as the four quadrants of the domain are symmetric, and the integrated tangential magnetic field is zero for each of the boundaries (top, bottom, left and right) separately.

Hence, total current density has to be conserved in the domain. The evolution will allow a redistribution of the initial current density and an accumulation of it at certain locations, but in integral over the whole domain must remain constant.

4.3 Previous work on current singularities in planar magnetic X-points

4.3.1 Analytical studies in force-free fields

Vekstein and Priest (1993) gave an analytical description of a force-free magnetic arcade which included an X-point on it and had been sheared in the ignorable coordinate, B_z . They start from the expression

$$\nabla^2 A_z = -B_z \frac{dB_z}{dA_z} , \quad (4.3.1)$$

which is analogous to the Grad-Shafranov equation, (1.3.11), where the magnetic component $B_z(x, y) = B_z(A_z)$ is specified by the shear of the foot points, $d(A_z)$, as

$$B_z(A_z) = \frac{d(A_z)}{V(A_z)} . \quad (4.3.2)$$

The volume $V(A_z)$ is defined in equation (1.2.7) in Section 1.2.2, as

$$V = \int_L \frac{dl}{B} ,$$

and for two-dimensional fields, is a function of the flux function, as $B = |\nabla A_z|$. Vekstein and Priest (1993) suggested that the initial X-point split into a pair of cusp-points, and considered the solution both inside and outside the cusps. They gave a description of the local field about the cusp using a poloidal flux function $A_z(r, \theta)$, where r is the radial coordinate whose origin is at the beginning of the cusp, and θ is the angular coordinate which is zero at the axis of the current sheet, so that each point on the separatrix is defined by a different pair (r, θ) (see Figure 4.1).

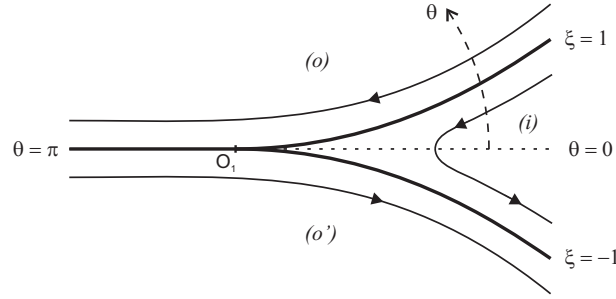


Figure 4.1: Poloidal magnetic field near the cusp O_1 . Based on Vekstein and Priest (1993), Fig. 2. Regions inside and outside the cusp are denoted with (i) and (o).

Inside the cusp, they suggested that for small values of r , the angle along the separatrix grew as $\theta = \pm K r^\beta$ and they wrote the flux function, inside the cusp, as

$$A_z(r, \theta) = r^\alpha f(\xi), \quad (4.3.3)$$

where α is a new parameter, and $\xi = \theta/Kr^\beta$, so that $\xi = \pm 1$ at the separatrices. The function f is chosen so that $f(\pm 1) = 0$, hence, the flux function is zero at the separatrices.

The poloidal field components for the region inside the cusp were found from $A_z(r, \theta)$ to be

$$B_r = \frac{1}{r} \frac{\partial A_z}{\partial \theta} = \frac{r^{\alpha-\beta-1}}{K} f'(\xi),$$

$$B_\theta = -\frac{\partial A_z}{\partial r} = -\alpha r^{\alpha-1} f(\xi) + \beta r^{\alpha-1} f'(\xi) \xi.$$

Here, the expression for B_r demands that $\alpha > 1 + \beta$ for the magnetic field to be finite as $r \rightarrow 0$. From equations (4.3.1) and (4.3.3), one gets the solution

$$\nabla^2 A_z = -m A_z^{-n}, \quad (4.3.4)$$

where $n = (2\beta + 2 - \alpha)/\alpha$ and $f(\xi)$ satisfies the equation $f''(\xi) = -mK^2 f^{-n}$. Now, to obtain a finite value of B_z , the volume of the separatrix field line, given by

$$V(0) = \int_L \frac{dl}{B} = 2 \int_0^R \frac{dr}{|B_r|} = 2K \int_0^R \frac{dr}{r^{\alpha-\beta-1}},$$

has to be finite, and hence, $\alpha - \beta - 1 < 1$. This, together with the previous condition for α leads to

$$1 + \beta < \alpha < 2 + \beta. \quad (4.3.5)$$

The solution outside the cusp was set to a potential poloidal field of the form

$$A_z = B_0 r \sin \theta + B_1 r^p \sin[p(\theta - \pi)]$$

with $p > 1$. This solution satisfies $A_z = 0$ at the separatrices. They then used magnetic pressure balance across separatrices and matched the solutions inside and outside the cusp, finding $\alpha = 1 + \frac{3}{2}\beta$, and

$$n = 1 - \frac{\beta}{1 + \frac{3}{2}\beta}. \quad (4.3.6)$$

4.3.2 Numerical studies in non-force-free fields

Rastätter et al. (1994) considered for the first time the effects of pressure perturbations in numerical experiments on the ideal relaxation of two-dimensional magnetic X-points, and studied the development of current layers with singular current densities in which, in the relaxed state, the initial X-point was replaced by either a T-point or a cusp-point geometry. For the relaxation, they used a frictional code, which damped the kinetic energy out of the system by adding a fictitious relaxing term to the momentum equation of the form $-\kappa\mathbf{v}$, but without any associated heating term in the energy equation. Their X-point relaxed to a singular two-dimensional equilibrium which contained a plasma pressure jump across the separatrices and included current layers extending along the whole separatrices. A key point in their discussion is that they argued that the finite width of their current sheet was due to the finite difference method in their numerical approach rather than being real. They found, nevertheless, the integrated current density over the sheet width (named as surface current) to be constant on each whole separatrix.

One decade later, Craig and Litvinenko (2005) reconsidered the problem of the relaxation of two-dimensional magnetic X-points and the formation of current singularities in non-force-free equilibria. The emphasis of their study lays in the evaluation of the strength of the current singularity at the end of their relaxation, since this may provide a measure of the energy that can be liberated by reconnection. They find that the peak current of the singularity follows a power law relationship to the grid resolution, which appears to be scaled with the plasma pressure. Again, they made use of a frictional code with a fictitious damping term, $-\kappa\mathbf{v}$, added to the momentum equation, but with no heating term in the energy equation, assuming the polytropic model $p \sim \rho^\gamma$, which imposes a condition of adiabaticity to the process. In analogy with the results of Rastätter et al. (1994), they found a distribution of current density extended along the magnetic separatrices, which they claimed to be almost uniform.

They then evaluated the singular behaviour of the null point current density in their relaxed state by comparing the peak current using various numerical resolutions. They presented a logarithmic increase of the peak current with resolution, at the same time as the area of the current layer above a given value for the current showed a logarithmic decrease. Hence, the current layer itself became narrower with higher resolution. Then, they evaluated the scalings of the peak current for different values of the background plasma pressure of the system, finding a weakening of the growth of the peak current density as the plasma pressure was enhanced. That is, a singularity is harder to achieve the higher the value of the plasma pressure, although the presence of a non-zero plasma beta would not prevent a singularity forming. Also, they looked at the collapse of one-dimensional anti-parallel magnetic fields, and demonstrated analytically that a singularity would develop only in the pressureless case. In practice, that means that an approach to the 2D problem through these means is not of any use.

4.3.3 Our approach to the problem

In this chapter, we make a numerical study on the non-force-free relaxation of magnetic X-points, very closely comparable to the work done by Craig and Litvinenko (2005). The first fundamental difference is that we use a full MHD code with a real viscosity term which also adds a heating term to the energy equation. The process is

non-linear and non-adiabatic. Then, we examine in detail the size and characteristics of the current accumulations, both around the null and along the magnetic separatrices, checking that force balance is correctly satisfied in our non-force-free equilibrium. We discuss how the approach given by Craig and Litvinenko (2005) is not valid in our more realistic magnetohydrodynamic evolution. Finally, by following the analytical study of Vekstein and Priest (1993) for sheared magnetic arcades, we try to give a description of the field around the null, which does not exactly match the numerical solution, but provides a mathematical tool to qualitatively study the dependence of the equilibrium on the initial quantities.

4.4 Numerical experiments

4.4.1 Numerical setup

We have run, using the LARE MHD code, a series of two-dimensional experiments on X-point magnetic configurations embedded in non-zero beta plasmas. The initial thermodynamic quantities have constant values, and the disturbance from the equilibrium is given by the magnetic field. In order to create the initial perturbed magnetic field, a current-free hyperbolic X-point, given by $A_z = (x^2 - y^2)/2$, is perturbed by squashing it in the vertical y -direction by a given amount, $(1 - h)$ times the height of the original system, without introducing any initial plasma flow, such that the flux function of the initial state is given by

$$A_z(x, y, 0) = \frac{1}{2} \left(x^2 - \frac{y^2}{h^2} \right). \quad (4.4.1)$$

The squashing creates a uniform non-zero current density whose z -component is

$$j_z(x, y, 0) = \frac{1}{h^2} - 1. \quad (4.4.2)$$

The initial plasma pressure, p_0 , density, ρ_0 , and current density, j_0 , are set to be constant everywhere. The size of the domain is $1 \times h$, with x varying from -0.5 to 0.5 and y varying from $-0.5h$ to $0.5h$. The grid is uniform and has a resolution of 1024×2048 . The particularly high resolution in the y -direction is chosen to permit any current layer that may form to be as thin as possible, but still resolvable across its width.

We choose the four boundaries of the domain to be closed. Magnetic field lines are line-tied, and all components of the velocity are set to zero on the boundaries. The other quantities have their derivatives perpendicular to each of the boundaries set to zero, following the specification of closed boundaries given in Chapter 3. Quantities that should be conserved over the whole domain are total energy, total current density and total mass. Since the process is ideal (there is no diffusion to within the numerical limits), the field is frozen to the plasma, and mass in a single flux tube (or along a field line) must be conserved.

We have run a number of experiments with various heights, $h = 0.1, 0.8, 0.7, 0.6$, with the subsequent initial current densities, $j_0 = 0.23, 0.56, 1.04, 1.78$, and various initial plasma pressures, from $p_0 = 0.125$ to $p_0 = 1$. The values for the plasma pressure are varied by changes in the plasma density, through $p_0 = \rho_0 \epsilon_0 (\gamma - 1)$, maintaining the initial value of the internal energy the same for all the experiments, at $\epsilon_0 = 0.75$. In all the experiments, the real viscosity is set to $\nu_r = 0.001$, and both shock viscosities are set to *zero*.

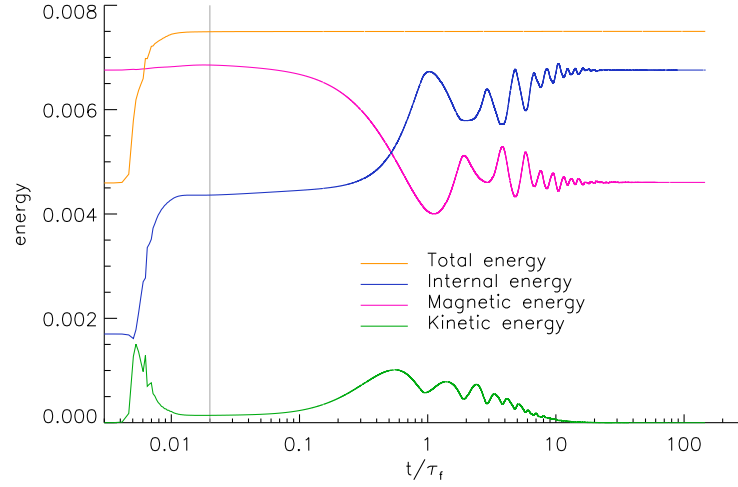


Figure 4.2: Time evolution of the energies of the system, integrated over the whole two-dimensional box, for the sample experiment with $j_0 = 1.04$ and $p_0 = 0.375$. The plot is logarithmic in time. The magnetic, internal and total energies have been shifted on the y -axis by subtracting the constant values 0.08, 0.39 and 0.48 respectively, but their amplitudes are not to scale.

4.4.2 Energetics

For the first part of our study, we center our attention in one sample experiment with $h = 0.7$, $j_0 = 1.04$ and $p_0 = 0.375$. When we look at the energy evolutions in the X-point experiment, we find an undesirable phenomenon at the very first time steps of the simulation, which is purely numerical. Figure 4.2 shows the time evolution of kinetic, magnetic, internal and total energies integrated over the whole box for that sample experiment. The time axis is normalised to the fast magnetoacoustic time, defined as the time for a fast wave starting from the left or right boundary to reach the location of the null point, $\tau_f = 0.5/c_f$.

Within the first time steps of the numerical simulation, a sudden increase of the kinetic energy occur. This is not physical, as it is not balanced with any other component of the energy. In fact, the total energy increases drastically. Soon after, this sudden perturbation disappears, dropping the kinetic energy and provoking a non-physical rise of the internal energy which also makes the total energy increase. After a short time, the relaxation continues normally and energy conservation is satisfied.

This behavior varies if we change the shock viscosity parameters, but we are not able to make it disappear. It might then be due to the sudden creation of a shock when the relaxation process starts, and we find it to have its origins at the boundaries of the system. Everywhere else in the domain, the quantities remain unperturbed. We check that the plasma pressure and current density in the rest of the domain at time = 0.006 are perfectly constant, and their values have changed from the initial prescribed ones by 1×10^{-5} . Furthermore, these do not seem to affect the final equilibrium state about the null, so it is not given any more importance throughout the chapter, and we consider the experiment from the time at which the total energy remains constant.

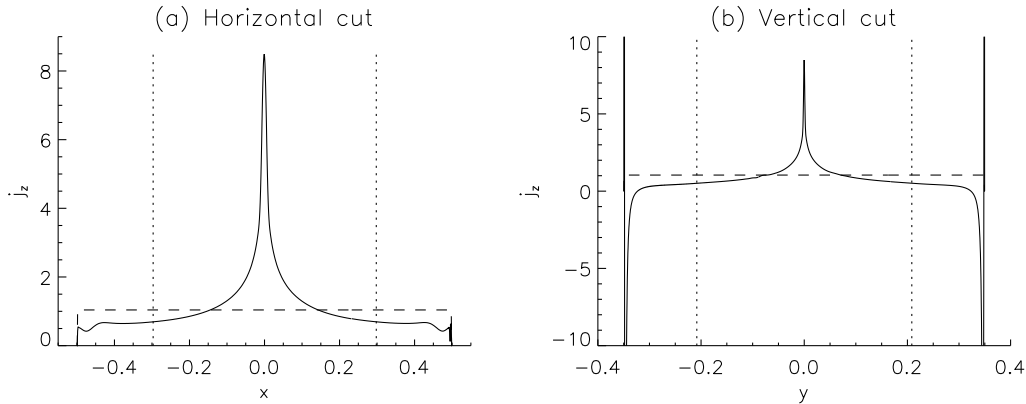


Figure 4.3: Plots of current density for (a) a horizontal cut at $y = 0$ and (b) a vertical cut at $x = 0$. We show initial (dashed) and final (solid) current density. In dotted lines, the boundaries of a subdomain where the integrated current in the final state equals the value in the initial state.

4.4.3 Final equilibrium

In order to proceed with the analysis, we first focus on the sample experiment of Figure 4.2 and then discuss how the results vary as the squash h , and initial plasma pressure p_0 are varied. In our sample experiment, the height of the box is $h = 0.7$, and the initial pressure is $p_0 = 0.375$.

Let's first have a look at a pair of cuts of the current density at $y = 0$ (horizontal cut) and $x = 0$ (vertical cut), as shown in Figure 4.3. It is clear that there exist some boundary effects at the four edges of the box. These are non-physical, and a direct consequence of them is to break some of the conservation laws, so, for example, the total current density of our simulations is not conserved. However, there is no evidence that these effects modify the field around the null point, hence, our way to deal with the problem is fairly simplistic. We can always find a subdomain in which the integrated current in the final state equals the value at the initial state and so we only consider this subdomain for each experiment. From this point, we will show results from inside this subdomain. The upper, bottom and left, right boundaries of this subdomain are overplotted in Figure 4.3. The size of the subdomain for the sample experiment is about 0.60×0.42 .

In Figures 4.4 and 4.5, we show two-dimensional contour plots and surface plots of the plasma pressure and electric current density, respectively, in the final state. At first sight, the results of Craig and Litvinenko (2005) appear to be faithfully reproduced by our numerical experiments. Departing from an initial state containing an X-point with uniform pressure and current density, we get an equilibrium where the X-point has produced a thick current layer from which arms of enhanced current extend along the curved separatrices (Figure 4.5). The separatrices form cusp shapes at the two ends of the current layer. The plasma pressure is enhanced within the cusps (to the left and right of the current layer), and decreased in the regions outside the cusp, above and below the current layer (Figure 4.4). Plasma pressure appears to be constant along field lines (see latter for a further discussion). However, although the electric current density is constant along most of the field lines, it is clearly not constant along the separatrices.

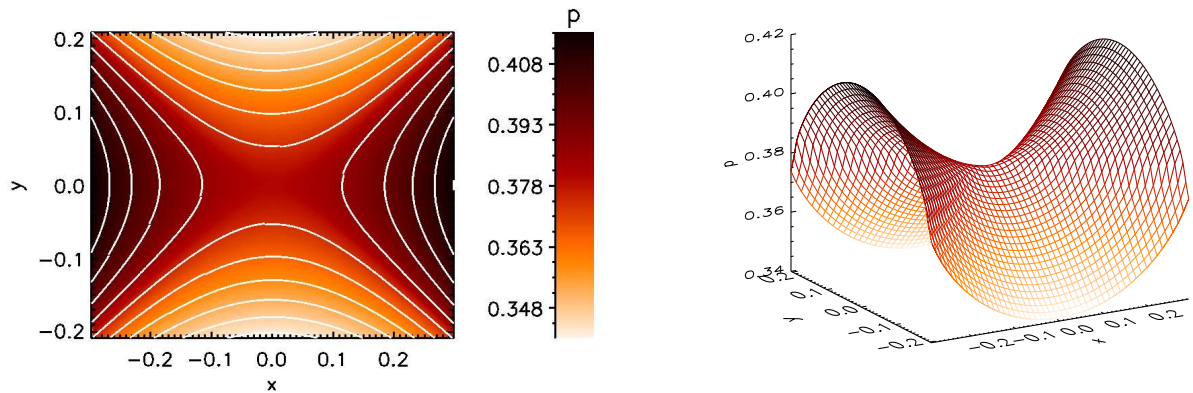


Figure 4.4: Two-dimensional contour plot (left) and surface (right) of plasma pressure for the final equilibrium state for the sample experiment with $h = 0.7$ and $p_0 = 0.375$. White solid lines on the left graph are the magnetic field lines as contours of the flux function A_z .

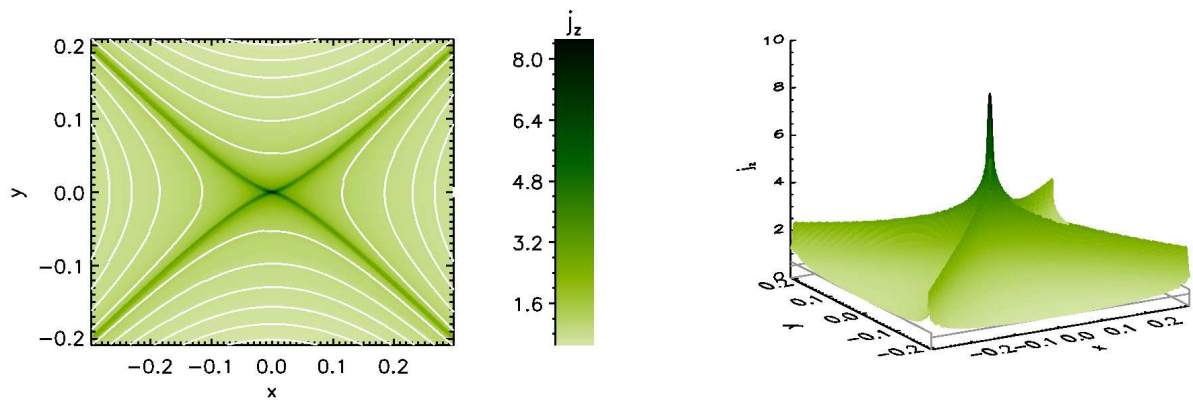


Figure 4.5: Two-dimensional contour plot (left) and surface (right) of current density for the final equilibrium state, for the same experiment as that shown in Figure 4.4. White solid lines on the left graph are the magnetic field lines as contours of the flux function A_z .

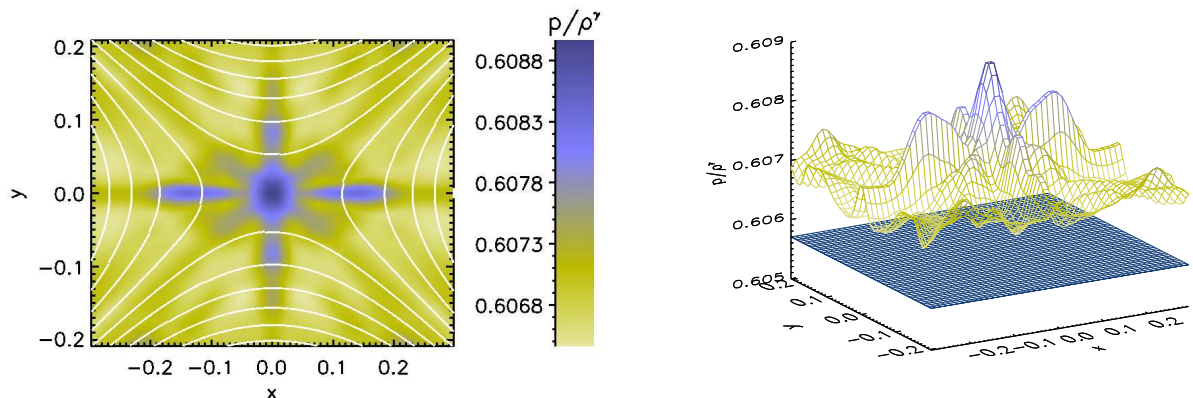


Figure 4.6: Two-dimensional contour plot (left) and surface (right) of p/ρ^γ for the final equilibrium state, for the same experiment as that shown in Figure 4.4. White solid lines on the left graph are the magnetic field lines as contours of the flux function A_z . The constant value in blue below the surface in the right corresponds to the initial value, $p_0/\rho_0^\gamma = 0.6057$.

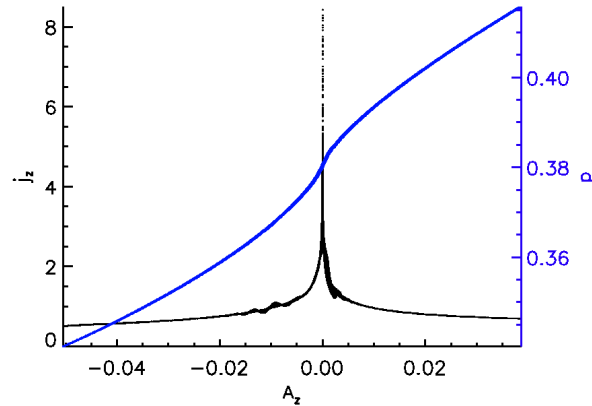


Figure 4.7: Test of the Grad-Shafranov condition for the magnetohydrostatic equilibrium for the sample experiment. Current density (black, y -axis on the left) and plasma pressure (blue, y -axis on the right) are plotted against the flux function A_z , for every single point in the numerical domain. Positive values of A_z refer to inside of the cusp, while negative A_z are outside the cusp.

Figure 4.6 shows two dimensional contour and surface plots of p/ρ^γ , which is proportional to the entropy. Note, that the process is nowhere near to being adiabatic, since this quantity is constant in the initial state, with the value $p_0/\rho_0^\gamma = 0.6057$. Now, everywhere in the final state has an increased entropy, with the greatest increase around the null point and directly above/below and to the left/right of the null. These regions of highest entropy mark the locations where most viscous dissipation occurs. A consequence of these localised increases of entropy is that, while plasma pressure is constant along field lines, density is not. Overall it is clear that the creation of a current layer cannot be achieved physically without some loss of magnetic energy which leads to a localised heating about the null rising the internal energy of the system.

Our relaxation process involves a heating term in the energy equation, responsible for the transfer of part of the magnetic energy in the system into internal energy. This effect is studied in detail in Chapter 3, and marks a difference with the results of Craig and Litvinenko (2005). The consequences of the non-adiabatic effects appear in our final results: Plasma pressure is constant along field lines, but density is not.

A direct check on the validity of our equilibrium may be done by testing the behaviour of the pressure p with respect to the flux function A_z , and also the consequences of the Grad-Shafranov condition, (1.3.11), which states that the current density j_z must be also a unique function of A_z . In Figure 4.7, we represent *every single point* of the two-dimensional domain (within the subdomain where j_z is conserved), for the plasma pressure and the current density against the flux function. Remember, that the current density is the derivative of the plasma pressure with respect to the flux function. It appears clear from this graph that the pressure is a unique function of A_z , and so is most of the the current density distribution. The biggest dispersion occurs when we approach $A_z = 0$, which is the value on the separatrices, and at the X-point. Here, we can see the first sign of the field trying to reach a singularity, which, from the Grad-Shafranov equation, implies an infinite derivative of the pressure with respect to A_z .

In order to check that the separatrices are in equilibrium, with the pressure gradient being able to hold a current accumulation along them, we look at the force balance across the separatrices. Figure 4.8 shows a contour plot of current density for the top-right quadrant with color-coded cuts perpendicular to the separatrix, and in Figure 4.9,

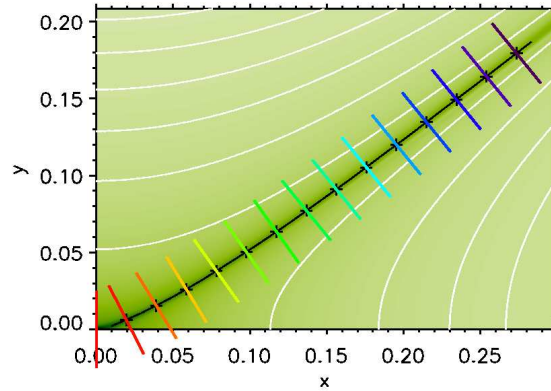


Figure 4.8: Contour plot of current density for the top-right quadrant showing the locations of cuts across a separatrix, which is used to check force balance.

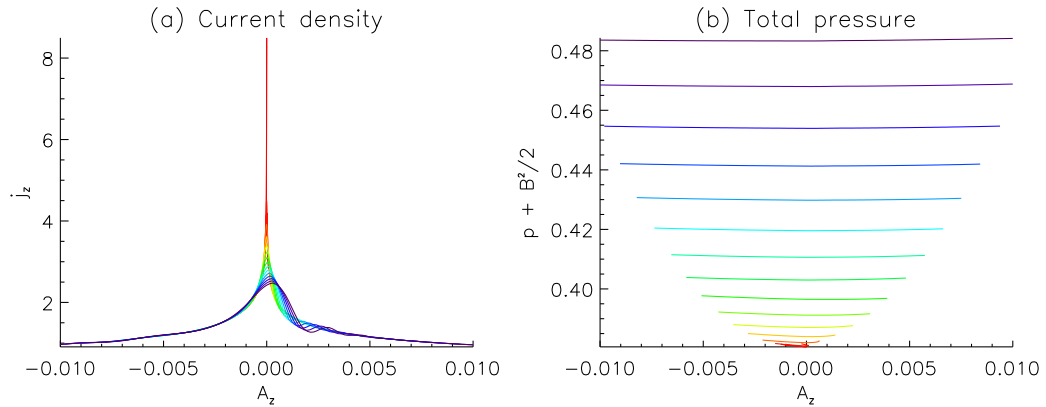


Figure 4.9: Cuts of current density (left) and total pressure (right) across the top-right separatrix, against the flux function A_z for our sample experiment. The colors follow the code in Figure 4.8. Note, the further the cut is from the X-point, the wider the range of A_z covered by the perpendicular cut.

the current density and the total pressure along these perpendicular cuts are plotted against A_z . From Figure 4.9a, we can see clearer how the current density is constant along field lines everywhere except at the regions about the separatrices. Along the separatrices the current clearly increases as they head towards the null point. Figure 4.9b shows that there is total pressure balance across the separatrices. That is, the gradients of plasma pressure are well balanced by the magnetic pressure force, hence, the system appears to be in force balance everywhere, save at the null.

Plasma pressure is constant along the separatrices, but current density is not, as shown in Figure 4.10a. A magnetic separatrix represents an inflection line in the plasma pressure surface, and the Grad-Shafranov equation, i.e. $dp/dA_z = j_z$, does not hold there. However, the surface current, I_s , defined as the integral of the current density, j_z , across the separatrix at a given position, over the width of the current layer, remains constant on the

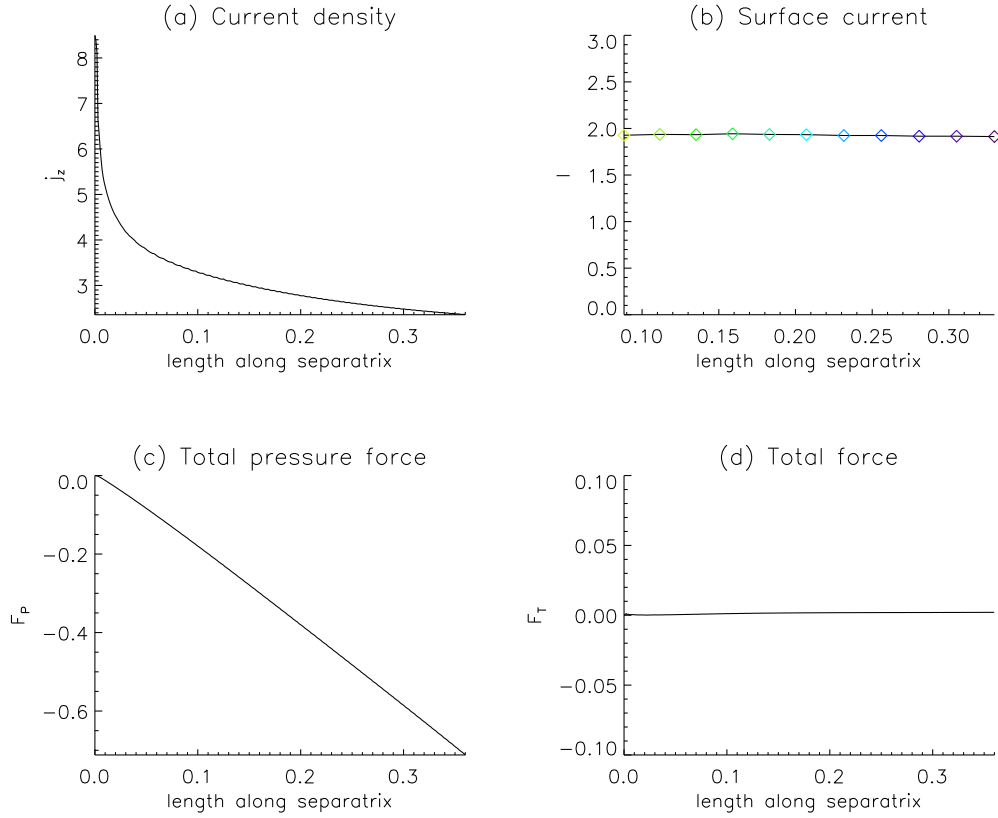


Figure 4.10: Plots of (a) current density, (b) surface current, (c) total magnetic pressure and (d) total pressure, along the top right separatrix.

whole separatrix. This can be seen in Figure 4.10b, where each colour symbol represents the integral

$$I_s = \int_{-0.002}^{0.002} j_z(A_z)_{\text{across}} dA_z, \quad (4.4.3)$$

for the cuts in Figure 4.8. Note, that the integral in equation (4.4.3) is done over the flux function, so the width of the current layer is assumed to be in between the two same field lines for every point, and hence, it is smaller as we move along the separatrix away from the X-point. The missing points in the plot are the null point, which is singular, and other points near the null whose current layer widths overlap with the separatrix below.

We define the total pressure force and the total force along a separatrix as

$$F_P = -\frac{d}{ds} \left(p + \frac{B^2}{2} \right),$$

$$F_T = |\mathbf{j} \times \mathbf{B} - \nabla p|,$$

where s indicates the path along the separatrix. Since the plasma pressure is constant along the separatrices, the total pressure force, F_P , is equivalent to the magnetic pressure force. This force is negative (Figure 4.10c), so it

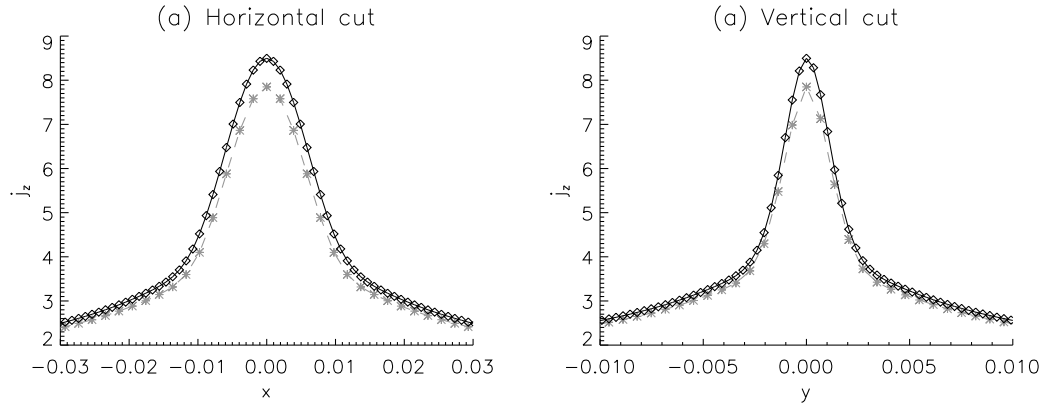


Figure 4.11: Electric current density across the width and along the length of the central current layer, for the same experiment with $h = 0.7$ and $p_0 = 0.375$. Results from the high resolution run (black diamonds) are compared with the results of a half-resolution run (grey stars).

pushes the plasma towards the null point, but it is completely balanced by the magnetic tension force, so the total force is zero also along the separatrixes (Figure 4.10d).

4.4.4 Current density layer

We now look closely at the dimensions of the current layer of the sample experiment and evaluate the nature of its finite width. Figure 4.11 shows cuts along the length (horizontal cut) and width (vertical cut) of the current layer at the location of the null, showing a length and width of the current layer which are respectively of around 23 and 15 points (around 0.02 and 0.005 length units). These may indicate that the current layer really has finite dimensions and are not a result of the resolution of the numerical experiment, as suggested in Rastätter et al. (1994). In order to check this, in Figure 4.11 we overplot the results from the same experiment, run with a resolution of 512×1024 (half the original resolution). As can be seen, the dimensions of the current layer coincide for both experiments, i.e. the finite width of the current layer is not a resolution effect, but a real characteristic of the equilibrium. These results contradict the ones from Craig and Litvinenko (2005), for which the dimensions of the current layer are decreased when increasing the resolution.

In Figure 4.12, we show vertical cuts of the current density across the central current layer, for six different experiments with the same squashing, $h = 0.7$, but with different initial pressures. The width of the central layer decreases for smaller plasma pressures, but remains finite. In Figure 4.13, we show horizontal cuts of the current density along the central current layer, for the same cases as in Figure 4.12. As the pressure is decreased, the length of the central current layer extends further, and the current density becomes more concentrated, developing a higher peak. The same behaviour is observed if the initial plasma pressure is held fixed, and the height of the box is systematically decreased (i.e. the squashing is increased). This means that decreasing the initial plasma pressure has a similar effect as increasing the initial current density, as the action of both is to make the Lorentz force dominate over the pressure force.

When the initial plasma pressure is small (e.g. in Figure 4.13f), the current layer has a length that is many times longer than its width. We consider whether the current layer is approaching the form found in Green's current sheet

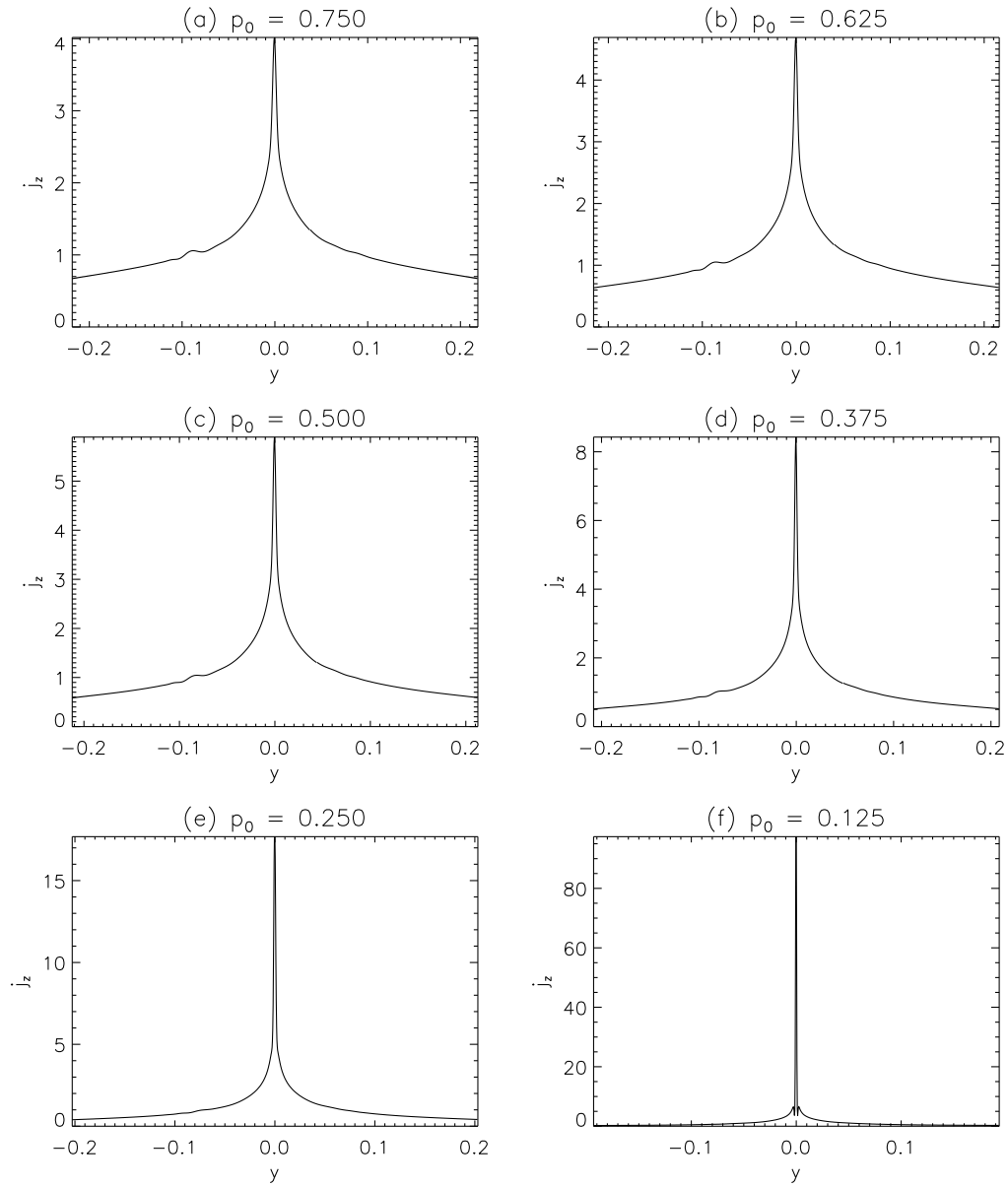


Figure 4.12: Plots of electric current density across the width of the central current layer, for six different experiments, with $h = 0.7$, but different initial plasma pressures.

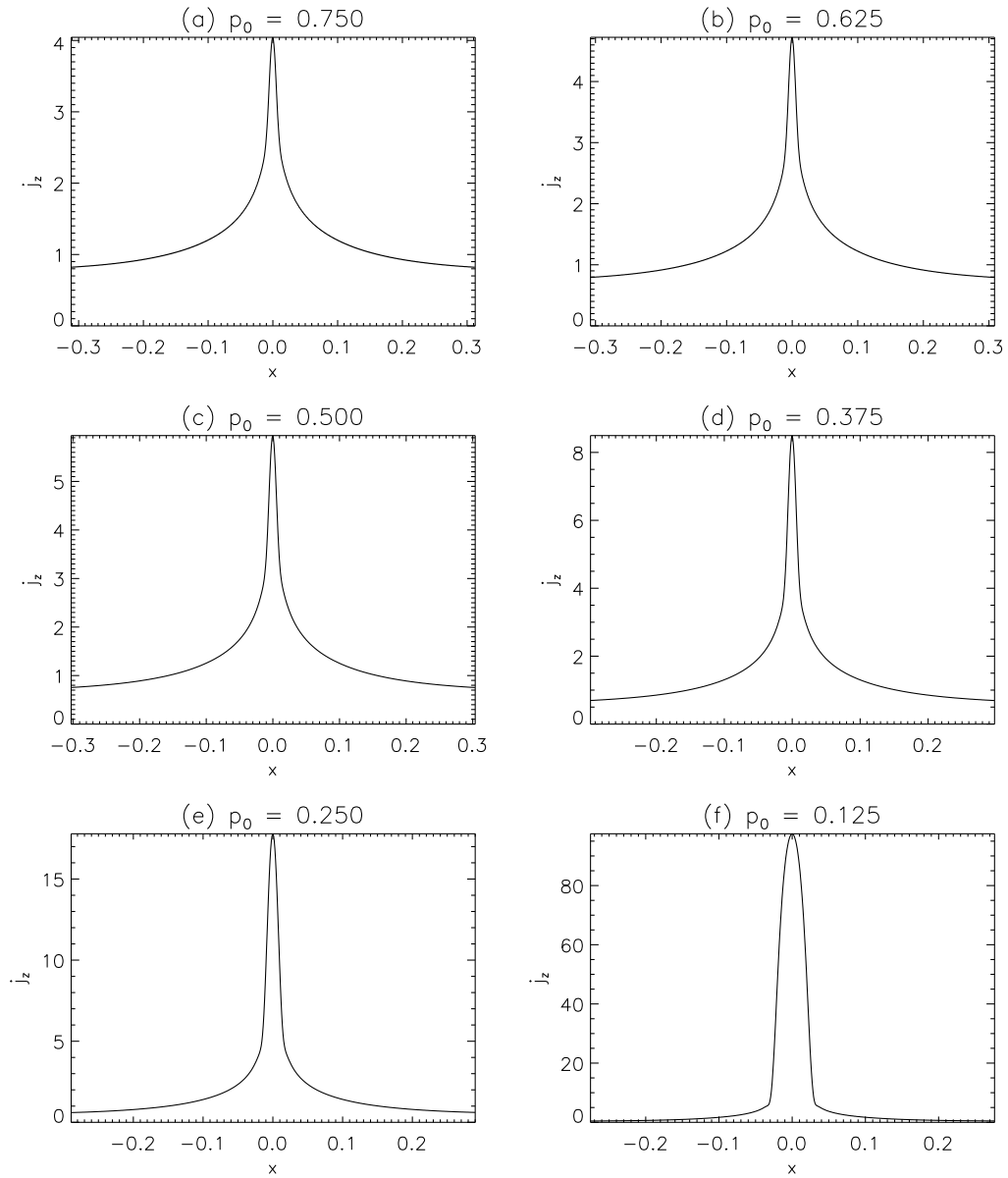


Figure 4.13: Plots of electric current density along the length of the main current sheet, for six different experiments, with $h = 0.7$, but with different initial plasma pressures.

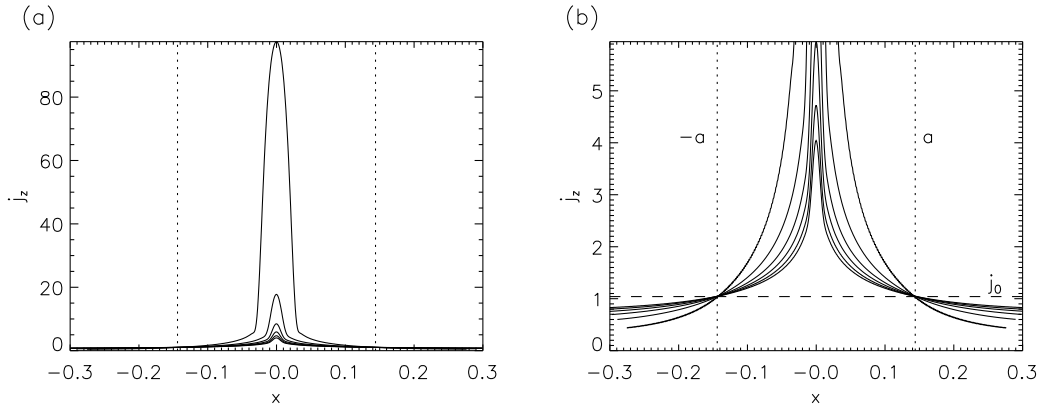


Figure 4.14: The six plots in Figure 4.13 are overplotted for comparison. The dimensions of the Green's potential solution are given in dotted lines. Figure (b) is a zoom of (a) over a smaller range of current densities. In (b), the initial current density is overplotted (dashed).

solution. This is checked by comparing these plots with the correspondant length of the Green's current sheet (Figure 4.14).

To derive Green's expression, complex variable notation is used to simplify the discontinuity in the magnetic field as cuts in the complex plane, $Z = x + iy$. The magnetic field around a potential current sheet is described as

$$B_y + iB_x = \sqrt{Z^2 - a^2} = \sqrt{x^2 - y^2 + 2ixy - a^2},$$

where $2a$ is the length of the current sheet. Following the derivations in Bungey and Priest (1995), the analytical profile of the current density along Green's potential thin current sheet is given by the magnetic field discontinuity as $j_z = 2B_x(x, y = 0)$, and can be calculated from the expression above as

$$j_z = 2B_x(x, y = 0) = 2\sqrt{a^2 - x^2}. \quad (4.4.4)$$

Integrating equation (4.4.4) along the length of the sheet, we get the total current in the sheet, as

$$j_T = a^2\pi. \quad (4.4.5)$$

Now, current density conservation implies that the Green's sheet associated with our equilibrium distribution should have a total current density equal to the total current density in the initial field, hence, the half-length of Green's current sheet is directly related to the initial constant current distribution. Looking at the results in Bungey and Priest (1995), it can be seen that our normalization requires a factor of $1/4$ in front of this length, hence, obtaining

$$a = \frac{1}{4}\sqrt{\frac{j_0}{\pi}}, \quad (4.4.6)$$

which for our sample experiment gives the value $a \approx 0.144$. Note, that equation (4.4.4) represents a singular current sheet containing the whole current in the domain, so in a hypothetical case of a numerical Green's state,

this would have to be compared with the integrated current density over the width of one resolution element. What we do for our experiments is compare our distributions with the length a .

In Figure 4.14, the six horizontal cuts of Figure 4.13 are overplotted, and the dimensions of Green's potential solution are marked. All the curves cross at the same points on x and y , namely $(\pm a, j_0)$, corresponding to the initial value of the current density in y , and the two ends of Green's current sheet in x . The main conclusion that may be extracted from these plots is that the field is in all cases very far from the potential solution, although the fact that all curves cross at the ends of Green's potential sheet seems to imply that Green's solution might be achieved (as far as we can get with the resolution) in the limit $p_0 \rightarrow 0$.

Following a systematic study, we find that the dependence of the equilibrium distributions with the initial quantities differs from one experiment to another, and is therefore determined by the initial plasma pressure and current density of the system. This is studied in detail in Section 4.5.

4.4.5 Singular current

In Section 4.4.3, we evaluated the plasma pressure and current density of the final state. We now check whether the current accumulation at the location of the null is held in a true equilibrium by evaluating force balance along and across the current layer. Figure 4.15 shows plots of the different forces along and across the current layer, namely, plasma pressure force, $-\nabla p$, magnetic force, $\mathbf{j} \times \mathbf{B}$, and total force, $\mathbf{j} \times \mathbf{B} - \nabla p$. At first sight (Figure 4.15a and b), the forces seem to be balanced, and the field seems to be in equilibrium. However, when we look closely about the origin (Figure 4.15c and d), there is a residual non-zero total force which appears to be trying to stretch the null in the horizontal direction, pushing from the top and bottom, and pulling from the sides. These forces could either be a result of a small amount of reconnection due to numerical diffusion, or may be the result of the current sheet trying to tend towards a singularity. If the cause is reconnection, then the amplitude of the forces at the same time of the relaxation should increase as the grid-cell size is reduced. If on the other hand, the forces are a result of the system attempting to form a singularity, they will decrease as the grid-cell size is decreased.

We have run the same sample experiment with $h = 0.7$ and $p_0 = 0.375$ for three different resolutions, namely 256×512 , 512×1024 and 1024×2048 . In Figure 4.16, we show those residual forces for the same experiment after the same time has elapsed. The amplitude of the forces is higher the better the resolution is, implying that the field is trying to converge to a singularity, and the higher the resolution, the closer the field is to achieving the singularity, and so, the bigger the forces around the current layer are. Note, that the length over which these forces extend is roughly the same for the three resolutions.

Furthermore, the peak current appears to be slowly increasing in time, even when the velocities are essentially zero everywhere in the domain (Figure 4.17). This is the last evidence of a singularity being formed, and, again, represents a difference with the work in Craig and Litvinenko (2005), in which they present scaling laws for the peak current, which for our experiments, is not well defined.

4.4.6 Overview

We have presented evidence that the field has achieved an equilibrium everywhere save at the null point, where the field is trying to converge to a singularity which is different in nature to the ones found by others in the force-free cases when using relaxation codes as opposed to a full MHD code. However, this state is impossible to reach numerically, because of the resolution constraint. Nonetheless, the forces are sufficiently small for us to consider

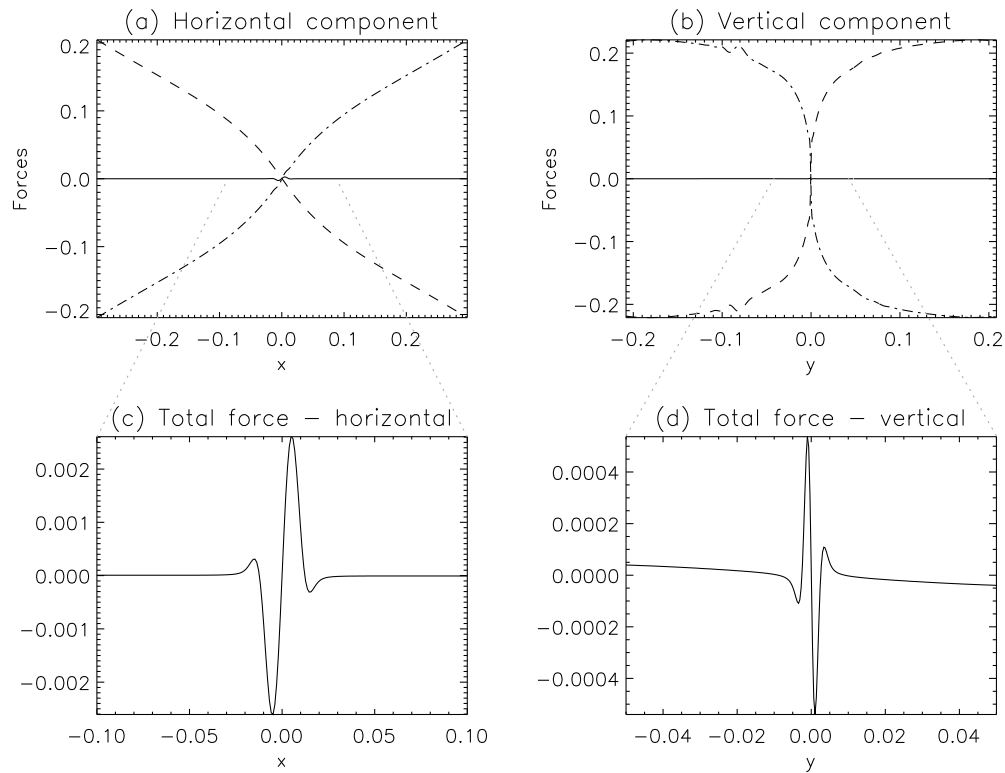


Figure 4.15: Pressure gradient force (dashed), magnetic Lorentz force (dashed-dot) and total force (solid), along (a) horizontal and (b) vertical cuts through the X-point for the sample experiment as shown in Fig. 4.4. The total force very close to the origin is plotted against (c) x and (d) y .

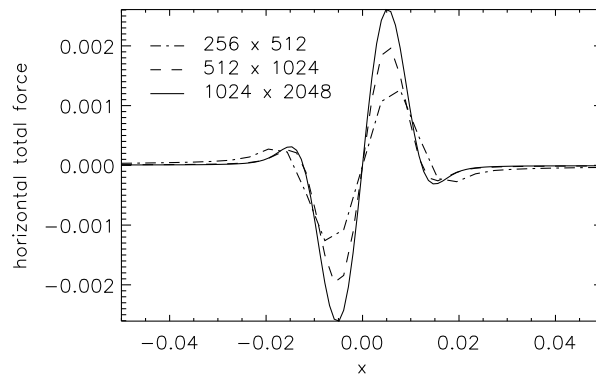


Figure 4.16: The total forces along the length of the current sheet after the same elapsed time for our sample experiment shown in Fig. 4.4, but run using different grid resolutions.

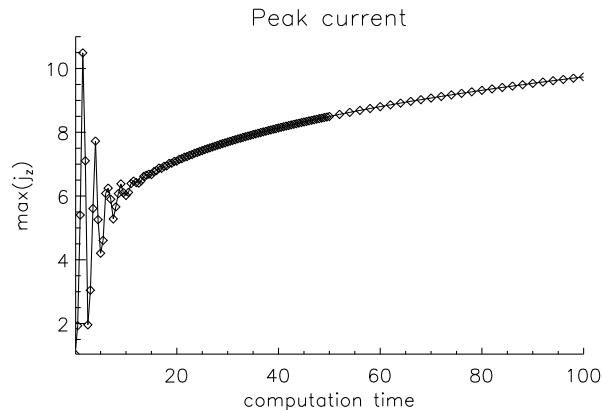


Figure 4.17: Magnitude of the electric current density at the location of the null, as a function of time, for the same experiment as shown in Fig. 4.4.

this state to be a *quasi-static state*, which can be understood as a magnetohydrostatic equilibrium.

An important result is that the form of the functions $p(A_z)$ and $j_z(A_z)$, which define Grad-Shafranov's condition, are different for each of our experiments. That is, the final equilibrium directly depends on the initial conditions of the experiments, i.e. on the initial plasma pressure and the initial current density. Also, the plots are not symmetric with respect to $A_z = 0$, showing that the system approaches the singularity in a different way for positive and negative values of A_z , i.e. inside and outside the cusp, respectively.

In comparison to the study of Craig and Litvinenko (2005), they use a frictional relaxation scheme with a fictitious mechanism for damping velocities, while our MHD numerical experiments involve a physical viscous term which is associated with a heating term, which heats the plasma, taking energy from the magnetic field. This affects in various ways to the final equilibrium state. First, they find a current layer about the null whose area is decreased when increasing the resolution. However, we suggest here that the system may achieve a state with a well defined and finite width and length of the current layer. It may happen that a non-negligible heating around the null point enables a larger finite width to be held. Also, our peak current density, at the origin, is not able to achieve a stable value, due to the presence of residual forces about the null that try to collapse the field towards a singularity, even if the field has achieved a good equilibrium everywhere else. These forces continue feeding the singularity if the simulation is run for longer, and hence, the strength of the singularity (as studied by Craig and Litvinenko, 2005) is not a good parameter to evaluate. Instead, we will try to give a qualitative description of the field around the null point, and see how this depends on the initial quantities of our experiments.

4.5 Analytical description of the field

4.5.1 Sample experiment

We follow the approach given by Vekstein and Priest (1993) in an attempt to give a mathematical description of the field about the null. The physics of their problem is different to ours, and they assumed a potential field outside the cusp, which we do not have. Nevertheless, we can test the form they gave for the separatrix curve (the angle

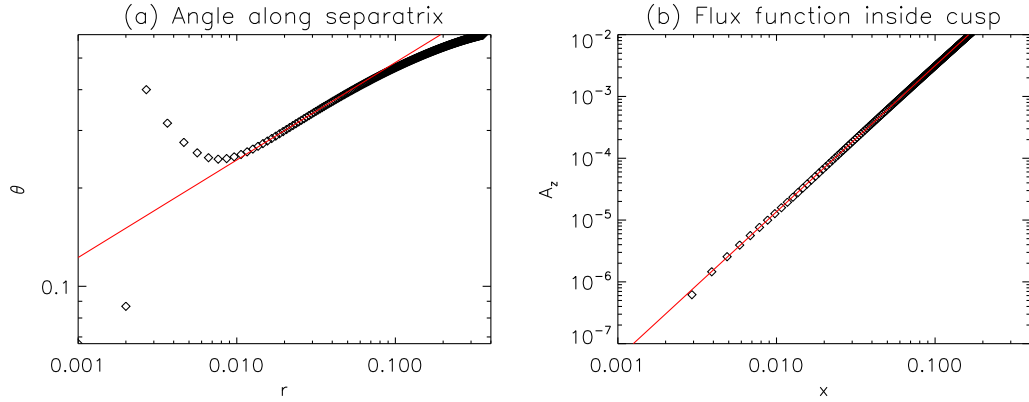


Figure 4.18: Logarithmic plots of (a) the angle θ along the separatrix versus the radius r and (b) the flux function inside the cusp, along the x -axis. In solid red, we present the best fit of a linear regression, to the points which seem to represent a straight line in each plot.

along the separatrix), in our experiments, and also their suggestions for the flux function, A_z , and current density, $j_z = -\nabla^2 A_z$, for the region inside the cusp.

First, they suggested a form for the angle along the separatrix as $\theta = Kr^\beta$, and for the flux function inside the cusp as in equation (4.3.3), i.e. $A_z(r, \theta) = r^\alpha f(\theta/Kr^\beta)$. A simpler form for A_z can be studied for $\theta = 0$, i.e. along the x -axis, for which equation (4.3.3) becomes $A_z = x^\alpha f_0$, where $f_0 \equiv f(0)$.

Figure 4.18a shows the angle along the separatrix as a function of the radius (where $r = 0$ is taken as the null point at $(0, 0)$). Both axes of the plot are logarithmically scaled, with a linear fit made to a set of points near the null. We observe that the plot is not completely linear in any region, and hence, we cannot expect good results from the form given by Vekstein and Priest (1993). On the other hand, Figure 4.18b shows the flux function inside the cusp, along the x -axis, also in logarithmic scale, and we observe a perfect linear behavior. The two linear regressions give the values of the two exponents, as $\alpha = 2.365$ and $\beta = 0.299$. Using $n = (2\beta + 2 - \alpha)/\alpha$, we get $n = 0.098$ for the exponent in equation (4.3.4),

$$j_z = mA_z^{-n}. \quad (4.5.1)$$

Now, in Figure 4.19 we show logarithmic plots of the current density, $j_z = -\nabla^2 A_z$ against the flux function A_z for inside and outside the cusp, with linear regressions over them. In the case of inside the cusp, we have overplotted a line using the exponent obtained above, following Vekstein and Priest (1993), and we can observe how that solution is far from our numerical results. We must then continue the analysis with direct fits to equation (4.5.1).

In Figure 4.20, we show a close-up to the plots of Figure 4.7, with a fit to equation (4.5.1). We have used the same form for the function inside and outside the cusp, but the fit has been made independently, thus the coefficients

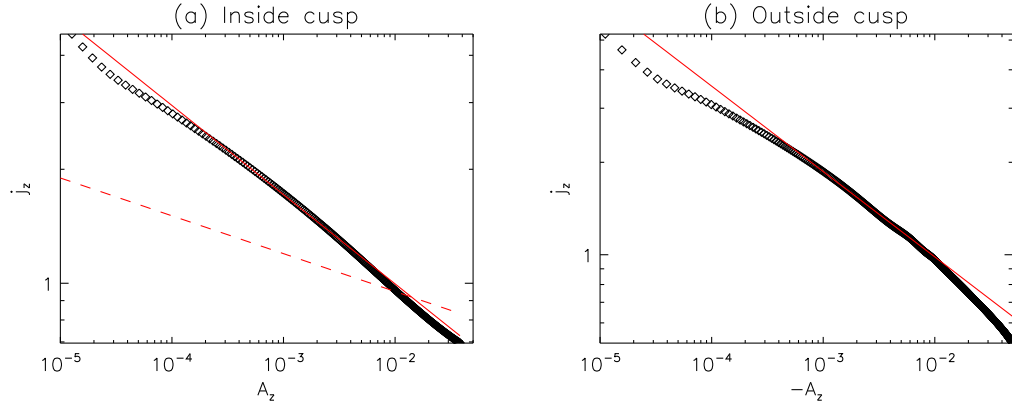


Figure 4.19: Logarithmic plots of the current density as a function of the flux function for (a) inside the cusp, showing a cut at $y = 0$, and (b) outside the cusp, showing a cut at $x = 0$. In solid red, we show a linear regression of the points which are close to being a straight line. In the left plot, in dashed red, we present the slope $n = 0.098$ for the exponent calculated following the suggestions of Vekstein and Priest (1993).

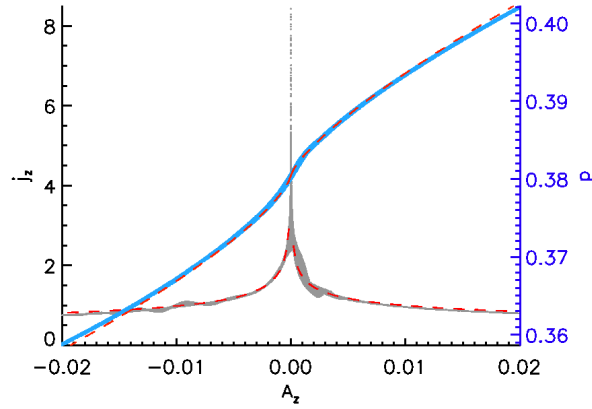


Figure 4.20: We present the fits in Figures 4.19a and 4.19b in linear scale. together with the fits for the total pressure, given by equations (4.5.2)-(4.5.5).

and exponents are different in both regions. The current density and plasma pressure distributions have the form

$$j_{z i}(A_z) = m_i A_z^{-n_i} , \quad (4.5.2)$$

$$p_i(A_z) = \frac{m_i}{1 - n_i} A_z^{1-n_i} + C , \quad (4.5.3)$$

$$j_{z o}(A_z) = m_o A_z^{-n_o} , \quad (4.5.4)$$

$$p_o(A_z) = \frac{m_o}{1 - n_o} A_z^{1-n_o} + C , \quad (4.5.5)$$

where the subscripts i and o refer to inside and outside the cusp, respectively. The values of the parameters for this sample experiment are $m_i = 0.337$, $n_i = 0.236$, $m_o = 0.273$, $n_o = 0.278$. The constant C is determined as the value of the equilibrium plasma pressure at the origin, i.e. $C = p_{eq}(0, 0) = 0.38$. Note, that this value is different from the initial constant pressure, $p_0 = 0.375$.

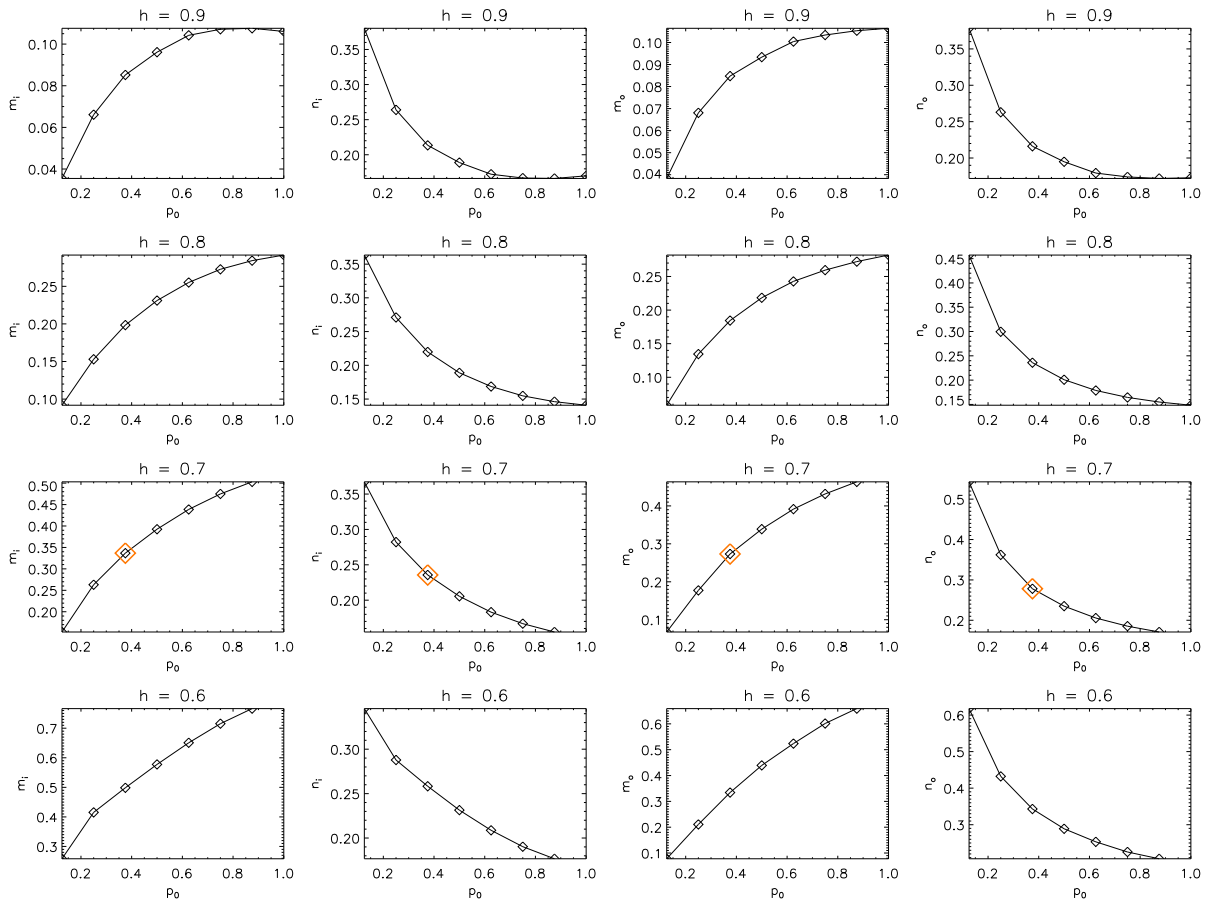


Figure 4.21: Parameters (m_i, n_i, m_o, n_o) as functions of the initial pressure, for all the different heights. First column are the coefficients m_i for inside the cusp, second column are the exponents n_i for inside the cusp, third column are the coefficients m_o for outside the cusp and fourth column are the exponents n_o for outside the cusp. The values for the sample experiment studied above are highlighted in orange.

4.5.2 Dependence with initial quantities

The process can be repeated for all the numerical experiments, finding a dependence with the initial pressure and initial current density. Figure 4.21 shows the dependence of the parameters (m_i, n_i, m_o, n_o) with initial pressure, for the different values of h , obtained using fits like the ones in Figures 4.19 and 4.20 for every single experiment.

The first conclusion that we directly obtain from Figure 4.21 is that there exists a clear functionality of the four coefficients with the initial values of the pressure and current density, i.e with the plasma beta and the initial perturbation. Both m_i and m_o increase as the initial pressure increases, but n_i and n_o decreases as the initial pressure increases. The second is that the solutions for inside and outside the cusp are different, as was already assumed in Vekstein and Priest (1993).

The pressureless limit case gives some hint about the results shown in Figure 4.21. When the plasma pressure tends to zero, then one would expect the system to approach the potential case where current density is zero everywhere (except in a thin current sheet where it becomes singular), hence, the coefficients m_i and m_o should go

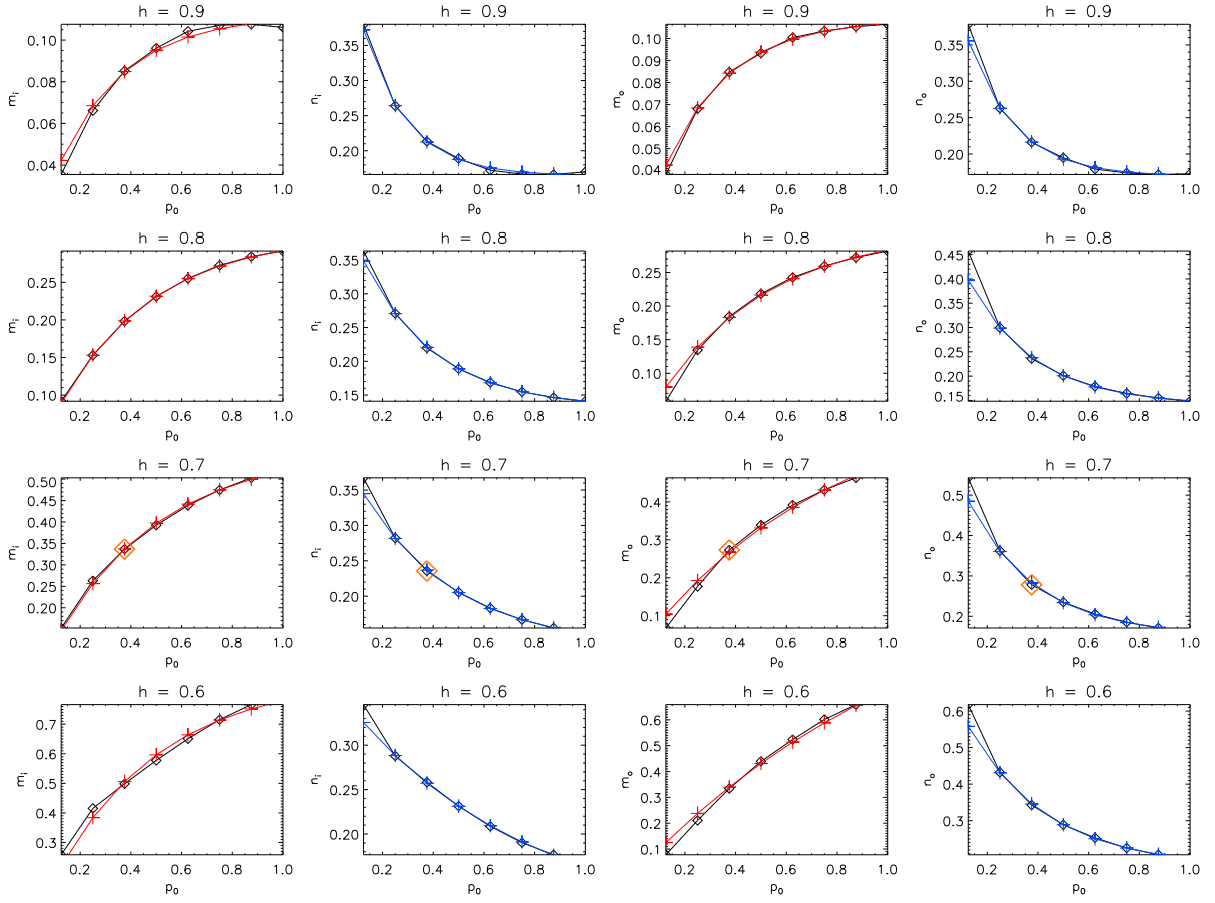


Figure 4.22: Here, we show the same plots as in Figure 4.21, with fits to the curves to the expressions (4.5.6) and (4.5.7), in red, for the coefficients m_i and m_o , and blue for the exponents n_i and n_o .

to zero when $p \rightarrow 0$. With that consideration, we can find a good fit to the plots of Figure 4.21, using exponential functions, as follows,

$$m = -A(e^{-Bp_0} - 1) , \quad (4.5.6)$$

$$n = C(e^{-Dp_0} - 1) + E , \quad (4.5.7)$$

where (A, B, C, D, E) are the parameters for a non-linear fitting. Figure 4.22 shows the fits of equations (4.5.6) and (4.5.7) to the plots in Figure 4.21. The non-linear fits have been done by using the *Levenberg-Marquardt method* for non-linear modeling, described in Press et al. (1992), “*Numerical Recipes*”, Chapter 15. The parameters after the fits are summarised in Table 4.1. No more conclusions can be obtained from the data, apart from the fact that these parameters preserve monotonicity.

In the limit $p \rightarrow \infty$, i.e. the plasma dominates over the magnetic field, the coefficients $m_{i/o}$ tend to $A_{i/o}$, and the exponents $n_{i/o}$ tend to $E_{i/o} - C_{i/o}$. These are summarised in Table 4.2. As an ambitious observation, if the parameter $E_i - C_i$ (and $E_o - C_o$) can be understood as constant with h (minus numerical errors), then the

h	j_0	A_i	B_i	C_i	D_i	E_i	A_o	B_o	C_o	D_o	E_o
0.9	0.23	0.112	3.786	0.432	5.848	0.596	0.109	3.971	0.370	5.501	0.540
0.8	0.56	0.314	2.669	0.339	3.550	0.470	0.313	2.341	0.417	3.893	0.558
0.7	1.04	0.570	2.392	0.306	2.764	0.434	0.689	1.312	0.532	3.772	0.685
0.6	1.77	0.860	2.366	0.273	1.420	0.370	1.271	0.829	0.575	3.208	0.748

Table 4.1: Parameters (A , B , C , D , E) as functions of the height of the box h , or the initial current density j_0 . The subscripts i/o refer to inside/outside the cusp respectively.

h	j_0	A_i	$E_i - C_i$	A_o	$E_o - C_o$
0.9	0.23	0.112	0.164	0.109	0.170
0.8	0.56	0.314	0.131	0.313	0.141
0.7	1.04	0.570	0.128	0.689	0.153
0.6	1.77	0.860	0.097	1.271	0.173

Table 4.2: Limits for $p \rightarrow \infty$ as functions of the height of the box h , or the initial current density j_0 .

exponents n_i (and n_o) in the limit $p \rightarrow \infty$, would then not depend on h . This is, when the plasma pressure is very big, the final equilibrium would not depend on the squashing, i.e. on the electromagnetic perturbation.

4.5.3 Overview

We have studied in close detail the same problem as Craig and Litvinenko (2005), making use of the full set of MHD equations, and we have found that our final equilibrium differs from their result in some aspects. Using the approach given by Vekstein and Priest (1993), we have given a qualitative description of the final equilibrium states by looking for fits to the equation $j_z = \mathcal{F}(A_z)$. Even if this is only a qualitative analysis, it describes a fair approximation of the behaviour of the final equilibrium as the values of the initial plasma pressure and current density are varied. These two-dimensional contexts are of high relevance for systems with translational or rotational symmetries, and their study is useful for some astrophysical environments which can be well approximated by these properties of symmetry.

In the next chapter, we evaluate current accumulations in three-dimensional equilibria which contain 3D magnetic null points. The characteristics of these environments are going to be completely different to the two-dimensional case, and the dynamical evolutions are less restrictive in the sense that the plasma has freedom to move in all three spatial directions. Hence, the approach to the problem will have to be different.

Chapter 5

Relaxation of 3D Magnetic Null Points

5.1 Introduction

Three-dimensional magnetic null points have been studied in detail within the last decade in the main context of three dimensional magnetic reconnection. Their importance for magnetic energy release in solar and magnetospheric environments have been observationally established by many authors, for example in solar flares (Fletcher et al., 2001), in solar active regions (Ugarte-Urra et al., 2007) or at the Earth's magnetotail (Xiao et al., 2006). However, a complete understanding of the formation of a current sheet through the collapse of a three-dimensional magnetic null point is still to be achieved, either mathematically or phenomenologically.

The processes of reconnection in three dimensions are significantly different to and much more complex than those in two-dimensions at X-type null points (e.g Hesse and Schindler, 1988; Priest et al., 2003). In general, in three-dimensions, magnetic reconnection can occur either at nulls or in the absence of them, and does not involve one-to-one breaking and rejoining of pairs of field lines, as in two-dimensions. A classification of the reconnection regimes at three-dimensional magnetic null points is made by Priest and Pontin (2009). The nature of the reconnection that takes place around a three-dimensional null depends directly on the flows and boundary conditions that are responsible for the reconnection (Figure 5.1). Below, we discuss the different reconnection regimes about 3D nulls, assuming initially a potential radial null, where the spine is perpendicular to the fan, and field lines in the fan plane extend radially from the null (Parnell et al., 1996).

1) A rotation of the fan plane about the spine drives a twist of the field lines around the spine (red arrows in Figure 5.1). An electric current density builds along and near the spine, in the direction of it. Reconnection of field lines may take place in that region, producing a slippage of the field lines in a counter-rotational direction to the twist, which dissipates the current density. This is called *torsional spine reconnection*. It does not involve flow across the fan or the spine, and hence, the global topology of the field remains unchanged. Note, that the reconnection does not take place at the location of the null. Models of torsional magnetic reconnection are given by Pontin et al. (2004) and Wyper and Jain (2010).

2) A rotation of the field lines about the spine, in different directions above and below the fan, creates an electric current in the fan plane that points in the direction of the spine but has different sign above and below the fan (yellow arrows in Figure 5.1). Reconnection of field lines can take place in the regions near the fan by a rotational slippage of the field lines there in opposite directions above and below the fan, so as to dissipate the

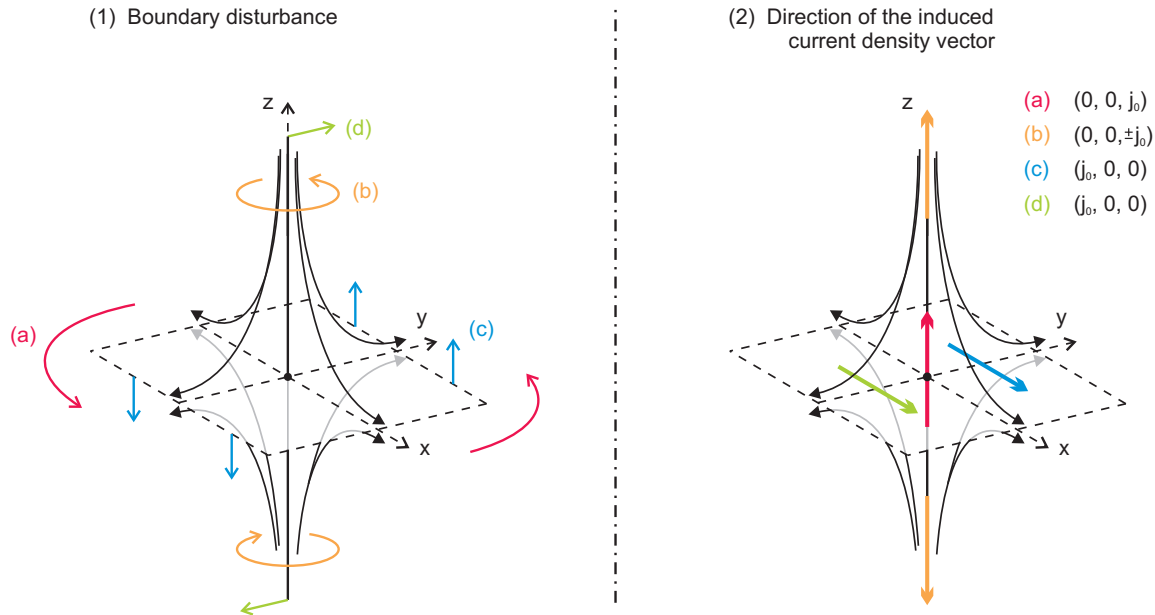


Figure 5.1: Possible boundary disturbances responsible for reconnection at a 3D positive null, showing the direction of the induced current density, for (a) *torsional-spine reconnection*: a rotation of the fan (red) induces a unidirectional current density, parallel (below the fan) and antiparallel (above the fan) to the spine, (b) *torsional-fan reconnection*: opposite rotations above and below the fan of the field lines about the spine (yellow) induce a current density antiparallel to the spine, (c) and (d) *fan-spine reconnection*: a shear of the fan plane (blue) or the spine (green), induces a current density perpendicular to the spine in these cases along the x -axis.

current density. This is called *torsional fan reconnection*. As before it does not produce a change in the topology of the field, and reconnection does not happen at the locations of the null (Pontin et al., 2004; Wyper and Jain, 2010).

3) A shear motion of the spine below and above the fan, in opposite directions (green arrows in Figure 5.1), or a shearing of the fan plane (blue arrows in Figure 5.1), producing a tilt with respect to the spine about a given axis, drives a collapse of the null point. That is, the resulting Lorentz forces act in the same direction as the initial disturbance, thus increasing it and resulting in a folding of the spine and fan towards each other. A current is created along the line to which the spine and fan are collapsing to, and so, it is perpendicular to the direction of the perturbation, similarly to the two-dimensional X-point collapse. Here, reconnection can take place in the vicinity of the null, and implies that flux is transferred across the spine and the fan, thus changing the global topology of the field lines, as in the two-dimensional case. Pontin et al. (2005) give a model for this type of reconnection, referred to as *fan-spine reconnection*.

All the previously mentioned studies of 3D reconnection at magnetic nulls assume a zero beta plasma model, solving the equations only for the electromagnetic field, and hence, neglecting the effects of the plasma in the evolution of the field. On the other hand, Pontin et al. (2007a) investigated current sheet formation and evolution of the field at 3D nulls after a shearing-type perturbation, using a full MHD description of the field. They then studied the subsequent reconnection processes using full MHD resistive numerical simulations, finding, at the time of maximum current, the biggest current accumulation at the location of the null, extended faintly along the spine

and the fan. Using the same MHD approach, they investigated the effects of compressibility (Pontin et al., 2007b) in their evolution, finding a significant reduction of the peak current and the reconnection rate as the limit of an incompressible fluid was approached.

However, the non-resistive evolution of three-dimensional nulls through a shearing-type perturbation and the development of singular currents, to our knowledge, has only been studied by Pontin and Craig (2005), who analysed the formation of a current singularity at the location of the null in a non-force-free equilibrium, in an equivalent manner to the two-dimensional singularities studied by Craig and Litvinenko (2005). The emphasis of their study was the evaluation of the scaling laws for the strength of the singularity, as a function of the grid resolution of their experiments. They also studied the effects of the plasma pressure in the relaxation, finding that, while a singularity was formed in all cases, the plasma pressure force weakened the strength of the singularity. For the evolution of the field, they assumed the adiabatic polytropic model $p \sim \rho^\gamma$, using a frictional code where no energy conversion was allowed.

Here, we study the non-resistive evolution of two configurations, 1) a torsional-spine-type and 2) a sheared-type perturbed magnetic null, using LARE3D. In particular, we are interested in the current accumulations that arise when a non-force-free equilibrium is reached. We evaluate the effects of both the plasma pressure and the heat transfer in the evolution, as both the initial disturbance (i.e. the torsion or the shear) and the background plasma pressure are changed systematically. In the case of a shearing perturbation, the formation of a current singularity at the location of the null is evaluated.

5.2 Magnetic field configurations and numerical setup

As seen in Section 1.4.2, the magnetic field \mathbf{B} around a null point may be expressed as

$$\mathbf{B} = \mathbf{M} \cdot \mathbf{r} , \quad (5.2.1)$$

where \mathbf{M} is a matrix with elements $M_{i,j} = \partial B_i / \partial x_j$, and \mathbf{r} is the position vector $(x, y, z)^T$. By choosing the right coordinate system in which the spine lies along the z -axis and the current density vector is directed somewhere in the xz -plane, the matrix \mathbf{M} can be reduced to equation (1.4.14),

$$\mathbf{M} = \begin{pmatrix} \frac{\partial B_x}{\partial x} & \frac{\partial B_x}{\partial y} & \frac{\partial B_x}{\partial z} \\ \frac{\partial B_y}{\partial x} & \frac{\partial B_y}{\partial y} & \frac{\partial B_y}{\partial z} \\ \frac{\partial B_z}{\partial x} & \frac{\partial B_z}{\partial y} & \frac{\partial B_z}{\partial z} \end{pmatrix} \sim \begin{pmatrix} 1 & \frac{1}{2}(q - j_{\parallel}) & 0 \\ \frac{1}{2}(q + j_{\parallel}) & p & 0 \\ 0 & j_{\perp} & -(p + 1) \end{pmatrix} ,$$

where j_{\parallel} and j_{\perp} are the components of the current density parallel and perpendicular to the spine, respectively, such that

$$\mathbf{j} = (j_{\perp}, 0, j_{\parallel}) .$$

The conditions $-1 < p < \infty$ and $q^2 \leq j_{\parallel}^2 + 4p$ (Parnell et al., 1996) ensure that the spine of the null is along the z -axis, and the null is positive, i.e. the spine above and below the fan is composed of a pair of field lines directed towards the null, and field lines in the fan emanate away from it.

In this chapter, we are going to study the MHD relaxation of two different null point configurations, with the current density vector entirely perpendicular or entirely parallel to the spine. As an initial magnetic field, we use a

linear field around a null as described in equation (5.2.1). For simplicity in our experiments, we have chosen $q = 0$ and $p = 1$, so that the field lines lying in the fan do not follow any predominant direction (i.e. they expand radially outwards), and are rotationally symmetric about the spine. Hence, we can rewrite the matrix \mathbf{M} as

$$\mathbf{M} = \begin{pmatrix} 1 & -\frac{1}{2}j_{\parallel} & 0 \\ \frac{1}{2}j_{\parallel} & 1 & 0 \\ 0 & j_{\perp} & -2 \end{pmatrix}. \quad (5.2.2)$$

We use the LARE code to run a series of non-resistive experiments on initial magnetic fields of 3D null points that have a uniform spine-aligned or fan-aligned current, embedded in a non-zero beta plasma. In order to investigate the dependence of the results on values for the initial pressure and current density, we consider two sets of experiments in which the magnitude of the background plasma pressure and the initial current density are varied independently. All the initial plasma quantities (i.e. plasma pressure, density and internal energy) are fixed as constants and there are no initial flows. The current density vector is also constant everywhere, as already explained, and equals $(0, 0, j_0)$ in the first set of experiments, and $(j_0, 0, 0)$ in the second.

The size of the numerical domain is $2 \times 2 \times 2$, and all x , y and z vary from -1 to 1 . The grid is uniform and has a resolution of $256 \times 256 \times 256$. All boundaries of the domain are closed, in the same way as those for the 2D null point experiments discussed in Chapter 4, and the magnetic field is line tied. At the boundaries, velocities are set to zero and the rest of the quantities have their first derivatives set to zero. The real viscosity is $\nu_r = 0.005$, and the two shock viscosities are zero in all the experiments.

5.3 3D nulls with spine-aligned current

5.3.1 Initial state

We first look at the relaxation of initial configurations of magnetic null points with a constant current density everywhere in the direction parallel to the spine, of the form $(0, 0, j_0)$. The magnetic field is then given by equations (5.2.1) and (5.2.2), as

$$B_x = x - \frac{j_0}{2}y, \quad (5.3.1)$$

$$B_y = \frac{j_0}{2}x + y, \quad (5.3.2)$$

$$B_z = -2z. \quad (5.3.3)$$

The fan is perpendicular to the spine and lies in the plane $z = 0$. We have run four experiments with a fixed value of the plasma pressure, $p_0 = 1$, varying the initial current as $j_0 = 0.025, 0.5, 1.0, 1.5$, and five experiments with the initial current fixed at $j_0 = 1$, and the initial pressure varying as $p_0 = 0.05, 0.5, 1.0, 1.5, 2.0$. Figure 5.2 shows the magnetic configuration of the initial state, for $j_0 = 1.0$ and $p_0 = 1.0$. The magnetic field lines show a homogeneous twist about the spine, and the field lines lying in the fan define a logarithmic spiral.

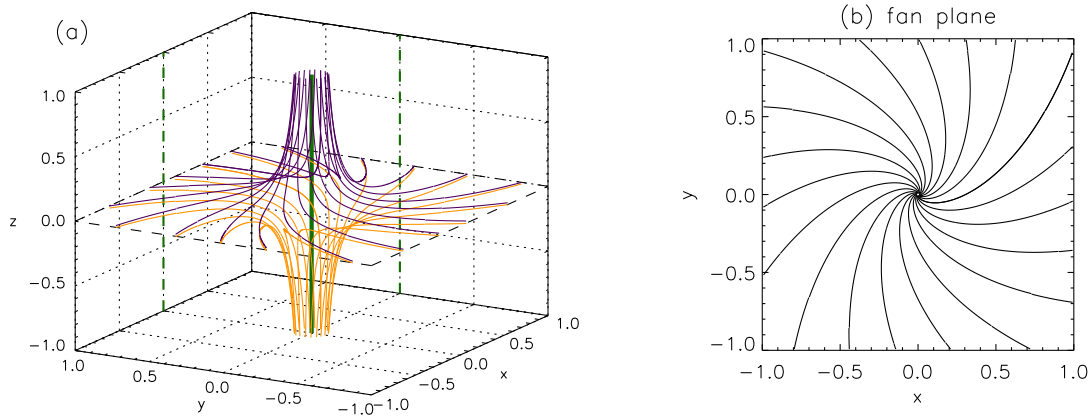


Figure 5.2: Magnetic configuration for the initial non-equilibrium state with homogeneous spine-aligned current, for $j_0 = 1.0$ and $p_0 = 1.0$, showing (a) the 3D configuration with field lines above the fan in purple and field lines below the fan in orange. The fan plane is outlined by a dashed black line. The spine is represented in green, with its projections onto the xz -plane and yz -plane in dashed green lines. In (b), we plot the field lines in the fan plane, at $z = 0$.

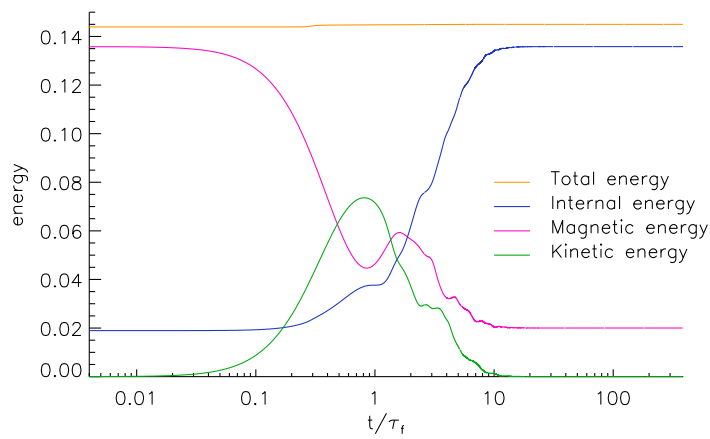


Figure 5.3: Time evolution of the energies of the system integrated over the whole domain, for the same experiment as in Figure 5.2. The magnetic, internal and total energies have been shifted on the y -axis by subtracting the constant values 8.5, 12.0 and 20.5 respectively, but their amplitudes are not scaled.

5.3.2 Final equilibrium state

We first concentrate on the case shown in Figure 5.2, which has $j_0 = 1.0$ and $p_0 = 1.0$. The evolution of the energies of the system integrated over the numerical domain is shown in Figure 5.3. The time unit is the time for a fast magnetoacoustic wave to get from one of the boundaries to the location of the null. The exchange from magnetic to internal energy is approximately 0.12, in normalised units, and the change in total energy is just 0.001, which is about 0.01 times the amount of exchanged energy and hence, it is negligible. Note that here, the numerical effects that violated energy conservation in the first few time-steps of the two-dimensional X-point experiments in the previous chapter (which were explained as being a consequence of sudden shock formation), do not appear in our three dimensional models. Thus it appears as if energy is essentially conserved in our experiments.

The magnetic field configuration at the end of the simulation is shown in Figure 5.4. Because of the line-tied boundaries, and the restriction of an ideal evolution, the field cannot dissipate the original twist. Instead, in comparison to the initial state (Figure 5.2), the relaxation appears to undo the original spiral of the fan field lines, transferring the twist to the field lines about the spine. However, the final relaxed field lines in our fan plane are not entirely radial.

In order to evaluate if an equilibrium has been achieved, we go back to the main result of magnetohydrostatics which states that, in a properly relaxed state, the plasma pressure is constant along field lines, and hence,

$$\mathbf{B} \cdot \nabla p = 0 .$$

By comparing, in the fan plane of the final state, the magnitudes of $\mathbf{B} \cdot \nabla p$ and the poloidal magnetic field, B_ϕ (Figure 5.5), we show that the regions in which $\mathbf{B} \cdot \nabla p \neq 0$ coincide with the regions where the poloidal field is large. This may indicate that these regions arise due to the residual forces trying to converge the field lines to a radial configuration that has not yet been achieved. The plasma pressure in the fan plane is effectively constant everywhere with an approximate value of 1.06, in comparison with its initial magnitude, $p_0 = 1$. The restriction of line-tide boundaries makes the final state hard to achieve, and the forces are fairly small, so the numerical simulation would need to run for much longer to make these disappear.

We now consider if the system has achieved a good equilibrium in the regions outside the plane of the fan by considering a vertical cut through the fan in a plane including the spine. As discussed above, in equilibrium, the plasma pressure has to be constant along the magnetic fields, implying $\mathbf{B} \cdot \nabla p = 0$. In Figure 5.6a we show that outside of the fan plane, the pressure is constant along magnetic field lines everywhere. The particular vertical cut chosen is a plane perpendicular to the fan which cuts through two of the regions of non-equilibrium in the fan (indicated in red in Figure 5.5a).

Figures 5.6b and 5.6c show vertical cuts in the plane $x = 0$ with contour plots of plasma pressure and current density. Plasma pressure is enhanced near the spine and in the fan plane, and current density concentrates principally along and about the spine, and is positive everywhere. The magnitude of the current density is reflectively symmetric about the fan plane, and rotationally symmetric about the spine. Note, that the main accumulations of current density occur in the locations where torsional-spine reconnection takes place in 3D null point reconnection studies (Pontin et al., 2004; Priest and Pontin, 2009; Wyper and Jain, 2010). The current is effectively zero in the fan plane, but has a small finite value at the location of the null itself, corresponding to small and highly localised gradients of the magnetic components at the location of the null. The scales of these gradients are of the order of the size of the numerical grid, and hence, we are not able to give a definitive answer as to whether the current at the null itself is different to zero.

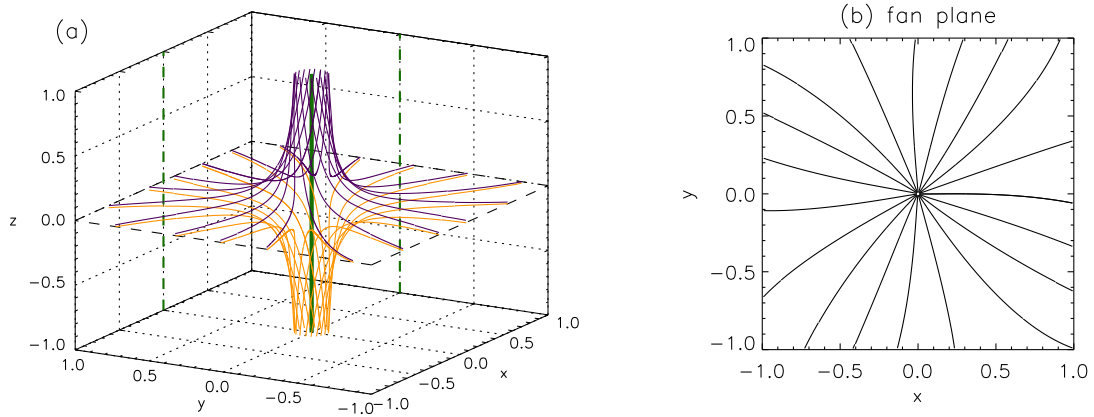


Figure 5.4: Magnetic configuration for the equilibrium state with spine-aligned current, for the same experiment as in Figure 5.2, showing (a) the 3D configuration with field lines above the fan in purple and field lines below the fan in orange. The outline of the fan is represented by dashed black lines. Also, the spine is represented in green, with its projections onto the xz -plane and yz -plane in dashed green lines. In (b), we plot the field lines in the fan plane, at $z = 0$.

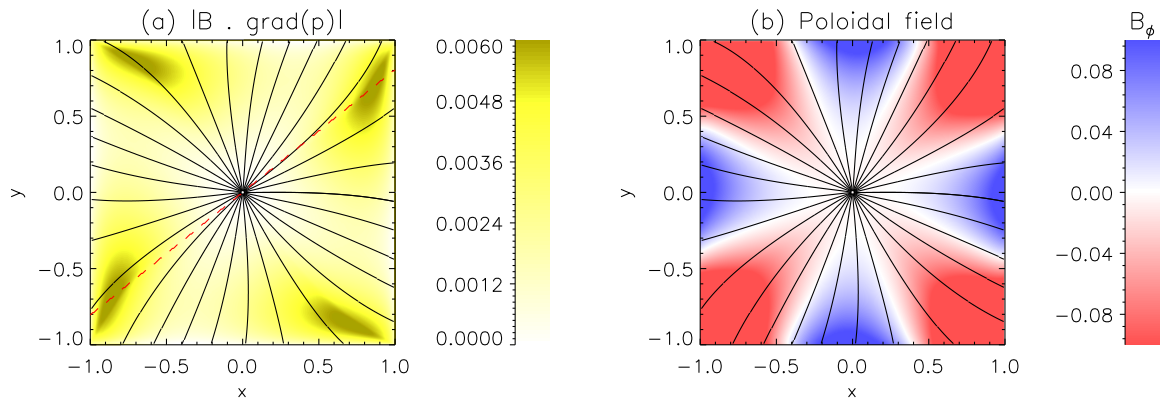


Figure 5.5: Contour plots of (a) $|\mathbf{B} \cdot \nabla p|$ and (b) poloidal field, B_ϕ , in the fan plane for the final state, for the same experiment as in Figure 5.2. In (b), blue means clockwise winding of the field lines, and red means anti-clockwise winding. The red-dashed line in (a) shows the line of the vertical cut shown in Figure 5.6a.

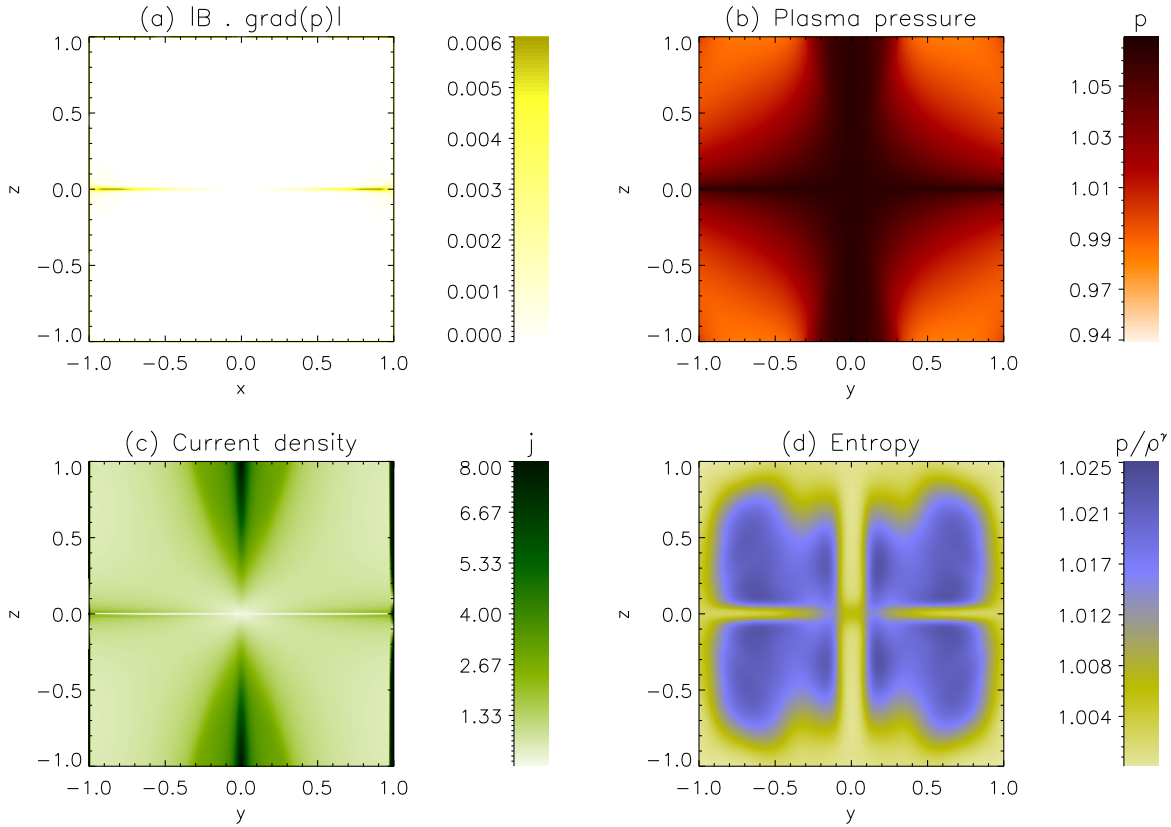


Figure 5.6: Contour-plots of (a) $|\mathbf{B} \cdot \nabla p|$, for a vertical plane crossing the fan through the red dashed line in Figure 5.5a, and (b) plasma pressure, (c) current density and (d) p/ρ^γ , in the yz -plane at $x = 0$, for the same experiment as in Figure 5.2

Parnell et al. (1997) describe how, an equilibrium involving a linear 3D null must satisfy $\mathbf{j} = 0$, i.e. the field has to be potential, as seen in Section 1.4, equation (1.4.18), since

$$\nabla \times (\mathbf{j} \times \mathbf{B}) = -\mathbf{M} \cdot \mathbf{j} = 0,$$

where \mathbf{M} is a non-singular matrix. Assuming that the field lying in the fan plane is linear in the final equilibrium, this condition requires the field to be potential everywhere in the fan, except for the null point itself, where $\mathbf{B} = 0$. There, a finite singular current could in principle be allowed, but this cannot be confirmed within our resolution limits.

The viscous heating term in the energy equation leads to non-adiabatic effects, from which it follows that the quantity p/ρ^γ changes throughout the dynamical evolution, and therefore, density is not constant along magnetic field lines in the final state. Figure 5.6d shows a vertical cut of p/ρ^γ in the plane $x = 0$. We see that it does not follow the same behaviour as the plasma pressure or the current density. The higher values do not occur in the fan nor along the spine. Instead, p/ρ^γ is near its minimum in those regions, indicating that the main dissipation of

magnetic energy does not happen at them.

The state of the plasma along the spine in the final state, compared to its initial state, is shown in Figure 5.7, where we plot the current density, plasma pressure and entropy (p/ρ^γ) along the spine for the final and initial states. Along the spine, the magnetic field is parallel (above the null) and antiparallel (below the null) to the electric current. Hence, the Lorentz force must equal zero, and, in equilibrium, the pressure gradients have to vanish, which they clearly do (Figure 5.7a). The current density is nearly zero at the origin, and increases almost linearly below and above the fan (Figure 5.7b). The entropy (p/ρ^γ) increases gradually along the spine, then more rapidly as it heads to the null, peaking at the null itself (Figure 5.7c). This indicates that there is marginally more energy dissipated near the null than along the rest of the spine, but even near the null there is a little dissipation compared to elsewhere in the domain (Figure 5.6d).

Figure 5.8 shows plots of the same quantities, across the spine, at three different heights, in the plane $x = 0$. We see that, in the region close to the spine $-0.1 < y < 0.1$, the plasma pressure gradients do not vary with height (Figure 5.8a), hence, in the equilibrium, the z -component of the Lorentz force is zero within a cylinder of radius 0.1 around the spine. Also in that region, p/ρ^γ is near its minimum (Figure 5.8c), as discussed above. It reaches, however, its maximum values away from the spine, where it gets much larger than at the null point itself. Hence, the largest dissipation of magnetic energy does not occur at or near the null in this torsional case.

5.3.3 Changes in current density and plasma pressure

Finally, we evaluate how the results above vary when increasing or decreasing the initial values of the plasma pressure and current density. By increasing the initial constant current density, j_0 , we naturally find a larger accumulation of current about the spine, but the qualitative aspects of the final equilibria are the same in all cases. Figure 5.9a shows plots of current density along the spine for four experiments with the fixed initial plasma pressure $p_0 = 1$ and current densities $j_0 = 0.25, 0.5, 1.0, 1.5$. The gradients of current on moving away from the null are steeper the higher the value of the initial current is. By comparing now the current distributions at the final state normalised by the initial value of the current density in each case (Figure 5.9b), we obtain a very similar behaviour for all the experiments. This suggests that the distributions of the current density in the final equilibria simply scale with the value of the initial current densities.

However, by changing the initial plasma pressure we do not find the same effect. The final distributions of current density are not affected by the magnitude of the initial plasma pressure, and hence by the value of the plasma beta. The current density distributions along the line of the spine are seemingly independent of the plasma pressure (Figure 5.10a), and so are the distributions across the spine, for small changes of the plasma pressure (Figure 5.10b). Only when the initial plasma pressure has been decreased by a factor of 20 (i.e. for $p_0 = 0.05$), can we see a small change in the regions about the spine, where the distribution of current density tends to be smoother.

5.3.4 Overview

The three-dimensional relaxation of magnetic null points with spine-aligned current has been investigated under non-resistive conditions. An initial field with a constant current density everywhere, in the direction of the spine, evolves by concentrating the initial constant current density around the spine lines, above and below the fan, maintaining the same direction in both hemispheres. The current along the spine points towards the null below the fan plane, and away from the null above the fan plane. Therefore, in the final equilibrium, the twist of the field lines,

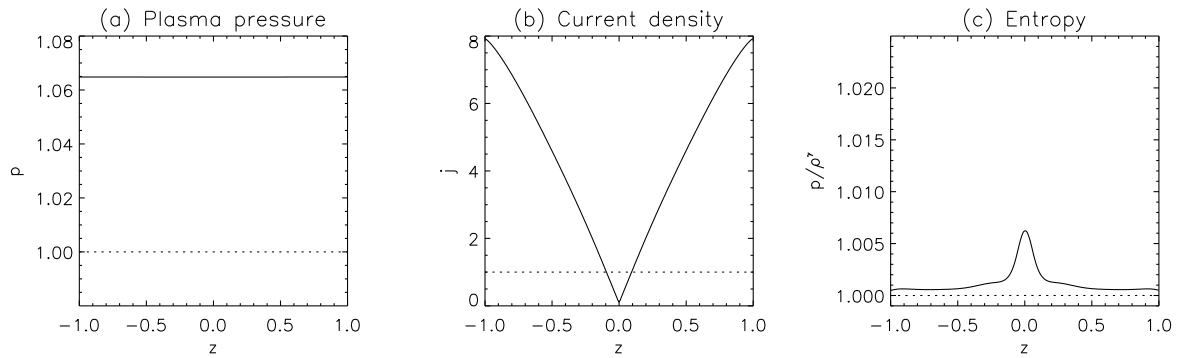


Figure 5.7: Cuts of (a) plasma pressure, (b) current density and (c) p/ρ^γ along the spine, for the same experiment as in Figure 5.2. Solid lines represent the final equilibrium state, and dotted lines represent the initial state.

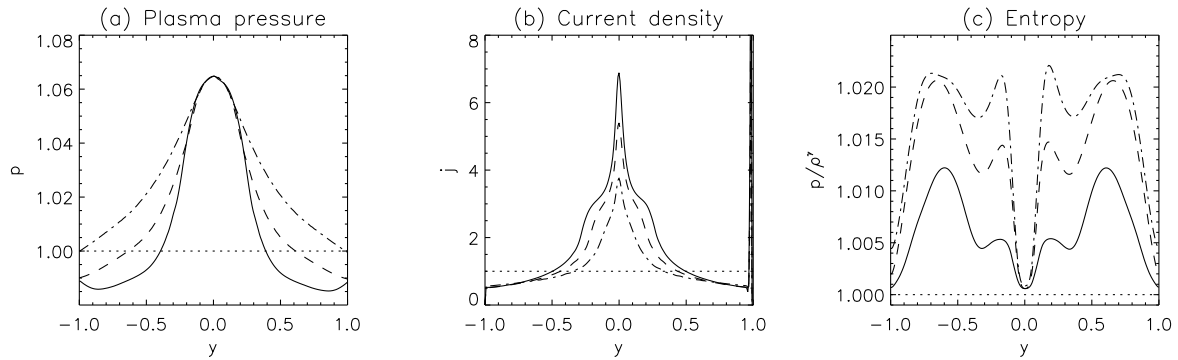


Figure 5.8: Cuts of (a) plasma pressure, (b) current density and (c) p/ρ^γ across the spine, at heights $z = 0.4$ (dash dot), $z = 0.6$ (dashed) and $z = 0.8$ (solid) for the same experiment as in Figure 5.2. Dotted lines represent the initial state.

which is initially homogeneous, accumulates about the spine, with the same sense of rotation above and below the fan. Our final equilibrium is such that the current density is effectively zero everywhere in the fan plane. Also, the field at equilibrium has rotational symmetry with respect to the spine. In order to reach the final equilibrium, we find that the main locations of viscous dissipation do not occur at the regions of higher accumulations of current, but they occur outside the separatrices and the null.

The effects of changes in the magnitude of the initial current density (or equivalently, in the integrated current density in the domain) are to increase the twist of the field lines about the spine, and hence, increase the current density around it. The current density along the spine increases monotonically as we move along the spine, with the rate of increase scaled according to the initial current density, j_0 , of the system. On the other hand, the results are only very weakly dependent of the magnitude of the initial plasma pressure, and in principle, the pressure gradients (pressure force) are able to hold the current density accumulation no matter what the magnitude of the plasma pressure is.

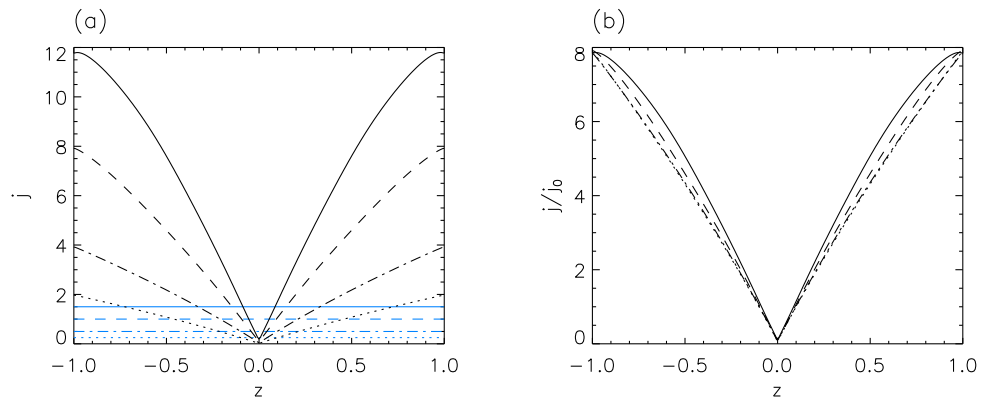


Figure 5.9: Cuts along the spine, of (a) current density, for four different experiments with initial plasma pressure $p_0 = 1$, and current densities $j_0 = 0.25$ (dotted), $j_0 = 0.5$ (dash dot), $j_0 = 1.0$ (dashed) and $j_0 = 1.5$ (solid). In blue, we represent the initial constant current for each experiment. The current normalised with respect to the initial values are overplotted in (b) for all four experiments.

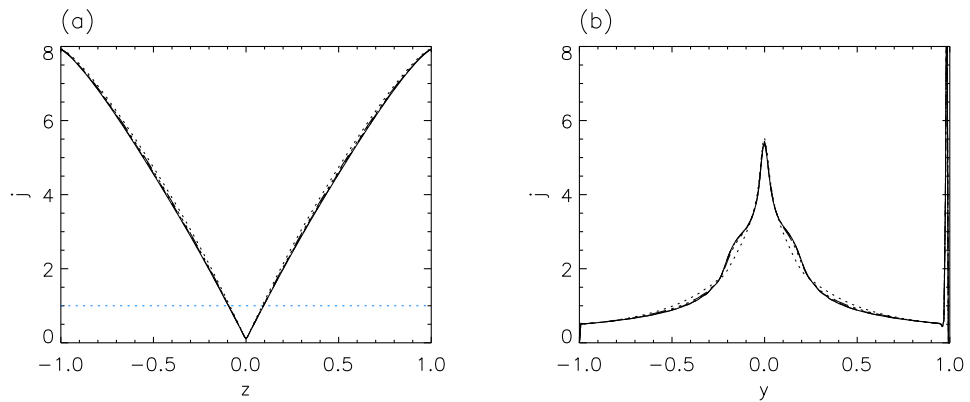


Figure 5.10: Cuts (a) along and (b) across the spine, at height $z = 0.6$, of current density, for five different experiments with initial current density $j_0 = 1$, and plasma pressures $p_0 = 0.05$ (dotted), $p_0 = 0.5$ (dash dot dot), $p_0 = 1.0$ (dashed dot), $p_0 = 1.5$ (dashed) and $p_0 = 2.0$ (solid). All plots overlap, except for the one with $p_0 = 0.05$.

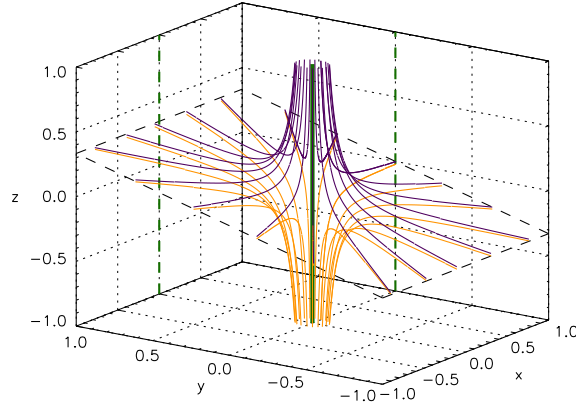


Figure 5.11: Magnetic configuration for the initial non-equilibrium state with homogeneous current perpendicular to the spine, pointing along the x -axis, with $j_0 = 1.0$ and $p_0 = 1.0$, showing the 3D configuration with field lines above the fan in purple and field lines below the fan in orange. The fan is represented by dashed black lines. Also, the spine is represented in green, with its projections onto the xz -plane and yz -plane in dashed green lines.

5.4 3D nulls with fan-aligned current

5.4.1 Initial state

In the second set of experiments, we look at the relaxation of magnetic null points with constant current density, pointing in the x -direction, perpendicular to the spine, of the form $(j_0, 0, 0)$. The magnetic field is now given by

$$B_x = x, \quad (5.4.1)$$

$$B_y = y, \quad (5.4.2)$$

$$B_z = j_0 y - 2z. \quad (5.4.3)$$

The fan plane for such a field tilts about the x -axis, so that it is not perpendicular to the spine. Initially, the plane of the fan is defined by

$$z = \frac{j_0}{3} y \quad (5.4.4)$$

(Parnell et al., 1996). We have run three experiments with a fixed value of the plasma pressure, $p_0 = 1$, varying the initial current as $j_0 = 0.5, 1.0, 1.5$, and another three experiments with the initial current fixed, $j_0 = 1$, and the initial pressure varying as $p_0 = 0.5, 1.0, 1.5$. Figure 5.11 shows the magnetic configuration of the initial state, for $j_0 = 1.0$ and $p_0 = 1.0$.

5.4.2 Final equilibrium state

We start analysing the results by focusing on the experiment in Figure 5.11, with $j_0 = 1.0$ and $p_0 = 1.0$. First, in Figure 5.12, we show the evolution of the integrated energies of the system. The time unit is the time for a fast magnetoacoustic wave to get from one of the boundaries to the location of the null. The exchange of magnetic to

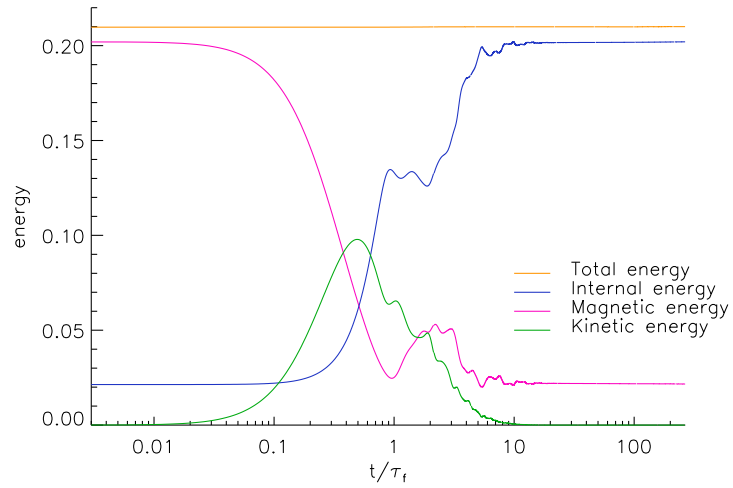
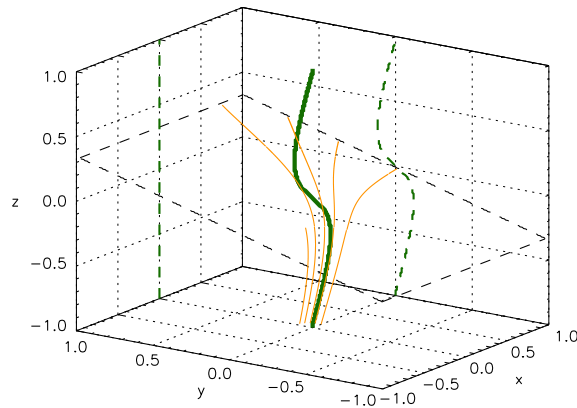


Figure 5.12: Time evolution of the integrated energies of the system for the same experiment as in Figure 5.11. The magnetic, internal and total energies have been shifted on the y -axis by subtracting the constant values 9.1, 12.0 and 21.1, respectively, but their amplitudes are not scaled.



internal energy is larger than in the previous case, and is approximately 0.18. In comparison, the change in total energy is of 0.0003, and hence, the total energy may be said to be conserved.

The magnetic field configuration at the end of the simulation is shown in Figure 5.13. In comparison to the initial state (Figure 5.11), the relaxation appears to collapse the spine and the fan towards each other in the region near the null. Far from the null, the spine appear to be trying to become perpendicular to the fan.

As in the previous sets of experiments, we check if our state has reached an equilibrium, by calculating the quantity $\mathbf{B} \cdot \nabla p$, which must equal zero everywhere for the plasma pressure to be constant along field lines. This condition holds everywhere save near and in the fan plane (Figure 5.14a). Interestingly, the non-zero regions of $\mathbf{B} \cdot \nabla p$ do not occur symmetrically about the fan plane, but occur in and above the fan when $z > 0$ and $y > 0$ and in and below the fan when $z < 0$ and $y < 0$. That is, they occur within the regions where the fan has been folded up towards the spine. These regions of non-equilibrium may account for residual forces which are trying to make the fan and the spine perpendicular away from the null. Note, that near the null, the spine and the fan appear to have collapsed to each other, and far from the null, they bend away, in a similar way to the separatrices in the two-dimensional X-point case.

The distribution of the plasma pressure in the plane $x = 0$ is similar to that in the 2D X-point case, with the pressure enhanced in the regions inside the “cusp” and decreased in the regions outside the “cusp” (Figure 5.14b), exactly as in the collapse of two-dimensional X-points. The current density appears to extend principally along the fan, but also very faintly along the spine (Figure 5.14c). The current density vector in this case points in the direction of the x -axis, i.e. perpendicular to the plane we show here, as in two dimensions. Hence, apart from the asymmetry of the current enhancements, this is also similar to the 2D behaviour we saw in the previous chapter. Finally, the entropy (p/ρ^γ) is maximum at the location of the null, as it is in the 2D case, and it extends along the fan plane, and along what appears to be the axis of the central current layer. Hence, it is at these locations where the main viscous dissipation has occurred.

In Figure 5.15a, we show a surface plot of the current density in the same plane as the contour plot in Figure 5.14c, confirming that the current density is enhanced mainly along this cut of the fan plane, and faintly along the spine. At the null, the current shows a spike, indicating that a singular current may be being formed. Figure 5.15b shows one-dimensional plots of the current density perpendicular to the fan at different points, in the same plane as before, $x = 0$. These results may be compared with the finite width of the current accumulations obtained in the two-dimensional X-point collapse. However, the resolution of the 3D experiments is insufficient, and the current in the fan has a width of 5 or 6 resolution elements. This result is then inconclusive.

We now look at the geometry of the fan plane itself. Initially, the fan is a plane defined by the equation (5.4.4), but in the final state, the surface of the fan is not planar. In order to appreciate the shape of the fan surface in the final state, Figure 5.16 shows a plot of the deformation of the fan surface from the initial state. The fan deforms towards the spine, upwards for positive values of y , and downwards for negative values of y , but is symmetric with respect to the $x = 0$ plane. Note, that the field is line-tied at the boundaries of the domain, thus the fan is forced to recover its initial position at the four edges.

The structure of the current density in the fan surface at the final equilibrium state is shown in Figure 5.17a. The current density over all the fan surface is larger than in the rest of the three dimensional domain, but we see that the largest values are along the x -axis, at $y = 0$, which is the tilt-axis. The absolute maximum is at the location of the null (Figure 5.15a). Near the null, the current has a layer of finite length extending along the axis of tilt. Similarly, the entropy (p/ρ^γ) in the fan plane has its higher values at the location of the current layer that forms about the null (Figure 5.17b).

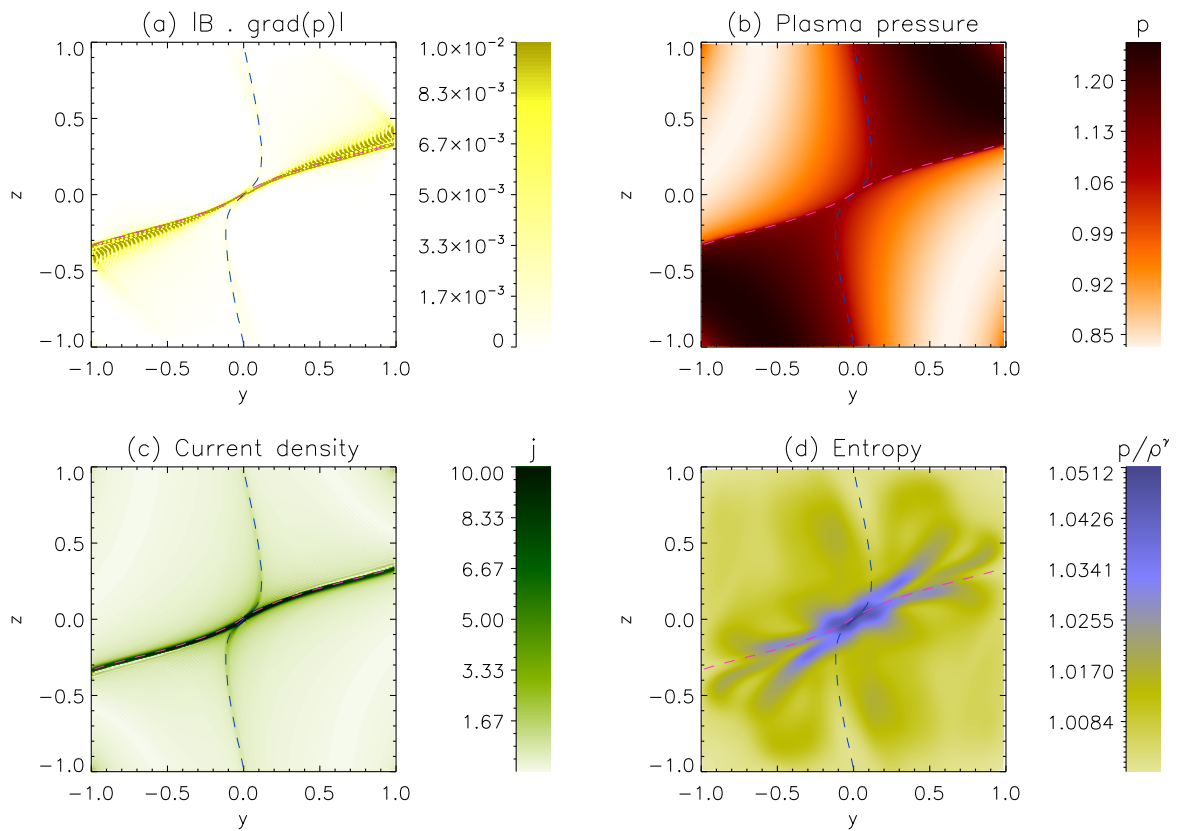


Figure 5.14: Contour plots of (a) $|\mathbf{B} \cdot \nabla p|$, (b) plasma pressure, (c) current density and (d) p/ρ^γ , in the yz -plane at $x = 0$, for the same experiment as in Figure 5.11. The pink dashed line shows the intersection of the fan plane, and the blue dashed line shows the spine.

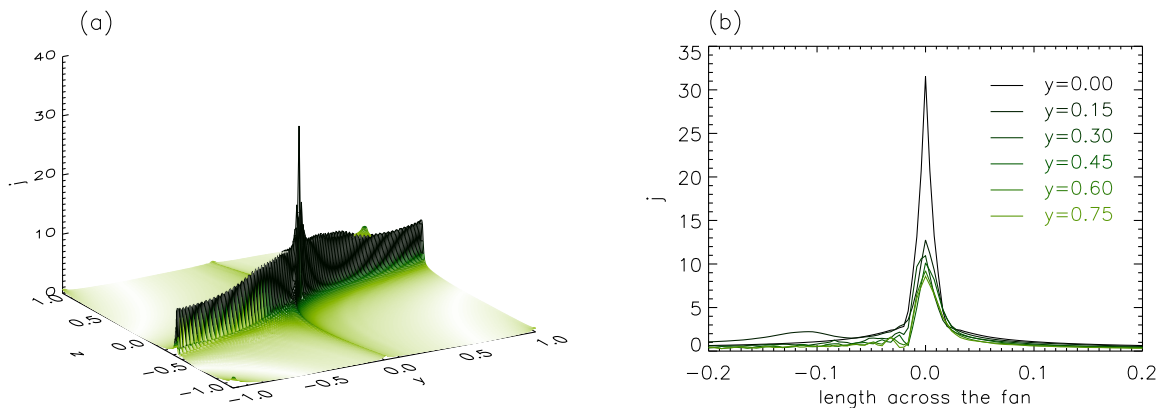


Figure 5.15: Current density in the plane $x = 0$, for the same experiment as in Figure 5.11, showing, (a) a surface plot of j , equivalent to the contour plot in Figure 5.14c, and (b) plots of current density across the fan surface for cuts perpendicular to it. Highlighted in the plot, we show the value of y at which each cut crosses the fan. The plots are centered at the location of the fan surface.

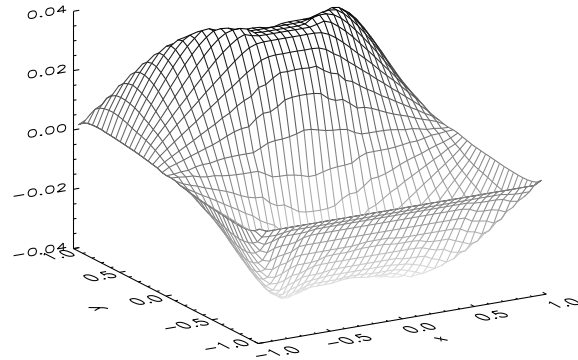


Figure 5.16: Fan surface at the final state, with the initial homogeneous tilt subtracted at each point.

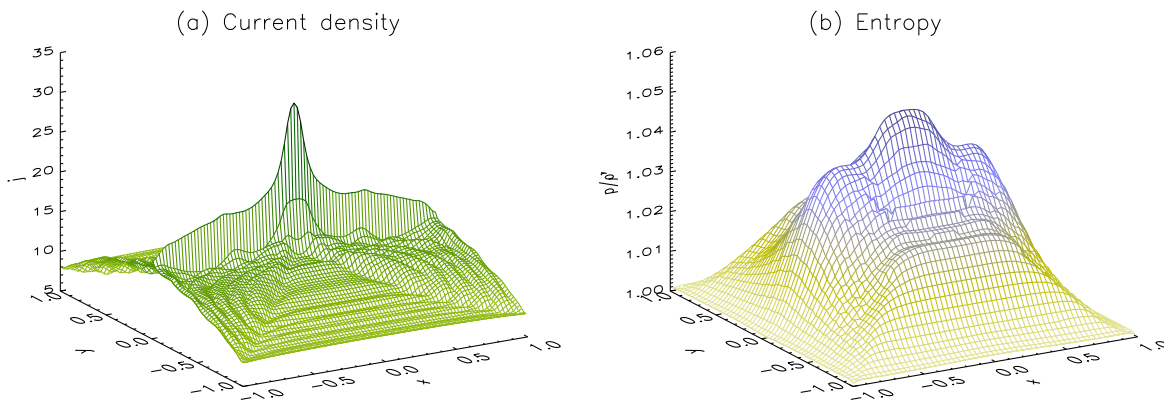


Figure 5.17: Surface plots of (a) current density and (b) p/ρ^γ , for the same experiment as in Figure 5.11, in the fan surface.

In Figures 5.14c, 5.15a and 5.17a, it looks like a current singularity may be trying to form. In the next section we investigate the formation of such a singularity.

5.4.3 Current singularity

The formation of current singularities at line-tied 3D null points in non-resistive magnetohydrodynamics has been studied by Pontin and Craig (2005). They show how these current singularities are formed in an equivalent manner to that in two dimensions, using a frictional code with no heating term. In agreement with their study, we find that the current density spreads mainly over the fan surface, with a smaller amount also concentrating along the spine, as shown in Figure 5.15.

In our two-dimensional results from Chapter 4, we investigated the formation of a singular current at the location of the null. It was found that small residual forces remained, concentrated about the null, stretching the

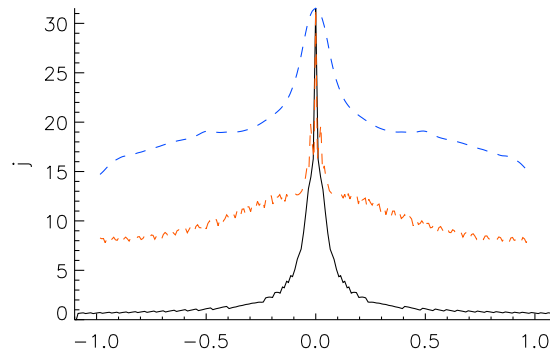


Figure 5.18: Current density along the spine (black-solid), along the tilt-axis of the fan (blue-dashed) and along the y -axis of the fan (orange-dashed), for the same experiment as in Figure 5.11

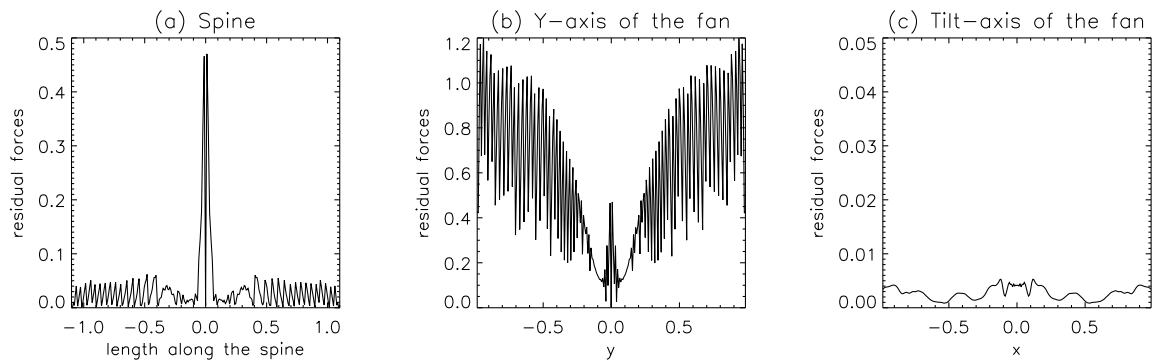


Figure 5.19: Magnitude of the residual forces (a) along the spine, (b) along the tilt-axis of the fan and (c) along the y -axis of the fan.

current layer in one direction and trying to converge it to a singularity in the other. Furthermore, as the grid resolution increased, so did the forces. Also, as the system evolved, the peak current kept slowly increasing. We aim to do a similar analysis for our three-dimensional null point. In Figure 5.18, we show plots of current density along the spine, along the x -axis of the fan surface (tilt-axis), and along the y -axis of the fan surface. Along the spine, a broad gradual increase of current over 0.3 length units from the null sees the current rise up from 0.7 to 13 before it peaks at over 30 at the null itself. This first broad enhancement is partly associated with the current accumulation about the fan plane. After that, the current shows a spike, which reveals the formation of the singularity at the null. The region in which the current distribution along the spine coincides with the current distribution along the y -axis of the fan is the region in which both the fan and spine lie concurrently, and where the singularity is to be formed.

By evaluating the residual forces, we expect to see a further indication of the formation of a singularity, but the low resolution of the experiments does not allow a conclusive result. The total forces evaluated along the spine show a sudden increase about the null, but are nearly zero at the exact location of the null itself (Figure 5.19a).

These may indicate the formation of a singularity, as studied in the two-dimensional case. However, the fan shows higher residual forces away from the null (Figure 5.19b), except in the axis of tilt of the fan, in which the forces are minima (Figure 5.19c). The reason why these forces are not sufficiently small is because they lie within the numerical error of the finite difference derivatives. The use of higher resolution runs is necessary for a firmer conclusion.

5.4.4 Changes in current density and plasma pressure

Finally, we discuss how the previous results vary when the initial current density and initial plasma pressure are varied, and compare our results to those of Pontin and Craig (2005). Pontin and Craig (2005) find a reduction in the peak current when the plasma pressure is increased.

Following the investigation of Craig and Litvinenko (2005) for the two-dimensional X-point relaxation, Pontin and Craig (2005) evaluate the scaling of the peak current density with the numerical grid size. As before, this scaling law does not make sense in our full MHD numerical experiment, as the equations do not permit the peak current to achieve a genuine singularity, but keeps slowly increasing as more time elapses.

First, from equation (5.4.4), the initial disturbance of the field (tilt of the fan) is defined by the magnitude of the initial constant current density. The higher the initial current density, the higher the angle of tilt. We find that the deformation of the spine in the final state directly depends on the steepness of the initial fan plane. The larger the initial current the greater the deformation (curvature) of the fan and the spine (Figure 5.20a). Similarly, a larger initial magnitude of the initial current density produces a steeper initial inclination and a bigger deformation of the fan plane (Figure 5.20b). The shape of the singularity along the spine for the two experiments with $j_0 = 0.5$ and 1.0 is shown in Figures 5.20c and d. Here we see that the strength of the singularity increases when increasing the initial current, and a clear well defined spike is only observed for the smaller values of j_0 , as the current layer gets broader for larger values of the initial current.

Changes in the initial background plasma pressure do not affect the the initial tilt of the fan surface, but they affect the final collapse of the fan and spine towards the null by varying the degree of the deformation (Figure 5.21a-b). It can be seen that a larger initial magnitude of the plasma pressure produces a smaller deformation of the fan plane and the spine line. This is not surprising since the plasma acts to reduce the effects of the initial Lorentz force, preventing a collapse in the null. The suppression of the current layer and singularity as the plasma pressure decreases is also seen in Figure 5.21c and d, where a weaker current in the fan surface and at the null is seen for a smaller plasma pressure.

Overall, the results are similar to that of the relaxation of two-dimensional magnetic X-points. The singularity becomes less pronounced if the initial current density is decreased, or the initial plasma pressure (and hence, the plasma beta) is increased.

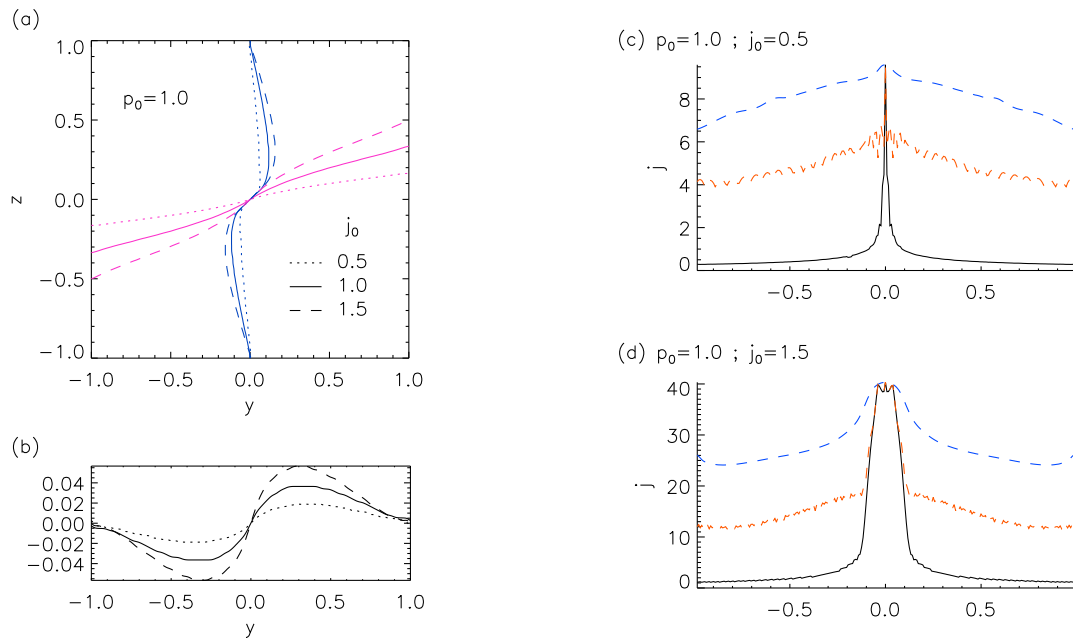


Figure 5.20: Dependence with current density, showing (a) fan (pink) and spine (blue) in the plane $x = 0$ for $j_0 = 0.5, 1.0, 1.5$, (b) shapes of the fan surfaces, after subtracting the initial tilt, and (c) and (d), current density along the spine (black-solid) and along the tilt-axis (blue-dashed) and y -axis (orange-dashed) in the fan plane, for two of the experiments, with $j_0 = 0.5$ and 1.5 .

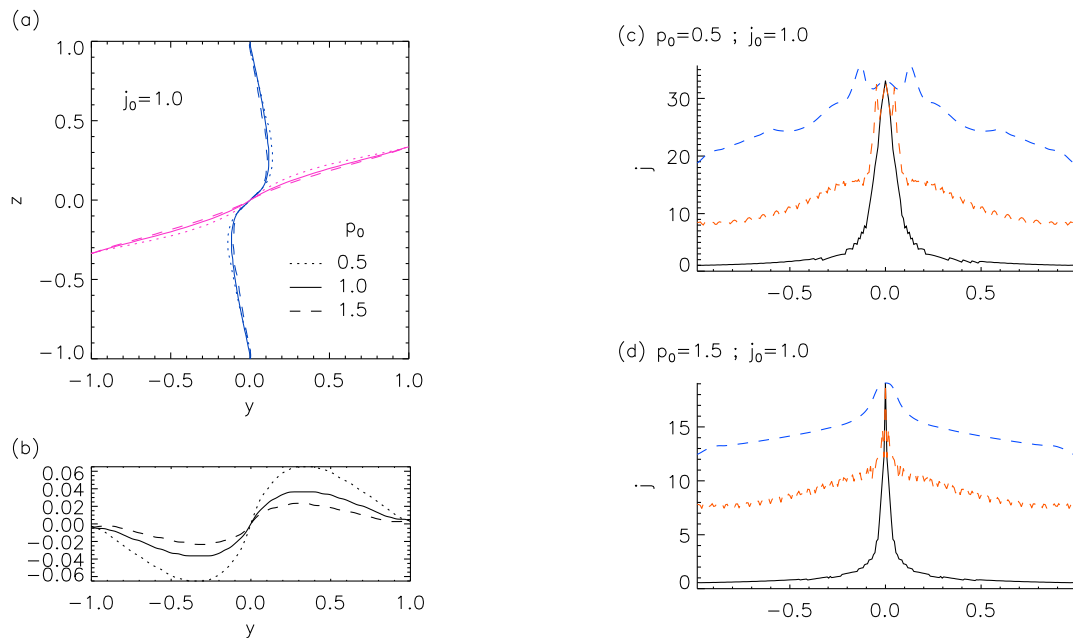


Figure 5.21: Dependence with plasma pressure, showing (a) fan (pink) and spine (blue) in the plane $x = 0$ for (a) $p_0 = 0.5, 1.0, 1.5$, (b) shapes of the fan surfaces, after subtracting the initial tilt, and (c) and (d) current density along the spine (black-solid) and along the tilt-axis (blue-dashed) and y -axis (orange-dashed) in the fan plane, for the two experiments with $p_0 = 0.5$ and 1.5 .

5.4.5 Overview

In the last set of experiments of this thesis, we have considered the dynamical evolution of three-dimensional magnetic null points with a shear-type perturbation in which the fan plane is tilted with respect to the spine, about a given axis. An initially homogeneous current density, perpendicular to the spine, pointing along the x -axis, evolves in time by collapsing the spine and the fan surface towards each other. The current density remains purely along the x -axis and it is accumulated around the final surface of the fan, and also along the spine, although with a much smaller magnitude. A large and very localised three-dimensional current layer with finite dimensions is formed about the null. It is found that this layer is wider in the direction of the tilt-axis of the fan, while it has a similar form along the spine and along the y -axis of the fan, in the region in which both the spine and the fan lie concurrently.

The $x = 0$ plane, to which the current density vector is perpendicular, shows a very similar structure to the two-dimensional case: (1) a cusp-like enhancement in current is found outlining the fan surface and the spine, (2) pressure is enhanced in the regions inside the cusp, (3) entropy peaks at the location of the null, (4) the current density tries to become singular at the null, but a true singularity is not possible to reach numerically, so instead a pronounced spike in current is seen about which small residual forces are trying to converge the current to a singular value.

The effects of decreasing the current density or increasing the plasma pressure are, first, to lessen the collapse of the spine and the fan, and second, to decrease the strength of the singularity at the three-dimensional null point, but producing a narrower layer about the null. These results agree qualitatively with Pontin and Craig (2005), but, as in the two-dimensional case, an evaluation of the magnitude of the peak current is not of any use, as in our case, residual forces keep feeding current to the null, trying to achieve an “impossible” singularity. The field is therefore in a quasi-static equilibrium, but strictly speaking, an equilibrium is impossible to be reached using an ideal MHD evolution (this is also true in the 2D X-point collapse).

In the last chapter, after giving a brief summary of the results found in this thesis, we discuss the implications of the equilibrium states found in two-dimensional X-points and three-dimensional magnetic nulls for current sheet formation and magnetic reconnection, which, in a resistive medium, would occur around the locations of large current density accumulations.

Chapter 6

Conclusions and Future Work

6.1 Discussion

In this thesis, the dynamical relaxation of four different hydromagnetic environments to static equilibria have been studied in detail, under the assumptions of zero resistivity and zero gravity, but taking viscous terms into consideration as mechanisms for damping velocities and heating the plasma. In each case, the initial state has been set up as a certain type of disturbance to a potential equilibrium, with no initial flows. The domain of study has been set to be closed for all the plasma and magnetic quantities. We have then analysed the electric current density accumulations at the final equilibrium states, which, in all cases, are non-force-free in nature, and thus the plasma pressure gradients are able to hold finite thick current layers at localised regions. We now summarise the results obtained in this thesis and give some conclusions for the four sets of experiments, being, the relaxation of parallel magnetic fields, of 2D magnetic X-points, and of 3D magnetic nulls with spine-aligned and fan-aligned current.

6.1.1 Results overview

Parallel magnetic fields

In Section 3, we have presented analytical and numerical calculations for the two and three dimensional evolution of untwisted magnetic fields embedded in a non-zero beta plasma (i.e. in a plasma with non-negligible pressure). The problem has been approached analytically by using a linear approximation to the equations, which allows the solution to be Fourier decomposed into a whole family of independent harmonic modes. To do this analytically meant that the heating terms had to be neglected, and the final equilibrium is found to depend uniquely on the redistribution of the total pressure. In the final equilibrium, non-zero plasma pressure forces are balanced with magnetic pressure forces, and hence, the equilibrium reached after the relaxation is non-force-free. We find that, in comparison to the numerical MHD results including viscous heating, the linear regime is well behaved for a wide range of amplitudes of the initial perturbations, due to the simple uniform field structure of the system. Indeed, the linear regime correctly predicts the behaviour of the plasma pressure for initial perturbations that are many times the equilibrium values, although it struggles to predict the plasma density correctly for any perturbations that are not small. However, using a condition of adiabaticity (i.e. assuming zero energy conversion), a fairly good result is found also for the plasma density. This is because the effects resulting from the viscous heating do not become important for a wide range of amplitudes of the initial disturbances.

2D magnetic X-points

In Section 4, we have studied the non-resistive relaxation of two-dimensional magnetic X-points embedded in non-zero beta plasmas. In the final equilibria, the initial magnetic X-point collapses to a pair of cusp-points in which the electric current density accumulates at the location of the null and around the four separatrices. The plasma pressure is enhanced in the regions inside the cusps and decreased outside them. The resulting field may be far from the potential description given by Green (1965), where an infinitesimally thin current sheet contains the entire current of the domain, and the field is potential everywhere else. Instead of a thin current sheet, we obtain a thick current layer with finite length and width. Such a finite thickness current layer is created because the plasma pressure gradients are able to hold a non-zero current density and balance the non-zero magnetic forces in the layer. The current accumulations at the null become thinner and more elongated as the plasma pressure is decreased. Moreover, when comparing the experiments with different values of the plasma pressure, the current distributions along the current layer intersect exactly at the extremes of the corresponding Green's current sheet, suggesting that the current may ultimately converge to Green's solution at the limit $p_0 \rightarrow 0$.

It is well known that the collapse of a two-dimensional X-point leads to a build up of current to form a singularity at the location of the null (e.g. Rastätter et al., 1994; Bungey and Priest, 1995; Craig and Litvinenko, 2005), where reconnection occurs in a resistive medium. We confirm the formation of this singularity, in non-force-free equilibria, but we note that this state is numerically impossible to reach due to the constraint of the grid resolution. Small residual forces about the null keep feeding current density into it, and hence, in contrast to the results of Craig and Litvinenko (2005), the strength of the singularity is not well defined by evaluating the peak current. Instead, we attempt to describe the nature of the singularity in the final equilibrium by following the description given by Vekstein and Priest (1993) for force-free sheared magnetic fields containing X-points. They suggest a form for the angle along the separatrix as $\theta = Kr^\beta$, where (r, θ) are the poloidal coordinates centered at the origin of the cusp, and for the flux function inside the cusp as $A_z = r^\alpha f(\theta/Kr^\beta)$, and combine them to give an equilibrium of the form

$$j_z = mA_z^{-n}, \quad (6.1.1)$$

with $n > 0$, so the current has a singularity at $A_z = 0$. Then they match the solution with a potential configuration outside the cusp. Unfortunately, we find that their results are not entirely valid for our case for several reasons. Their expression for the angle of the separatrices does not match our numerical results, and we do not have a potential field anywhere in the domain. However, we use a fit to equation (6.1.1) for the current density as a function of the flux function, A_z , and we find a fair match which gives a qualitative systematic dependence of the shape of the singularity with the initial quantities. We evaluate the dependence of the coefficients m and the exponents n for different values of the initial current density and the initial plasma pressure. This works well both inside and outside the cusp, but the parameters are different, so the field behaves differently, in both regions. We fit the dependence of these two parameters on the initial plasma pressure to exponential functions of the form

$$\begin{aligned} m &= -A(e^{-Bp_0} - 1), \\ n &= C(e^{-Dp_0} - 1) + E, \end{aligned}$$

where (A, B, C, D, E) are parameters which depend on the initial current density, and are different for the inside and outside regions of the cusp. We are not able to conclude anything definitive from these results, except for the fact that they preserve the monotonicity with initial current density.

3D magnetic nulls

In Section 5, we study the non-resistive relaxation of two configurations of three-dimensional magnetic null points, with a rotational and a shearing disturbance of the field. In the first case, we find a current accumulation along the line of the spine, and directed parallel to the spine. In the second case, the current accumulates in the fan plane predominantly and also faintly along the spine, but it is directed perpendicular to the spine and the angle of tilt of the fan surface.

In the first set of experiments, an initial overall twist of the field lines evolves by concentrating the twist and hence the current along the spine. We find the current to be essentially zero at the fan plane, except at the null point, where it may have a non-zero value which cannot be confirmed within our numerical resolution. The current along the spine appears to increase linearly from the null point, at a rate that is proportional to the initial value of the current density. The final equilibrium state seems to be independent of the initial plasma pressure, and only when the plasma pressure is varied by a large amount do we find a weak variation of the final current redistribution.

In the second set of experiments, a tilt of the fan plane with respect to the spine causes the spine and fan to collapse to each other in a similar way to the two-dimensional X-point separatrixes, finding a similar redistribution of the thermal quantities to that of the 2D case. Current density is enhanced along the fan, and also weakly along the spine. As discussed in Pontin and Craig (2005), the current has a singularity at the location of the null. But again, in contrast with their study, residual forces feed the singularity to a state which is impossible to be reached by numerical means, and hence the value of the peak current is not well defined at the final equilibrium.

6.1.2 Implications for current sheet formation and magnetic reconnection

The dynamical processes studied in this thesis about two and three dimensional magnetic null points, with line tied boundaries, lead in all cases to high current density accumulations at specific locations. These are not infinitesimally thin current sheets, rather they are current layers with a finite width and length, which do not contain the whole current of the numerical domain. In a real plasma, these localised regions with high current density would mean that the electric resistivity can no longer be ignored, and would lead to magnetic reconnection processes.

In both the two-dimensional X-point experiments and the three-dimensional shearing experiments, the separatrixes collapse to each other and the current builds a singularity at the exact location of the null point. Reconnection in these cases would lead to changes in the overall topology of the magnetic field, and hence, to flux transport across the separatrixes. However, the singularity weakens and the current density layer becomes thicker when the plasma pressure is increased. This suggests that the presence of a high-beta plasma may inhibit the formation of current layers and hence weakens (slow down) any reconnection, making it harder to rapidly release the large amounts of magnetic energy required for eruptive events in solar and magnetospheric plasmas.

For the three-dimensional torsional null experiments, no infinite singular current density is created, instead the current is mainly accumulated along and about the spine. Such a current accumulation would lead to the torsional spine reconnection studied in Pontin et al. (2004) and Wyper and Jain (2010). This type of reconnection does not change the global topology of the field, and does not allow flow through the separatrixes. It causes the slippage of the field lines around the spine, dissipating the twist of the field and hence the current density there. We have found that the current accumulations do not depend strongly on the initial plasma pressure, and hence, the twist around the spine is independent of it. This suggests that reconnection in this case is not strongly affected by the presence of high beta plasmas, and can occur regardless of the value of the plasma pressure.

6.1.3 General conclusions

The interaction between plasma forces and magnetic forces matters when studying the dynamics of a hydromagnetic medium. The energetics of the processes are significant, because the transfer from one type of energy to another can affect the evolution of the system.

The study of non-resistive evolutions in suitable environments for magnetic reconnection is a useful tool to understand the consequences that changes in plasma environments may have on the process of release of magnetic energy. By doing this we can predict in which environments magnetic reconnection will be more or less effective, and what thermal quantities constrain the dissipation of the energy stored by the magnetic fields.

In the cases where an infinite singularity is formed at a null point, it is numerically impossible to reach a perfect equilibrium, because the singularity is not accessible due to the finite grid resolution. In locations outside the null point, the field achieves a good static equilibrium, within numerical error, so the field can be described (in the 2D case), at least qualitatively, by using a singular power law whose parameters that depend exponentially with the initial plasma pressure. On the other hand, we have found that for torsional disturbances, the value of the plasma pressure has low relevance for the final redistribution of the current, and hence, for reconnection.

Magnetic reconnection is an important process of energy release in scenarios like the solar corona and the Earth's magnetotail. In the second case, it provides a mechanism for particle acceleration and for the global aurora mechanism. In the first case, it is the mechanism for solar flares and CME's and is highly likely to be a key mechanism providing a source of energy for the high temperatures observed in the corona, although it competes with numerous other models involving magnetoacoustic waves coming from inside the Sun (see Walsh and Ireland, 2003; Hood, 2010). Therefore, many studies are currently being carried out in many different reconnection environments, and are using different approaches. The detailed studies of the characteristic of the most fundamental processes such as current sheet formation are crucial.

6.2 Future work

The work presented in this thesis leaves several open paths, in different directions, for future studies. First, our analytical attempts to describe the field around a two-dimensional magnetic X-point, lack a physical explanation and cannot be given more than a mere qualitative character. The problem can be approached from other start points. For instance, Vainshtein (1990) proposed a description of the field about special magnetic points in two-dimensions, such as cusp points at the ends of thin current sheets, seeking a solution at small r of the form

$$A_z(r, \theta) = r^{\alpha_1} g_1(\theta) + r^{\alpha_2} g_2(\theta) + \dots$$

with $1 \leq \alpha_1 < \alpha_2 < \dots$, thus avoiding $A_z \rightarrow \infty$ when $r \rightarrow 0$.

One such form of this may be

$$A_z(r, \theta) = a_0 r^{p_0} + a_1 r^{p_1} \cos(2\theta) + a_2 r^{p_2} g(\theta), \quad (6.2.1)$$

with $1 \leq p_0 < p_1 < p_2$. The current density is then given given by $j_z = -\nabla^2 A_z = m A_z^{-n}$. But then, the form for $g(\theta)$ is not trivial. We plan a further investigation of this approach.

The work in three-dimensional magnetic nulls, on the other hand, has been analysed in less detail. Higher resolution experiments and a wider range of values for the initial quantities would provide tools for making a more comparative analysis to the one made in 2D X-points. Also, we only cover here two null point configurations, but do not consider the entire family of magnetic structures around three-dimensional nulls. For instance, considering deformations of improper non-radial nulls, or mixing rotational and shearing disturbances together.

Once the final state of our numerical simulations is well understood, we may “switch on” the resistivity in the equations of our numerical code, and study the reconnection processes and the amount of energy transferred to the plasma in the cases with different plasma betas, comparing these to the parameters that define the non-resistive equilibria obtained within this thesis.

Finally, the work done here can be extended to more complex scenarios in two and three-dimensions including a wider family of magnetic null points, and involving magnetic fields with multiple nulls. For instance, one such field is one including two 3D null points and a single magnetic separator, which is the line determined by the intersection of two separatrix surfaces (which are the extensions of the fan planes), and join a positive null to a negative one (Figure 6.1). The relaxation in this kind of environments may then be compared in detail with studies of separator reconnection (e.g. Parnell et al., 2010).

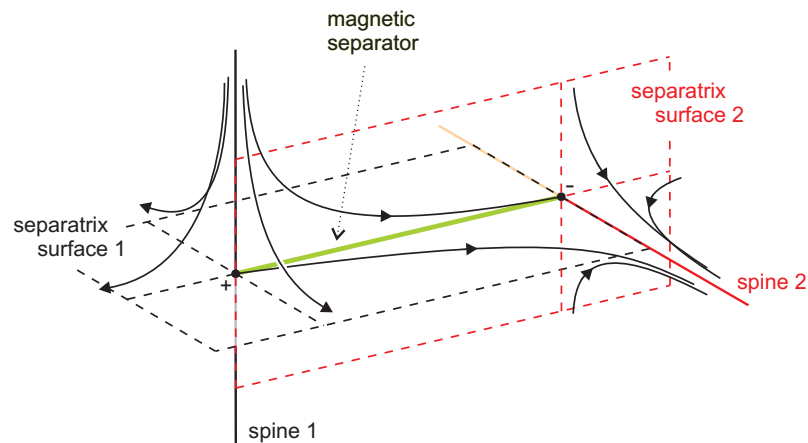


Figure 6.1: Sketch of magnetic separator in 3D.

Bibliography

- Al-Salti, N., T. Neukirch, and R. Ryan, Three-dimensional solutions of the magnetohydrostatic equations: rigidly rotating magnetized coronae in cylindrical geometry, *Astronomy and Astrophysics*, 514, A38, 2010.
- Alfvén, H., Existence of Electromagnetic-Hydrodynamic Waves, *Nature*, 150, 405–406, 1942.
- Altschuler, M. D., and G. Newkirk, Magnetic Fields and the Structure of the Solar Corona. I: Methods of Calculating Coronal Fields, *Solar Physics*, 9, 131–149, 1969.
- Amari, T., T. Z. Boulmezaoud, and Y. Maday, A regularization method for the extrapolationbreak of the photospheric solar magnetic field. I. Linear force-free field, *Astronomy and Astrophysics*, 339, 252–260, 1998.
- Antiochos, S. K., C. R. DeVore, and J. A. Klimchuk, A Model for Solar Coronal Mass Ejections, *Astrophysical Journal*, 510, 485–493, 1999.
- Arber, T. D., A. W. Longbottom, C. L. Gerrard, and A. M. Milne, A Staggered Grid, Lagrangian-Eulerian Remap Code for 3-D MHD Simulations, *Journal of Computational Physics*, 171, 151–181, 2001.
- Benson, D. J., Computational Methods in Lagrangian and Eulerian Hydrocodes, *Computer Methods in Applied Mechanics and Engineering*, 99, 235–394, 1992.
- Bhattacharyya, R., M. S. Janaki, B. Dasgupta, and G. P. Zank, Solar Arcades as Possible Minimum Dissipative Relaxed States, *Solar Physics*, 240, 63–76, 2007.
- Birn, J., Three-dimensional magnetotail equilibria with prescribed boundary shapes, *Journal of Geophysical Research (Space Physics)*, 110, 7203, 2005.
- Birn, J., and E. R. Priest, *Reconnection of magnetic fields : magnetohydrodynamics and collisionless theory and observations*, 2007.
- Birn, J., K. Schindler, and M. Hesse, Formation of thin current sheets in the magnetotail: Effects of propagating boundary deformations, *Journal of Geophysical Research (Space Physics)*, 108, 1337, 2003.
- Biskamp, D., Magnetic Reconnection Via Current Sheets (Invited paper), *Magnetic Reconnection and Turbulence*, 19, 1986.
- Biskamp, D., *Nonlinear magnetohydrodynamics*, 1993.
- Bittencourt, J. A., *Fundamentals of Plasma Physics*, Springer-Verlag, 2004.
- Bogdan, T. J., and B. C. Low, The three-dimensional structure of magnetostatic atmospheres. II - Modeling the large-scale corona, *Astrophysical Journal*, 306, 271–283, 1986.
- Browning, P. K., C. Gerrard, A. W. Hood, R. Kevis, and R. A. M. van der Linden, Heating the corona by nanoflares:

- simulations of energy release triggered by a kink instability, *Astronomy and Astrophysics*, 485, 837–848, 2008.
- Bungey, T. N., and E. R. Priest, Current sheet configurations in potential and force-free fields., *Astronomy and Astrophysics*, 293, 215–224, 1995.
- Burlaga, L. F., *Interplanetary magnetohydrodynamics.*, 1995.
- Courant, R., K. Friederichs, and H. Lewy, Über die partiellen Differenzgleichungen der mathematischen Physik, *Mathematische Annalen*, pp. 215–234, 1928.
- Courant, R., K. Friederichs, and H. Lewy, On the partial difference equations of mathematical physics, *IBM Journal*, 100, 32–74, 1967.
- Cowling, T. G., Solar Electrodynamics, in *The Sun*, edited by Kuiper, G. P., p. 532, 1953, 1953.
- Craig, I. J. D., Current sheet formation and dissipation in general X-point topologies, *Astronomy and Astrophysics*, 283, 331–338, 1994.
- Craig, I. J. D., and Y. E. Litvinenko, Current singularities in planar magnetic X points of finite compressibility, *Physics of Plasmas*, 12, 2005.
- Dasgupta, B., P. Dasgupta, M. S. Janaki, T. Watanabe, and T. Sato, Relaxed States of a Magnetized Plasma with Minimum Dissipation, *Physical Review Letters*, 81, 3144–3147, 1998.
- Davidson, P. A., *An Introduction to Magnetohydrodynamics*, 2001.
- De Rosa, M. L., C. J. Schrijver, G. Barnes, K. D. Leka, B. W. Lites, M. J. Aschwanden, T. Amari, A. Canou, J. M. McTiernan, S. Régnier, J. K. Thalmann, G. Valori, M. S. Wheatland, T. Wiegmann, M. C. M. Cheung, P. A. Conlon, M. Fuhrmann, B. Inhester, and T. Tadesse, A Critical Assessment of Nonlinear Force-Free Field Modeling of the Solar Corona for Active Region 10953, *Astrophysical Journal*, 696, 1780–1791, 2009.
- Dungey, J. W., Conditions for the occurrence of electrical discharges in astrophysical systems, *Philosophical Magazine*, 44, 725–738, 1953.
- Edenstrasser, J. W., Unified treatment of symmetric MHD equilibria, *Journal of Plasma Physics*, 24, 299–313, 1980a.
- Edenstrasser, J. W., The only three classes of symmetric MHD equilibria, *Journal of Plasma Physics*, 24, 515–518, 1980b.
- Evans, C. R., and J. F. Hawley, Simulation of magnetohydrodynamic flows - A constrained transport method, *Astrophysical Journal*, 332, 659–677, 1988.
- Fletcher, L., T. R. Metcalf, D. Alexander, D. S. Brown, and L. A. Ryder, Evidence for the Flare Trigger Site and Three-Dimensional Reconnection in Multiwavelength Observations of a Solar Flare, *Astrophysical Journal*, 554, 451–463, 2001.
- Forbes, T. G., J. A. Linker, J. Chen, C. Cid, J. Kóta, M. A. Lee, G. Mann, Z. Mikić, M. S. Potgieter, J. M. Schmidt, G. L. Siscoe, R. Vainio, S. K. Antiochos, and P. Riley, CME Theory and Models, *Space Science Reviews*, 123, 251–302, 2006.
- Fuentes-Fernández, J., C. E. Parnell, and A. W. Hood, Magnetohydrodynamics dynamical relaxation of coronal magnetic fields . I. Parallel untwisted magnetic fields in 2D, *Astronomy and Astrophysics*, 514, A90, 2010.
- Furth, H. P., J. Killeen, and M. N. Rosenbluth, Finite resistivity instabilities of a sheet pinch, *Phys. Fluids*, 6,

- 459–484, 1963.
- Gary, G. A., Potential Field Extrapolation Using Three Components of a Solar Vector Magnetogram with a Finite Field of View, *Solar Physics*, 163, 43–64, 1996.
- Gary, G. A., Plasma Beta above a Solar Active Region: Rethinking the Paradigm, *Solar Physics*, 203, 71–86, 2001.
- Gary, G. A., Evaluation of a Selected Case of the Minimum Dissipative Rate Method for Non-Force-Free Solar Magnetic Field Extrapolations, *Solar Physics*, 257, 271–286, 2009.
- Green, R. M., Modes on annihilation and reconnection in magnetic fields, *Stellar and Solar Magnetic Fields*, pp. 398–404, 1965.
- Habbal, S. R., M. Druckmüller, H. Morgan, I. Scholl, V. Rušin, A. Daw, J. Johnson, and M. Arndt, Total Solar Eclipse Observations of Hot Prominence Shrouds, *Astrophysical Journal*, 719, 1362–1369, 2010.
- Harris, E. G., On a plasma sheath separating regions of oppositely directed magnetic field, *Il Nuovo Cimento*, 1, 115–121, 1962.
- Harrison, M. G., and T. Neukirch, One-Dimensional Vlasov-Maxwell Equilibrium for the Force-Free Harris Sheet, *Physical Review Letters*, 102(13), 135003, 2009.
- Hesse, M., and J. Birn, Three-dimensional magnetotail equilibria by numerical relaxation techniques, *Journal of Geophysical Research*, 98, 3973–3982, 1993.
- Hesse, M., and K. Schindler, A theoretical foundation of general magnetic reconnection, *Journal of Geophysical Research*, 93, 5559–5567, 1988.
- Hesse, M., and K. Schindler, The onset of magnetic reconnection in the magnetotail, *Earth, Planets, and Space*, 53, 645–653, 2001.
- Heyvaerts, J., and E. R. Priest, Coronal heating by reconnection in DC current systems - A theory based on Taylor's hypothesis, *Astronomy and Astrophysics*, 137, 63–78, 1984.
- Hoeksema, J. T., Large-scale solar and heliospheric magnetic fields, *Advances in Space Research*, 11, 15–24, 1991.
- Hood, A. W., Coronal Heating, *Lecture Notes in Physics*, Berlin Springer Verlag, vol. 793 of *Lecture Notes in Physics*, Berlin Springer Verlag, 109, 2010.
- Hood, A. W., P. K. Browning, and R. A. M. van der Linden, Coronal heating by magnetic reconnection in loops with zero net current, *Astronomy and Astrophysics*, 506, 913–925, 2009.
- Inoue, S., K. Kusano, S. Masuda, T. Miyoshi, T. Yamamoto, T. Magara, T. Tsuneta, T. Sakurai, and T. Yokoyama, Three-Dimensional Structure Analysis of Coronal Magnetic Field in AR NOAA 10930 Based on Vector Magnetogram Observations with Hinode/SOT, *First Results From Hinode*, vol. 397 of *Astronomical Society of the Pacific Conference Series*, 110, 2008.
- Isaacson, E., and H. B. Keller, *Analysis of numerical methods*, 1966.
- Janse, Å. M., and B. C. Low, The Topological Changes of Solar Coronal Magnetic Fields. I. Spontaneous Current Sheets in Three-Dimensional Fields, *Astrophysical Journal*, 690, 1089–1104, 2009.
- Ji, H., G. Huang, and H. Wang, The Relaxation of Sheared Magnetic Fields: A Contracting Process, *Astrophysical Journal*, 660, 893–900, 2007.
- Lemon, C., F. Toffoletto, M. Hesse, and J. Birn, Computing magnetospheric force equilibria, *Journal of Geophys-*

- ical Research (Space Physics)*, 108, 1237, 2003.
- Longcope, D. W., Topology and Current Ribbons: A Model for Current, Reconnection and Flaring in a Complex, Evolving Corona, *Solar Physics*, 169, 91–121, 1996.
- Longcope, D. W., A Model for Current Sheets and Reconnection in X-Ray Bright Points, *Astrophysical Journal*, 507, 433–442, 1998.
- Longcope, D. W., and C. E. Parnell, The Number of Magnetic Null Points in the Quiet Sun Corona, *Solar Physics*, 254, 51–75, 2009.
- Low, B. C., Eruptive solar magnetic fields, *Astrophysical Journal*, 251, 352–363, 1981.
- Low, B. C., Magnetostatic atmospheres with variations in three dimensions, *Astrophysical Journal*, 263, 952–969, 1982a.
- Low, B. C., Magnetic field configurations associated with polarity intrusion in a solar active region. I - The force-free fields, *Solar Physics*, 77, 43–61, 1982b.
- Low, B. C., Three-dimensional magnetostatic atmospheres - Magnetic field with vertically oriented tension force, *Astrophysical Journal*, 277, 415–421, 1984.
- Low, B. C., Three-dimensional structures of magnetostatic atmospheres. I - Theory, *Astrophysical Journal*, 293, 31–43, 1985.
- Low, B. C., Models of partially open magnetospheres with and without magnetodisks, *Astrophysical Journal*, 310, 953–965, 1986.
- Low, B. C., Three-dimensional structures of magnetostatic atmospheres. III - A general formulation, *Astrophysical Journal*, 370, 427–434, 1991.
- Low, B. C., Three-dimensional structures of magnetostatic atmospheres. IV - Magnetic structures over a solar active region, *Astrophysical Journal*, 399, 300–312, 1992.
- Low, B. C., Three-dimensional structures of magnetostatic atmospheres. V - Coupled electric current systems, *Astrophysical Journal*, 408, 689–692, 1993a.
- Low, B. C., Three-dimensional structures of magnetostatic atmospheres. VI - Examples of coupled electric current systems, *Astrophysical Journal*, 408, 693–706, 1993b.
- Low, B. C., Spontaneous Current Sheets in an Ideal Hydromagnetic Fluid, *Astrophysical Journal*, 649, 1064–1077, 2006.
- Mackay, D. H., and A. A. van Ballegoijen, Models of the Large-Scale Corona. I. Formation, Evolution, and Liftoff of Magnetic Flux Ropes, *Astrophysical Journal*, 641, 577–589, 2006.
- McLaughlin, J. A., and A. W. Hood, MHD wave propagation in the neighbourhood of a two-dimensional null point, *Astronomy and Astrophysics*, 420, 1129–1140, 2004.
- McLaughlin, J. A., and A. W. Hood, MHD mode coupling in the neighbourhood of a 2D null point, *Astronomy and Astrophysics*, 459, 641–649, 2006.
- Metcalf, T. R., M. L. De Rosa, C. J. Schrijver, G. Barnes, A. A. van Ballegoijen, T. Wiegmann, M. S. Wheatland, G. Valori, and J. M. McTiernan, Nonlinear Force-Free Modeling of Coronal Magnetic Fields. II. Modeling a Filament Arcade and Simulated Chromospheric and Photospheric Vector Fields, *Solar Physics*, 247, 269–299,

- 2008.
- Miller, K., B. Fornberg, N. Flyer, and B. C. Low, Magnetic Relaxation in the Solar Corona, *Astrophysical Journal*, 690, 720–733, 2009.
- Nandy, D., M. Hahn, R. C. Canfield, and D. W. Longcope, Detection of a Taylor-like Plasma Relaxation Process in the Sun, *Astrophysical Journal*, 597, L73–L76, 2003.
- Narain, U., and P. Ulmschneider, Chromospheric and Coronal Heating Mechanisms II, *Space Science Reviews*, 75, 453–509, 1996.
- Narukage, N., H. S. Hudson, T. Morimoto, S. Akiyama, R. Kitai, H. Kurokawa, and K. Shibata, Simultaneous Observation of a Moreton Wave on 1997 November 3 in $H\alpha$ and Soft X-Rays, *Astrophysical Journal*, 572, L109–L112, 2002.
- Neukirch, T., On self-consistent three-dimensional analytic solutions of the magnetohydrostatic equations., *Astronomy and Astrophysics*, 301, 628, 1995.
- Neukirch, T., and L. Rastätter, A new method for calculating a special class of self-consistent three-dimensional magnetohydrostatic equilibria, *Astronomy and Astrophysics*, 348, 1000–1004, 1999.
- Neukirch, T., F. Wilson, and M. G. Harrison, A detailed investigation of the properties of a Vlasov-Maxwell equilibrium for the force-free Harris sheet, *Physics of Plasmas*, 16(12), 122102, 2009.
- Osterbrock, D. E., The Heating of the Solar Chromosphere, Plages, and Corona by Magnetohydrodynamic Waves., *Astrophysical Journal*, 134, 347, 1961.
- Parker, E. N., Sweet's Mechanism for Merging Magnetic Fields in Conducting Fluids, *Journal of Geophysical Research*, 62, 509–520, 1957.
- Parker, E. N., Topological Dissipation and the Small-Scale Fields in Turbulent Gases, *Astrophysical Journal*, 174, 499, 1972.
- Parnell, C. E., J. M. Smith, T. Neukirch, and E. R. Priest, The structure of three-dimensional magnetic neutral points, *Physics of Plasmas*, 3, 759, 1996.
- Parnell, C. E., T. Neukirch, J. M. Smith, and E. R. Priest, Structure and collapse of three-dimensional magnetic neutral points, *Geophysical and Astrophysical Fluid Dynamics*, 84, 245–271, 1997.
- Parnell, C. E., A. L. Haynes, and K. Galsgaard, Structure of magnetic separators and separator reconnection, *Journal of Geophysical Research (Space Physics)*, 115, 2102, 2010.
- Petrie, G. J. D., and T. Neukirch, The Green's function method for a special class of linear three-dimensional magnetohydrostatic equilibria, *Astronomy and Astrophysics*, 356, 735–746, 2000.
- Petrovay, K., and G. Szakaly, The origin of intranetwork fields: a small-scale solar dynamo, *Astronomy and Astrophysics*, 274, 543, 1993.
- Petschek, H. E., Magnetic Field Annihilation, *NASA Special Publication*, 50, 425, 1964.
- Pontin, D. I., and I. J. D. Craig, Current singularities at finitely compressible three-dimensional magnetic null points, *Physics of Plasmas*, 12, 072112, 2005.
- Pontin, D. I., G. Hornig, and E. R. Priest, Kinematic reconnection at a magnetic null point: spine-aligned current, *Geophysical and Astrophysical Fluid Dynamics*, 98, 407–428, 2004.

- Pontin, D. I., G. Hornig, and E. R. Priest, Kinematic reconnection at a magnetic null point: fan-aligned current, *Geophysical and Astrophysical Fluid Dynamics*, 99, 77–93, 2005.
- Pontin, D. I., A. Bhattacharjee, and K. Galsgaard, Current sheet formation and nonideal behavior at three-dimensional magnetic null points, *Physics of Plasmas*, 14(5), 052106, 2007a.
- Pontin, D. I., A. Bhattacharjee, and K. Galsgaard, Current sheets at three-dimensional magnetic nulls: Effect of compressibility, *Physics of Plasmas*, 14(5), 052109, 2007b.
- Pontin, D. I., G. Hornig, A. L. Wilmot-Smith, and I. J. D. Craig, Lagrangian Relaxation Schemes for Calculating Force-free Magnetic Fields, and Their Limitations, *Astrophysical Journal*, 700, 1449–1455, 2009.
- Press, W. H., S. A. Teukolsky, W. T. Vetterling, and B. P. Flannery, *Numerical recipes in FORTRAN. The art of scientific computing*, 1992.
- Priest, E., and T. Forbes, *Magnetic Reconnection*, 2000.
- Priest, E. R., *Solar magneto-hydrodynamics*, 74P pp., 1982.
- Priest, E. R., and P. Démoulin, Three-dimensional magnetic reconnection without null points. 1. Basic theory of magnetic flipping, *Journal of Geophysical Research*, 100, 23443–23464, 1995.
- Priest, E. R., and T. G. Forbes, New models for fast steady state magnetic reconnection, *Journal of Geophysical Research*, 91, 5579–5588, 1986.
- Priest, E. R., and D. I. Pontin, Three-dimensional null point reconnection regimes, *Physics of Plasmas*, 16(12), 122101, 2009.
- Priest, E. R., and M. A. Raadu, Preflare current sheets in the solar atmosphere, *Solar Physics*, 43, 177–188, 1975.
- Priest, E. R., G. Hornig, and D. I. Pontin, On the nature of three-dimensional magnetic reconnection, *Journal of Geophysical Research*, 108, 1285, 2003.
- Rastätter, L., A. Voge, and K. Schindler, On current sheets in two dimensional ideal magnetohydrodynamics caused by pressure perturbations, vol. 1, 3414, 1994.
- Régnier, S., What Can we Learn from Nonlinear Force-Free Extrapolations?, *First Results From Hinode*, vol. 397 of *Astronomical Society of the Pacific Conference Series*, 75, 2008.
- Ruan, P., T. Wiegmann, B. Inhester, T. Neukirch, S. K. Solanki, and L. Feng, A first step in reconstructing the solar corona self-consistently with a magnetohydrostatic model during solar activity minimum, *Astronomy and Astrophysics*, 481, 827–834, 2008.
- Rudenko, G. V., Extrapolation of the solar magnetic field within the potential-field approximation from full-disk magnetograms, *Solar Physics*, 198, 5–30, 2001.
- Schindler, K., and J. Birn, Magnetotail theory, *Space Sci. Rev.*, 44, 307–355, 1986.
- Schindler, K., M. Hesse, and J. Birn, General magnetic reconnection, parallel electric fields, and helicity, *Journal of Geophysical Research*, 93, 5547–5557, 1988.
- Schrijver, C. J., M. L. De Rosa, A. M. Title, and T. R. Metcalf, The Nonpotentiality of Active-Region Coronae and the Dynamics of the Photospheric Magnetic Field, *Astrophysical Journal*, 628, 501–513, 2005.
- Schrijver, C. J., M. L. De Rosa, T. R. Metcalf, Y. Liu, J. McTiernan, S. Régnier, G. Valori, M. S. Wheatland, and T. Wiegmann, Nonlinear Force-Free Modeling of Coronal Magnetic Fields Part I: A Quantitative Comparison

- of Methods, *Solar Physics*, 235, 161–190, 2006.
- Schrijver, C. J., M. L. De Rosa, T. Metcalf, G. Barnes, B. Lites, T. Tarbell, J. McTiernan, G. Valori, T. Wiegelmann, M. S. Wheatland, T. Amari, G. Aulanier, P. Démoulin, M. Fuhrmann, K. Kusano, S. Régnier, and J. K. Thalmann, Nonlinear Force-free Field Modeling of a Solar Active Region around the Time of a Major Flare and Coronal Mass Ejection, *Astrophysical Journal*, 675, 1637–1644, 2008.
- Somov, B. V., and S. I. Syrovatskii, Hydrodynamic plasma flow in a strong magnetic field, *Neutral Current Sheets on Plasmas*, pp. 13–72, 1976.
- Sweet, P. A., The Neutral Point Theory of Solar Flares, *Electromagnetic Phenomena in Cosmical Physics*, vol. 6 of *IAU Symposium*, 123, 1958.
- Syrovatskii, S. I., On the time evolution of force-free fields, *Solar Physics*, 58, 89–94, 1978.
- Taylor, J. B., Relaxation of toroidal plasma and generation of reverse magnetic fields, *Phys. Rev. Lett.*, 33(19), 1139–1141, 1974.
- Tur, T. J., and E. R. Priest, The formation of current sheets during the emergence of new magnetic flux from below the photosphere, *Solar Physics*, 48, 89–100, 1976.
- Ugarte-Urra, I., H. P. Warren, and A. R. Winebarger, The Magnetic Topology of Coronal Mass Ejection Sources, *Astrophysical Journal*, 662, 1293–1301, 2007.
- Vainshtein, S. I., Cusp-points and current sheet dynamics, *Astronomy and Astrophysics*, 230, 238–243, 1990.
- van Ballegoijen, A. A., Electric currents in the solar corona and the existence of magnetostatic equilibrium, *Astrophysical Journal*, 298, 421–430, 1985.
- van Leer, B., Towards the Ultimate Conservative Difference Scheme, V. A Second Order Sequel to Godunov’s Method, *Journal of Computational Physics*, 32, 101–136, 1979.
- Vekstein, G., and E. R. Priest, Magnetostatic equilibria and current sheets in a sheared magnetic field with an X-point, *Solar Physics*, 146, 119–125, 1993.
- Walsh, R. W., and J. Ireland, The heating of the solar corona, *Astronomy and Astrophysics Review*, 12, 1–41, 2003.
- Wesseling, P., *Principles of Computational Fluid Dynamics*, 2001.
- Wheatland, M. S., and S. Régnier, A Self-Consistent Nonlinear Force-Free Solution for a Solar Active Region Magnetic Field, *Astrophysical Journal*, 700, L88–L91, 2009.
- Wiegelmann, T., B. Inhester, and T. Sakurai, Preprocessing of Vector Magnetograph Data for a Nonlinear Force-Free Magnetic Field Reconstruction, *Solar Physics*, 233, 215–232, 2006.
- Wiegelmann, T., J. K. Thalmann, C. J. Schrijver, M. L. De Rosa, and T. R. Metcalf, Can We Improve the Preprocessing of Photospheric Vector Magnetograms by the Inclusion of Chromospheric Observations?, *Solar Physics*, 247, 249–267, 2008.
- Woodward, P., and P. Collela, The Numerical Simulation of Two-Dimensional Fluid Flow with Strong Shocks, *Journal of Computational Physics*, 54, 115–173, 1984.
- Wyper, P., and R. Jain, Torsional magnetic reconnection at three dimensional null points: A phenomenological study, *Physics of Plasmas*, 17, 092902, 2010.
- Xiao, C. J., X. G. Wang, Z. Y. Pu, H. Zhao, J. X. Wang, Z. W. Ma, S. Y. Fu, M. G. Kivelson, Z. X. Liu, Q. G. Zong,

- K. H. Glassmeier, A. Balogh, A. Korth, H. Reme, and C. P. Escoubet, In situ evidence for the structure of the magnetic null in a 3D reconnection event in the Earth's magnetotail, *Nature Physics*, 2, 478–483, 2006.
- Zaharia, S., J. Birn, and C. Z. Cheng, Toward a global magnetospheric equilibrium model, *Journal of Geophysical Research (Space Physics)*, 110, 9228, 2005.
- Zuccarello, F. P., C. Jacobs, A. Soenen, S. Poedts, B. van der Holst, and F. Zuccarello, Modelling the initiation of coronal mass ejections: magnetic flux emergence versus shearing motions, *Astronomy and Astrophysics*, 507, 441–452, 2009.
- Zwingmann, W., K. Schindler, and J. Birn, On sheared magnetic field structures containing neutral points, *Solar Physics*, 99, 133–143, 1985.